Analysis and interpretation of Fermi Gamma-Ray Bursts in the framework of an internal shock synchrotron model, and contributions to the multi-messenger astronomy.

Lorenzo Scotton

THESIS TO OBTAIN THE GRADE OF DOCTOR

In Astrophysics

Doctoral school I2S

Research unit UMR 5299

Analysis and interpretation of *Fermi* Gamma-Ray Bursts in the framework of an internal shock synchrotron model, and contributions to the multi-messenger astronomy

Presented by Lorenzo SCOTTON

On January 18, 2023

Under the supervision of Frédéric PIRON

In front of the jury composed by

Mrs. Ana PALACIOS, Astronomer, Université de Montpellier - LUPM	President
Mrs. Sheila McBREEN, Professor, University College Dublin	Referee
Mr. Jean-Luc ATTEIA, Astronomer, Université de Toulouse - IRAP	Referee
Mrs. Elisabetta BISSALDI, Associate Professor, Politecnico and INFN Bari	Examiner
Mr. Frédéric PIRON, Director of Research, CNRS - LUPM	Supervisor

UNIVERSITÉ DE MONTPELLIER

Summary

Introduction

I performed my thesis work at the "Laboratoire Universe et Particules de Montpellier" (CNRS/IN2P3/LUPM), within the scientific team "Expériences et Modélisation en Astroparticules et Cosmologie". The scientific interest of this team spans from theoretical aspects such as the understanding of the production of ultra high-energy cosmic rays to experimental aspects such as the observations of high-energy gamma-ray transients. This team is involved in gamma-ray experiments *Fermi*, SVOM, H.E.S.S., and CTA, as well as in the ground based optical observatory Vera Rubin. The study of gamma-ray bursts (GRBs) is one of the main research topics of *Fermi* and the main one of SVOM.

The GRB field is an actively evolving scientific branch of modern gamma-ray astronomy. GRBs were discovered in the 1960s and important questions remain regarding the physical mechanisms involved in their formation. These cosmological and powerful sources are brief and extremely luminous bursts of gamma-rays, which are emitted in relatively short time scales (fractions of second to minutes). The widely accepted scenario to explain their high luminosity is the formation of a stellar mass black-hole, which acts as a central engine powering relativistic and collimated ejecta (jet). The GRB emission light curves consist of a so-called "prompt" phase (the "burst" itself), followed by the afterglow phase which lasts much longer (hours to months). In the prompt phase, the gamma-ray non-thermal emission that is produced within the jet is highly erratic and variable. In the afterglow phase, the broad-band non-thermal emission decays rapidly yet more smoothly, and it is believed to result from the interaction of the jet with the circumburst medium.

More than 14 years after the launch of the *Fermi* observatory (on June 11, 2008), its instruments are still operating at full scientific performance. These instruments, the Gamma-Ray burst Monitor (GBM) and the Large Area Telescope (LAT), were built by two international collaborations that comprise research institutions mainly in the United States, in Europe and in Japan. Together the GBM and the LAT cover more than 7 decades of energy, from 8 keV to more than 300 GeV. This broad coverage of the electromagnetic spectrum has been key to investigate the physics of GRBs. Incremental GRB catalogs have been released by the *Fermi* collaborations over the years. Several thousands of GRBs have been detected by the GBM to date, and several hundreds by the LAT. The LAT observations have renewed our understanding of GRB physics, shedding light on their properties at high energies (>100 MeV), which had been barely investigated by its predecessor CGRO/EGRET in the 1990s.

The EMAC team is involved in the Fermi/LAT collaboration and in the Fermi GRB science group. One of the service tasks is the LAT Burst Advocate (BA) activity, which consists in monitoring the high-energy transient sky and promptly analyzing the LAT data following GBM GRB alerts or external alerts on gravitational wave (GW) sources. I performed 18 BA shifts each one lasting one week. This activity helped me to strengthen my expertise in LAT GRB analysis and allowed me to participate in follow-up observations of GW sources. The results obtained in quasi-real time were distributed to the world-wide community via circulars of the Gamma-ray Coordinates Network. I contributed to the circulars for 5 GRBs, one of which is the most distant LAT detected GRB to date (GRB 220101A, z=4.618). Moreover, in the first 5 months of my thesis work I participated in the follow-up of GW events during the third LIGO-Virgo observing run. No EM counterpart was found, and flux upper limits were distributed to the community. I contributed to 7 GCN circulars reporting the LAT analysis results on these events.

The physical mechanisms at work in the prompt phase of GRBs are still a matter of debate. In the vast

majority of GRBs, the prompt non-thermal emission is dominant in the keV-MeV energy domain, yet it is sometimes accompanied by a thermal emission from the jet expanding plasma. Different scenarios for the jet acceleration and kinetic energy dissipation lead to different mixtures of these emission components, which are the central topic of this thesis.

The prompt emission spectra of GRBs are often characterized with pure mathematical functions such as the Band function. However, the inference of GRB physical properties from the Band spectral fits is prone to bias. Instead of comparing *a posteriori* the mathematical representation of GRB spectra with theoretical expectations, the use of physical models directly in spectral fits is progressively becoming standard in the community. To further this aim, I explored the internal shock model proposed by collaborators at the Institut d'Astrophysique de Paris. Their numerical model simulates the emissions from electrons accelerated by internal shocks in GRB jets, the shock dynamics and the radiative effects, based on realistic prescriptions for the jet micro-physics. In a past thesis [Yassine 2017], an analytical function named ISSM (for "Internal Shock Synchrotron Model") was built to parameterize the synthetic keV-MeV spectra provided by the numerical model in various physical configurations. I compared it to observations by performing a time-integrated and a time-resolved spectral analysis of the 460 most fluent GRBs detected by the GBM so far.

In some cases, the use of ad-hoc functions to describe the keV-MeV spectra of GRBs has highlighted an excess at low energies. Interestingly, this excess has been interpreted as the contribution of an underlying thermal component. In my work I revisited the analyses of three bursts of such type within the framework of the of the synchrotron internal shock model, and assess the significance of a possible additional thermal component fitting the ISSM model to the keV-MeV GRB spectra.

The very energetic GRB 220101A is the most distant LAT detected burst to date. At the same time it is one of the rare cases in which the spectrum is significantly attenuated at the highest energies (tens of MeV) in temporal coincidence with the main variable episode seen by the LAT. This spectral cutoff, along with the variability of the observed emission can be interpreted as the result of annihilation of high-energy photons with low-energy ones within the burst jet. The theoretical framework describing this opacity to pair creation allowed me to determine directly the speed of the ejecta and the radius at which the observed emission was produced.

This thesis manuscript is organized as follows. The GRB phenomenon is introduced in chapter 1, along with the results of the GRBs detected by *Fermi* so far. Moreover, I present the different model classes and introduce the ISSM spectral function. The *Fermi* instruments are described in chapter 2, along with the *Fermi* main results in the broad field of gamma-ray astronomy. The analysis techniques that I will use in the following chapters are also described in this chapter. The analysis of the keV-MeV emission spectra of *Fermi* GRBs is presented in chapter 3. I determined the performances of different spectral models and compared the widely used Band function with the physically motivated ISSM model. The case of a photospheric emission from the three GRBs 100724B, 120323A, and 131014A is investigated in detail in § 4, in the framework of the internal-shock synchrotron emission as the main source of their non-thermal emission. The analysis of GRB 220101A is described in chapter 5.

Chapter 1

Gamma-ray Bursts at high energies

In this chapter I briefly introduce the Gamma-ray Burst (GRB) phenomenon, present the relevant *Fermi* results concerning the GRB science, and detail the models that explain the GRB observed emission with a particular focus on the synchrotron class of models. Specifically, I describe the internal shock model developed by the team of the Institut d'Astrophysique de Paris and its parametric spectral representation called ISSM, for Internal Shock Synchrotron Model. At the end I present the spectral functions that I adopt through my analysis in the following chapters.

1.1 Gamma-ray Bursts

1.1.1 The GRB paradigm

Gamma-ray Bursts are extra-galactic and extremely energetic transient emissions of gamma-rays, which are thought to be associated with the death of massive stars or the merger of compact objects in binary systems. They are characterized by extremely high luminosities, which suggest that the central engine of a GRB is a newborn stellar-mass black hole, which emits a relativistic collimated outflow that accelerates particles and produces electromagnetic radiation from the very high-energy range (TeV) to the radio domain. Figure 1.1 shows the development of the burst ejecta from the central engine to the collision with the circumburst medium. At lower radii $R \sim 10^{11-12}$ cm the jet becomes transparent to thermal radiation, which is free to travel and is possibly observed as thermal component of the GRB spectrum. At intermediate radii $R \sim 10^{14-15}$ cm from the central engine either the kinetic energy carried by the jet dissipates into shocks either its magnetic energy is released via magnetic reconnection: as a common result charged particles are accelerated and emit highly variable synchrotron radiation. Both the thermal radiation, possibly reprocessed below the photoshere, and the non-thermal synchrotron radiation emitted at this intermediate region represent the prompt emission of the GRB. At larger radii $R \sim 10^{16-17}$ cm the jet collides with the circumburst medium and the generated external shock accelerates charged particles which emit synchrotron radiation in this so-called afterglow phase.

The prompt GRB emission is a short phase of intense and highly variable emission in the hard X-rays and gamma-rays, which lasts from fractions of seconds to hundreds of seconds, while the sub-sequent afterglow phase is a long lasting (hours, days) and decaying emission from (very) high energies (GeV-TeV) down to radio frequencies. An example of prompt variable emission is presented in Figure 1.2, which shows the composite light curve of GRB 190114C for increasing energy bands ranging from 15 keV to more than 100 MeV. GRB 190114C is well known for the detection of its early afterglow at very high energies (>200 GeV) by the MAGIC observatory and for the subsequent broad band follow-up campaign, which provided observations ranging over 17 decades in energy [MAGIC Collaboration et al. 2019]. The observed emission from this bursts allows to track the transition from the prompt variable phase detected by instruments such as the GBM and the LAT to the long lasting and decaying afterglow emission detected by the LAT, the XRT onboard the Neil Gehrels Swift Observatory, optical, and radio instruments. Figure 1.3 presents the broad band lightcurve obtained combining the observed data from very high energies to radio frequencies. The vertical dashed line at ~ 25 s from the trigger time indicates the transition from the prompt variable emission to the more smoothly decaying and long lasting afterglow emission, which is still detected after one

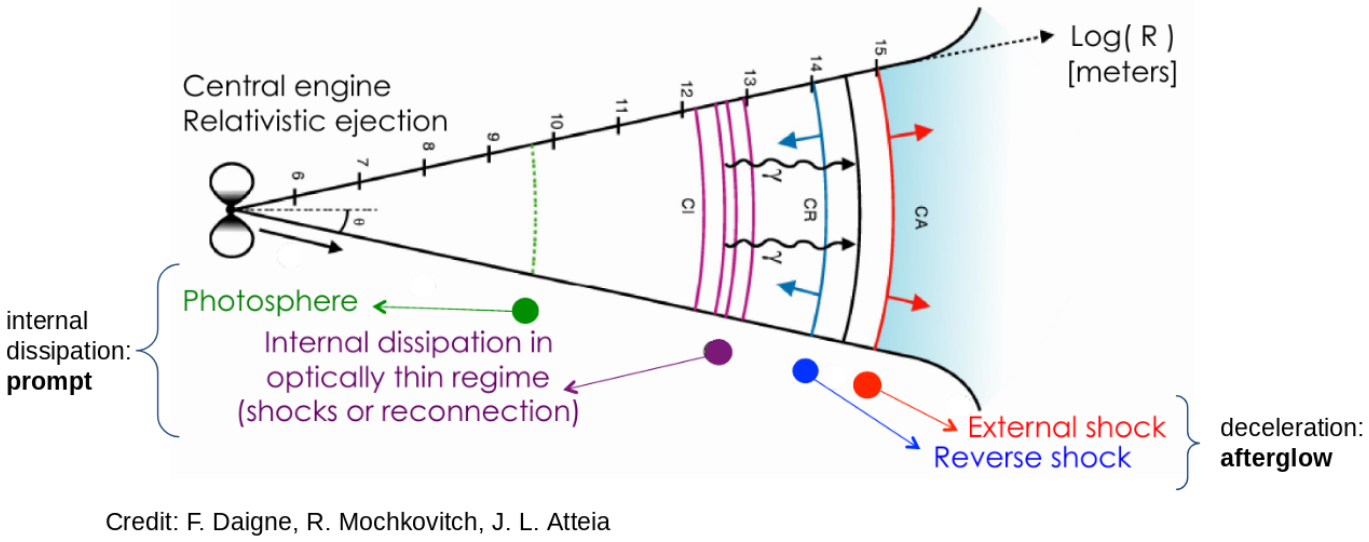

Figure 1.1: GRB jet development from the central engine to the impact with the circumburst medium.

day.

When a GRB is well localized and its luminosity distance is estimated via a redshift measurement then it is possible to estimate the amount of energy released by the burst. In the assumption that the energy is distributed isotropically, then the typical amount of energy relased E_{iso} lies in range 10^{51-54} erg [Zhang 2019]. The short time scale over which this energy is emitted implies a huge luminosity which typically is 10^{50-53} erg/s. The first GRB catalog of the Burst and Transient Source Experiment (BATSE), on board the Compton Gamma Ray Observatory (CGRO), revealed a bimodality in the temporal and spectral distribution of GRBs [Kouveliotou et al. 1993]: short GRBs have a duration of less than ~ 2 s and are characterized by harder spectra, while long GRBs have a duration greater than ~ 2 s and are typically softer. Short GRBs are believed to be produced by the merging of two compact objects in binary systems (two neutron stars, [Eichler et al. 1989, Narayan et al. 1992, Piran 2004], or a neutron star and a stellar-mass black hole, [Paczynski 1991, Piran 2004]). In August 17 2017, the direct association of the gravitational wave GW 170817 emitted by the merger of a binary neutron star system, and the short GRB 170817A [Abbott et al. 2017] proved that binary neutron star mergers are the progenitors of at least some short GRBs. On the other hand, long GRBs are believed to be produced by the collapse of fast rotating massive stars ($> 30 M_{Sun}$, Collapsar model [Woosley 1993, Piran 2004]), as suggested by the association of nearby long GRBs with core-collapsed supernovae of types Ib/Ic [Galama et al. 1998, Bloom et al. 2002, Hjorth et al. 2003, Piran 2004]. In both scenarios the merger of two compact objects or the collapse of a massive star result in the formation of a stellar mass black hole, which acts as central engine powering the collimated relativistic outflow.

1.1.2 GRBs as relativistic collimated outflows

The fast variability observed in GRB light curves constrains the size R of the prompt emission zone through a causality argument, $R < ct_{var}$, where t_{var} is the emission variability time scale. The huge isotropic luminosity L_{iso} of GRBs implies a huge density of photons in such a small region, and a high opacity to pair creation ($\gamma + \gamma \rightarrow e^+e^-$), which should prevent gamma rays from escaping the emitting zone. Denoting E and E' the energies of the interacting photons (with $E > E'$), the pair production occurs essentially when $E \times E' \simeq m_e^2 c^4$. If one approximates its cross section as the Thomson cross section $\sigma_T = 6.65 \times 10^{-29}\,\mathrm{m}^2$, then the optical depth to pair creation can be written as:

$$\tau_{\gamma\gamma}(E) \simeq n(E')\sigma_T R = \sigma_T \frac{L_{iso,E'}}{4\pi m_e c^3 R} > 10^{13} \left(\frac{L_{iso,E'}}{10^{51}\,\mathrm{erg/s}}\right)\left(\frac{t_{var}}{10\,\mathrm{ms}}\right)^{-1} \quad (1.1)$$

where $n(E')$ is the low-energy photon number density. For typical values of $L_{iso,E'} \sim 10^{51}$ erg/s and $t_{var} \sim 10$ ms, the optical depth to pair creation is greater than 10^{13}. This huge value would confine the radiation in a small region, which consequently would emit blackbody radiation. The prompt emission is

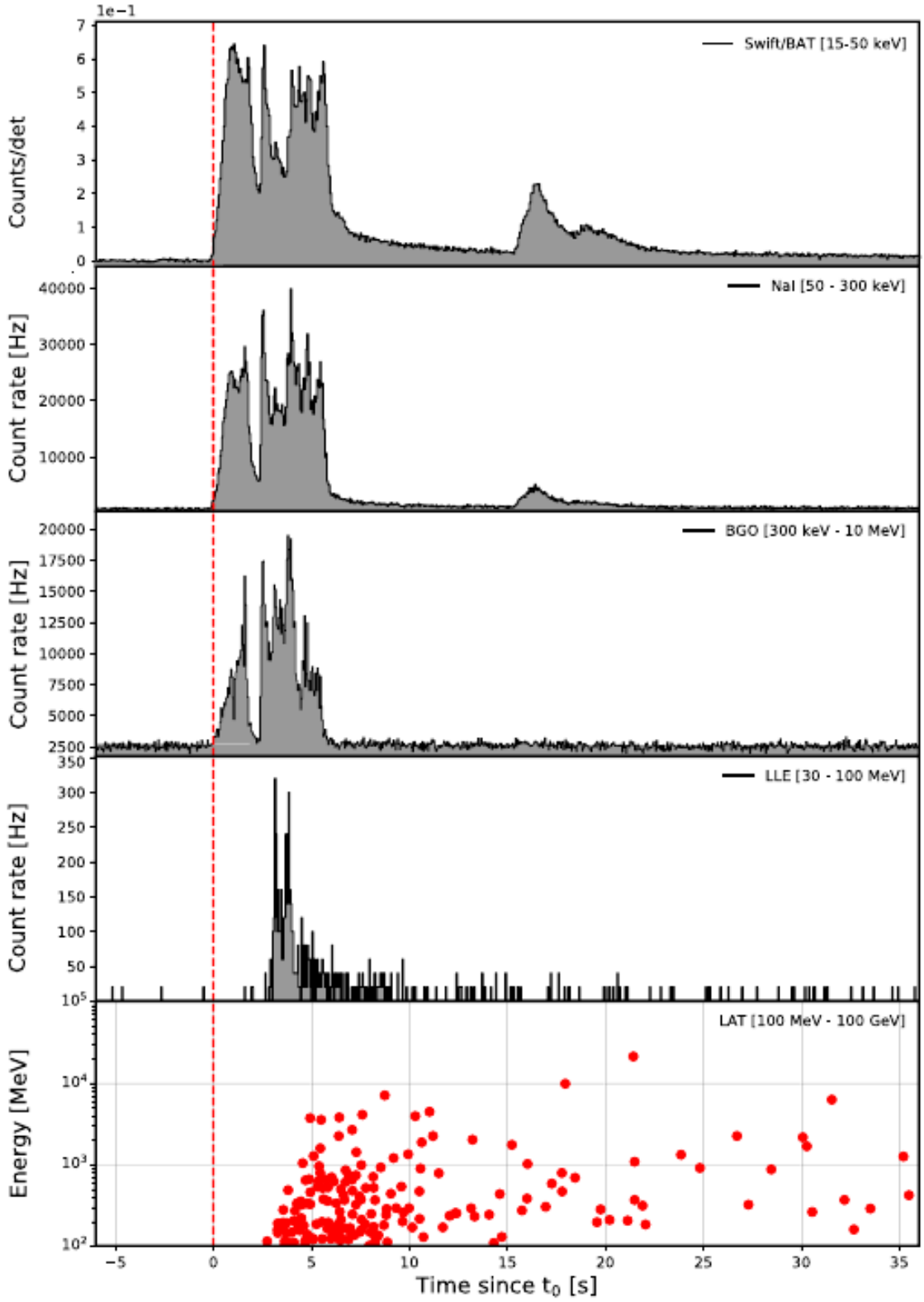

Figure 1.2: Composite light curve of GRB 190114C as observed by Swift and *Fermi*. Energy bands increase from (15-50) keV of Swift, to (50-300) keV of the GBM NaIs, to (0.3-10) MeV of the GBM BGO, to (30-100) MeV of the LLE event selection, and to more than 100 MeV of the LAT. Credit Ajello et al. 2020a.

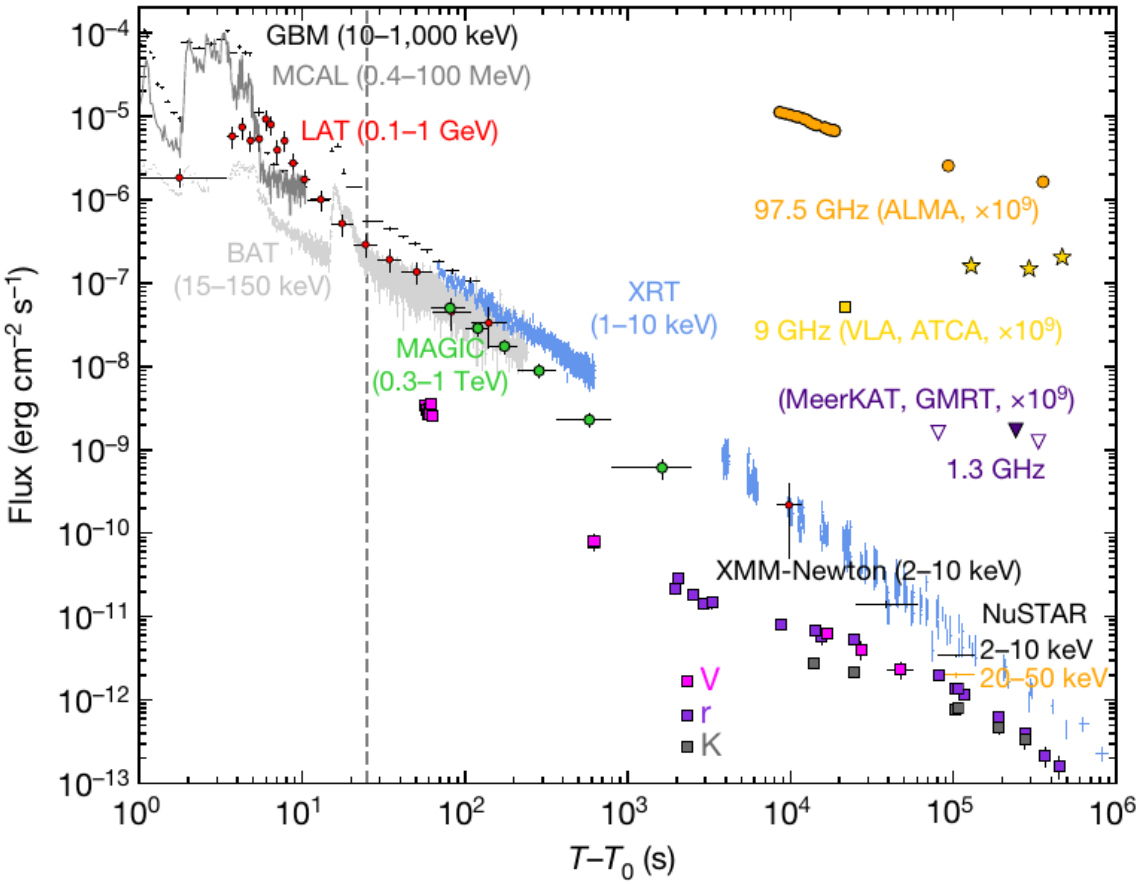

Figure 1.3: Broad band light curve of GRB 190114C from very high energies (MAGIC) to radio frequencies (VLA, and ATCA at 9 GHz). Credit MAGIC Collaboration et al. 2019.

most of the time non-thermal, so this poses a problem which is referred to as the **compactness problem**. The solution was provided by Meszaros et al. 1993, who invoked a relativistic outflow. In such condition, the optical depth is reduced by a factor $\Gamma^{2(1-s)}$, where s is the index of the assumed power law distribution of the target photon field [Granot 2009]. For a typical high-energy index of the prompt spectrum $s \sim -2.3$, the optical depth is reduced by a factor $\sim \Gamma^7$, and it can be less than unity for a jet Lorentz factor greater than a minimum value $\Gamma_{min} \sim 100$.

If the GRB distance (redshift) is known, the bulk Lorentz factor Γ_{bulk} of the relativistic outflow can sometimes be constrained from observations in the prompt phase or in the afterglow phase. When high-energy photons are detected during variable episodes in the prompt light curves, a lower limit on Γ_{bulk} can be set:

$$\Gamma_{min} \propto t_{var}^{\frac{1}{(s-1)}} (1+z)^{\frac{(s+1)}{(s-1)}} E_{max}^{\frac{(s+1)}{2(s-1)}} \tag{1.2}$$

using the energy E_{max} of the most energetic detected photon. This method is used when the high-energy non-thermal spectrum, e.g. as measured by the Fermi/LAT, seemingly keeps a constant spectral slope up to the most energetic detected photons. More interestingly, several LAT-detected GRBs exhibit a cutoff at the high end of their spectrum, which has been interpreted as a flux attenuation caused by the opacity to pair creation. In these rare cases, a direct estimate of Γ_{bulk} can be obtained by replacing E_{max} by the energy of the spectral cutoff in equation 1.2. It is worth noting that this approach does not rely on the specific nature of the emission mechanism, but only on the knowledge of the burst distance, of its emission variability, of its broad-band spectrum and of the cutoff energy. As presented in § 5, I have successfully applied this method to GRB 220101A, the most distant GRB detected by the Fermi/LAT so far.

In addition, independent estimates of Γ_{bulk} can be obtained in the framework of the early afterglow model. In the first LAT GRB catalog [Ackermann et al. 2013], the constraints shown in Figure 1.4 have been ob-

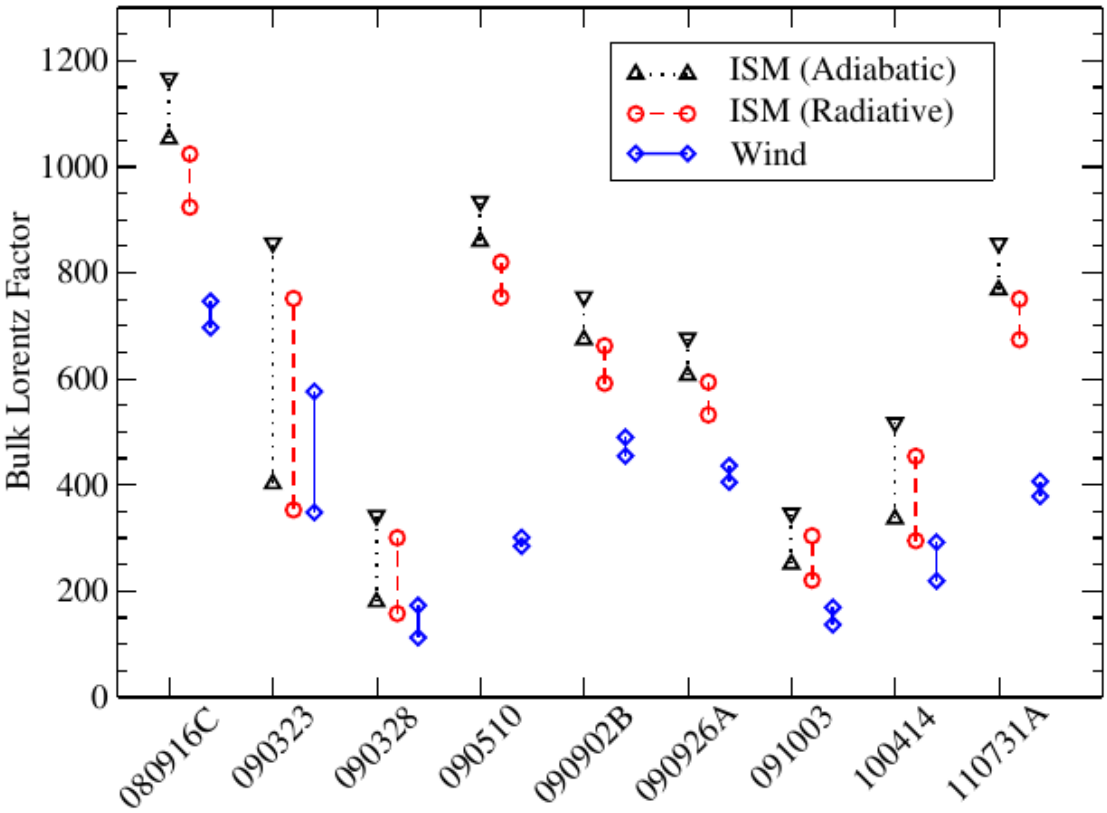

Figure 1.4: Bulk Lorentz factors of the LAT bursts derived under the assumption that the peak flux time in the LAT represents the fireball deceleration time (credit Ackermann et al. 2013).

tained by assuming that the peak-flux time of the high-energy emission is similar to the fireball deceleration time. In this figure, the choice of an interstellar medium with constant density is more appropriate for the short GRB090510, while the wind-like environment best applies to the other GRBs, all of the long class.

Finally, there is also a strong reason to believe that the ultra-relativistic outflow of GRBs is collimated. Assuming that the GRB emission is isotropic, the total energy that is released in gamma rays can reach values as high as $E_{\gamma,iso} \sim 10^{54-55}$ erg (6 orders of magnitude higher than the energy radiated by a supernova $E \sim 10^{49}$ erg). This extreme energy sets stringent constraints on the initial source energy budget, for instance as discussed by Abdo et al. 2009b for GRB 080916C where $E_{\gamma,iso} \sim 8.8 \times 10^{54}$ erg. In order to relax this energetic constraint, it was suggested that the GRB emission occurs within a conical collimated jet of opening angle θ_j of few degrees. This hypothesis implies that the visible radiation is produced within an angle $\propto 1/\Gamma$, which increases with the deceleration of the jet until becoming wider than the jet physical opening angle θ_j. This transition translates into an achromatic break in the observed afterglow flux [Harrison et al. 1999, Rhoads 1999, Piran 2004]. The first clear example was GRB 990510 [Harrison et al. 1999, Stanek et al. 1999], where the temporal decay of its afterglow presented a break clearly detected in optical and radio bands. However, more recently Racusin et al. 2009 found that achromatic breaks in GRB afterglows detected by Swift in X-ray and optical bands are not so common. Though the unambiguous detection of achromatic breaks is still an open subject of debate, the collimated nature of GRB ultra-relativistic outflows provides a natural explanation for their energetics.

1.2 The *Fermi* view of Gamma-Ray Bursts

1.2.1 GRB prompt keV-MeV emission as seen by the GBM

As of November 2022 the GBM has triggered on 3392 GRBs. The GBM 10-years GRB catalog is the most complete compilation so far [von Kienlin et al. 2020], with 2356 GBM detected GRBs. Of these bursts, 395

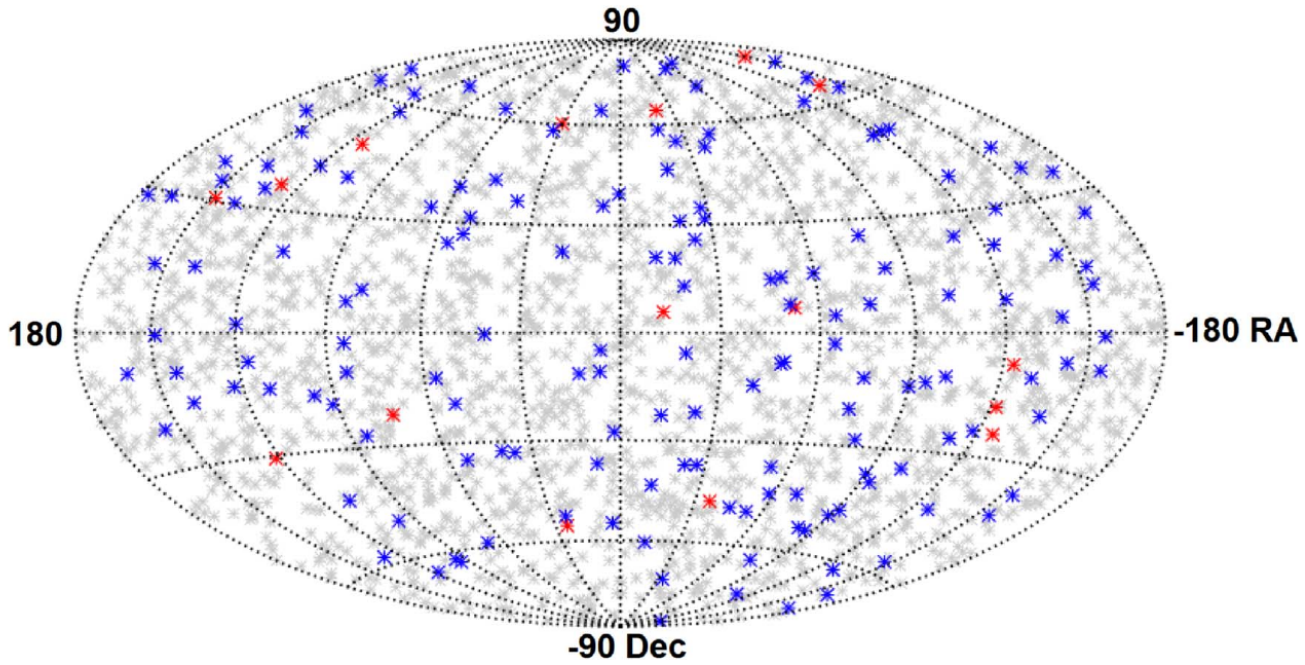

Figure 1.5: Distribution of the GBM and LAT detected bursts in the first 10 years of operations between 2008 July to 2018 July in equatorial coordinates. Grey asterisks denote the 2356 GBM detected bursts, blue ones for the 160 LAT detected long bursts, and red ones for the 16 LAT detected short bursts (credit Ajello et al. 2019).

(17%) are short GRBs, and 1958 (83%) are long GRBs. Figure 1.5 shows the 2356 GBM detected bursts (grey asterisks) along with the LAT bursts (blue asterisks for long GRBs, red for short GRBs) detected in the first 10 years of operations. The spectral properties of these GRBs are discussed in the GBM 10-year GRB spectral catalog [Poolakkil et al. 2021], where the following models were used to fit the differential photon spectrum $f(E)$ in units of $cm^{-2}s^{-1}keV^{-1}$:

- power law (PL): 2 parameters, the spectral slope and the normalization;
- cutoff power law (COMP), adding an exponential cutoff to the PL at high-energy through the E_p parameter, which is the peak of the spectral energy distribution $E^2f(E)$;
- Band law (introduced by Band et al. 1993): two smoothly-connected power laws, with 4 parameters (low-energy and high-energy spectral slopes α and β, peak energy E_p, normalization);
- smoothly broken power law (SBPL): 4 parameters, similarly to the Band model.

The mathematical expression of these models is given in § 1.3.5. As shown in Figure 1.6 most GRBs are best fit by PL or COMP, which often results from the lack of photon statistics at high energies. In fact, the differential photon spectrum $f(E)$ always decreases when energy increases. The median value of the low-energy index is -1.08, and the median value of the high-energy is -2.20. Additionally, the high-energy index resulting from the fit of the phenomenological Band spectral function is particularly hard and greater than -2 for a sizeable fraction of bursts: in these cases the spectral energy is attenuated and peaks beyond the GBM energy range.

1.2.2 GRB high-energy emission as seen by the LAT

As of November 2022 the LAT detected 231 GRBs. The first *Fermi*-LAT GRB catalog (1FLGC, Ackermann et al. 2013) covers 3 years of observations at high energies (>100 MeV). It includes 35 GRBs (30 long, 5 short) detected between 2008 August and 2011 July. This catalog shows three peculiar features of the LAT detected GRBs: (i) the emission above 100 MeV is systematically delayed with respect to the emission at

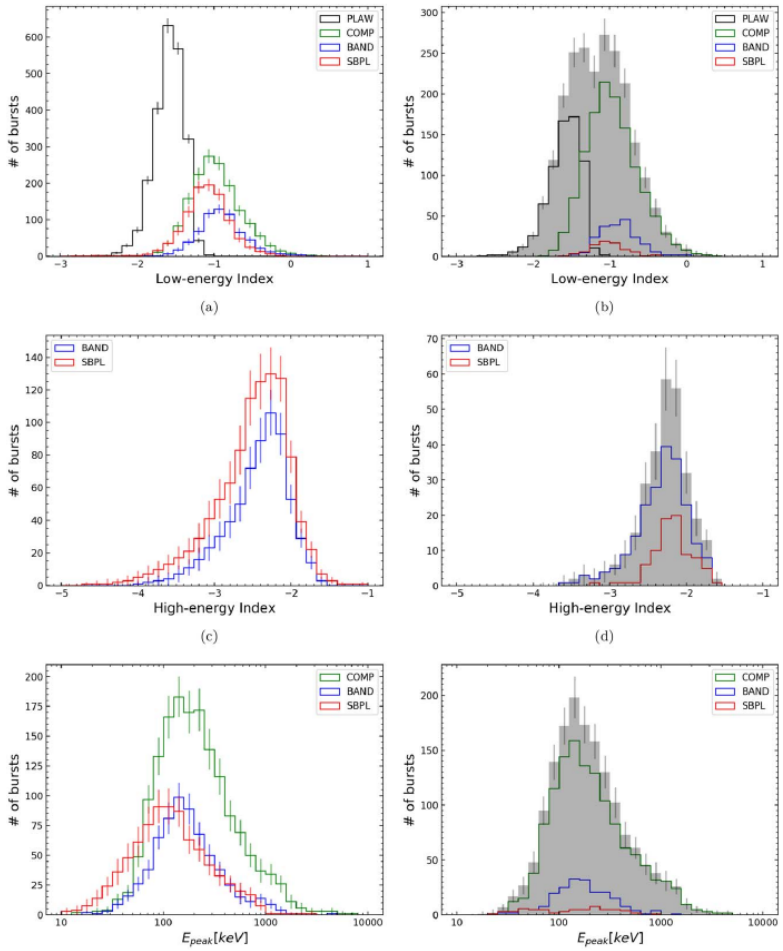

Figure 1.6: Distribution of the low-energy index, the high-energy index, and E_p obtained from the GOOD fluence spectral fits (left panels) and the BEST spectral fits (right panels). The GOOD fluence sample is a set of spectral fits integrated over the duration of the bursts and whose spectral parameters are well constrained. The BEST sample is the set of the best-fitting model per each burst of the overall sample. Credit Poolakkil et al. 2021

lower energies in the keV-MeV range; (ii) additional spectral components are required in many bright GRBs to account for the spectrum at high-energies, in particular an hard power law is required in the LAT energy range for four GRBs in addition to the keV-MeV spectral component measured by the GBM; (iii) the high-energy emission lasts longer than the low-energy one.

The second *Fermi*-LAT GRB catalog (2FLGC, Ajello et al. 2019) covers the first 10 years of observations and it is the most complete compilation of LAT detected GRB properties to date. It extends the previous sample to 186 detected GRBs (169 long, 17 short). Within this broader sample the high-energy emission starts significantly later and lasts longer than the low-energy one, which confirms the results of 1FLGC. The high-energy emission is delayed, yet it starts generally before the end of the keV-MeV emission. This suggests that part of the LAT detected emission has a common origin with the low-energy emission, in particular a fraction of this high-energy emission might have an origin internal to the burst jet. At later times, the temporally-extended emission observed above 100 MeV is believed to result from the interaction of the jet with the circumburst medium. In this afterglow scenario, the detected flux decays smoothly with the time and the radiation is observed over a broad energy range. GRB 1901014C is an examplary burst which presents the mentioned features at high-energy. Figure 1.2 shows the composite light curve of this burst for increasing energy bands starting from 15-50 keV in the Swift/BAT instrument to more than 100 MeV in the LAT. LAT high-energy emission is detected from $\sim$ 2.5 s after the time of the trigger. It is variable at the beginning, showing a double peaked structure in the LAT Low Energy event selection between 30 and 100 MeV. In this

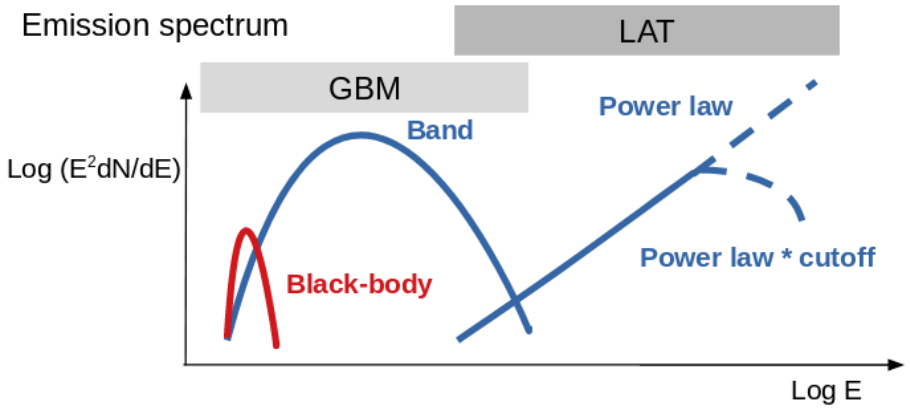

Figure 1.7: Schematic view of a typical prompt emission spectrum observed by the GBM and the LAT.

time interval the low-energy emission is still detected by Swift and the GBM. The transition from the variable prompt phase to the long lasting and decaying afterglow phase of the LAT emission is shown in Figure 1.3. After the first $\sim$ 10 s of the prompt variable LAT emission, the LAT flux decays smoothly with the time with a power-law index $\delta = -1.22 \pm 0.11$, and it is well detected up to more than 100 s after the time of the trigger.

Fermi observations support the hypothesis that the early emission above 100 MeV, that is observed during the prompt keV-MeV emission phase, does not always belong to the afterglow phase. In particular, the correlated variability with the low-energy emission that is observed in some cases suggests that the LAT early emission can also have an internal origin. Indeed, some bursts such as GRB 090926A and GRB 131008A present a fast temporal variability above 100 MeV, which indicates that the high-energy emission is produced along with the low-energy one inside the burst jet. Additionally, some bursts such as GRB 090926A, GRB 100724B, GRB 160509A, GRB 170405A, and GRB 220101A present a spectral cutoff at high energies. In these cases the fast variability of the observed emission suggests that the attenuation at high energies could be due to opacity to pair creation, as it was proven for GRB 090926A by Yassine et al. 2017. As discussed in § 1.1.2, these bursts are precious cases in which a direct estimate of Γ_{bulk} has been performed. More specifically, the Γ_{bulk} of the ejecta and the region of the detected emission can be directly estimated regardless of the nature of the emission process. I detail such approach in § 5 for GRB 220101A, following Yassine et al. 2017 who determined Γ_{bulk} and the observed emission radius for GRB 090926A.

A handful of bursts have been firmly detected at very high-energy (VHE) by the ground-based imaging atmospheric Cherenkov telescopes of MAGIC and H.E.S.S., in the either early afterglow phase (GRBs 190114C and 201216C) or in the late afterglow phase (GRBs 180720B and 190829A) [Noda et al. 2022]. The LAT did not detect the low-luminosity GRB 190829A and provided flux upper limits, neither GRB 201216C which was outside the LAT field of view at the time of the trigger. Very recently, the so-called BOAT ("brightest of all time") GRB 221009A, located at close distance (z=0.151), has been detected up to 99 GeV by the Fermi/LAT [Pillera et al. 2022], up to 18 TeV by the LHAASO experiment [Huang et al. 2022] and possibly up to 200 TeV by the Carpet experiment [Dzhappuev et al. 2022].

1.3 Prompt emission models

1.3.1 Spectral components

The comprehension of the physics of the GRB phenomenon is still a matter of debate. On one hand there is a general consensus regarding the afterglow phase: the radiation observed is synchrotron radiation emitted by charged particles which are accelerated by the external shock produced by the impact of the burst ejecta with the circumburst medium. On the other hand the understanding of the observed radiation emitted in the prompt phase is not fully understood. A phenomenological function was proposed by Band et al. 1993 and provided successfull fits to CGRO/BATSE bursts. However, the Band function is a pure

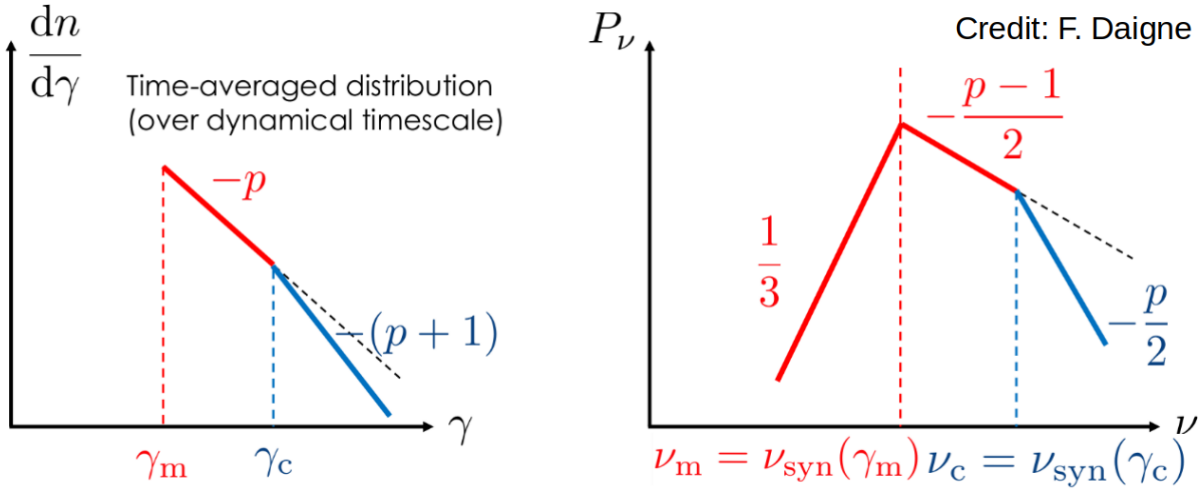

Figure 1.8: **Slow-cooling regime**. Left: time-averaged differential spectrum of accelerated electrons as a function of their Lorentz factor γ. Right: power spectrum of the emitted synchrotron radiation as a function of the frequency. The SED peak energy corresponds to ν_c, and the photon spectral index at low energies is $\alpha = 1/3 - 1 = -2/3$. In both panels, the dashed curves correspond to the instantaneous spectra at injection time.

mathematical tool that is not based on physical grounds, therefore one must be cautious when infering physics from its fits to the data. It is indeed worth recalling that the reconstruction of GRB spectra at high energy relies on the so-called forward-folding technique (see § 2.4), where the spectral shape must be assumed a priori, folded with instrument responses, and finally compared with observations (count spectra). As a result, the fitted parameters strongly depends on the initial hypothesis for the spectral shape, and can vary significantly from one hypothesis to another. Namely, the forward-folding technique never provides the GRB true spectrum, and can only be used to compare the likelihoods of different hypotheses.

A schematic view of the prompt emission spectra observed by *Fermi* is presented in Figure 1.7. The Band function describes the keV-MeV bulk non-thermal component of the spectrum, which is typically interpreted as synchrotron emission. A thermal component has been invoked to describe the whole observed spectrum of GRB 090902B [Abdo et al. 2009a] or it has been detected in addition to the Band function in a handful of GRBs (Guiriec et al. 2011, Guiriec et al. 2013, Guiriec et al. 2015a). The additional power law component in the LAT energy range has been found in a significant fraction of LAT detected GRBs (1FLGC and 2FLGC), and an additional cutoff at high energies have been found in 5 LAT detected burst so far, as mentioned in § 1.2.2.

Two main physical GRB models based on physical assumptions have been proposed over the years [Zhang 2020]: on one side synchrotron models invoke synchrotron radiation of the electrons accelerated in the regions of the jet where the jet kinetic energy is dissipated (via internal shocks or magnetic reconnection); on the other side the so-called photospheric models invoke quasi-thermal emission from a relativistic fireball in expansion. Both models have limitations: owing to the bright and highly variable emission, synchrotron models predict that all electrons emit synchrotron radiation efficiently (the so-called fast-cooling regime). This implies a low-energy index of -3/2, which is not compatible with the typical observed value of -1 (see low-energy spectral index distributions in the upper panels of Figure 1.6), though the latter is distributed over a relatively wide range. On the contrary, the simplest versions of the photospheric models predict a low-energy spectral index as high as $+3/2$, which again is not compatible with the typical observed value. Which model does correctly describe the physics of the GRB prompt emission, if a unique model that accounts for all the observations exists?

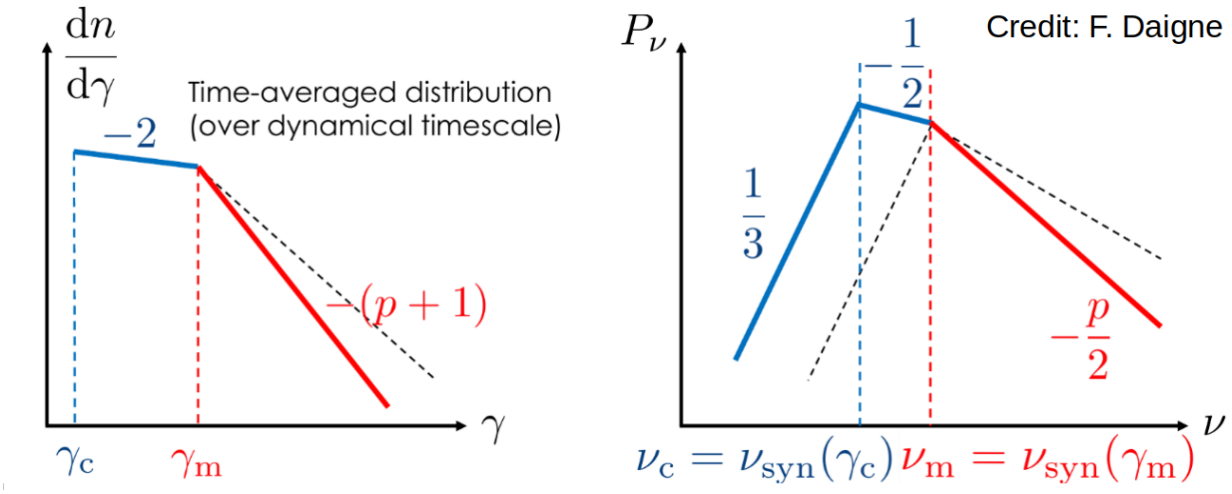

Figure 1.9: **Fast-cooling regime**. Left: time-averaged differential spectrum of accelerated electrons as a function of their Lorentz factor γ. Right: power of the emitted synchrotron radiation emitted as a function of the frequency. The SED peak energy corresponds to ν_m, and the photon spectral index below E_p is $\alpha = -1/2 - 1 = -3/2$. In both panels, the dashed curves correspond to the instantaneous spectra at injection time.

1.3.2 Synchrotron emission and line-of-death problem

In the case of a single electron traveling with a Lorentz factor γ inside a magnetic field of strength B, the power of the emitted synchrotron radiation is proportional to $B^2\gamma^2$. The characteristic synchrotron cooling time scale is equal to the relativistic energy of the electron divided per the power of the emitted synchrotron radiation: $t_{syn}(\gamma) \propto \frac{1}{B^2\gamma}$. This time scale has to be compared with the dynamical time scale, t_{dyn}, for the electron energy losses due to the GRB jet adiabatic expansion. If $t_{syn} < t_{dyn}$, then the electron synchrotron losses are dominant and the electron radiates efficiently. In this case, $\nu_{syn}(\gamma) > \nu_{syn}(\gamma_c) = \nu_c$, where γ_c is the Lorentz factor at which both energy losses are equal, and $\nu_{sync}(\gamma)$ is the peak frequency of the synchrotron emitted power for a single electron of energy $\gamma m_e c^2$. Then, considering a typical power-law energy distribution of the accelerated electrons ($dn/d\gamma \propto \gamma^{-p}$) above a minimum value of γ_m, the instantaneous synchrotron power spectrum peaks at $\nu_m = \nu_{sync}(\gamma_m)$, with a power-law slope equal to 1/3 below ν_m and $-(p-1)/2$ above ν_m. Finally, after integrating over the dynamical time scales, two regimes can be distinguished [Sari et al. 1998], :

- **Slow-cooling regime ($\nu_m < \nu_c$)**: the synchrotron losses are dominant only for a fraction of accelerated electrons, those with a Lorentz factor greater than γ_c. Figure 1.8 shows the time-averaged differential spectrum of accelerated electrons (left panel) and the total synchrotron power spectrum (right panel). The corresponding spectral energy distribution (SED, defined as νP_ν) peaks at ν_c. The value of the photon spectral index is $1/3 - 1 = -2/3$ below ν_m (and $-(p+1)/2 \sim -1.65$ over a limited range between ν_m and ν_c, for a typical value $p = 2.3$).

- **Fast-cooling regime ($\nu_m > \nu_c$)**: the synchrotron losses are dominant for all of the accelerated electrons. Figure 1.9 shows their time-averaged differential spectrum and the total synchrotron power spectrum. The corresponding SED peaks at ν_m, and the value of the photon spectral index is $-3/2$ below ν_m and $-2/3$ below ν_c. This situation is likely to happen in the GRB prompt phase, where the high luminosity and the emission fast variability suggest that the accelerated electrons radiate efficiently.

The observed value of the photon spectral index at low energies is $\alpha \sim -1$ on average (see upper panels of Figure 1.6), with $-3/2$ being a rare value. Moreover, a significant fraction of GRBs have α values exceeding the highest limit of $-2/3$ allowed by the synchrotron theory (see above), and this issue is often referred to as the **synchrotron "line-of-death" problem**. At least in those cases, variants of the synchrotron model or alternative models are needed to reconcile the expected value of α with the observed ones.

On the side of the data analysis it has been proposed to fit multi-component spectra, such as the phenomenological Band function with an additional black-body function (Guiriec et al. 2011, Guiriec et al. 2013, Guiriec et al. 2015b, Guiriec et al. 2015a). This two-component model allows indeed to soften the Band α value, as the black-body component accounts for part of the flux at low energies. Moreover, the spectral break at ν_c in the fast-cooling regime has been searched in the power-law segment of the Band function at low energies (Toffano et al. 2021, Oganesyan et al. 2017, Oganesyan et al. 2018, Ravasio et al. 2018, Ravasio et al. 2019). Toffano et al. 2021 found convincing evidence for such a break between few keV and hundreds of keV in 12 *Fermi* long GRBs within a sample of 36 *Fermi* GRBs. This sample comprises 27 long and 9 short bursts, which have been chosen according to their high fluence and the high value of peak energy, which provide the photon statistics and enough energy lever arm to search for a spectral break at low energies. As a result the authors found that the spectral index below the break has an average value of -0.71, which is close to the expected value of $-2/3$ at the lowest energies, while the spectral index above the break has an average value of -1.71, which is close to the expected value of $-3/2$. The mean value of α -1 is then understood as an average spectral slope.

On the theoretical side the following scenarios have been proposed to reconcile the expected value of α with the observations. A class of models interprets the observed prompt emission of GRBs as the radiation emitted at or below the burst photosphere: photospheric models (e.g., Ryde et al. 2009) imply a quasi-thermal spectrum that on one side can explain hard values of α, but on the other side is rare among the observed GRB spectra. Dissipative photospheric models such as the one proposed by Beloborodov 2013 and Beloborodov 2017 assume that the sub-photospheric radiation is somehow reprocessed and can lead to non-thermal spectra in agreement with observations in the keV-MeV energy range. Variants of the GRB synchrotron model in the fast-cooling regime include the effect of inverse Compton scattering in the Klein-Nishina regime, which can naturally harden the value of α from $-3/2$ to -1 (Derishev et al. 2001, Daigne et al. 2011). Moreover, Daigne et al. 2011 and Beniamini et al. 2013 proposed physical conditions where the cooling frequency ν_c can approach the synchrotron characteristic frequency ν_m of the less energetic injected electrons at γ_m. In this so-called marginally fast-cooling regime, α can take harder values up to $-2/3$. Finally, Derishev 2007, Pe'er et al. 2006, and Bošnjak et al. 2022 investigated the effect of a turbulent magnetic field which typically decays over a length that is much smaller than the shocked region. In these models, the most energetic electrons radiate efficiently in a small region where the magnetic field is maximal, while the rest of the electrons see a less intense magnetic field. This affects essentially the low-energy part of GRB spectra, where much harder spectral slopes can then be obtained.

1.3.3 Which physical model for the prompt emission?

Which model is able to account for most of the observed GRB properties? As explained by Zhang 2020, the diversity of GRB spectra can be understood as resulting from a competition between different physical mechanisms. Specifically, two sources of energy power can be distinguished: the gravitational energy of the central engine, which is transformed into the thermal energy of the fireball, and the rotational energy of the central engine, which is converted into Poynting flux. Figure 1.10 shows different ways in which these two energy sources can shape the GRB spectra. Part of the fireball energy is radiated at the photosphere and is observed as a thermal component in GRB spectra. Meanwhile, the kinetic energy of the outflow increases under the fireball thermal pressure or by magnetic acceleration, and is eventually dissipated into internal energy by shocks. Alternatively, the Poynting flux can be directly dissipated by magnetic reconnection. The internal energy is then distributed to the magnetic field and to accelerated particles, which emit the observed synchrotron radiation. As a result, GRB prompt spectra at keV-MeV energies are expected to consist of both thermal and synchrotron components, with relative intensities that depend on the dominant initial energy reservoir (fireball vs. Poynting flux). In the fireball model, a bright thermal component is expected. However, it has been observed in rare cases such as GRB 090902B [Ryde et al. 2010], which might favor the Poynting flux scenario as a more general case. As noted by Zhang 2020, infering the jet composition and the physical mechanisms which are responsible for the prompt emission will need dedicated analyses in the future, where physical models of either scenario will be fitted to the observations, instead of using

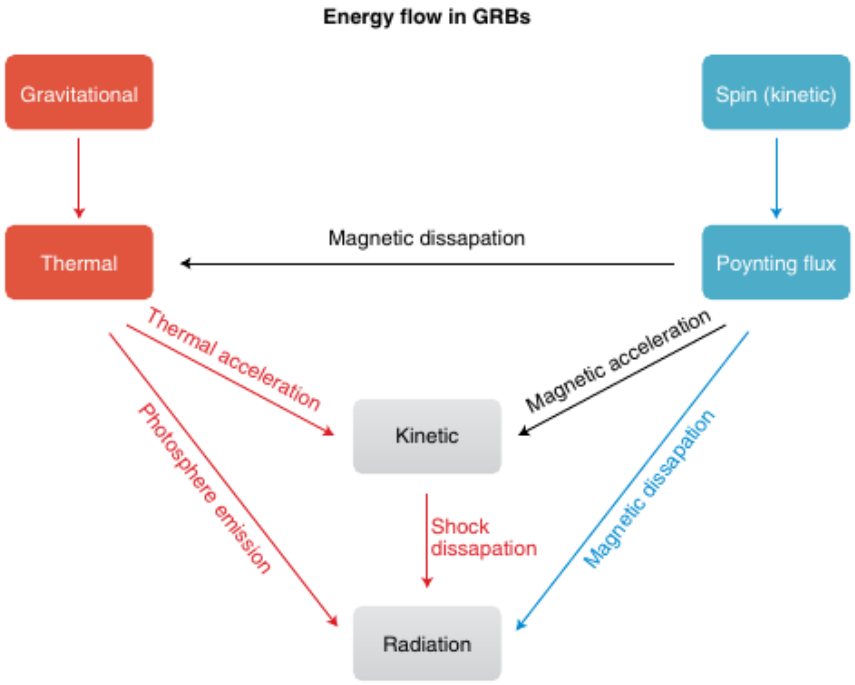

Figure 1.10: Flux diagram of the different energy flows which can shape the GRB spectra. The dominance of the thermal component or Poynting flux component depends on the initial allocation of the energy budget. Credit Zhang 2020.

phenomenological or mathematical models such as the Band function.

1.3.4 The Internal Shock Synchrotron Model

A physically motivated approach to describe the prompt emission has been proposed by the team at the Institut d'Astrophysique de Paris (Daigne et al. 1998, Bošnjak et al. 2009, Daigne et al. 2011, Bošnjak et al. 2014). Their numerical model mimics internal shocks as the product of the collision between solid layers moving with different Lorentz factors. These midly-relativistic shocks dissipate the jet kinetic energy into internal energy, and they accelerates a fraction ζ of the electrons. The energy spectrum of the accelerated electrons is assumed to follow a power law with a slope $-p$ (typically from -2.3 to -2.9), and to contain a fraction ϵ_e ($1/3$ typically) of the dissipated energy. In addition, the turbulent magnetic field carries a fraction ϵ_B (possibly as low as 10^{-3}) of the internal energy. The model accounts for adiabatic cooling and implements all needed emission processes, such as synchrotron and inverse Compton radiations, synchrotron self-absorption and gamma-gamma annihilation. The numerical code couples the radiative processes to the shock dynamics. It simulates the temporal evolution of the micro-physical conditions in the shocked regions, and follows the evolution of the electron and photon distributions to generate light curves and spectra from keV to GeV energies.

The Internal Shock Synchrotron model (ISSM, Yassine et al. 2020) is a parametric spectral function based on this internal shock model. Like the phenomenological Band function, the ISSM function is characterized by four parameters: the low and high-energy spectral indices α and β, the peak energy of the spectral energy distribution E_p, and a normalization factor. Its differential photon energy spectrum in units of $cm^{-2}s^{-1}keV^{-1}$ is:

$$f_{ISSM}(E) = \frac{A}{\left[1 - \frac{E_p}{E_r}\left(\frac{2+\beta}{2+\alpha}\right)\right]^{\beta-\alpha}} \left(\frac{E}{E_r}\right)^{\alpha} \left[\frac{E}{E_r} - \frac{E_p}{E_r}\left(\frac{2+\beta}{2+\alpha}\right)\right]^{\beta-\alpha} \tag{1.3}$$

where E_r is the reference energy fixed to 500 keV. At $E = E_r$, $f_{ISSM}(E_r) = A$, which means that the value of the reference energy only affects the value of the normalization A and not the shape of the function. The local spectral index of ISSM reads:

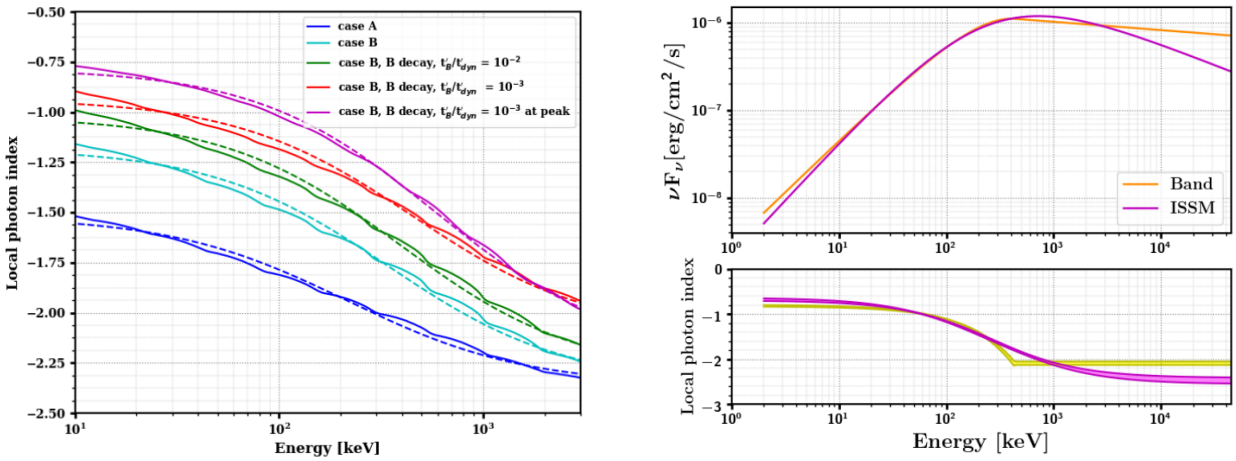

Figure 1.11: Left: least-square fit (dashed lines) of the $\Gamma_{ISSM}(E)$ function to the local photon index (solid lines) of the internal-shock synchrotron spectra of synthetic bursts in different micro-physical configurations (credit Yassine et al. 2020). Right: spectral energy distribution and local photon index from the Band and ISSM fits of the *Fermi*/GBM burst GRB 150403913 [Yassine et al. 2020].

$$\Gamma_{ISSM}(E) = \alpha + (\beta - \alpha)\frac{E}{E - E_p\left(\frac{2+\beta}{2+\alpha}\right)} \tag{1.4}$$

The local photon index $\Gamma_{ISSM}(E)$ decreases continuously with energy, thus the ISSM function is continuously curved unlike the phenomenological Band function and other simplified versions of the synchrotron model based on a pure power law energy distribution of accelerated electrons. The ISSM spectral curvature actually results from the superposition of instantaneous electron synchrotron spectra, which evolve rapidly with time due to the variations of the micro-physical conditions in the shocked region.

Yassine et al. 2020 built the ISSM function from simulations of single-pulse bursts with the numerical code in different micro-physical configurations. The left panel of Figure 1.11 shows the excellent agreement between the local photon index of the synthetic bursts and the fit by the $\Gamma_{ISSM}(E)$ function (eq. 1.4). As discussed in Yassine et al. 2020, the ISSM spectral shape is also suitable to describe more complex spectra, e.g. time-integrated spectra including different emission pulses. The authors tested the ISSM model on 74 fluent bursts detected by the Fermi/GBM, and found that ISSM reproduces 81% of their time-integrated spectra versus 59% for Band. They also found that the low-energy index of ISSM α is greater than the low-energy index of Band, and that the high-energy index β of ISSM is smaller than the high-energy index of Band. This can be explained by the continous curvature of ISSM: the low-energy and the high-energy indices of ISSM are asymptotic values which may not be reached within the observable GBM energy range. For this reason the authors defined $\alpha_{10,ISSM}$ and $\beta_{b,ISSM}$ as the values of the local photon index of ISSM at 10 keV and at the break energy E_b of the Band function (see its definition in the next section § 1.3.5), respectively. These indices are well measured and within the GBM energy range, and they can be compared with the corresponding values of Band. The authors found that $\alpha_{10,ISSM}$ is only slightly larger than the corresponding local photon index of Band evaluated at 10 keV $\alpha_{10,Band}$, while $\beta_{b,ISSM}$ is systematically harder than β_{Band} (see the example GRB shown in the right panel of Figure 1.11).

1.3.5 Spectral models

In this subsection I present the spectral functions that I will employ in the following chapters. I present them in terms of increasing complexity, namely their number of spectral parameters. These functions are differential photon energy spectra and the units of their amplitude A are $cm^{-2}s^{-1}keV^{-1}$.

- **BB** (2 free parameters): black body spectrum. It reads:

$$f_{BB}(E) = \frac{A \times 8.0525\, E^2}{(kT)^4\,[\exp(E/kT) - 1]} \tag{1.5}$$

where kT is the temperature in keV, and the normalization A corresponds to L_{39}/D_{10}^2, where L_{39} is the source luminosity in units of 10^{39} erg/s and D_{10} is the distance to the source in units of 10 kpc. The peak energy of the spectral energy distribution is the energy at which $\frac{\partial \log{(E^2\, f_{BB})}}{\partial \log E}(E) = 0$. Setting $x = E/kT$ the equation becomes $\frac{d}{dx}(\frac{x^4}{e^x - 1}) = 0$, which can be solved numerically with solution $x = 3.92$. Therefore $E_{p,BB} = 3.92\, kT$.

- **PL** (2 free parameters): it is a power law, and reads

$$f_{PL}(E) = A \left(\frac{E}{E_{piv}}\right)^{\alpha} \tag{1.6}$$

where for the LAT spectral analysis of § 5 the normalization A units are $cm^{-2}s^{-1}MeV^{-1}$ and E_{piv} is the reference energy fixed to 150 MeV. α is the spectral index.

- **COMP** (3 free parameters): it is a power law with an exponential cutoff at high energies, and reads

$$f_{COMP}(E) = A \left(\frac{E}{E_{piv}}\right)^{\alpha} \exp\left[-\frac{E(2+\alpha)}{E_p}\right] \tag{1.7}$$

where E_{piv} is the reference energy fixed to 100 keV, and E_p is the peak of the spectral energy distribution. For $E_p \to \infty$, COMP reduces to PL.

- **Band** (4 free parameters): it has four spectral parameters and it was introduced by Band et al. 1993. It reads

$$f_{Band}(E) = A \times \begin{cases} \left(\frac{E}{E_{piv}}\right)^{\alpha} \exp\left[-\frac{E(2+\alpha)}{E_p}\right] & \text{if } E \le E_b = E_p \frac{\alpha - \beta}{2+\alpha} \\ \left(\frac{E}{E_{piv}}\right)^{\beta} \exp(\beta - \alpha) \left[\frac{E_p(\alpha-\beta)}{E_{piv}(2+\alpha)}\right]^{\alpha-\beta} & \text{otherwise} \end{cases} \tag{1.8}$$

where α is the low-energy spectral index, β is the high-energy spectral index, E_p is the peak energy of the spectral energy distribution, E_b is the break energy, and E_{piv} is the reference energy fixed to 100 keV. For $\beta \to -\infty$, $f_{Band}(E) = f_{COMP}(E)$.

The local spectral index of Band reads:

$$\Gamma_{Band}(E) = \begin{cases} \alpha - \frac{2+\alpha}{E_p} E & \text{if } E \le E_b \\ \beta & \text{otherwise} \end{cases} \tag{1.9}$$

- **ISSM** (4 free parameters): Internal Shock Synchrotron Model, presented in § 1.3.4. For $\beta \to -\infty$, $f_{ISSM}(E) = f_{COMP}(E)$. In fact:

$$\lim_{\beta \to -\infty} \Gamma_{ISSM}(E) = \alpha - \frac{E(2+\alpha)}{E_p} \tag{1.10}$$

Recalling that $\Gamma_{ISSM}(E) = \frac{\partial \ln(f_{ISSM})}{\partial \ln(E)}$ and integrating with respect to E we recover $f_{ISSM}(E) = f_{COMP}(E)$. ISSM can be reparameterized as follows when the reference energy is chosen to scale with the SED peak energy and set to $E_0 = -\frac{2+\beta}{2+\alpha} E_p$:

$$f_{ISSM}(E) = A \left(\frac{E}{E_0}\right)^{\alpha} \left(\frac{\frac{E}{E_0} + 1}{2}\right)^{\beta - \alpha} \tag{1.11}$$

- **SBPL** (4 free parameters): smoothly broken power law. It was introduced by Ryde 1999 and reparameterized by Kaneko et al. 2006 as:

$$f_{SBPL}(E) = A \left(\frac{E}{E_{piv}}\right)^{b} 10^{(a-a_{piv})} \tag{1.12}$$

where

$$a = m\Lambda \ln\left(\frac{e^{q}+e^{-q}}{2}\right), \quad a_{piv} = m\Lambda \ln\left(\frac{e^{q_{piv}}+e^{-q_{piv}}}{2}\right),$$
$$q = \frac{\log(E/E_b)}{\Lambda}, \quad q_{piv} = \frac{\log(E_{piv}/E_b)}{\Lambda},$$
$$m = \frac{\lambda_2-\lambda_1}{2}, \quad b = \frac{\lambda_1+\lambda_2}{2}.$$

A is the differential flux evaluated at E_{piv}, λ_1 and λ_2 are the low-energy and the high-energy spectral indices, E_b is the break energy, and E_{piv} is the reference energy fixed to 100 keV. The fifth parameter Λ is the break scale in decades of energy. It is fixed to 0.3 as in the second GBM spectral catalog [Gruber et al. 2014], so globally SBPL has four free spectral parameters.

Chapter 2

The *Fermi* Gamma-ray Space Telescope

2.1 The *Fermi* observatory

The *Fermi* Gamma Ray Space Telescope, formerly known as Gamma-ray Large Area Space Telescope (GLAST), is an observatory sensitive in the energy range from 10 keV to more than 300 GeV. The satellite carrying *Fermi* was launched into a near-earth orbit at 25.3 °of inclination on 11 June 2008, with an expected lifetime of 5 years, and a goal of being operative for an extended period of 5 years. The *Fermi* instruments are composed of materials that are not affected by significant degradation in orbit, and they continue to operate with excellent efficiency after 14 years. An artistic impression of the *Fermi* spacecraft in orbit is shown in Figure 2.1. There are two instruments on the *Fermi* observatory, the Large Area Telescope (LAT), which covers the energy range 20 MeV to $>$ 300 GeV, and the Gamma-ray Burst Monitor (GBM), which covers the energy range 8 keV to 40 MeV. Figure 2.2 shows the LAT and GBM on ground. *Fermi* is an observatory in charge of monitoring the high-energy gamma-ray sky, therefore its instruments have been designed with large fields of view (FOV). The LAT sees approximately 20% of the sky at any time (FOV=2.4 sr) and the GBM sees the full sky unocculted by the Earth (FOV$\sim$ 9 sr). Figure 2.3 shows the LAT and the GBM FOVs. Initially, because the LAT FOV is so large, it was possible to sweep across the full sky with good uniformity, exposing all part of the sky for 30 minutes, every two orbits (3 hr). In March 2018, *Fermi* experienced the first serious hardware failure of the mission: one solar array drive assembly stopped moving and could not be revived. The *Fermi* Team studied a new observing strategy in order to preserve a correct orientation of the panel to the Sun as well as uniform exposure to the sky, and this resulted in a minimum impact on the scientific performance of the two instruments.

Figure 2.1: Artistic representation of *Fermi* satellite (credit NASA).

Fermi is the fruit of and it is managed by an international collaboration. The LAT collaboration counts among its members more than 400 scientists and students from more than 90 universities and laboratories all around the World. The collaboration is structured into several scientific groups led by the most experienced

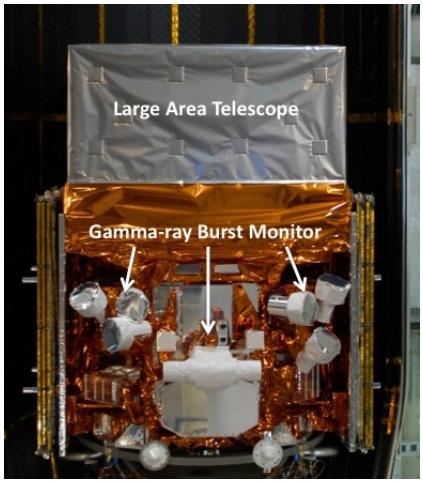

Figure 2.2: The *Fermi* Gamma-ray Space Telescope: the Large Area Telescope (LAT) is above the Gamma-ray Burst Monitor (GBM) (credit NASA).

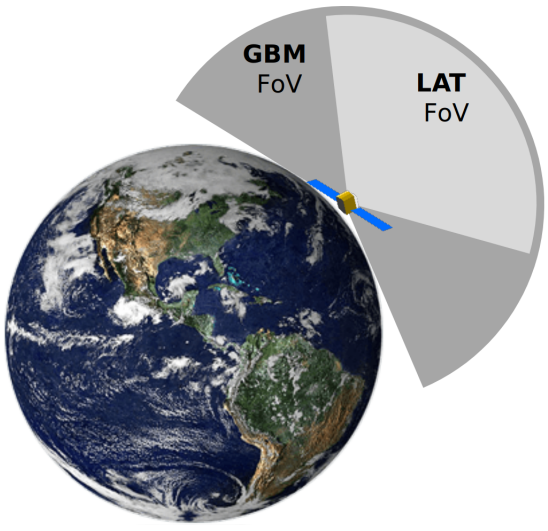

Figure 2.3: Representation of the field of view of the two *Fermi*'s instruments: the GBM sees the entire unocculted sky (9 sr), whereas the LAT has an instantaneous coverage of 20% (2.4 sr) of the sky (credit NASA).

members of the collaboration. The GBM Team is mainly constituted by scientists and students of the University of Alabama and of the NASA Marshall Space Flight Center in Huntsville (Alabama, USA), and of the German Max Plack Institute for Extraterrestrial Physics Team (MPE). The scope of the *Fermi* mission has been fostering our knowledge of the high-energy gamma-ray sky in an unprecedented broad energy range, more than seven decades in energy, and with the greatest possible spatial and temporal coverage with the highest sensitivity.

2.2 The instruments on board *Fermi*

2.2.1 The Large Area Telescope

Operating principle

The LAT [Atwood et al. 2009] is an imaging, wide FOV, high-energy pair-conversion telescope, covering the energy range from 20 MeV to more than 300 GeV. The LAT is 0.72 m deep with a 1.8 m×1.8 m square base, and its total mass is 2789 kg. Unlike visible light, high-energy gamma-rays cannot be refracted by a lens or focused by a mirror. They are instead detected with the same technology used by detectors in high-energy

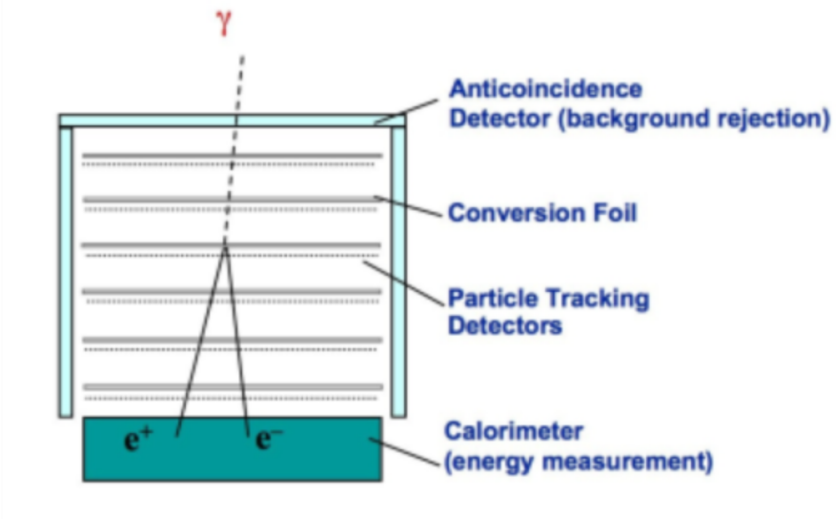

Figure 2.4: LAT detection principle: the incoming gamma-ray interacts with one atom of the tungsten foil producing an e^+e^- pair. The progress of the charged particles produced is tracked down to the calorimeter, that measures their energy (credit LAT collaboration).

particle accelerators. The sub-systems of the LAT therefore include a converter-tracker made of precision silicon-strips detectors, a CsI(Tl) calorimeter, each consisting of a 4×4 array of 16 modules supported by a low-mass aluminium structure, a segmented anti-coincidence detector (ACD) that covers the tracker array, and a programmable trigger and data acquisition system. The LAT detection principle can be summarized as following: incoming gamma-rays pass essentially freely through the thin ACD (see Figure 2.4), while high-energy charged cosmic rays scatter on the atoms of the ACD producing a flash of light, that is used as veto. A photon continues right along its path until it interacts with an atom of the thin tungsten foils of the converter-tracker producing a positron e^+ and an electron e^- pair. The foils are alternated to thin silicon strip detectors and detect the charged particles. The silicon strips alternate in two perpendicular directions, allowing to track the progress of the particles. The particles are stopped by the calorimeter which measures the total energy deposited. The information given by the ACD, tracker-converter and calorimeter is combined, and the energy and the direction of the gamma-ray are estimated. The calorimeter's depth and segmentation enable the high-energy reach of the LAT and contribute significantly to background rejection. The aspect ratio of the tracker (height/width) is 0.4, which yields a large FOV and its ensures that most pair-conversion events initiated in the converter-tracker will pass into the calorimeter for energy measurement.

The LAT sub-systems have been continuously monitored and in-flight calibrations have been performed [Abdo et al. 2009c] since the beginning of in-orbit operations on June 23, 2008. Calibrations correspond to synchronization of trigger signals, optimization of delays for latching data, determination of detector thresholds, gains and responses, evaluation of the perimeter of the South Atlantic Anomaly (SAA), measurements of live time, and internal and spacecraft boresight alignments. The in-orbit calibrations results were obtained using known astrophysical sources, galactic cosmic rays, and charge injection into the front-end electronics of each detector. As a result, the calibration remained stable and only minor changes were observed since launch as expected [Ajello et al. 2021].

Sub-systems

The converter-tracker is comprised of 4×4 modules, each composed of 18 planes. The first 16 planes contain a material with high atomic number (tungsten) to facilitate the conversion of incoming gamma-rays to an e^+e^- pair. All planes contain two orthogonal layers of single-sided silicon strip detectors to track the particles resulting from pair conversion. This information is used to reconstruct the directions of the incident gamma-rays. The left panel of Figure 2.5 shows the completed 16 module tracker array before integration with the ACD.

The calorimeter is comprised of 4×4 modules, each composed of 96 CsI(Tl) crystals ($2.7 \times 2.0 \times 32.6\ cm^3$).

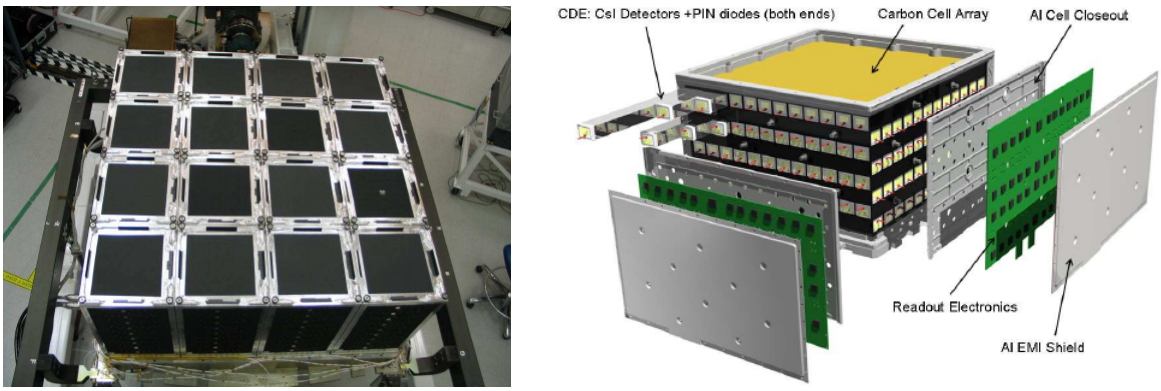

Figure 2.5: Left: completed tracker array before integration with the ACD. Right: exploded view of a LAT calorimeter module. The 96 CsI(Tl) scintillator crystal detector elements are arranged in 8 layers, with the orientation in adjacent layers rotated by 90 degrees [Atwood et al. 2009].

Event class	Description
transient	Event class with the loosest cut on the background rate.
source	It provides good sensitivity for analysis of point sources and moderately extended sources.
ultracleanveto/sourceveto	These are the cleanest event classes.

Table 2.1: LAT event classes. For details refer to Cicerone.

The crystals are disposed in 8 layers, each one being orthogonal to its neighbours (see right panel of Figure 2.5). At the end of each crystal two photodiodes record the deposited energy, a large one with area 147 mm^2 and a small one with area 24 mm^2. The large photodiodes cover the range 2 MeV-1.6 GeV, while the small photodiodes cover the range 100 MeV-70 GeV. This hodoscopic configuration allow to measure the energy of the electromagnetic shower created by the e^+e^- pair and to profile its development. Therefore, the calorimeter also contributes to the reconstruction of the incoming photon direction, and its longitudinal segmentation enables energy measurements up to a TeV.

The anti-coincidence detector (ACD) covers the converter-tracker array and provides charged-particle background rejection. Secondary particles from the electromagnetic shower in the calorimeter can Compton scatter back to the ACD and produce a false veto signal. The ACD is segmented and only the tiles close to the incident candidate photon direction are considered in the event reconstruction and classification to limit that backsplash effect and to keep a large gamma-ray detection efficiency.

Event classification and reconstruction

The LAT events are classified according to their probability of being astrophysical photons, and on the quality of their reconstruction. In particular they are divided into different event classes and each one is characterized by its own set of instrument response functions. The current event classes are organized into a nested hierarchy, where higher probability photon selections are subsets that fall into less restrictive selections. Higher probability photon selections are characterized by smaller effective areas, narrower point spread functions, and lower contamination of background events. The loosest selection criteria are labeled as *transient* classes: they are designed for short duration events, such as GRBs, and timing studies that need a greater photon statistics and can tolerate a higher background fraction and broader point spread functions. The cleaner photon selections *ultracleanveto* and *sourceveto* provide lower background contamination at the expense of lower effective areas. The intermediate *source* class is the recommended for most analyses: it provides good sensitivity to inspect point and extended sources on medium and long timescales. The most restrictive selections *ultracleanveto* and *sourceveto* are recommended to analyze large regions of the sky, where the effect of the instrumental background is higher. Table 2.1 presents the mentioned event classes sorted per increasing restriction on background contamination.

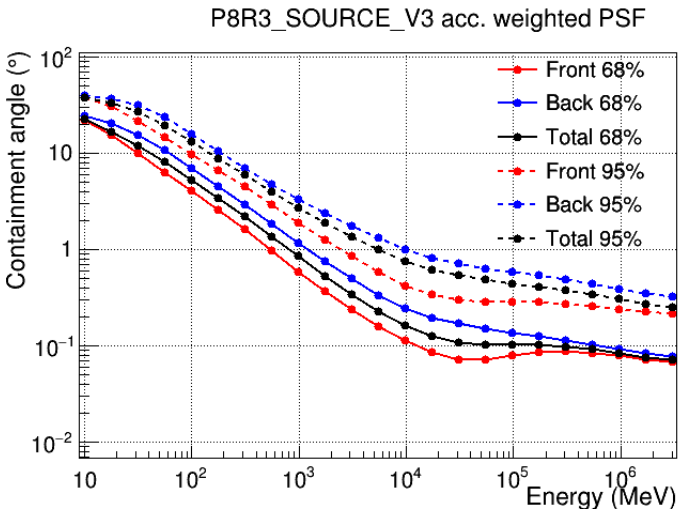

Figure 2.6: Dependence of the 68% and 95% containment angles of the PSF on the event energy. Here are shown the PSF for the FRONT, BACK event types, which are subdivisions of the *source* class. Those types correspond to the location where the photon converts to a pair in the tracker (credit LAT collaboration).

The software dedicated to reconstruct each event features has been ameliorated many times during the course of the mission because of the improvements in the understanding of the LAT. There have been four major data releases (Passes) since launch: Pass 6, Pass 7, Pass 7 Reprocessed, and Pass 8 [Atwood et al. 2013]. Pass 8 was released in June 2015 and it introduced significant changes to the event-level reconstruction. In particular it reduced the impact of ghost events, which were instrumental pile-up signals from cosmic-rays contaminating the gamma-ray signal. The response functions of Pass 8 are thus more accurate than the response functions of the other Passes. Moreover Pass 8 contains more events for a given time interval and especially at low-energy: spectral analyses can start at 50 MeV as opposed to 100 MeV before Pass 8.

Instrument response functions and performance

The instrument response functions (IRFs) describe the response of the LAT in measuring an event property (e.g., energy, position) given its true value. The observed count rate is the result of the actual incoming flux folded with the IRFs. The IRFs of the LAT are the point spread function (PSF), the effective area (A_{eff}), and the energy dispersion.

The point spead function (PSF) describes the response of the LAT to a point-like source, and it determines the image of the source as seen by the detector. The main cause of the spreading of the PSF is the multiple Coulomb scattering. Not only the gamma-ray cannot be focalized, but the elastic interaction of the produced pair with the atoms of the detector broadens the PSF and worsens the angular resolution especially at low energies. The PSF of the LAT is a function of the incident photon energy and incident angle. Figure 2.6 shows the dependence of the containment radius of the LAT PSF as a function of the photon energy for the P8R3 *source* class. The PSF goes as $\sim E^{-1}$ up to 10 GeV: in this energy range the PSF is dominated by the multiple scattering. For energies greater than 10 GeV the intrinsic resolution of the instrument dominates so the PSF tends asymptotically to a plateau.

The effective area is the LAT detection area which includes event selection efficiencies. It is a function of the photon energy and incidence angles. The left panel of Figure 2.7 shows the trend of the effective area A_{eff} as a function of the θ angle and averaged over the azimuthal angle ϕ for the P8R3 *source* class at 10 GeV. A_{eff} is maximum for $\theta = 0$, i.e. for photon directions parallel to the LAT optical axis. The left panel of Figure 2.8 shows the trend of A_{eff} as a function of energy for the *source* class and $\theta = 0$. The effective area is an increasing function of the energy until 3 GeV, it remains stable onwards, and decreases after 500 GeV. The acceptance $A(E)$ of the LAT is the integral of the effective area A_{eff} over the solid angle Ω. It reflects the LAT's ability to detect diffuse gamma-ray emission at a given time. It also can be used to define the LAT field of view, as a function of the photon energy: $FOV(E) = \frac{A(E)}{A_{eff}(E,0°)}$. The right panel of Figure 2.8 shows the trend of the acceptance as a function of energy for the P8R3 *source* class.

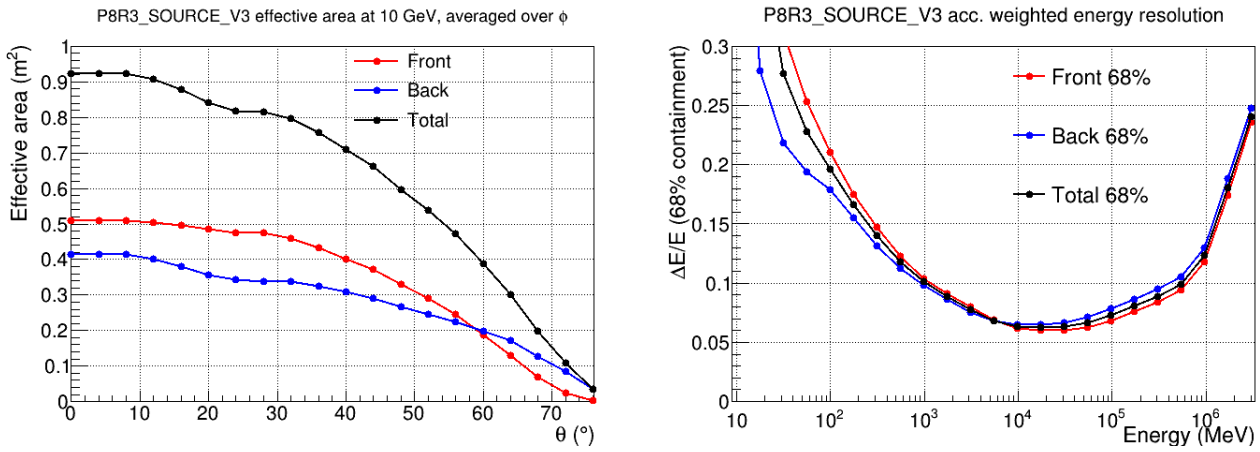

Figure 2.7: Left: the effective area A_{eff} as a function of the angle θ from the LAT boresight for the P8R3 *source* class and at 10 GeV. A_{eff} is averaged over the azimuthal angle ϕ. The different colors represent different event types for the *source* class. Right: the LAT energy resolution as a function of the true energy E of an photon (credit LAT collaboration).

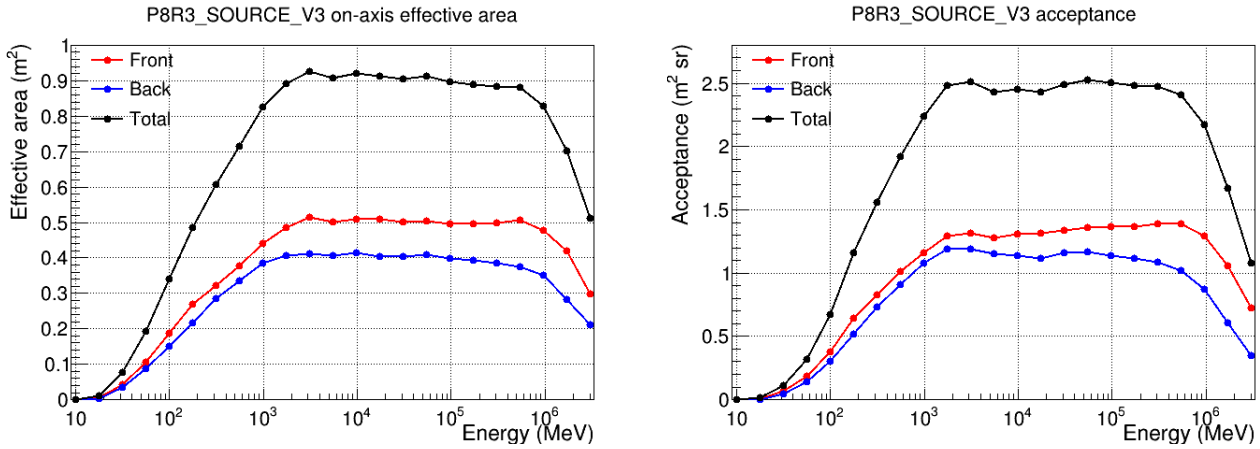

Figure 2.8: Left: the LAT effective area as a function of the energy of the incoming photon. The photon incides normally to the LAT, that is $\theta = 0$. Right: the LAT acceptance as a function of the photon energy (credit LAT collaboration).

The energy resolution of the LAT for an event of true energy E is computed as the difference between the true energy E and the reconstructed energy E' for that event. The right panel of Figure 2.7 shows the trend of the energy resolution ΔE normalized to the energy E. The energy resolution reaches its minimum (i.e. good resolution) at 10 GeV. At lower (<100 MeV) and higher (>1 TeV) energies the resolution worsens: the reconstructed energy is not longer a good estimate of the true energy E. One expects that since the low and high-energy photons deposit only a fraction of their energy within the calorimeter: low energy photons loose a big part of their energy in the tracker, while high-energy showers are not fully developed in the calorimeter.

Data products

The LAT data are downlinked from the *Fermi* spacecraft and are processed at the LAT Instrument Science Operations Center of the SLAC National Laboratory (California). The processing pipeline reconstructs the energy and direction of each event and classifies the event downloaded as cosmic rays or gamma-rays of various qualities. Table 2.2 presents the LAT data types. The most relevant parameters characterizing each photon are the following:

- Energy (MeV).
- Reconstructed arrival direction (Right Ascension, Declination) [degrees].

Name	Description
LAT events	Large number of parameters describing a large subset of the events telemetered to the ground (many did not result from photons.)
LLE events	LAT Low Energy events with an energy greater than $\sim$ 30 MeV. They are selected by the on board GAMMA filter and leave at least one event track in the tracker.
LAT photons	Selected parameters from the subset of events identified as gamma-ray photons.
LAT Pointing and Livetime History	LAT orientation and mode at 30-second and 1-second intervals; used to calculate exposures.

Table 2.2: LAT data types.

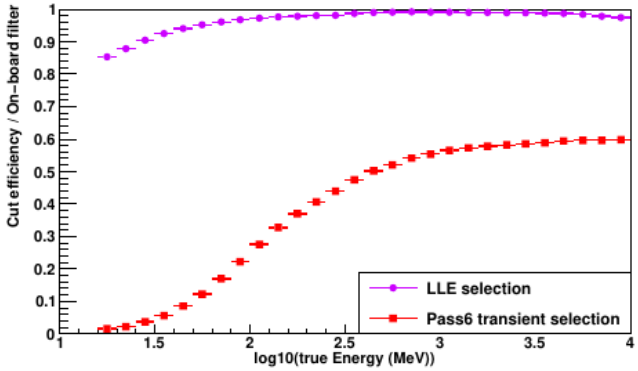

Figure 2.9: Fraction of events from a large data set of simulated photons passing the standard Pass6 *transient* class quality selections (red squares) and LLE relaxed selections (violet circles), both normalized to the onboard GAMMA filter. Credit Pelassa et al. 2010.

- θ angle between the direction of the event and the boresight of the LAT. The cone at $\theta \sim 65°$ defines the LAT field of view (see above).
- ζ angle between the direction of the event and the zenith (the vector from Earth to the spacecraft). This information is important, because from $\zeta \sim 100°$ to higher angles the gamma-rays emitted by the Earth Limb dominate the flux of detected events. In that case no reliable detection of astrophysical gamma-rays is possible. For that reason a cut typically at $\zeta < 100°$ allows to exclude the Earth Limb contamination.
- The mission elapsed time (MET) of the event (the number of seconds since January 1, 2001 at 00h:00m:00s in the Universal Time Coordinated [UTC] system).
- Event class (see above).

LAT Low Energy data

LAT standard analyses consider LAT data above 100 MeV, and don't cover the energy range down to the high-energy bound of the GBM (40 MeV) where high-energy GRB prompt emission is expected. Pelassa et al. 2010 proposed a non standard analysis technique to consider LAT data down to $\sim$ 30 MeV in order to fill this gap, and thus providing useful data to better constrain the high-energy part of GRB prompt spectra. The LLE data are defined by less stringent cuts than LAT standard data: they are selected by applying the GAMMA filter [Atwood et al. 2009] and requiring that at least one event track can be found in the tracker. Another advantage of the LLE data is the higher photon statistics than the LAT standard data above 100

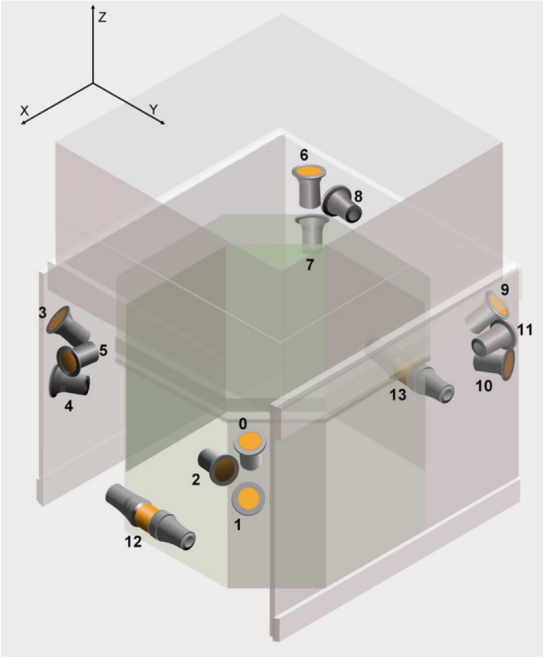

Figure 2.10: Locations and orientations of the GBM detectors. (credit Meegan et al. 2009).

MeV, which allows to better define the GRB prompt spectral features at high energies. Figure 2.9 shows the higher efficiency of the LLE data selection with respect to the standard Pass 6 *transient* event class selection. The spectral analysis of LLE data is based on the same forward-folding technique that is used for the analysis of GBM data. As in a GBM data preparation (see § 2.4.2), an on-source interval containing the burst emission is defined and two adjacent off-source intervals are chosen to extrapolate the background rate in the on-source interval. The event rate is subtracted by the estimated background rate, is binned, and subsequently is compared with a spectral model, which is folded through a dedicated Detector Response Matrix (DRM). More details on the forward folding technique and on such data analysis are provided in § 2.4.2.

2.2.2 The Gamma-ray Burst Monitor

The role of the GBM is to extend the energy range of GRB observations from the LAT threshold (20 MeV) down to the range widely explored by previous instruments dedicated to high-energy transient sources, such as the Burst and Transient Source Experiment (BATSE), which covered the energy band 30 keV-1.9 MeV on board the Compton Gamma Ray Observatory (CGRO; Gehrels et al. 1994). The GBM gives the low-energy context for transient sources jointly detected with the LAT. In particular it measures the main component of GRBs which typically peaks at hundreds of keV and contains the bulk of their energy throughput. Moreover the GBM detects and localizes bursts over a wider FOV than the LAT. GBM detections have triggered a repointing for remarkable bursts and have enabled LAT observations of delayed high-energy emission.

The GBM comprises 12 Sodium Iodide (NaI) scintillation detectors, 2 Bismuth Germanate (BGO) detectors, a Data Processing Unit (DPU), and a Power Supply Box (PSB). The NaI detectors are 1.27 cm thick with a diameter of 12.7 cm. They have a thin Beryllium entrance window, which is coupled to a 12.7 cm photomultiplier tube (PMT). They cover the energy range from 8 keV to 1 MeV and are used to determine GRB localizations. The BGO detectors are 12.7 cm thick with a diameter of 12.7 cm, and have two PMTs at their opposite sides. They cover the 150 keV to 30 MeV energy range and provide overlap with both the NaI detectors and the LAT. Figure 2.10 shows the orientation of the GBM detectors in spacecraft coordinates. The detectors are oriented and positioned on the spacecraft so as to provide approximately uniform coverage of the unocculted sky. Bursts typically illuminate three or more of the NaI detectors and one of the BGO detectors. Figure 2.11 shows one NaI detector unit and one BGO detector. The GBM normally produces two types of data, which are called CTIME and CSPEC. Those are histograms of count spectra from each detector and they have different temporal and spectral resolutions. Time-tagged event (TTE) data are also

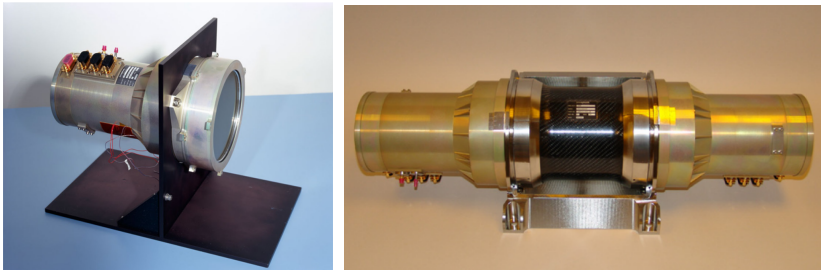

Figure 2.11: NaI(Tl)-detector unit (left panel), BGO detector (right panel) (credit Meegan et al. 2009).

Name	Purpose	Temporal resolution	Energy resolution
CSPEC	Continuous high spectral resolution	Daily: 4.096 s On burst: 1.024 s	128 energy channels
CTIME	Continuous high time resolution	Daily: 0.256 s On burst: 0.064 s	8 energy channels
TTE	Time-tagged events during burst	$2\,\mu s$ time tags for 300 s after trigger; 5×10^5 events before trigger	128 energy channels

Table 2.3: The GBM data types.

transmitted to the ground when a burst occurs. These data encode the time of arrival and energy of each event in each detector. Those data types are summarized in Table 2.3.

The GBM flight software implements an on board burst trigger that initiates an increase in data transmission. A trigger occurs if the count rates in two or more of the NaI detectors exceed a specified statistical significance above the background rate. A total of 120 different trigger algorithms may be defined and run at the same time. The available energy ranges for triggering have not changed since the launch of *Fermi*, and these are in units of keV: 25-50, 50-300, >100, and >300. The available trigger time scales range from 0.016 s to 8.192 s in steps of a factor of two. The nominal trigger is always enabled and it uses the 50-300 keV energy band and the 1.024 s time scale. The nominal significance threshold is 4.5σ. See Paciesas et al. 2012 for a more detailed discussion on the trigger engines. When a burst trigger occurs the GBM begins transmitting time-tagged event data for 300 s. A ring buffer of 5×10^5 pre-trigger time-tagged events is also transmitted. The on board software also computes the direction of the trigger event, the classification likelihood (GRB, solar flare, particle precipitation, etc.), and peak flux and fluence estimates. The on board localization is determined by comparing the relative count rates of the NaI detectors to a table of predicted rates corresponding to 1634 directions specified in spacecraft coordinates. The classification of the trigger is done considering its localization, spectral hardness, and the geomagnetic latitude of the observatory. The parameters determined on board are sent to the LAT and to the ground in near real time. Trigger information is distributed to ground-based observers via the Gamma-ray Coordinates Network (GCN).

2.3 *Fermi* main results

The scientific objectives the LAT has addressed include the investigation of the high-energy gamma-ray sky, the determination of the nature of the unidentified gamma-ray sources, and the origin of the isotropic diffuse emission previously observed by EGRET. Moreover the LAT science regards the understanding of the mechanisms of particle acceleration in celestial sources, including active galactic nuclei, pulsars, and supernovae remnants. The LAT scientific objectives include also the study of the high-energy behaviour of Gamma-Ray Bursts and other transient sources, and the use of high-energy gamma-rays to probe the early Universe and the nature of Dark Matter. The number of diversified science topics that are addressed by *Fermi* has allowed to release several catalogs, such as the LAT Source Catalog, the Active galactic Nuclei Catalog, and the Pulsar Catalog.

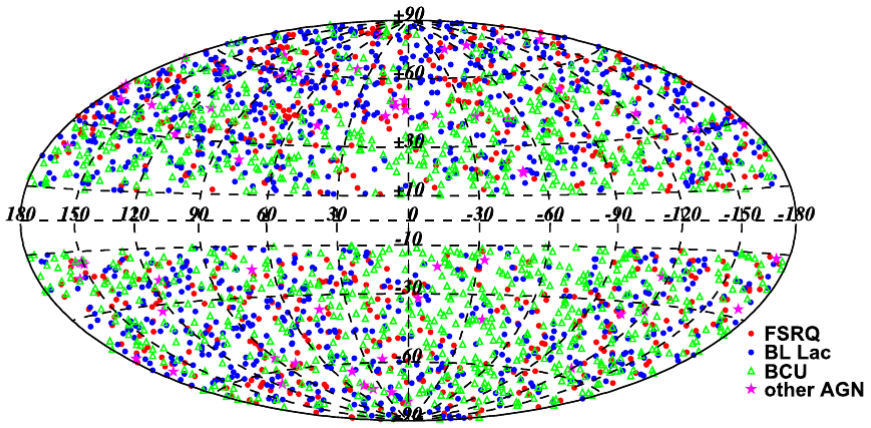

Figure 2.12: Source distribution in galactic Coordinates from 4LAC-DR1 [Ajello et al. 2020b]

.

2.3.1 Fourth LAT Source Catalog

The LAT collaboration produced several increments of high-energy gamma-ray catalogs. The major change in the gamma-ray catalogs came with the first release of the Fourth LAT source catalog by Abdollahi et al. 2020, which is labeled 4FGL. A great improvement of the catalog has been brought by the last background diffuse emission model since the significance of detection or non detection of a source depends on the background model assumed in the analysis. Moreover the latest event reconstruction algorithm Pass 8, now at its third reprocessed version, improved the quality of the catalog. Pass 8 data benefits of an improved angular resolution above 3 GeV and about a 20% larger acceptance at all energies. Moreover a small correction has been introduced to account for the effect of energy dispersion. The current third data relase of the catalog, labeled 4FGL-DR3, extends the results of the 4FGL from 8 years of observations to 12 years. This incremental version preserves the existence and positions of the sources present in the previous versions, and adds new sources. The 4FGL-DR3 includes 6658 sources in the energy range from 50 MeV to 1 TeV, 1695 of which are found to be significantly variable on one year time scale. 3388 (51%) sources are best fit with curved spectral shapes, which are more complex than the simple power law. 389 sources (6%) are considered identified, based on pulsations, correlated variability, or correlated angular sizes with observations at other wavelengths. The authors found likely lower-energy counterparts for 4112 sources (62%). The remaining 2157 sources (32%) were unassociated. The identified and associated sources in the 4FGL-DR3 include many galactic and extragalactic source classes. The largest galactic source class is represented by 255 pulsars, with 135 young and 120 millisecond gamma-ray pulsars. Blazars are the largest class of extragalactic sources with 1435 sources associated to a BL Lac object and 750 associated to Flat Spectrum Radio Quasars (FSRQs).

2.3.2 Fourth LAT Catalog of Active galactic Nuclei

Blazars are Active galactic Nuclei (AGN) whose relativistic jet points towards the line of sight of the observer. Those objects constitute the most populated extra-galactic class of the LAT source catalog. As the catalog accomodate for new events, new active galactic nuclei catalogs are released. The Fourth Catalog of Active galactic Nuclei (4LAC) was based on the observations of 8 years of the LAT data. It contained 2863 sources, among which 655 (23%) FSRQs, 1067 (37%) BL Lac objects, and 1077 (38%) blazar candidates of unknown types. It is currently at its second release (4LAC-DR2) and it takes into account the first 10 years of observations of the LAT. It is consistent with the second release of the Fourth LAT Source Catalog (4FGL-DR2). 4LAC-DR2 contains 694 FSRQs, 1126 BL Lacs, 1262 blazar candidates of unknown type, and the 2 radio galaxies NGC 3078 and NGC 4261. At high galactic latitude the most common sources are the active galactic nuclei of blazar type. The wealth of data provided by the 2 4LAC releases allowed to investigate the dichotomy of the two blazar subclasses, FSRQs and BL Lacs [Ghisellini et al. 2017], to test the connections between gamma-ray loudness, brightness, and polarization at other energy ranges [Angelakis et al. 2016], and to probe the possible connection of AGN gamma-rays and ultra high-energy cosmic rays [Kagaya et al. 2017]

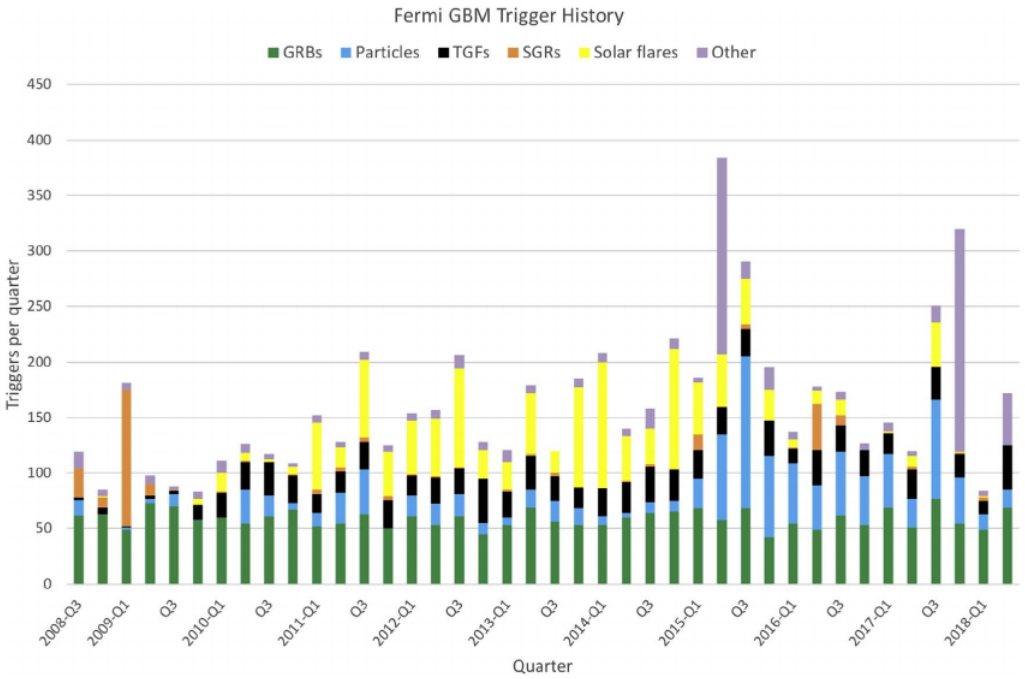

Figure 2.13: Trigger statistics for the first 10 years of observations of the GBM, from July 2008 to June 2018 [von Kienlin et al. 2020].

or high-energy neutrinos [Padovani et al. 2016]. Figure 2.12 shows the distribution of the different AGN classes in galactic coordinates. The BL Lacs objects are distributed anisotropically over the two galactic hemispheres, in particular the BL Lacs are 42% more aboundant in the galactic Northern hemisphere than the Southern one. The observed anisotropy can be explained from the larger and better spectroscopic data available in literature for the Northern hemisphere, which provide material to associate and assess the nature of the BL Lac objects.

2.3.3 Pulsar science with the LAT

The LAT observations confirmed that pulsars represent a sizeable fraction of the EGRET unassociated low galactic latitude gamma-ray sources [Romani et al. 1995]. A pulsar is a rapidly-rotation and highly-magnetized neutron star, which is surrounded by a plasma-filled magnetosphere. The LAT discovered dozens of radio-quiet gamma-ray pulsars and millisecond pulsars (MSPs), and established pulsars as the dominant GeV gamma-ray source class in the Milky Way [Abdo et al. 2010]. According to the public list of the LAT detected pulsars a total of 276 were detected in gamma-rays up to December 16, 2021. On 15 April 2020 the LAT detected high-energy gamma-rays emanating from a giant flare of a magnetar located in the Sculptor Galaxy [Fermi-LAT Collaboration et al. 2021]. Magnetars are neutron stars which have extremely high magnetic fields and they rotate slower than typical neutron stars. A magnetar giant flare is a rare and short duration emission of hard X-rays and gamma-rays. The LAT detection of the initially mis-classified GRB 200415A [Omodei et al. 2020] is the first detection of gamma-rays at energies greater than 100 MeV from a magnetar giant flare.

2.3.4 The GBM sources

The fourth GBM Burst Catalog [von Kienlin et al. 2020] presents the observational results for the bursts detected during the first 10 years of operations, from July 12 2008 to July 11 2018. In that period the GBM triggered almost twice a day on transient events, 2356 of which were identified as GRBs. Additional triggers comprises emission from 258 Soft Gamma Repeaters, 880 terrestrial gamma-ray flashes, 1176 solar flares, 1023 charged particle events, and 708 as galactic sources or other events. Figure 2.13 presents a resume of the events on which the GBM triggered. The rate of GRB detections (2 GRBs every 3 days on average)

makes the GBM one of the most prolific GRB hunters! The GBM detected 395 short GRBs (17% of the total) and 1958 long GRBs (83%) over the first 10 years. For comparison purposes, the BATSE detected a total of 2704 bursts [Goldstein et al. 2013], among which 497 (18%) were short GRBs, and 1540 (57%) long GRBs (for 667 (25%) bursts the T_{90} has not been computed). The third Gamma-ray Burst Catalog [Lien et al. 2016] of the *Swift* Burst Alert Telescope (BAT) reports the detection of ~ 1000 bursts over the first 11 years of observations (an average of 2 bursts each 8 days). Among those bursts, 850 were long GRBs (85%), 90 short GRBs (9%), and 94 (9%) were either short GRBs with extended emission, or ultralong GRBs, or bursts with unconstrained duration.

2.4 Spectral analysis methods

2.4.1 LAT spectral analysis

The statistical method that is employed to detect a burst with the LAT is the Likelihood Ratio Test (LRT, Neyman et al. 1928). This test compares two hypotheses, one comprising the background which includes the galactic diffuse emission, the isotropic emission and the point sources, and one having in addition a test point source at a given position and with definite spectral parameters. For each hypothesis the likelihood is maximized and the following test statistic is evaluated:

$$TS = -2 \ln \frac{max_{\hat{b}} L(\hat{b})}{max_{\hat{b}\hat{s}\hat{p}} L(\hat{b}, \hat{s}, \hat{p})}$$

where $\hat{b}$ contains the parameters of the background, while $\hat{s}$ and $\hat{p}$ comprise the spectral and spatial parameters of the additional source. Under the hypothesis of the large sample limit the Wilks Theorem [Wilks 1938] states that the TS behaves like a χ^2 with a number of degrees of freedom equal to the number of the free parameters of the additional source. If the position of the source is already known, and the spectral model of the source is chosen as a power law with an index equal to -2 as for many LAT detected bursts, then the free parameter of the source is just the normalization of the power law. In this case, the significance of the additional source is equal to $\sqrt{TS}$, and a $TS > 25$ is required for a significance larger than 5σ. In case the position of the burst is not known then the relation is no more valid and the source must be localized with the *fermitools* *gtfindsrc* and *gttsmap*. The first tool allows for a quick localization profiling the likelihood with respect to the source position. The localization given by *gtfindsrc* can be used as input for *gttsmap*, which performs a likelihood analysis on a grid of points centered around the input position, and it estimates the improved localization of the source as the localization that maximizes the TS. Once the source has been localized, or a more precise localization has been provided by optical observations, the LAT spectral analysis quantifies the significance of the observed gamma-rays flux received at the position of the source. The *fermitool* *gtlike* fits the free parameters of the model components to the data. In the case of a GRB study the free parameters are its flux, spectral index, and the normalization of the isotropic emission model. The procedure can be briefly summarized as following: 1. space, time, energy and event class cuts are applied to the event file (see Table 2.2), in particular the study of point-like sources as GRBs requires the selection of a region (called region of interest or ROI) with a typical radius of 12°; 2. the history of LAT orientation is taken into account by computing the time that the LAT observed a given position on the sky at a given inclination angle; 3. definition of a source model which includes the background components and the additional point source in a region which encompasses the ROI to account for the PSF extension; 4. the flux contribution of the diffuse sources to the ROI is calculated, and 5. the TS of the additional source is computed. More details on the analysis sequence can be found in chapter 3 of Yassine 2017 and in the LAT official documentation in Cicerone.

2.4.2 GBM spectral analysis

Background and response files

As standard data preparation an event file and a corresponding background file are produced. The event file is a PHA2 file which conforms to the OGIP standards. Given a burst and a detector, the events of the

corresponding TTE file (see Table 2.3) are binned into 128 energy channels to form a total count spectrum file. The lowest energy channel for a NaI event file starts at 5 keV, and the highest energy channel stops at 2 MeV. The lowest energy channel for a BGO event file starts at 200 keV and the highest energy channel stops at 50 MeV. In practice, the lowest and highest energy channels are ignored in the spectral analysis because they are affected by overflow events. Moreover the channels corresponding to the energy range 30-40 keV in the NaIs detectors are ignored in the event file because they contain the energy of the photons emitted in the K-edge transition of the iodide element. The binned event file is produced via the standard software which is used to analyze the LAT data, the *fermitools*. In particular the tool *gtbin* takes as input file the TTE file containing the information on each tagged event recorded by the selected detector and it provides the energy binned event file as output. Each event file is coupled with a corresponding background file, which contains the best estimate of the background rate during the burst emission time interval. In my work, I prepared the background file with the software developed within the LAT GRB science group, *GBMtoolkit*, which also allows to produce the response file for each detector for a given burst (see next paragraph). It is not possible to know the exact background during the burst emission phase, but it is possible to approximate it. In particular, the background model is determined by fitting a polynomial function to the count light curve in the pre- and post-burst time intervals for each channel of the detector. The procedure can be detailed as following:

- Decide the degree D of the polynomial: *GBMtoolkit* considers the count light curve over all channels and fit polynomials of increasing order (starting from 0 to a maximum of 4) minimizing the χ^2 until it reaches a χ^2 probability greater than 0.5.
- Fit a polynomial of degree D to every channel: the fit is done by minimizing a Poisson log-likelihood to account for the low count statistics especially in the high-energy channels.
- Compute the residuals: all the best fitting models (one per channel) are summed up to give an integrated model. The residual corresponding to the i-th bin in the light curve is defined as $R_i = \frac{d_i - m_i}{\sqrt{m_i}}$, where d_i and m_i are the observed and model counts in the i-th bin of the light curve.

Natively *GBMtoolkit* prompts the user to choose the on- and off-burst time intervals for each burst. My contribution to the software was adapting it to automate this selection. It is then possible to produce a background file automatically by providing the edges of the off-source intervals. In this way it is possible to prepare automatically the spectral data for several bursts. In my work the off-source intervals last 150 s and are separated by a margin of 10 s from the burst duration interval provided by the GBM spectral catalog. The margin of 10 s was chosen long enough to exclude possible contamination of the burst emission and small enough to reproduce as accurately as possible the real contribution of the background during the burst emission. Figure 2.14 shows the lightcurve of GRB 081221681 in the NaI1 detector, where the on-source and the off-source intervals are highlighted. The left panel of Figure 2.15 shows the reduced chi-square of the background fit in each channel for that detector. I denote it as q^2_{red} to remind that this statistics is not necessarily χ^2 behaved since the large sample limit is not reached in some bins especially at high energies. The mean value of q^2_{red} is very close to one and its distribution is not much scattered, which indicates that all background fits for this detector are of excellent quality (see subsection 3.1.4 for more details). One of the GBM data products is an RSP2 file which contains the time dependent detector response matrix (DRM) in intervals of some tens of seconds. The DRM is equal to the detector effective area times its energy redistribution function. An example of DRM is shown in the right panel of Figure 2.15. *GBMtoolkit* produces for each detector a response matrix which is weighted by the number of events that are recorded for the time interval covered by each time-dependent response matrix. The ultimate product is then a single weighted response matrix which is employed in the spectral analysis.

Spectral fits

Most of my spectral analyses are performed through the frequentist approach of the maximum likelihood estimation. Indeed the instrumental response can not be inverted to recover the true spectrum of the source. Instead the so-called *forward-folding* procedure is used, which compares the observed counts with the expected counts that are obtained from the convolution of a spectral model with the IRFs. The likelihood

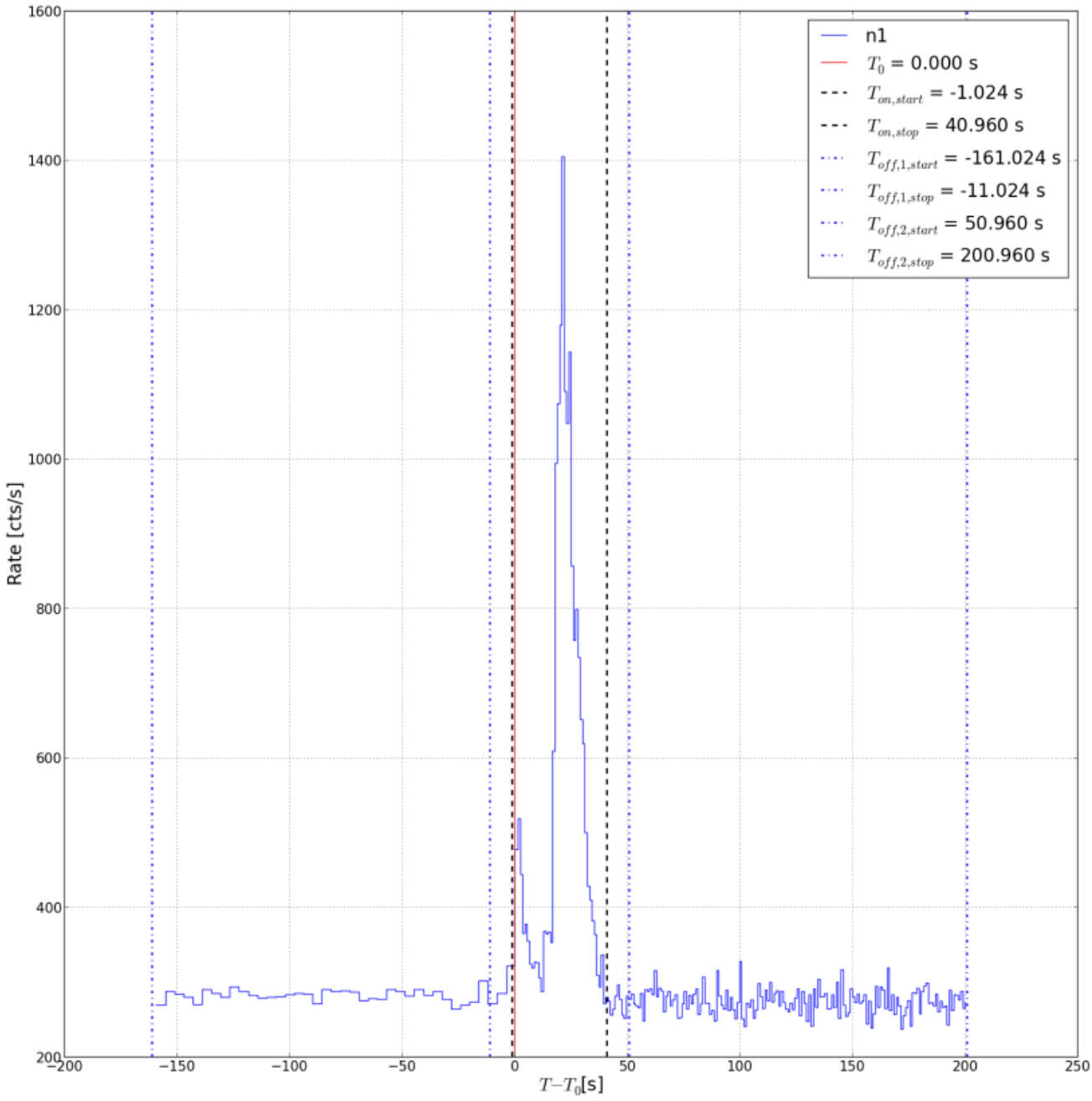

Figure 2.14: Lightcurve of GRB 081221681 for the GBM detector NaI1. The red vertical line corresponds to the time of the trigger, the black vertical dashed lines delimitate the on-source interval, and the blue vertical point-dashed lines delimitate the first and second off-source intervals.

function $L(\hat{D}, \hat{B}|\hat{\Theta})$ is computed as the probability of obtaining the observed counts (total spectral counts $\hat{D}$ and background counts $\hat{B}$) given the assumed spectral model and its parameters $\hat{\Theta}$. The likelihood function is then maximized to find the best-fit parameters of the model. The ability of this analysis to reconstruct a spectrum as close as possible to the true one of the source depends strongly on the quality of the background fits in the data preparation steps (see above), and more importantly on the choice of the spectral shape that is assumed to represent the source spectrum. In practice, we minimize the fit statistics $-2 \log L(\hat{D}, \hat{B}|\hat{\Theta})$, which behaves like a χ^2 in the large sample limit. Since this limit is almost never reached the likelihood function must account for the true distribution of the observed counts. In my work the total counts $\hat{D}$ are always Poisson distributed, and I chose a Gaussian distribution for the background counts $\hat{B}$ because they are obtained by polynomial fits. The resulting fit statistics that I used is the sum of a Poissonian likelihood and a Gaussian likelihood, and it is called *PG-stat*. Its detailed expression is given in appendix A, along

with other common fit statistics that I will mention in the manuscript.

In my work I employed the fitting software *XSPEC* and I used its Python interface *pyXSPEC*. The advantage of using *pyXSPEC* is that it is possible many useful Python libraries, for example *matplotlib* to display the results, or *pandas* to manipulate ordered tables of data. *XSPEC* implements the forward folding method in the maximum likelihood formalism. The objects that are necessary to perform a fit with *XSPEC* are the observed total count spectra, the background spectra, the detectors' responses, and a model. *pyXSPEC* offers also the possibility to define custom models. In all my work I implemented, tested, and employed local models defined in Python.
The workflow of a typical spectral analysis can be summarized as follows:

- Prepare the spectral data for the selected burst, namely get an event, background, and response file for each of the selected detectors.
- Select the energy channels that will be used in the spectral analysis. In fact, as mentioned in § 2.4.2 overflow channels must be excluded, as well as the channels corresponding to the K-edge transition between 30 keV and 40 keV.
- Load the local models.
- Set the initial values of the model's parameters, along with their boundaries. In fact, two different boundaries can be defined, which are treated differently by XSPEC. The soft low and high edges define the interval in which the parameter is desiderable but not obliged to be. On the other hand, the hard low and high edges define the interval within which the parameter is constrained. It is also possible to define the parameter step that the fitting engine will use to vary the parameter during the minimization process. In my work I set the parameter step to 10^{-3}.
- Choice of the minimizer and minimization. *XSPEC* employs *MINUIT* for the minimization process. In my work I have found that using first *simplex* and then *migrad* as minimizers methods is a solid way of find the minimum of the fit-statistic.
- Plot and store the results using my Python scripts. The source counts spectra are shown with the best-fit folded model for each detector, along with the residuals which are the ratio between the difference of the GRB counts spectra and the model counts spectra over the error on GRB counts spectra. The latter includes the error on the background. Two examples of those plots can be found at the upper panels of Figure 2.16 for GRB 150902733. Moreover I plot the spectral energy distribution (SED) and its 1σ contour. This contour is equal to the standard deviation of 5000 randow draws based on the best-fit covariance matrix. Two examples of that plot are shown in the lower panels of Figure 2.16. I store the best-fit values of the model's parameters, their errors, and the value of the best fit-statistic to a text file.

In my work on GRB 220101A I employed also another spectral fitting software called *3ML* (see § 5.2.5). *3ML* allows to perform a joint likelihood fit between different instruments. In particular it allows to use the native likelihood of each instrument. For the LAT this is a considerable advantage since in order to use the LAT data with *pyXSPEC* it is necessary to bin them, then it is inevitable to lose the power and the information of the full unbinned likelihood while it is precisely kept in *3ML*. Moreover *3ML* allows to perform the spectral data preparation, the maximum likelihood analysis, and also the Bayesian analysis.

2.5 Real-time analysis

2.5.1 GBM notices and circulars

From 2016 an automated localization algorithm called the RoboBA [von Kienlin et al. 2020] is operative within the GBM automatic pipeline for detecting and localizing bursts (Burst Alert Pipeline). The RoboBA is a set of automated algorithms developed to replace the intervention of the Burst Advocate (BA), which is the person in charge of monitoring the ongoing analysis until the localization. RoboBA estimates whether a burst is likely to be short or long. After the RoboBA localization, the GBM Burst Alert Pipeline submits

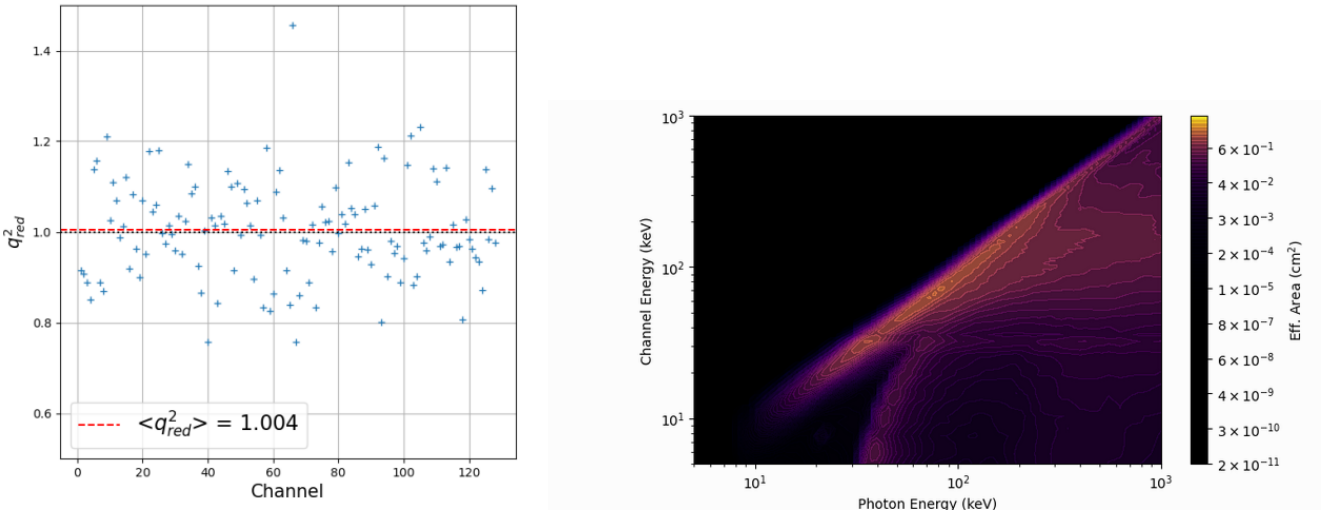

Figure 2.15: Left: reduced chi-square of the background fit in each channel of the detector NaI1 for GRB 081221681. Right: An example of DRM for one NaI detector. The diagonal corresponds to a conversion one-to-one between the photon energy channels and the measured energy channels. The presence of non diagonal elements means that there is no one-to-one correspondence between the true energy channels and the measured energy channels (credit NASA).

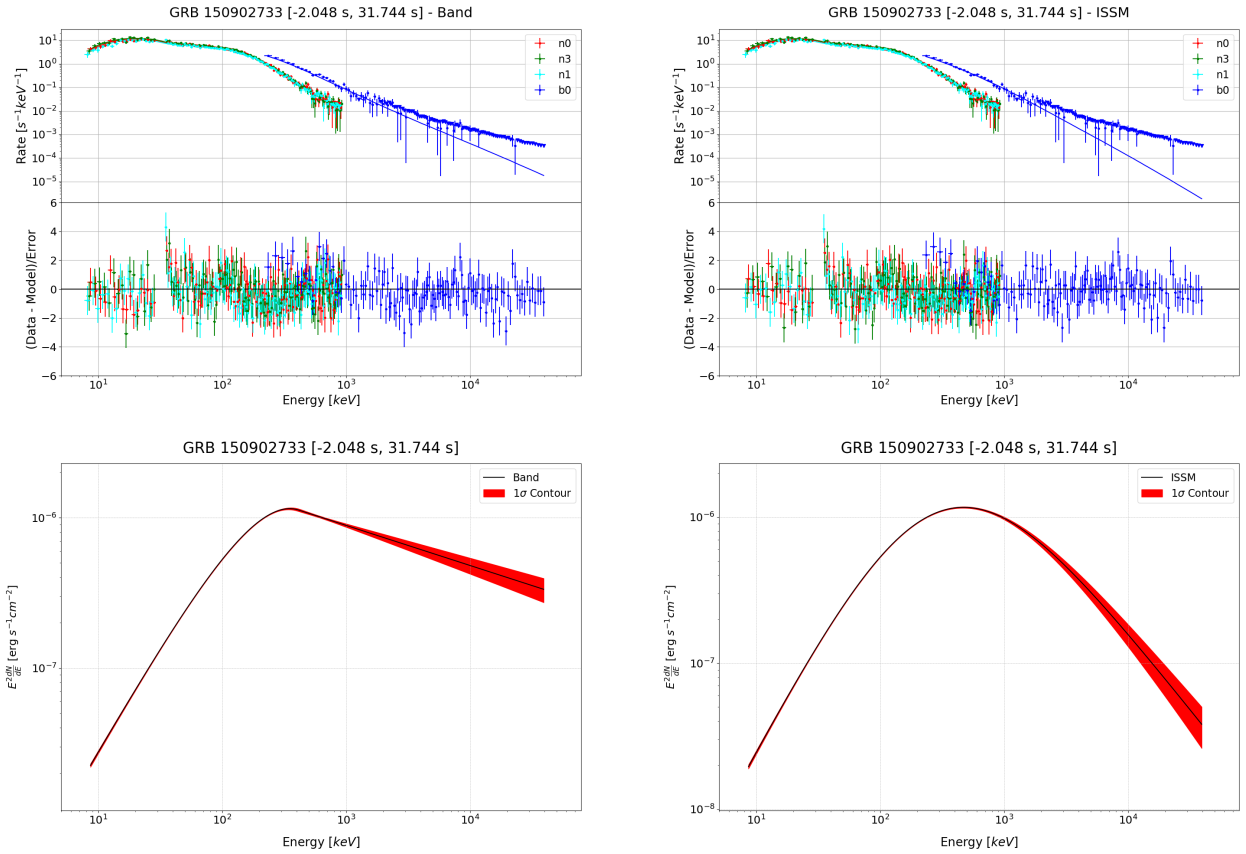

Figure 2.16: Upper panels: Band (left) and ISSM (right) GRB counts spectra with the folded model, and residuals. Lower panels: Band (left) and ISSM (right) spectral energy distributions. GRB 150902733 is well fitted by ISSM and Band with a *PG-stat* = 692 and 743 respectively, for 474 degrees of freedom.

Event	GCN circular
GRB	191220A, 220101A, 220408B, 220527A, 221027A
BBH	S191204r, S200208q, S200224ca, S200225q
NS-BH	S191205ah
Unmodeled transient candidate	S200114f
Mass gap	S200115j

Table 2.4: GCN circulars to which I contributed as author or co-author. Legend: BBH stands for binary Black Hole, NS-BH stands for Neutron Star (NS) - Black Hole (BH), Mass gap stands for a binary coalescence in which one component has a mass higher than the predicted maximum mass for a NS and lower than the minimum mass for a BH.

a GCN notice and circular providing the information. Notices are automated and parsable messages, and they are released typically from tens of second to 10 minutes after the GBM trigger. The flow of notices can be summarized as follows: an initial alert provides the trigger time of the event, along with its significance, the algorithm that triggered, and the event time scale. Then the initial localization of the event is computed on board and it is distributed as notice. After some minutes, when more information on the event becomes available, an intermediate localization of the trigger is distributed to the community. Finally, around 10 minutes from the time of the trigger, the final localization of the event is computed on ground [Connaughton et al. 2015], and a notice which provides the time of the trigger, the duration, and the localization of the trigger is distributed. Circulars are text messages which report on the trigger main properties, such as the localization estimated by the RobaBA and the results of the spectral analysis performed by the BA after downlink of the complete data set.

2.5.2 LAT Burst Advocate activity

The Burst Advocate (BA) is the person responsible for cross-checking the alerts of two the automatic pipelines, LAT Transient Factory and BA Tool, that run over the LAT data. Those pipelines look for significant excesses that can be identified as GRBs. The BA is on shift for one week, and is coupled with a deputy BA from another time zone. Having the BA and the deputy BA from different time zones allows to cover completely each day for the week of the shift. The BA is required to report the alert of the pipelines to the *Slack* channel of the LAT GRB group, to discuss the significance of the signal, and to manually cross-check the alert. The final product of the process is a GCN circular which contains the main spectro-temporal characteristics of the event, and its localization completed with its uncertainty. The 90% error is typically less than 1° for normal bursts and can reach 0.1-0.2° for the brightest ones. It is important to provide the most accurate and precise localization to the community to allow other observatories, which have more accurate localization capabilities, to promptly follow-up and localize the event. The ideal aim is the measurement of the redshift of the galaxy hosting the burst. **During the period of my work I performed 18 shifts as BA or deputy BA, and I am author or co-author of 12 GCN circulars, as summarized in Table 2.4.**

Gamma-Ray Bursts

Two pipelines, the LAT Transient Factory and the BA Tool, analyze the LAT data for redundancy and they are triggered by alerts issued by the GBM or instruments of other observatories. When one or both pipelines find a significant excess in the data the BA reports the detection internally to the Fermi GRB science group through the Slack GRB channel. Afterwards the BA performs a manual cross-check of the analysis with the standard software provided by the group which is called *gtburst*. Once a general agreement of the LAT GRB group is reached around the gathered results, then those results are reported to the community via the GCN circular. The most relevant information that is released by the LAT is the localization of the event. In case the localization determined by the LAT improves on the localization of the instrument which provided the trigger, the BA sends an off-line notice to the community reporting the LAT localization. Followingly, the probability of association of each recorded photon to the burst is determined via the *fermitool* *gtsrcprob*.

Among the photons with the highest association probability (typically greater than 0.99), the highest energy photon is reported in the GCN circular. The power law spectral index, and the photon flux above 100 MeV are also reported in the circular. Afterwards the BA performs a more detailed analysis of the GRB and reports the results to the bi-weekly meeting of the Fermi GRB group.

Gravitational Wave sources

Similarly to the GRB analysis, two pipelines called GWFUP and GW-BA Tool analyzed the LAT data for redundancy and for robustness over the triggers issued by the LIGO-Virgo Collaboration during the third observing run O3. No electromagnetic counterpart (EM) to Gravitational Wave (GW) events was found. The duty of the BA was monitoring the results of the automatic pipelines and to distribute the determined flux upper limits to the community. GWFUP runs two parallel searches for EM counterparts to GW sources [Vianello et al. 2017]. The fixed time window looks for a significant excess in a time window lasting 10^4 s from the time of the trigger in a grid of positions distributed over the localization region of the LIGO-Virgo event. This kind of search is done also by the GW-BA Tool. The second type of search uses an adaptive time window to look for a significant excess in the localization region of the GW source candidate. In particular for a given point of the grid the time-window starts when the point was observable by the LAT and stops when the point was no longer observable. My work started in November 2019 when the O3 observing run was ongoing. **The run lasted until March 2020, and over the last four months of O3 I was author or co-author of 7 GCN circulars as presented in Table 2.4**.

In the following page I present an example of circular for a GRB, namely GRB 220101A, and an example of a circular for a LIGO-Virgo event, namely S191205ah (NS-BH). Concerning S191205ah (NS-BH), two plots present the typical analysis products of the follow-up of a LIGO-Virgo event. The upper panel of Figure 2.17 presents the flux upper limits found by the fixed time interval search of GWFUP for that event. The lower panel shows the cumulative probability coverage of the event localization region as a function of the time since the trigger. At 6.2 ks all the region has been covered by the LAT.

TITLE: GCN CIRCULAR
NUMBER: 31350
SUBJECT: **GRB 220101A: Fermi-LAT detection**
DATE: 22/01/01 14:08:57 GMT
FROM: Lorenzo Scotton at CNRS/IN2P3/LUPM <lorenzo.scotton@lupm.in2p3.fr>

M. Arimoto (Kanazawa Univ.), L. Scotton (CNRS/IN2P3/LUPM) and F. Longo (University and INFN, Trieste) report on behalf of the Fermi-LAT Collaboration:

On January 1st, 2022, Fermi-LAT detected high-energy emission from GRB 220101A, which was also detected by Swift (trigger 1091527, Tohuvavohu et al. GCN Circ. 31347)

The best LAT on-ground location is found to be
RA, Dec = 1.52, 31.75 (degrees, J2000)
with an error radius of 0.46 deg (90% containment, statistical error only).

This was 18 deg from the LAT boresight at the time of the Swift trigger:
T0 = 05:10:11.5 UT.

The data from the Fermi-LAT show a significant increase
in the event rate after the Swift trigger that is spatially correlated with the Swift emission (0.14 degrees from the Swift-XRT location) with high significance.
The photon flux above 100 MeV in the time interval 0-600s after the Swift trigger is 2.5E-5 +/- 5E-6 ph/cm2/s.

The estimated photon index above 100 MeV is -2.46 +/- 0.25.

The Fermi-LAT point of contact for this burst is
Lorenzo Scotton (lorenzo.scotton AT lupm.in2p3.fr).

The Fermi-LAT is a pair conversion telescope designed to cover the energy band from 20 MeV to greater than 300 GeV. It is the product of an international collaboration between NASA and DOE in the U.S. and many scientific institutions across France, Italy, Japan and Sweden.

TITLE: GCN CIRCULAR
NUMBER: 26363
SUBJECT: **LIGO/Virgo S191205ah: No counterpart candidates in Fermi-LAT observations**
DATE: 19/12/06 13:04:09 GMT
FROM: Lorenzo Scotton at CNRS/IN2P3/LUPM <lorenzoscotton@live.it>

L. Scotton (CNRS/IN2P3/LUPM), M. Axelsson (KTH & Stockholm Univ.), E. Bissaldi (Politecnico & INFN Bari), D. Kocevski (NASA/MSFC), N. Omodei (Stanford Univ.), F.Longo (University and INFN, Trieste) and M. Arimoto (Kanazawa Univ.) report on behalf of the Fermi-LAT Collaboration:

We have searched data collected by the Fermi Large Area Telescope (LAT) on December 5th, 2019, for possible high-energy (E > 100 MeV) gamma-ray emission in spatial/temporal coincidence with the LIGO/Virgo trigger S191205ah (GCN 26350).

We define "instantaneous coverage" as the integral over the region of the LIGO probability map that is within the LAT field of view at a given time, and "cumulative
coverage" as the integral of the instantaneous coverage over time. Fermi-LAT had an instantaneous coverage of ~10% of the LIGO probability at the time of the trigger (T0 = 2019-12-05 21:52:08 UTC), and reached 100% cumulative coverage after ~6.2 ks.

We performed a search for a transient counterpart within the observed region of the 90% contour of LIGO map in a fixed time window from T0 to T0 + 10 ks.
No significant new sources are found.

We also performed a search which adapted the time interval of the analysis to the exposure of each region of the sky, and no additional excesses were found.

Energy flux upper bounds for the fixed time interval between 100 MeV and 1 GeV for this search vary between 4e-11 and 2e-07 [erg/cm^2/s].

The Fermi-LAT point of contact for this event is
Lorenzo Scotton (lorenzo.scotton@lupm.in2p3.fr).

The Fermi-LAT is a pair conversion telescope designed to cover the energy band from 20 MeV to greater than 300 GeV. It is the product of an international collaboration between NASA and DOE in the U.S. and many scientific institutions across France, Italy, Japan and Sweden.

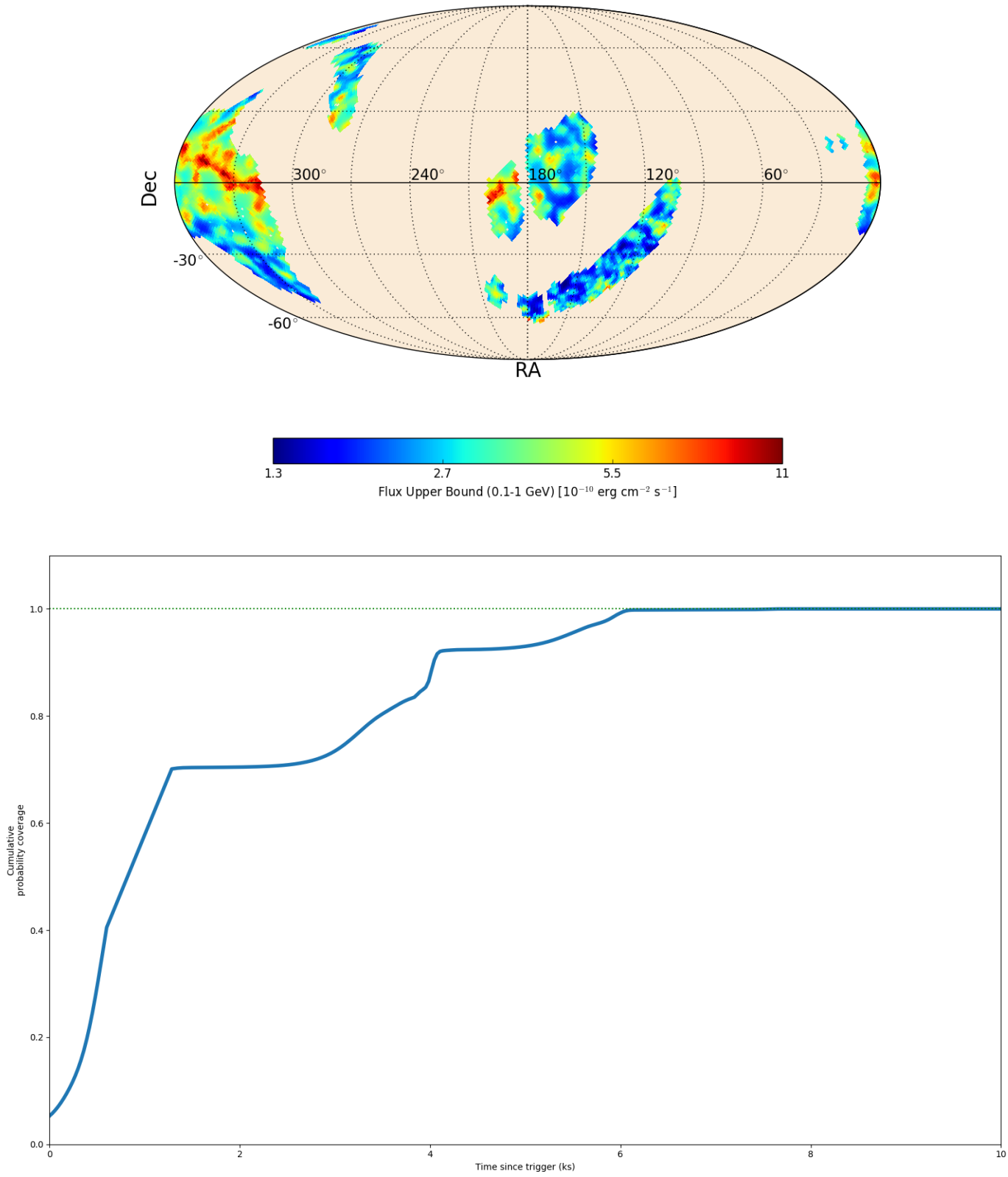

Figure 2.17: Upper panel: upper-limits computed by the fixed time window search of GWFUP for the LIGO-Virgo event S191205ah over its localization region. The coordinate system is equatorial. Lower panel: cumulative probability coverage of the localization map as a function of time since the trigger.

Chapter 3

The prompt non-thermal emission of *Fermi* GRBs

The aim of this chapter is to show the performance of the internal shock synchrotron model represented by the ISSM spectral function introduced in § 1. This study is based on the most fluent GBM bursts observed in the first 10 years of operations. I compare ISSM to the common literature models, and in particular to the Band function. In § 3.1 I describe the procedure I adopted to select the sample of GBM bursts, and in § 3.2 I present the results of the spectral analysis integrated for their duration. In § 3.3 I compute the temporal segmentation of each spectra applying the Bayesian blocks algorithm introduced by Scargle et al. 2013, and I present the results of the analysis focused on the most significant blocks that provide the best spectroscopic precision.

3.1 Selection of the GBM burst sample

I considered the bursts detected by the GBM in the first 10 years of operation. This period corresponds to the largest spectral catalog published by the GBM science team so far [Poolakkil et al. 2021]. This selection corresponds to a total of 2361 bursts, the first being GRB 080714086 and the last being GRB 180715755. In the following I describe the incremental selections I made on the bursts list. For each step I present the criterium of the selection, the number of bursts that survived the cuts, and the number of bursts excluded (see Table 3.1).

3.1.1 Step 1: selection on the best-fit model

I considered the bursts presenting enough statistics at high-energy to perform a spectral fit. For that reason I excluded all the bursts whose spectrum is best fitted by a power law (PL), as presented in the GBM catalog for the so-called "fluence spectra". Those spectra are integrated for the entire duration of the burst as selected by the GBM duty-scientist and their boundaries are presented in the fields "Flnc_Spectrum_Start" and "Flnc_Spectrum_Stop" of the GBM spectral catalog. I included the bursts whose GBM best-fit model is either COMP, SBPL, or Band, which I introduced in § 1. Moreover I considered all and only the bursts that could be interpreted as having a single component in the keV-MeV range, where the synchrotron emission is expected. Indeed the ISSM function has been built for the purpose of describing the single synchrotron component of the burst emission, then bursts whose spectra have been best-fit with a composite model had to be removed. I excluded the bursts which has been interpreted as having an additional thermal component at low energies (GRB 090424, GRB 090820B [Tierney et al. 2013], GRB 090902B [Abdo et al. 2009a], GRB 090926A [Guiriec et al. 2015b], GRB 100724B [Guiriec et al. 2011], GRB 110721A [Axelsson et al. 2012]), the bursts that presented an additional power law component at high energies (GRB 080916C [Ackermann et al. 2013], GRB 090926A [Ackermann et al. 2011]), and one burst that presented a strong spectral evolution (GRB 081215A [Tierney et al. 2013]). This selection resulted in 1778 bursts with a difference of 583 bursts with respect to the 10 years sample of the GBM spectral catalog. It is worth to note that in the 10 years sample PL is the preferred model 30% of the time, COMP 57%, Band and SBPL together only 13%.

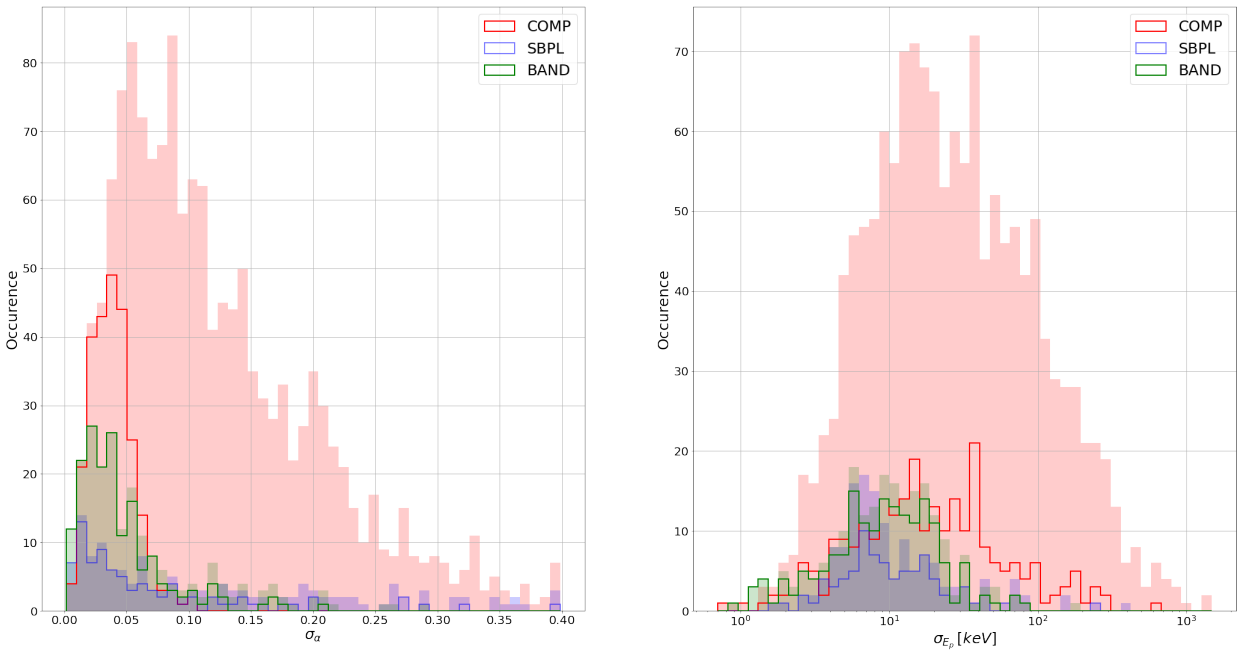

Figure 3.1: This figure shows the distribution of the error on the low-energy index (left panel) and on the peak energy (right panel) before and after the cut on the energy fluence. The colored area corresponds to the distribution before the cut, while the simple step histogram presents the distribution after the cut. COMP is the model which is most affected by the selection. Notably the distribution of the error on its low-energy index shifts to lower values, meaning that the cut selects the cases in which the low energy index of COMP is better measured. This is natural because more statistics is available in the selected cases. The same is not true for the distribution of the error on the peak energy of COMP, and on all the other distributions of Band and SBPL. Band and SBPL are not significantly affected by the energy fluence cut.

3.1.2 Step 2: selection on the energy fluence

This step had the highest incidence among the selection cuts, but it was necessary to select a proper sample of the most fluent bursts. I considered the GRBs with enough photon statistics so I excluded the cases whose fluence was smaller than 10^{-5} erg/cm^2 as presented in the GBM spectral catalog. The impact of this cut is shown in Figure 3.1. The left (right) panel presents the distribution of the error on the low-energy index (peak energy) of COMP, SBPL, and Band. The color filled histograms represent the distributions before the cut, while the simple step histograms represent the distribution of the parameters after the cut. The figure shows that the distribution of COMP is the most affected by the selection. The bursts excluded are 1264, which represent 71% of the sample of the previous step. This is not bad since I selected the bursts which presented enough statistics at high energies to constrain the high-energy index. This is particularly relevant to compare ISSM with Band and SBPL. As a result I selected 514 bursts.

3.1.3 Step 3: select the detectors with well-measured responses

In order to maximize the statistics available for the spectral fits I selected the detectors which have the best burst viewing angle. In particular I chose the NaIs that have a viewing angle smaller than 60°. Moreover I excluded the detectors which have not an accurate response file. The angle under which a detector saw the burst θ_{burst} may differ from the angle θ_{rsp} at which the corresponding response file was produced. This happened for the bursts which were better localized by other observatories such as Swift, XMM-Newton, or Chandra. In those cases the response should have been produced at the angle corresponding to the more accurate localization. Since the effective area stored in the response file must be as close as possible to the real effective area at which the detector saw the burst, I excluded the detectors for which the relative variation in effective area between θ_{burst} and θ_{rsp} exceeds a threshold of 5% for the NaIs and 20% for the BGOs. I used a $\cos\theta$ dependency of the effective area to compute that difference. Additionally I removed the pathological cases, which are the bursts whose trigger time fell in a data gap of the spacecraft files. In

Step	Description	Excluded bursts	Selected bursts
-	GBM Burst Catalog at 10 years	-	2361
1	Spectral models: COMP, SBPL, or Band	583	1778
2	Fluence $> 10^{-5}$ erg/cm^2	1264	514
3	Burst viewing angle $< 60°$ and good response	29	485
4	At least 1 NaI and 1 BGO with a good background fit	11	474
5	At least 1 NaI with $SNR > 20$	14	460

Table 3.1: GBM spectral catalog selection steps.

fact those files are needed to know both the exact orientation of the satellite and the exact angle under which the detectors saw the burst. I also excluded the GRBs whose spacecraft files does not exist (first four bursts at the beginning of the mission), and the bursts which have no temporal coverage in the spacecraft file. The selection length after this step resulted into 485 bursts, with a difference of 29 bursts with respect to the previous selection step 2.

3.1.4 Step 4: at least 1 NaI and 1 BGO with a good background fit

I performed the background fit for each detector per each burst, as described in § 2.4.2. I excluded the detectors with a bad background fit. I define a background fit as good if the following two conditions are satistifed at the same time:

1. $\frac{|<q^2_{red}>-1|}{\sigma_{<q^2_{red}>}} < 3$;
2. $\frac{V_{<q^2_{red}>}}{V_{<\chi^2_{red}>}} < 1.5$.

where $<>$ stands for the arithmetic mean over all energy channels, $\sigma_{<>}$ for the error on the arithmetic mean, and $V_{<>}$ is the variance on the mean. The first condition ensures that the mean value of q^2_{red} approaches the unity as it should be for a good background fit in all channels. In the second condition I compare the variance on the mean of the q^2_{red} and the theoretical variance expected for the arithmentic mean of a reduced χ^2 with the same number of degrees of freedom. This condition ensures that the distribution of q^2_{red} is not too much scattered, and it means that the background fit is accurate over the totality of the energy channels. The upper panel of Figure 3.2 shows an example of good background fit. The other panels show examples of bad background fit, where one or both the quality conditions are not satisfied. The selection length after this step is 474 bursts. The 11 excluded bursts don't have at least 1 NaI and 1 BGO with a good background fit.

3.1.5 Step 5: at least 1 NaI with a good *SNR*

I computed the signal to noise ratio (SNR) for any NaIs in the energy range 10 keV - 1 MeV as $SNR = \frac{D-B}{\sqrt{B}}$, where D is the total number of photons and B is the number of the estimated background photons. In order to determine a reasonable threshold to select the NaIs with enough signal and not to exclude too many detectors I built the distribution of SNR for all the NaIs as shown in Figure 3.3. For the sake of the plot quality I excluded 19 detectors which had a negative SNR and that would have been excluded anyway. The median SNR is 47. The value of $SNR = 20$ seems a reasonable threshold to exclude the detectors with a low SNR while maintaining a reasonable number of detectors (1415 over a total of 1664 - 85%). For each burst I kept at maximum 3 NaIs and 1 BGO with the highest SNR. The selection length after this step is 460 bursts with a difference of 14 bursts with respect to the previous selection.

The number of selected and excluded bursts at each selection step is summarised in Table 3.1. The burst fluence histogram per each step of the selection is presented in Figure 3.4.

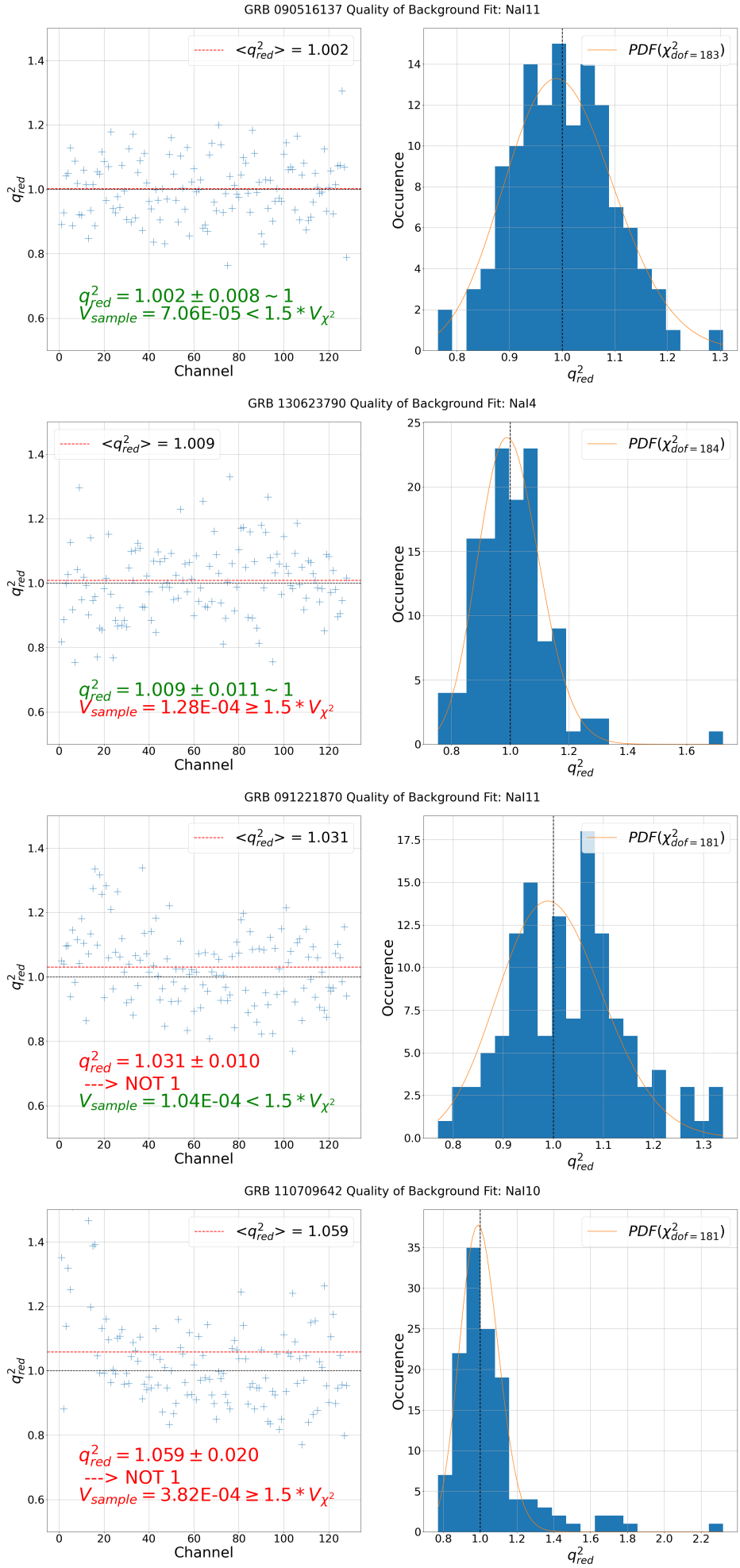

Figure 3.2: Examples showing the four possible combinations of the conditions on the quality of the background fit.

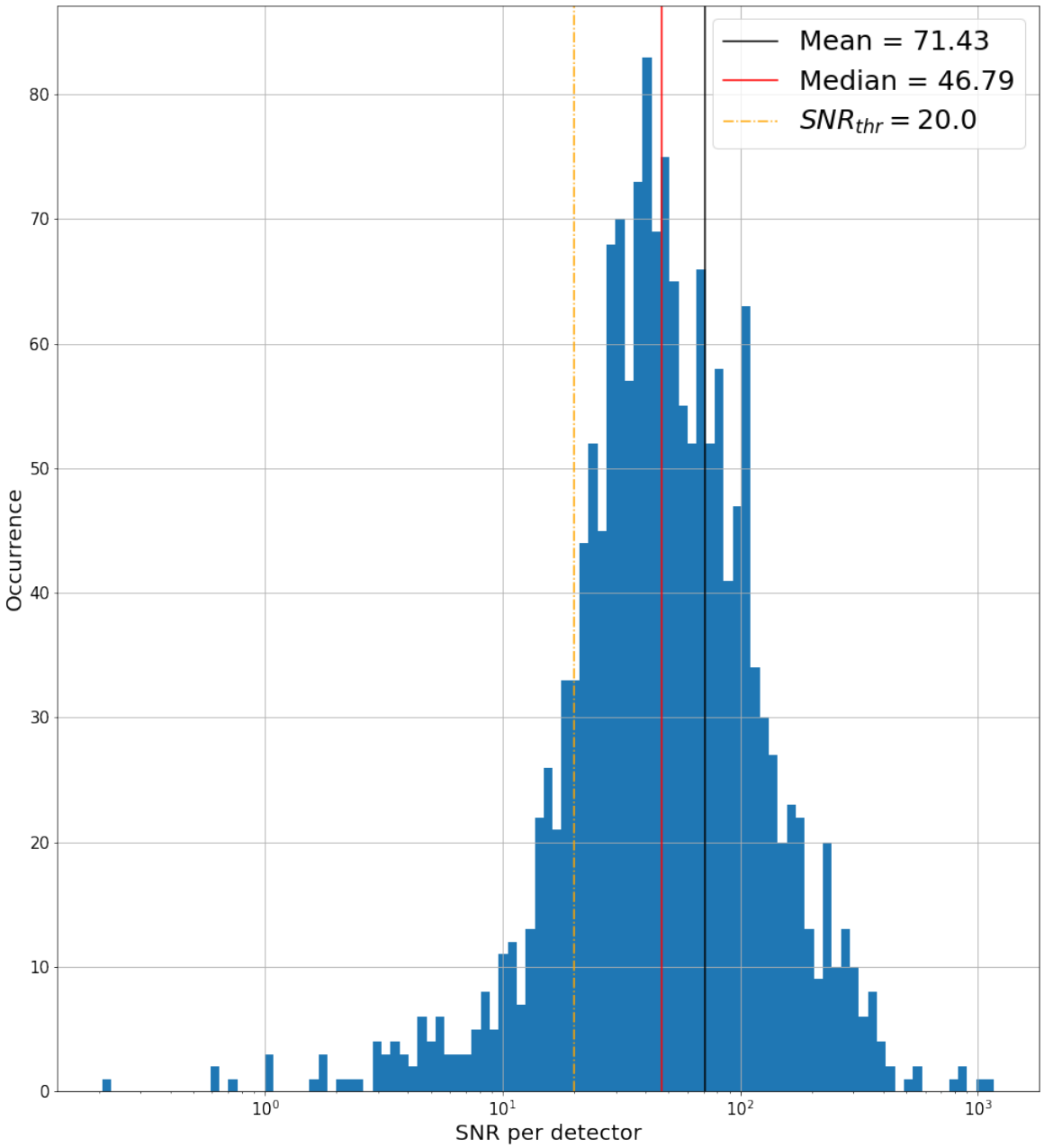

Figure 3.3: Distribution of *SNR* for all NaI detectors of each burst selected after step 4. The total number of detectors is 1664 and the number of detectors with $SNR < 20$ is 249 (15%). I excluded those detectors representing the lower tail of the histogram to ensure that there was enough signal for the burst spectral analysis.

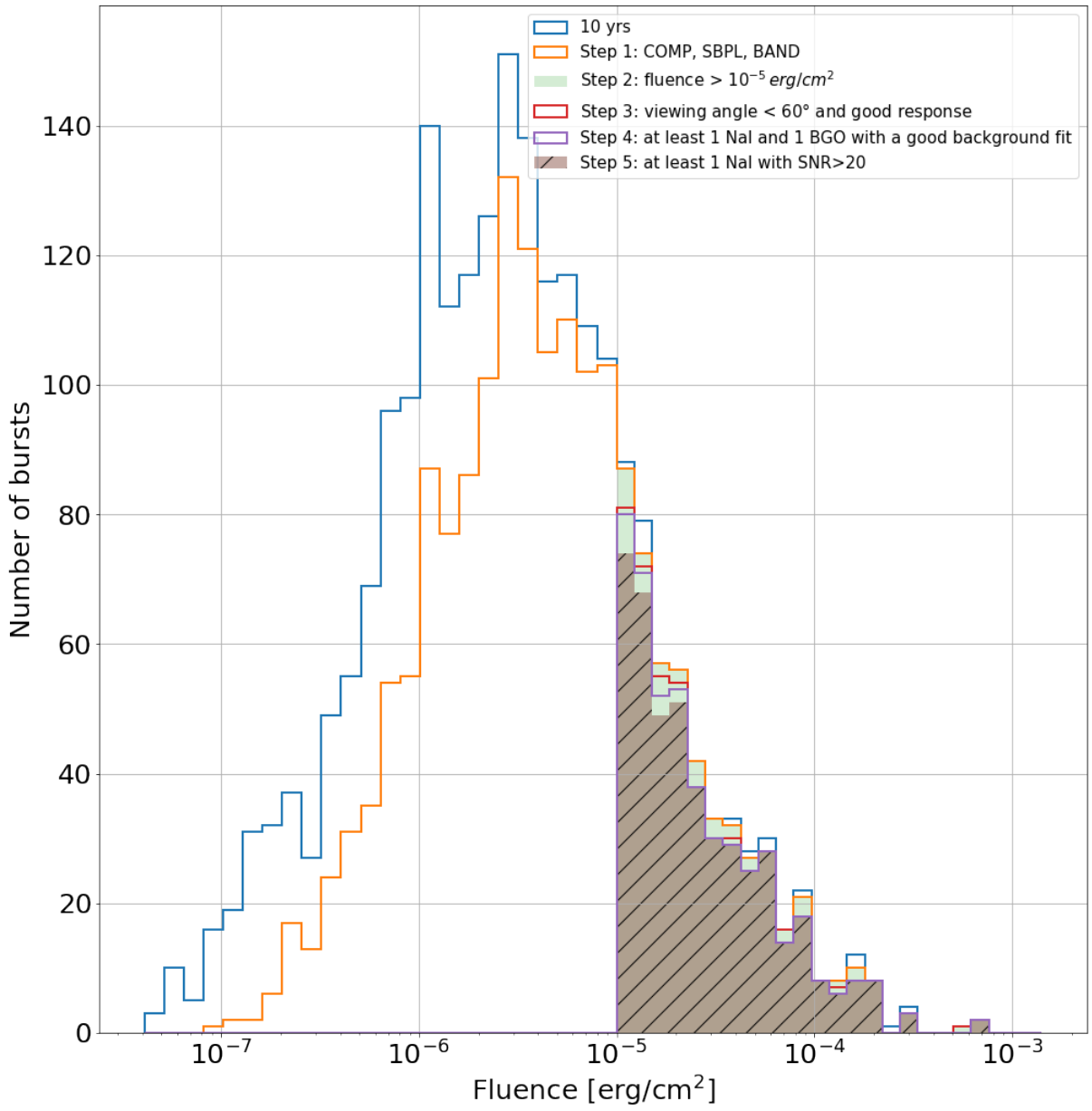

Figure 3.4: Histogram of the bursts energy fluence per each selection step. The green colored area corresponds to the selection step cutting on the energy fluence: it induces the most significant reduction of the sample. The brown area filled with lines corresponds to the last selection step, which excludes the burst which don't have at least one NaI with $SNR > 20$.

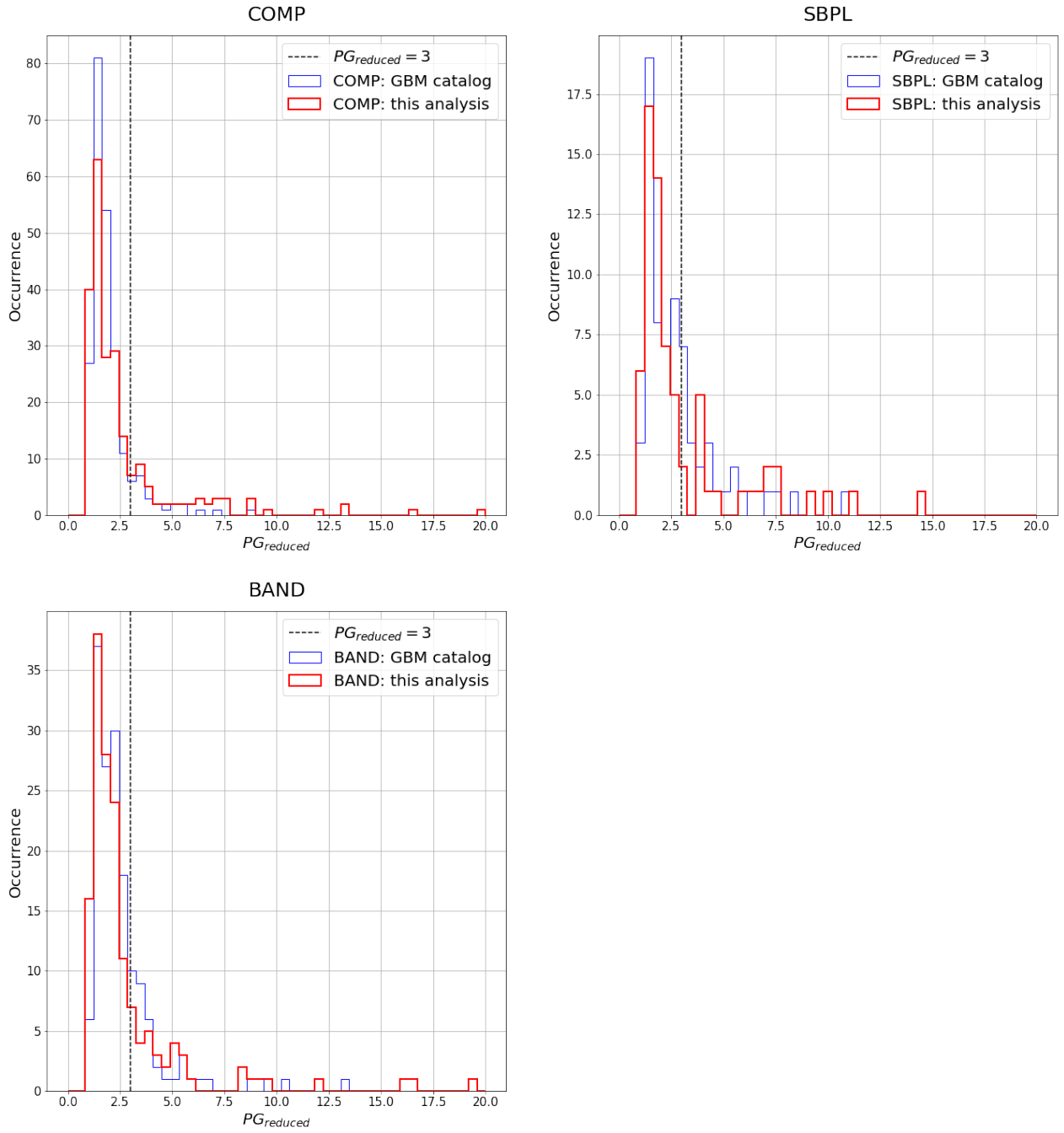

Figure 3.5: Reduced fit statistic obtained by fitting each burst of my selection with the corresponding GBM spectral catalog best-fit model. The distribution of my results follows closely the distribution of the GBM spectral catalog. All the distributions peak before the 3 meaning that overall the quality of the fits is acceptable.

3.2 Time-integrated spectral analysis

3.2.1 Validation against the GBM spectral catalog

I performed a time-integrated analysis for each of the 460 selected bursts. Before proceeding to fitting each model described in § 1 I chose to fit the GBM best-fit model as presented in the GBM spectral catalog and to compare with the catalog in order to confirm my results and to ensure that there were no issues in the selection steps and in the data preparation. In order to quantify the quality of the fit I normalized the *PG-stat* for the number of degrees of freedom. The mean value of the reduced *PG-stat* expected for an excellent fit is 1 in theory, but the systematics of the response and the background estimation affect the

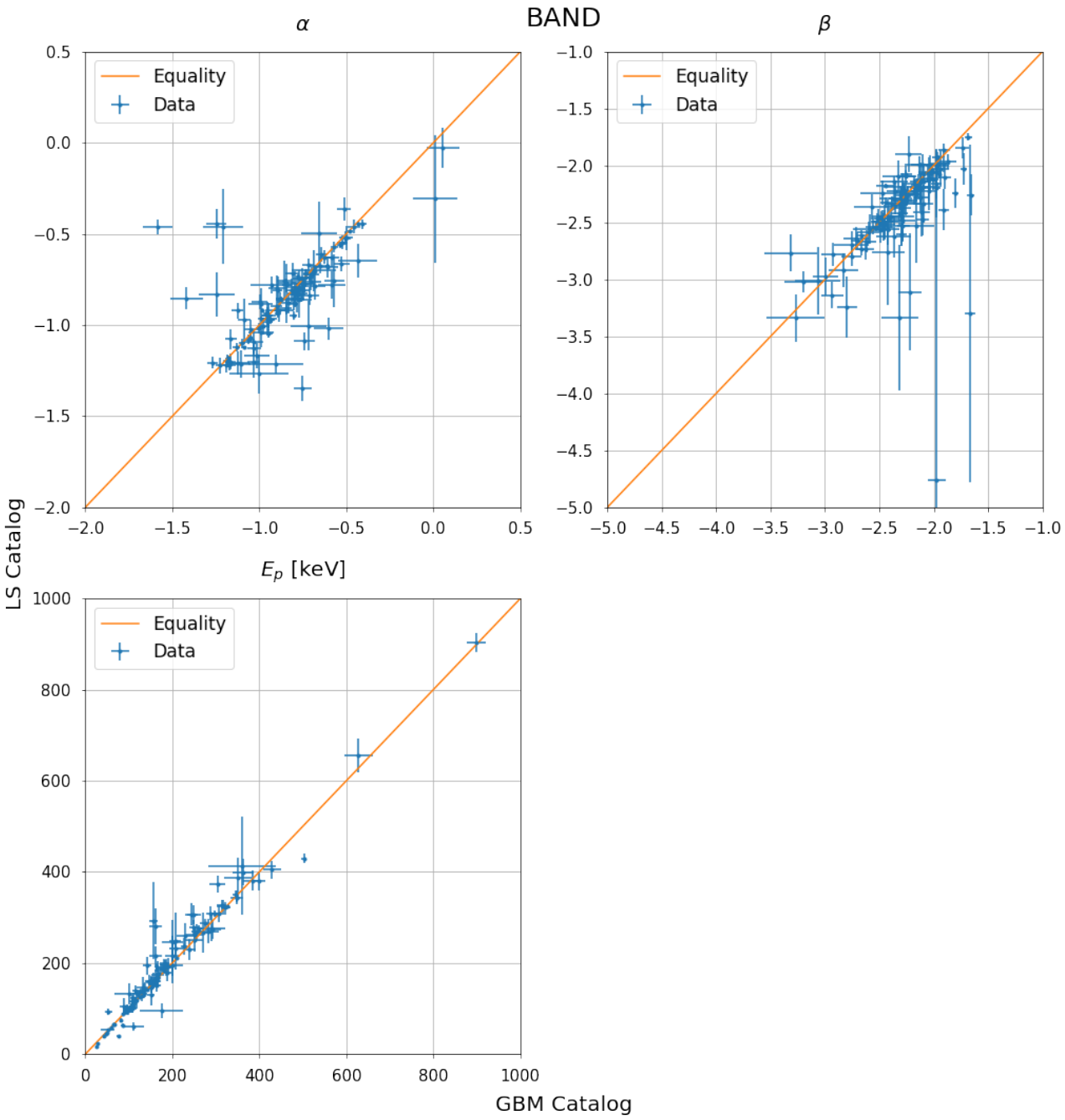

Figure 3.6: Comparison of the spectral parameters obtained in this analysis ("LS catalog") with the results of the GBM spectral catalog.

resulting value so that it is typically greater than 1. Therefore I consider that a fit is acceptable when the reduced *PG-stat* is smaller than 3. Figure 3.5 presents the distribution of the fit statistics (*PG-stat* for my analysis and *Castor C-stat* [see Appendix A]) for the GBM spectral catalog) normalized for the number of the fit degrees of freedom. The distributions of my analysis are consistent with the distributions of the GBM spectral catalog. In the GBM spectral catalog the percentage of bursts with a reduced fit statistic smaller than 3 is 90% for COMP, 64% for SBPL, and 76% for Band. In my analysis the reduced *PG-stat* is below 3 in 78% of the cases for COMP, 67% for SBPL, and 74% for Band, consistently with the results of the GBM spectral catalog. My analysis yields an overall acceptable quality of the spectral fits meaning that my selection process and data preparation were accurate enough. Additionally I compared the spectral parameters obtained in my good fits (reduced *PG-stat* < 3) with the results of the GBM spectral catalog. Figure 3.6 shows the distribution of the Band parameters as found by my analysis as a function of the

Selection	COMP	SBPL	Band	ISSM
All bursts (181)	0%	12%	22%	66%
$SNR < 108$ (61)	0%	23%	34%	43%
$108 < SNR < 196$ (60)	0%	7%	18%	75%
$196 < SNR < 1752$ (60)	0%	7%	13%	80%

Table 3.2: Probability of COMP, SBPL, Band, and ISSM to be the reference model ($\Delta PGstat = 0$) for the whole sample of GRBs with $TS_\beta > 9$, and for each of the three *SNR* classes (time-integrated spectral analysis). The probability values are rounded to unity and their errors are typically of the order of unity.

corresponding values of the GBM spectral catalog. The distributions for α, β, and E_p follow closely the equality line within errors. This means that the best-fit parameter found by this analysis are consistent with the values of the GBM spectral catalog. In Appendix B I present the histograms of the parameters values and their errors compared with the GBM spectral catalog. The same conclusions can be drawn for COMP and SBPL. Their scatter plots and histograms can be found in the same appendix. As a result I proved that my selection, data preparation, and spectral fit processes were reliable. Therefore I proceeded with the comparison of Band and ISSM.

3.2.2 Performance of the Band and ISSM models

In order to test the fitting performance of ISSM I compared its results with those obtained employing the Band function. Apart from being widely used in literature Band shares the same number of spectral parameters of ISSM, and both functions are parameterized as a spectral index at low and high energies, the energy value at the peak of their spectral energy distribution, and their normalization. In the comparison between the two models I define three specific samples each one focusing on specific parameters. In this section as well as in section § 3.2.3 I consider the bursts whose spectrum is better fitted by Band and ISSM with respect to COMP in order to compare the high-energy spectral indices and the peak energies of Band and ISSM. In § 3.2.4 I focus on the bursts for which the low-energy indices of both models are adequately constrained for a proper comparison. In § 3.2.5 I consider the well characterized bursts for which the two mentioned conditions are both satisfied.

I selected the sample of bursts whose spectrum is significantly better fitted by Band and ISSM with respect to COMP by demanding that the high-energy spectral index β is required with a significance greater than 3σ. Since COMP is a special case of Band and ISSM for β approaching $-\infty$, imposing that β is required by the data at more than 3σ means that the difference in *PG-stat* between COMP vs Band and COMP vs ISSM is greater than 9 units: $TS_\beta > 9$. The number of bursts that satisfy this condition is 181 (39%) out of 460 selected bursts. In order to compare the ISSM and Band functions for different levels of *SNR* I divided the sample in three classes of *SNR* (small, medium and high) with same size ($\sim$ 60 bursts each). The higher the *SNR* the better the spectroscopic precision, so the ability to distinguish the models with the highest likelihood increases. As a matter of comparison each class contained almost the same number of bursts considered by Yassine et al. 2020 (hereafter Y20), who introduced ISSM and characterized it for the time-integrated spectra of 74 fluent GBM bursts. **As in Y20 I defined the reference model of each burst as the model which yields the smallest *PG-stat* for that burst**. The probability for each model to be the reference model is shown in Table 3.2. **ISSM has the greatest probability of being the reference model over the whole sample and the three *SNR* classes**. I define $\Delta PGstat$ as the difference between the *PG-stat* provided by a model and the *PG-stat* of the reference model for the same burst. Specifically $\Delta\, PGstat(m_i) = PGstat(m_i) - min(PGstat(m_j))$ for m_j = COMP, SBPL, Band, ISSM. **In order to quantify the performance of each model to approach the reference model, thus being a good model, I computed its probability to yield a $\Delta PGstat$ smaller than the reference values of 5 and 10**. The threshold to determine whether Band or ISSM better fits the data cannot be found with a likelihood ratio test since the two models are not nested. Y20 performed Monte-Carlo simulations to find the difference in fit statistic which conservatively allows to claim when ISSM fits better than Band.

Selection	$\Delta PGstat < 5$	$\Delta PGstat < 10$
All bursts (181)		
COMP	0%	0%
SBPL	36%	50%
Band	49%	60%
ISSM	83%	89%
***SNR* < 108 (61)**		
COMP	0%	0%
SBPL	67%	82%
Band	79%	89%
ISSM	79%	85%
108 < *SNR* < 196 (60)		
COMP	0%	0%
SBPL	28%	50%
Band	45%	63%
ISSM	87%	92%
196 < *SNR* < 1752 (60)		
COMP	0%	0%
SBPL	12%	18%
Band	23%	27%
ISSM	85%	90%

Table 3.3: Probability of COMP, SBPL, Band, and ISSM to be a good model, i.e. to yield a $\Delta PGstat$ smaller than 5 and 10 with respect to the reference model (time-integrated spectral analysis). The bursts considered here have $TS_\beta > 9$ and are divided into classes of low, medium, and high *SNR*. The probability is approximated to the unity and its error is order of some units.

Y20 found that the 5σ (Gaussian) threshold was $\Delta PGstat = 20$ for bursts with low *SNR* and 3 for bursts with medium *SNR*. **Therefore I chose the intermediate values of 5 and 10 as references to discern between the fitting performance of Band and ISSM**. The results are shown in Table 3.3. **Overall ISSM is the model which presents the highest probability and especially when the burst *SNR* is high**. In other words ISSM provides good fits most often than the other models and in particular when the burst signal is high. The probability values found are fully consistent with the previous work of Y20. In order to see how each spectral model performs I show in Figure 3.7 the distribution of its $\Delta PGstat$ as a function of the bursts index sorted per increasing *SNR*. It appears that the distribution is more scattered as the burst *SNR* increases and that ISSM systematically approaches the null horizontal line especially at high *SNR*. The results are confirmed when computing the cumulative distribution of $\Delta PGstat$ per each model as shown in Figure 3.8. The left panel of the figure includes all bursts of the sample while the right panel focuses on the highest *SNR* class. In both cases the cumulative distribution of ISSM is higher than the one of the other models: ISSM provides a fit of better quality most often. A complementary way to show how well ISSM performs is considering the totality of the bursts with a strict cut $\Delta PGstat < 5$. The resulting cumulative distribution of *SNR* is shown in the left panel of Figure 3.9, where the black histogram denotes the cumulative distribution over the whole sample, that is without the cut on $\Delta PGstat$. ISSM provides the highest cumulative fraction, especially at high SNR where models can be more easily distinguished. While the fraction of good fits with ISSM is similar for the whole sample (83%) and the bursts with high SNR (85%), the fraction of good fits with Band is much smaller and limited to 49% and 23% in both cases. The right panel of Figure 3.9 shows the fraction of cases in which a model is a good one (same cut on $\Delta PGstat$) as a function of *SNR*. I binned the *SNR* in classes with the same size of 20% (36 bursts) of the total number of bursts. The error on each fraction is approximated as $\sqrt{n_g}/n_b$, where n_g is the number of good fits among

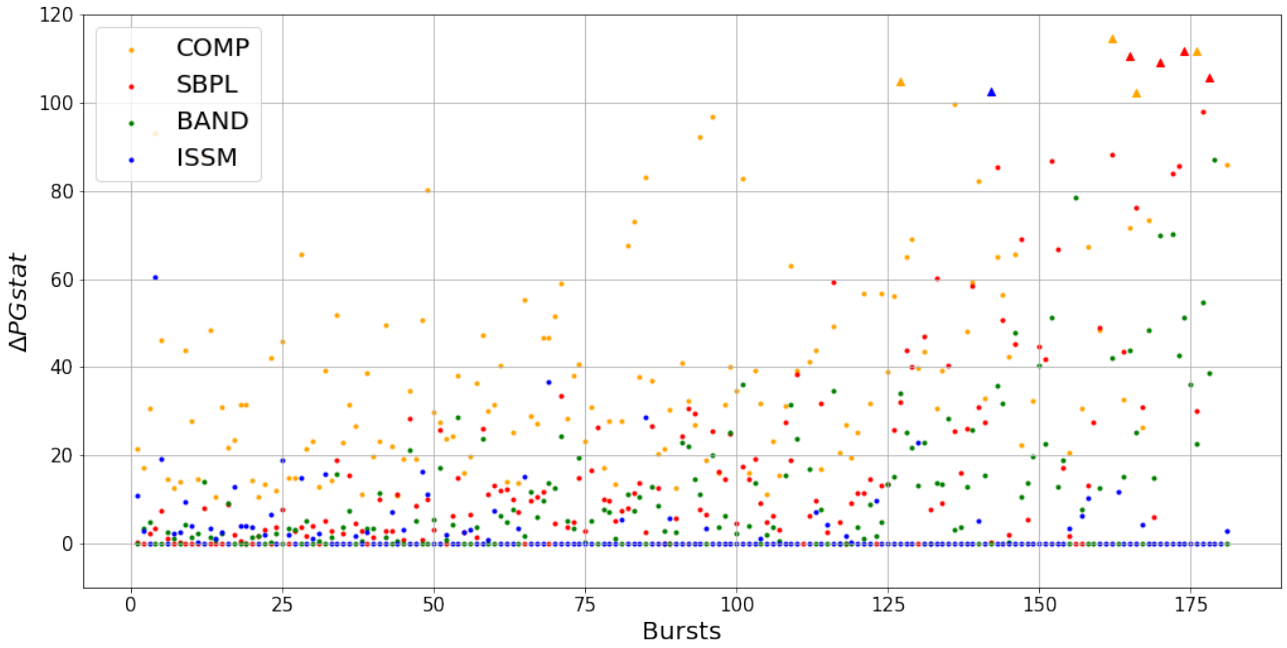

Figure 3.7: Distribution of $\Delta PGstat$ of each model with respect to the reference model for each burst with a $TS_\beta > 9$ (time-integrated spectral analysis). The bursts indices are ordered per increasing burst *SNR*.

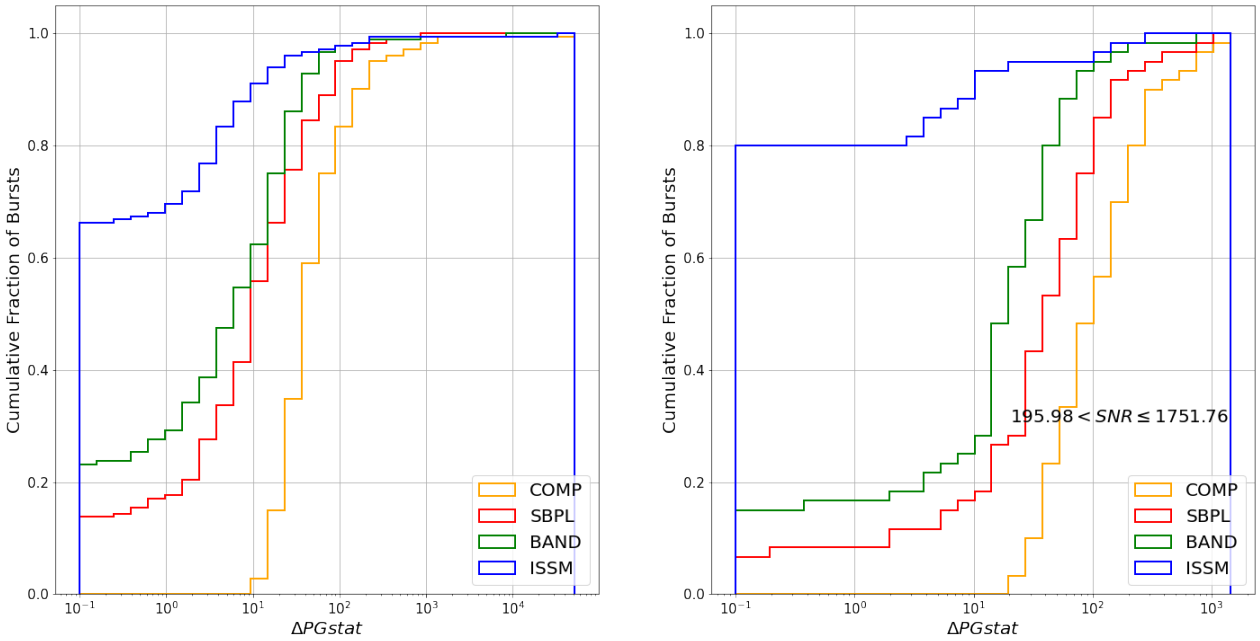

Figure 3.8: Left: cumulative distribution of $\Delta PGstat$ per each model for the whole sample of burst with $TS_\beta > 9$ (time-integrated spectral analysis). Right: cumulative distribution for the high *SNR* class.

the n_b bursts of a given *SNR* interval. When the signal is most significant the fraction of cases in which ISSM approaches the reference model within 5 units of *PG-stat* is greater than Band and SBPL. **In the highest *SNR* bin the fraction of times ISSM is a good model is larger than 80%, while it has dropped below 20% for Band and SBPL**.

3.2.3 High-energy spectral parameters

I focus on a direct comparison of ISSM and Band by considering their peak energy and high-energy index. Concerning the peak energy of the two models Y20 found that ISSM typically peaks at higher energies than

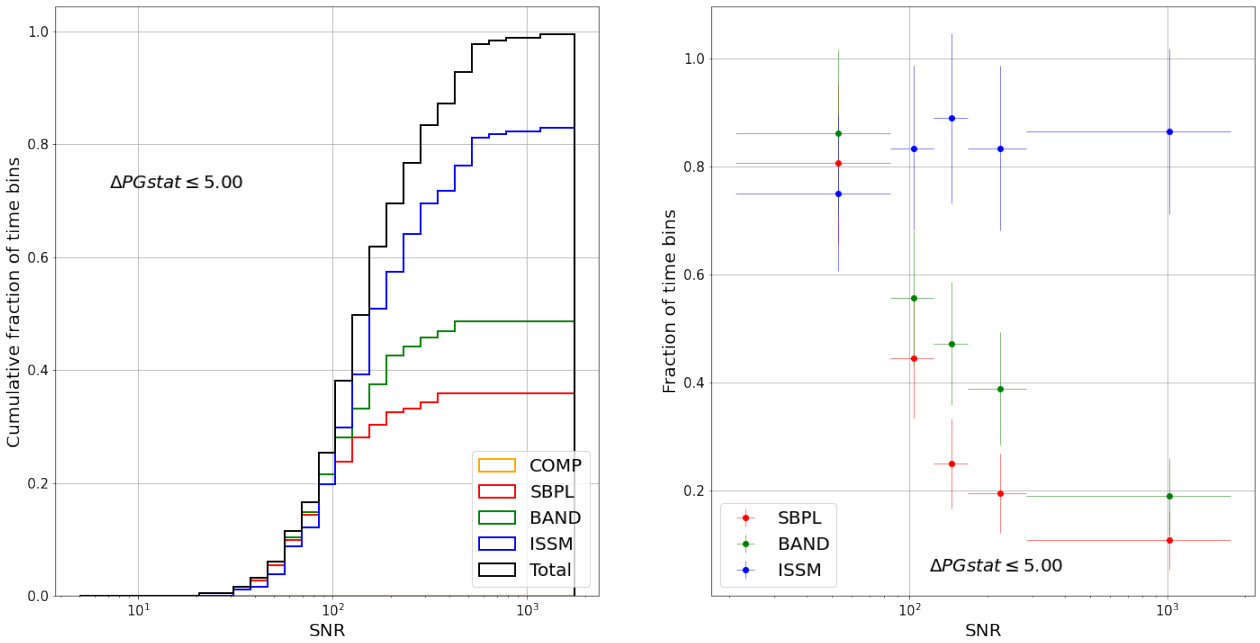

Figure 3.9: Left: cumulative distribution of SNR per each model when the corresponding $\Delta PGstat$ with respect to the reference model is smaller than 5 (time-integrated spectral analysis). The black line denote the cumulative distribution of SNR over the complete sample with $TS_\beta > 9$. Right: fraction of bursts with the same cut on $\Delta PGstat$ as function of SNR.

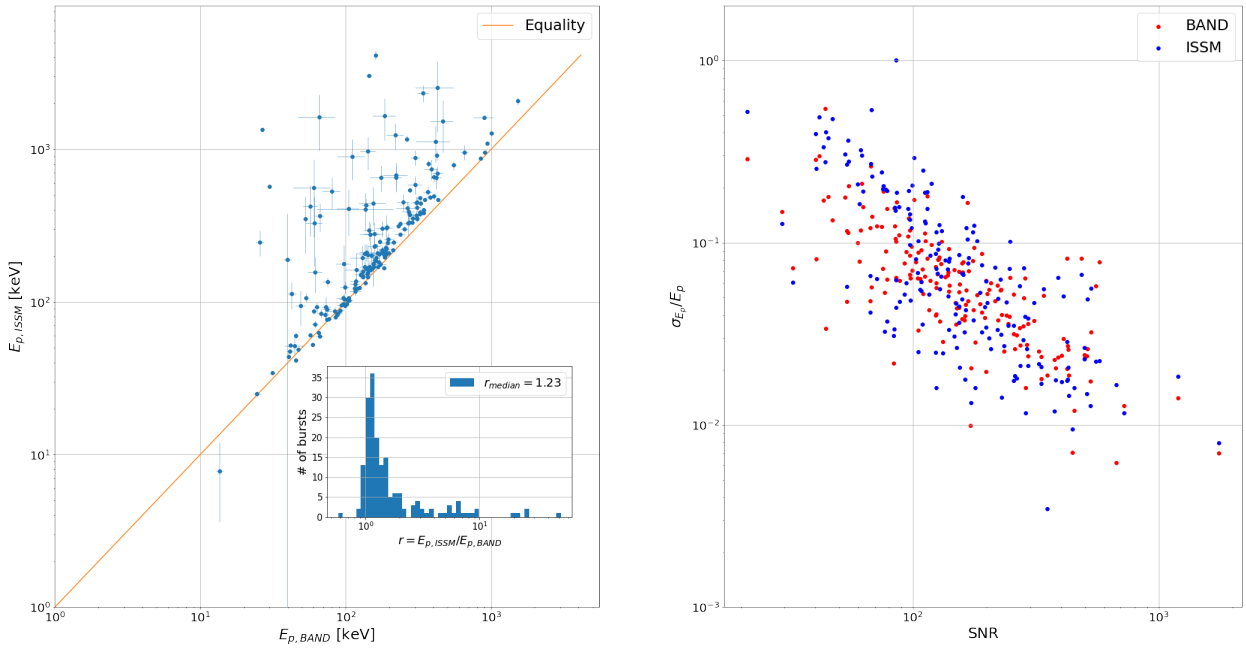

Figure 3.10: Left: $E_{p,ISSM}$ as a function of $E_{p,Band}$ for the sample of bursts with $TS_\beta > 9$ (time-integrated spectral analysis). The median value of the ratio between $E_{p,ISSM}/E_{p,Band}$ is 1.23. Right: relative error on E_p for Band and ISSM as a function of the burst SNR.

Band. This is confirmed in my analysis, as displayed in the left panel of Figure 3.10. This figure includes one case where the relative error on $E_{p,ISSM}$ is of the order of the unity: it is GRB 111010709, whose ISSM spectral parameters are unconstrained and the fit quality is very poor. The ratio between the peak energy of ISSM over Band has a median of 1.23, which is very close to 1.21 found by Y20 and it has a tail extending to values as high as ~ 10. This may have implications on the so-called Amati and Yonetoku relations (Amati et al. 2002, Yonetoku et al. 2004, Heussaff et al. 2013, Fana Dirirsa et al. 2019) that should be investigated

using the 21 GRBs with redshift in the current sample. The relative error on the peak energy decreases from $\sim 40\%$ to a few percents as the burst *SNR* increases as shown in the right panel of Figure 3.10. This is expected since the more intense the signal of the burst the more accurate the constraint on the peak energy. A more detailed view on the peak energy and its relative error distributions is shown in Figure 3.11. The left panel shows that the peak energy of ISSM extends to higher values than Band and the right panel shows that also the relative error has a longer tail at higher values. As shown in § 1.3.4, the shape of ISSM spectra is continuously curved and it is wider than Band around the peak energy. This greater flexibility of the ISSM function allows the spectral fitting engine to explore a bigger parameter space. Additionally the correlation with the low and high-energy spectral indices pushes for greater errors on $E_{p,ISSM}$.

The high-energy index β_{ISSM} is an asymptotic value, which is typically not reached within the GBM observable energy range. Following Y20 I computed the spectral index $\beta_{b,ISSM}$ at the energy equal to the break energy of Band, namely $\beta_{b,ISSM} = \Gamma_{ISSM}(E_b)$ using Equation 1.4, which is always within the observable energy range so that $\beta_{b,ISSM}$ can be adequately constrained. The hierarchy of the spectral indices is $\beta_{b,ISSM} > \beta_{Band} > \beta_{ISSM}$ as shown in the left panel of Figure 3.12 and in the left panel of Figure 3.13. One indeed expects that β_{ISSM} is softer than the other two indices as it is an asymptotic limit. Y20 found that ISSM is wider than Band around its peak energy, so one expects that $\beta_{b,ISSM}$ is harder than β_{Band}. The results shown are in agreement with Y20. The distribution of β_{ISSM} presents 6 cases with a value smaller than -5.

- GRB 131028076: $\beta_{ISSM} = -6.04 \pm 0.82$. This burst peaks at high energies: $E_{p,ISSM} = 951 \pm 20$ keV. The fact that the parameter is constrained finds a natural explanation noting that this burst has a high SNR = 293 and in particular at high energies where for BGO0 the SNR=86. Given the significant signal the fitting engine manages to constrain beta.

- GRB 150201574 (and similarly for GRB 161106499): $\beta_{ISSM} = -5.8 \pm 0.8$. This burst peaks at relatively low energies $E_{p,ISSM} = 146 \pm 1$ keV, but has a soft spectrum with the BGO $SNR = 10$. As the burst $SNR = 377$ the fitting engine managed to reasonably constrain β_{ISSM} with an error smaller than 1.

- GRB 130427324: $\beta_{ISSM} = -8.5 \pm 2.3$. This burst has an extremely high $SNR = 1752$ and a high peak energy: $E_{p,ISSM} = 870 \pm 7$ keV. Despite the high *SNR* the quality of the fit is very poor: *PG-stat* = 7582 for 474 degrees of freedom. This GRB is well known for its extremely high photon fluence which saturated the GBM detectors inducing pulse pile-up in the GBM data [Ackermann et al. 2014]. It should have been discarded in the first place.

- GRB 161218356: $\beta_{ISSM} = -9.3 \pm 2.7$. This burst has a particularly hard $\alpha_{ISSM} = -0.43 \pm 0.03$. Despite its high $SNR = 444$ at high energies the BGO has $SNR = 10$, which induces a big error on β_{ISSM}.

- GRB 110426629: $\beta_{ISSM} = -19.319 \pm 0.002$. The fit quality for this burst is very poor despite the remarkably small error on the high-energy index: *PG-stat* $= 1.9 \times 10^5$ for 474 degrees of freedom. The number of bursts with a reduced *PG-stat* greater than 10 is 9, which represents a tiny fraction (5%) of the whole sample. Therefore this spectral fit is pathological and an exceptional case.

The right panel of Figure 3.12 shows the distributions of the errors on the high-energy indices. As expected $\beta_{b,ISSM}$ tends to be better constrained than β_{Band} and β_{ISSM} apart from 4 exceptions (GRBs 111010709, 150105257, 150726877, and 170514180). In those cases either the spectrum peaks at low energy or the peak energy is badly constrained: as a result α_{ISSM} pushes towards the hardest limit allowed by the fit (+6) and it is totally unconstrained. The great errors propagate on $\beta_{b,ISSM}$, which becomes unconstrained too. I discard the mentioned outliers from the following discussion. As shown in the right panel of Figure 3.13, the error on the high-energy index decreases as the index increases, as expected from the increased photon statistics when the spectrum gets harder. This $\beta - \sigma_\beta$ anti-correlation is also consistent with Figure 3.12 and Figure 3.13 (left): the local photon index $\beta_{b,ISSM}$ is computed at the Band break energy which lies within the GBM observable energy range, thus it is harder and has a smaller error than the β_{ISSM} asymptotic index. Besides, it is constrained by the overall photon statistics in the GBM due to the continuous curvature of the ISSM function, unlike β_{Band} which is measured only from the high-energy counts. As a

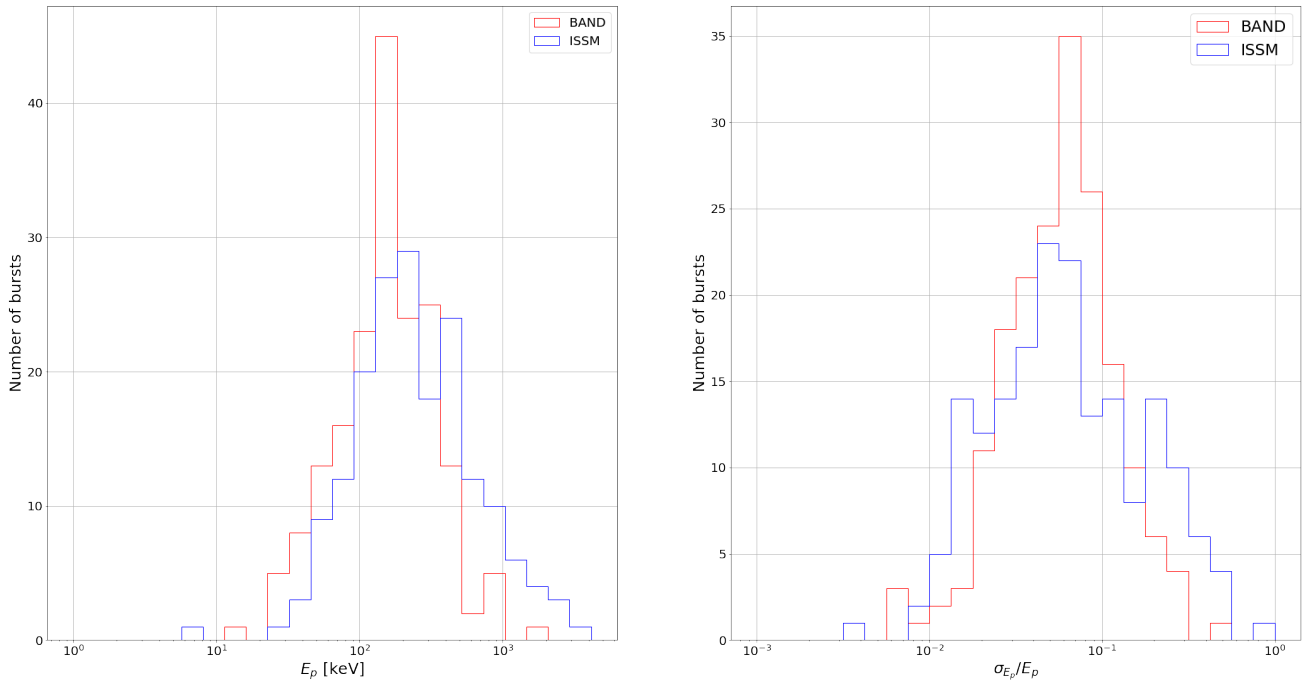

Figure 3.11: Left: distribution of E_p for ISSM and Band for the sample of bursts with $TS_\beta > 9$ (time-integrated spectral analysis). On average $E_{p,ISSM}$ is greater than $E_{p,Band}$. Right: distributions of their relative errors. As for the peak energy, the distribution of its relative error has a tail extending to higher values in the ISSM case.

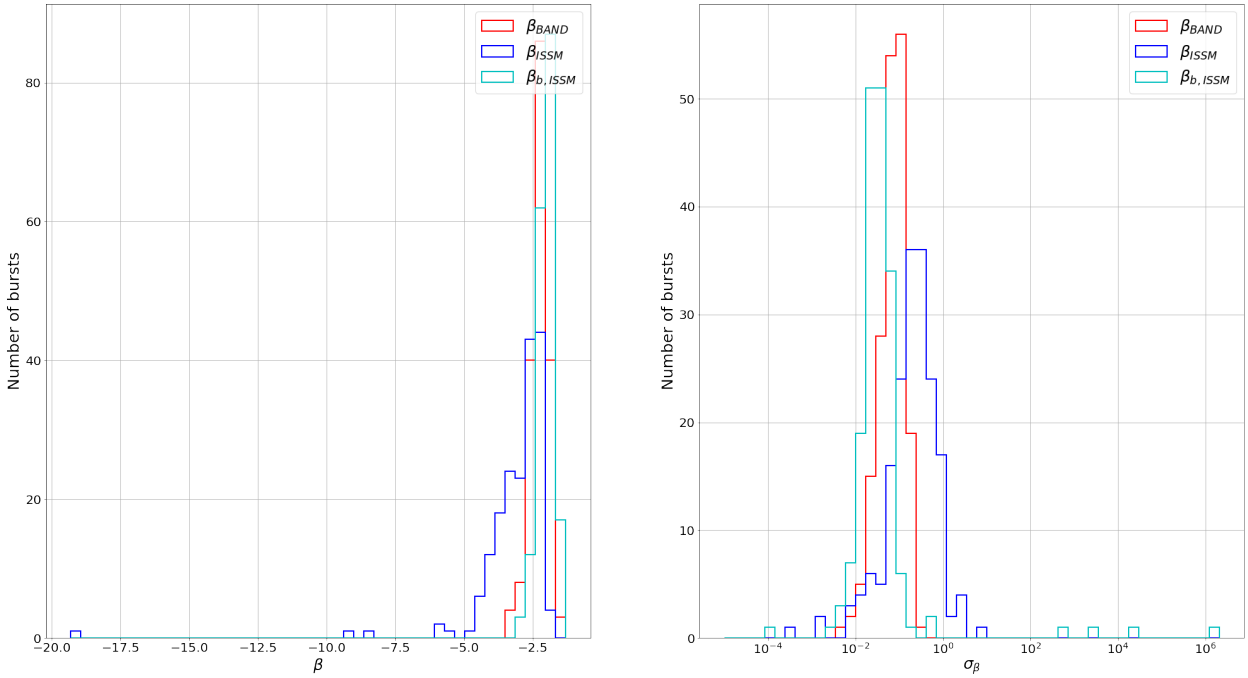

Figure 3.12: Distributions of $\beta_{b,ISSM}$, β_{Band}, β_{ISSM}, and of their errors for the sample of bursts with $TS_\beta > 9$ (time-integrated spectral analysis).

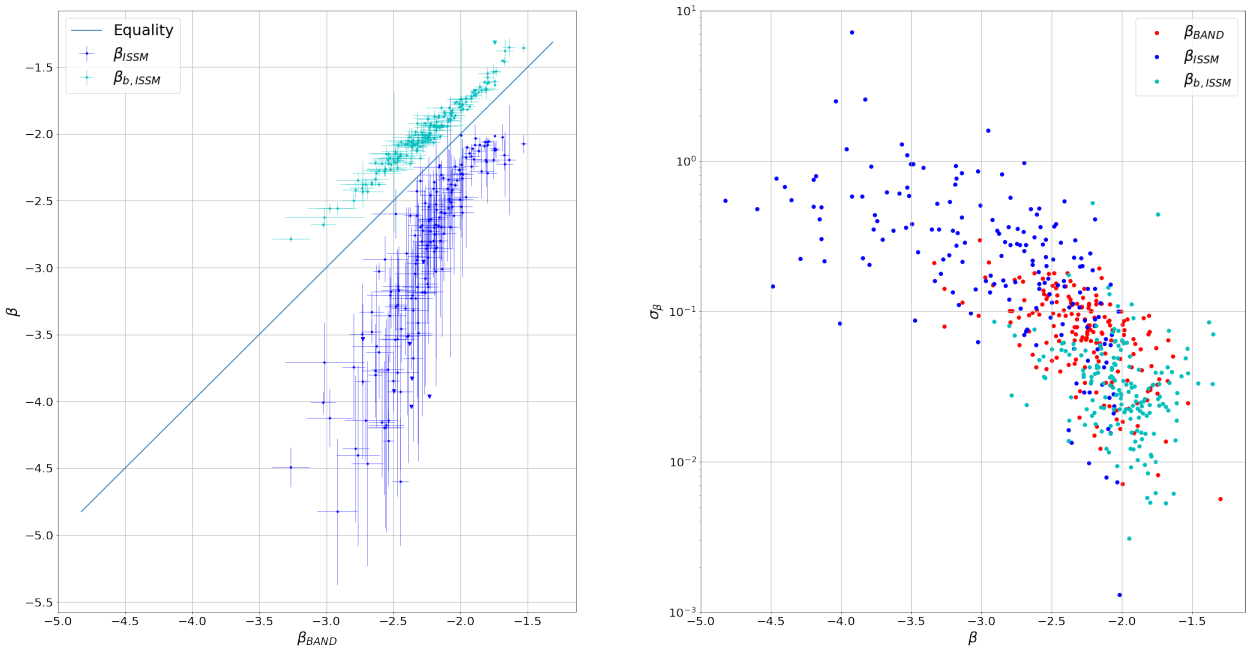

Figure 3.13: Left: comparison of β_{ISSM} and $\beta_{b,ISSM}$ with β_{Band} for the sample of bursts with $TS_\beta > 9$ (time-integrated spectral analysis). The figure shows that $\beta_{b,ISSM} > \beta_{Band} > \beta_{ISSM}$. The marker is a triangle when the error on β_{ISSM} or $\beta_{b,ISSM}$ is greater than 1. From this figure I excluded the cases with $\beta_{ISSM} < -5$ that are discussed in the text. Right: error on the high-energy index β as a function of β for the sample of bursts with $TS_\beta > 9$ (time-integrated spectral analysis).

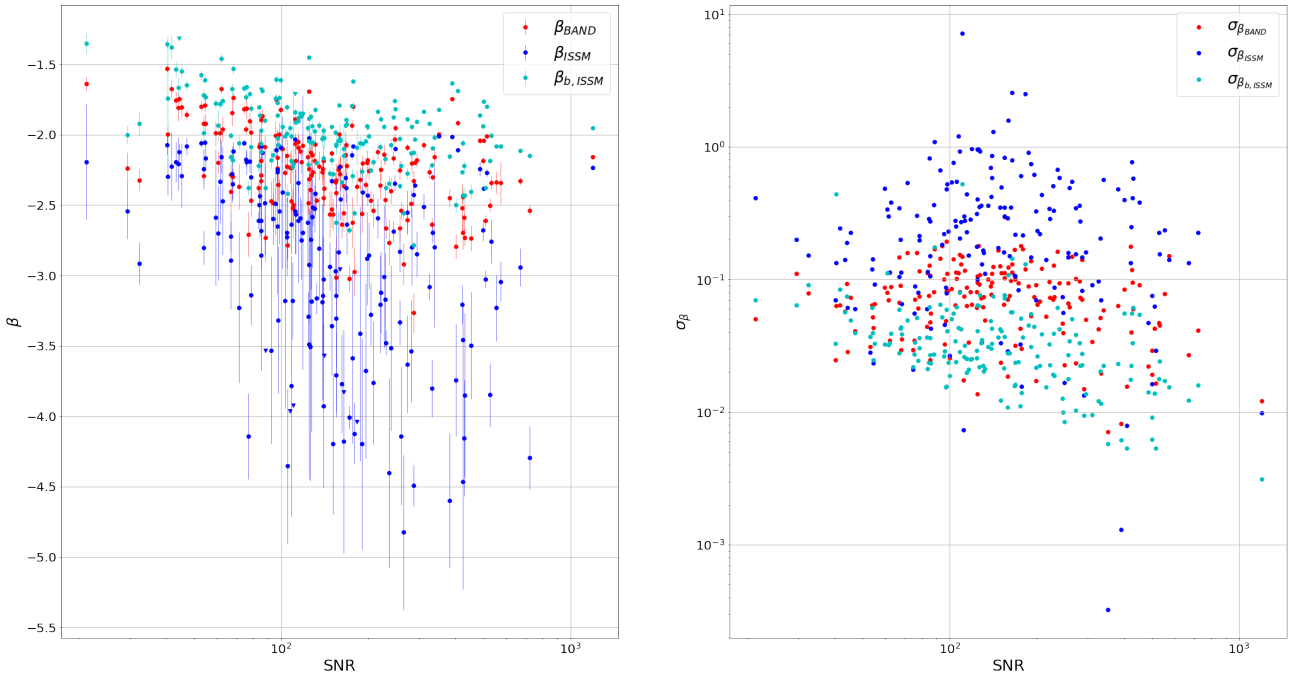

Figure 3.14: Left: high-energy index β as a function of *SNR* for the sample of bursts with $TS_\beta > 9$ (time-integrated spectral analysis). When the error on the high-energy index is greater than 1 its value is represented by a triangle. Right: high-energy index error as function of *SNR*.

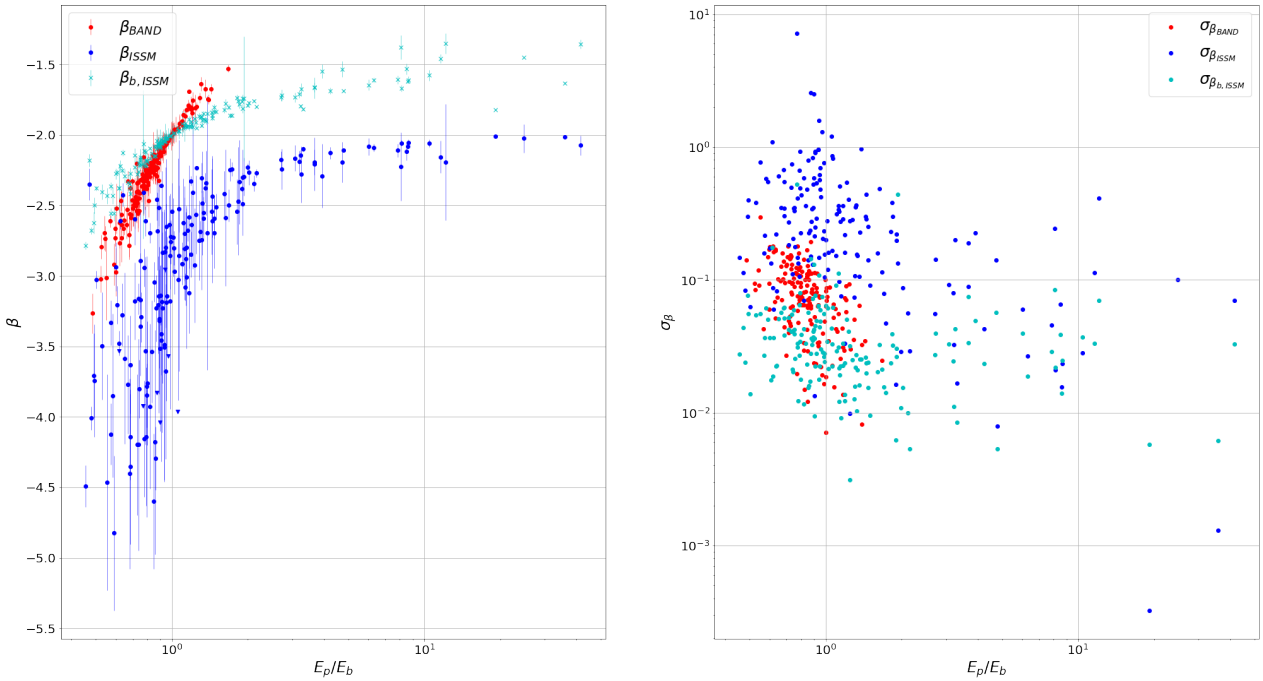

Figure 3.15: Left: high-energy index β as a function of E_p/E_b, where E_p is taken from the same model as β for the sample of bursts with $TS_\beta > 9$ (time-integrated spectral analysis). When the error on the high-energy index is greater than 1 then its value is represented by a triangle. Right: error on the high-energy index β as a function of E_p/E_b, as for the left plot.

result, $\beta_{b,ISSM}$ is harder and better measured than β_{Band} as well. Figure 3.14 shows the high-energy index (left panel) and its error (right panel) as functions of the burst *SNR*. The error on the high-energy index tends to decrease as the *SNR* increases, which is naturally expected. In addition, Figure 3.14 shows that the range of fitted values for the high-energy indices does not depend on the *SNR*, provided that the *SNR* exceeds ~ 100. Conversely, β_{Band} and $\beta_{b,ISSM}$ seem to decrease when the *SNR* increases from 20 to ~ 100. This behaviour is due to a combined effect of the sample selection and of a bias in the fit. Firstly, bursts with a steep high-energy index are missing in the bottom-left corner of the figure since they did not pass the $TS_\beta > 9$ cut, and they are best fitted by the COMP model due to the lack of counts in the highest-energy channels. Secondly, for the bursts in the top-left corner with β_{Band} values greater than -2, the SED true peak energy lies close to (or even beyond) the upper bound of the GBM energy range. The limited energy lever arm and the insufficient *SNR* lead the spectral fit to unrealistic values of E_p and of the high-energy index. Since $E_{p,Band} > E_b$ when $\beta_{Band} > -2$, E_p is indeed not the SED peak energy in these cases, and the SED keeps increasing with energy. An example is given Figure 4.12 in § 4.5. This is also illustrated in Figure 3.15, which compares the high-energy index (left panel) and its error (right panel) with the ratio of the ISSM or the Band peak energy E_p to the Band break energy E_b. This figure also shows that the ISSM SED often peaks at higher energy than the Band SED, especially when $E_{p,ISSM} > E_b$ (namely $\beta_{b,ISSM} > -2$).

The results reported so far are consistent with the results found by Y20, which are confirmed with greater precision using an extended GRB sample. β_{ISSM} is systematically softer than β_{Band} for the same burst, which is a known consequence of the continuous curvature of ISSM. The average values of the β indices and their sample standard deviations are presented in Table 3.6 for the selection cut $TS_\beta > 9$. **The value of $\beta_{\mathbf{b,ISSM}} = -1.99 \pm 0.26$ means that on average the ISSM SED peaks at the break energy of the Band SED**. These values have to be compared with the value expected from the synchrotron emission theory, where β is related to the slope p of the electron power law distribution by $\beta_{sync} = -(p/2 + 1)$ (see § 1.3). A typical value of $p = 2.7$ implies that $\beta_{sync} = -2.35$, which is consistent with the average value found for β_{Band}, yet at the limit of the range of β_{ISSM} values. However, large uncertainties exist on the microphysical parameters in mildly internal shocks such as internal shocks, and values of p up to ~ 3 are possible (see section 4.1 of Bošnjak et al. 2014). Interestingly, the range of β_{ISSM} is twice wider than the

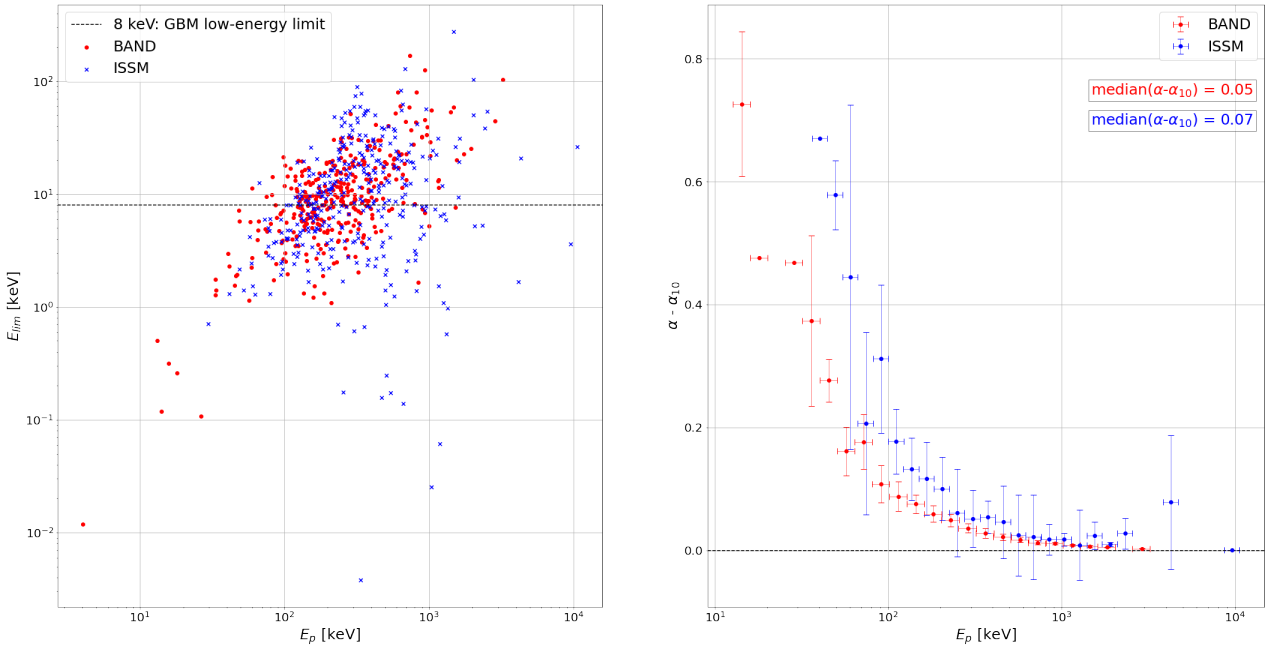

Figure 3.16: Left: energy E_{lim} as a function of the peak energy E_p. E_{lim} is the energy at which the local indices Γ_{Band} and Γ_{ISSM} reach their corresponding low-energy asymptotic values within errors for the sample of bursts with $\sigma_\alpha < 0.3$ (time-integrated spectral analysis). Right: Difference between α and α_{10} as a function of the peak energy of Band and ISSM for the same sample.

range of β_{Band} (standard deviations of 0.67 vs. 0.30). This is likely to result from the higher flexibility of the ISSM in the spectral fits. It might also suggest that the use of a physical model such as ISSM allows accessing the diversity of microphysical configurations in GRB jets. In the future, fitting the (micro)physical parameters of the numerical model directly to the data should shed light on these conclusions.

3.2.4 Low-energy spectral parameters

I built a second sample containing the bursts whose low-energy spectral index is well constrained. I required that both the errors on α_{Band} and α_{ISSM} were below 0.3, a threshold reasonably low to constrain the parameters and reasonably high to select a significant sample of bursts. The number of GRBs selected is 349 (75%) from the initial sample of 460 bursts. α_{ISSM} is an asymptotic value and, like β_{ISSM}, it is typically not reached within the GBM observable energy range. The left panel of Figure 3.16 shows the energy E_{lim} at which α is reached within errors as the peak energy varies. The increase of E_{lim} with E_p is expected (see also equations 18 and 19 in Y20). As a result only 58% of the time α_{Band} is reached above 8 keV with a similar percentage of 56% for ISSM. Following Y20 I computed the value of the spectral index at 10 keV α_{10} for a proper discussion. The right panel of the figure shows that the difference of α and α_{10} tends to zero when the peak energy of the spectrum increases, which is expected.

The impact of the selection cut on the distribution of the errors on the low-energy indices is shown in Figure 3.17. The distribution of the error on $\alpha_{10,ISSM}$ presents a tail extending to very low values. Those errors correspond to the bursts which are well fitted by COMP and have a moderate/high $E_{p,ISSM}$. In those cases ISSM fits the spectra just equally well as COMP and it adapts well at high energies yielding a little error on the low-energy index given its natural curvature. Figure 3.18 is explanatory: it shows the error on $\alpha_{10,ISSM}$ as a function of $E_{p,ISSM}$. The filled circles indicate bursts whose spectrum is fitted equivalently by COMP and ISSM ($TS_\beta < 9$). The tiny errors at moderate/high $E_{p,ISSM}$ belong to those cases.

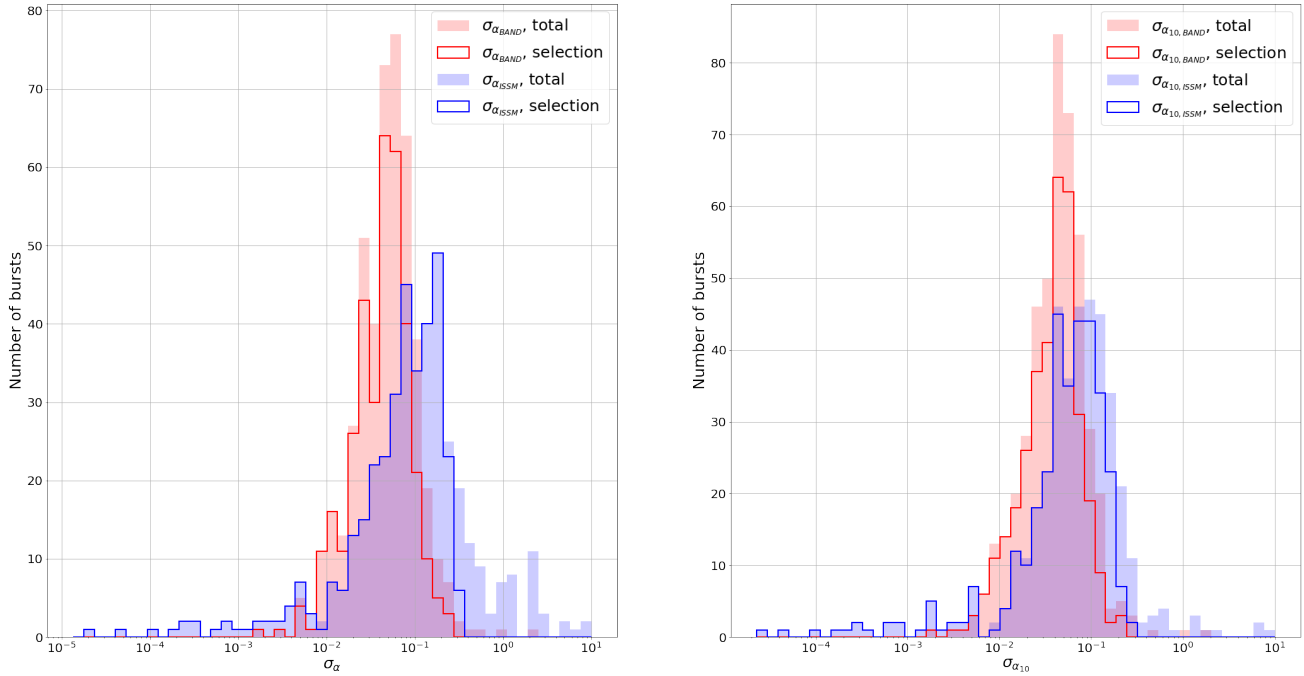

Figure 3.17: Distribution of the error on α (left) and α_{10} (right) for Band and ISSM before and after the selection cut $\sigma_\alpha < 0.3$ (time-integrated spectral analysis).

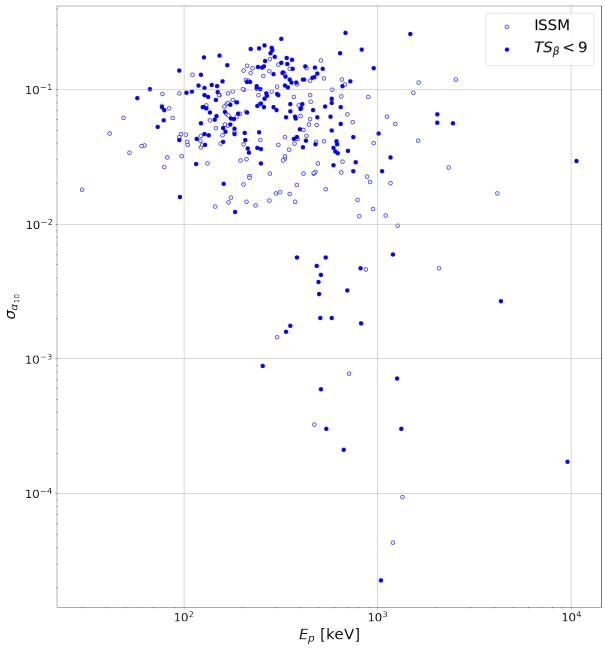

Figure 3.18: Error on $\alpha_{10,ISSM}$ as a function of $E_{p,ISSM}$ for the sample of bursts with $\sigma_\alpha < 0.3$ (time-integrated spectral analysis). The filled circles correspond to the spectra that are best fitted by a COMP model ($TS_\beta < 9$). Their fit can reach very small errors for moderate/high values of the peak energy.

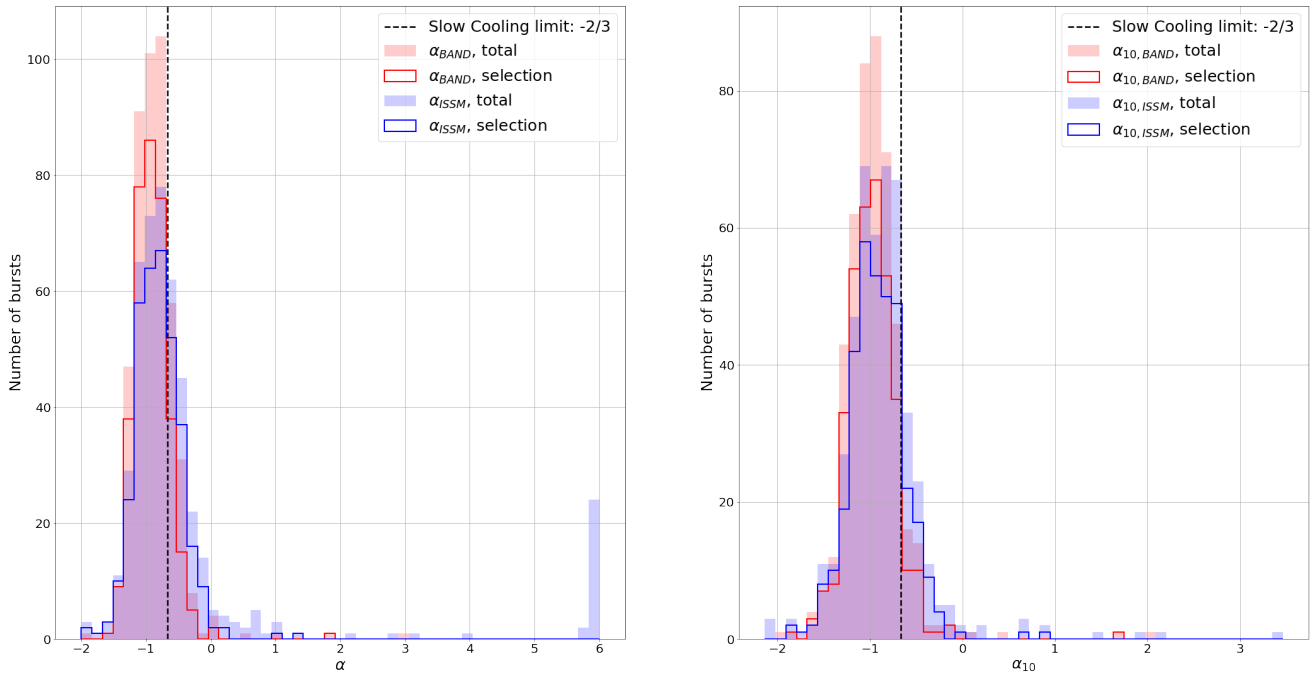

Figure 3.19: Distribution of α (left) and α_{10} (right) for Band and ISSM before and after the selection $\sigma_\alpha < 0.3$ (time-integrated spectral analysis).

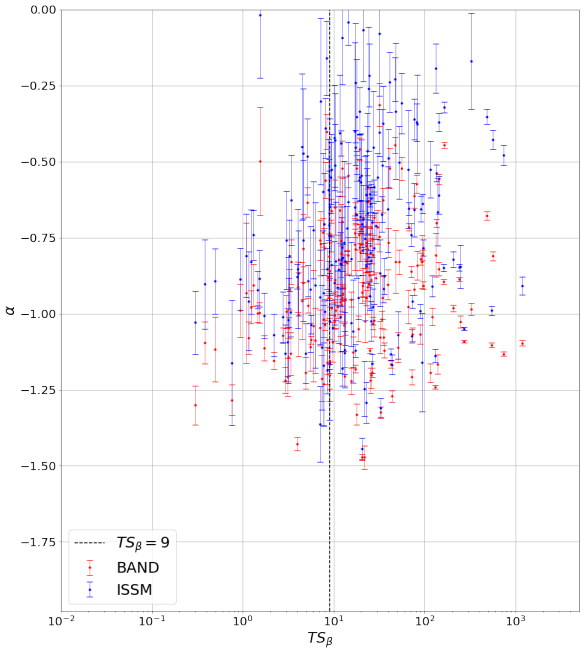

Figure 3.20: α as a function of TS_β for the sample of bursts with $\sigma_\alpha < 0.3$ (time-integrated spectral analysis).

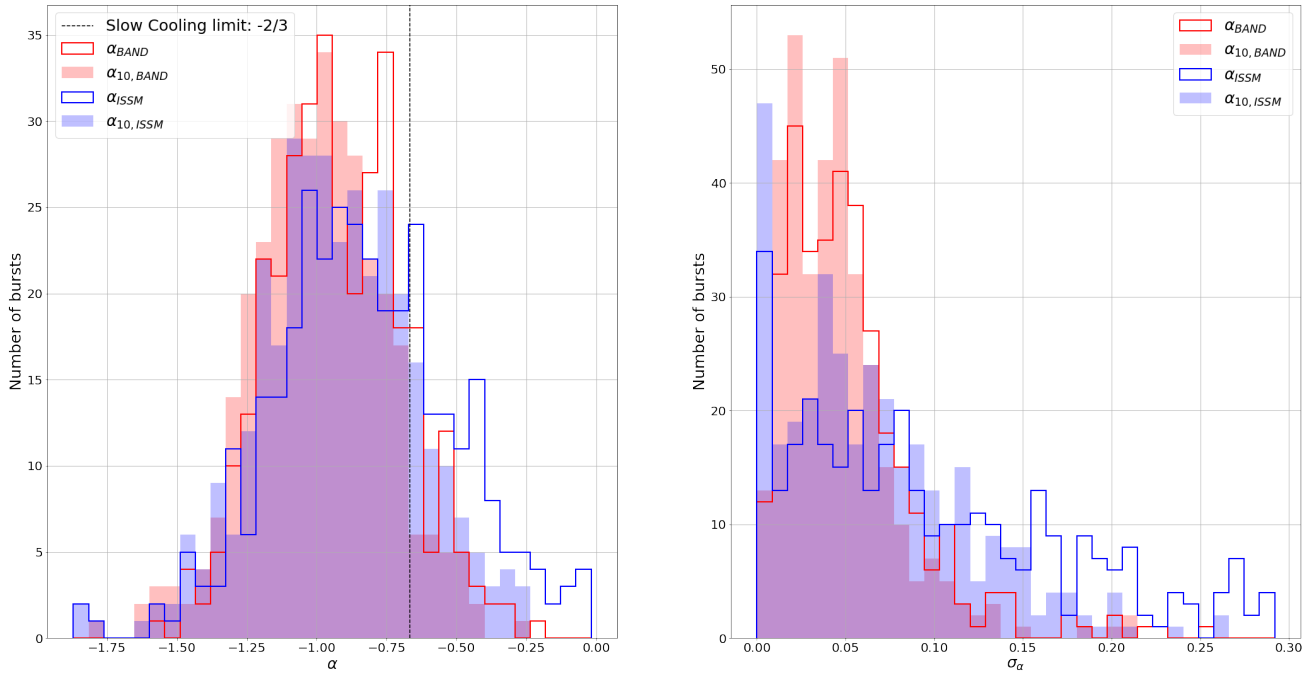

Figure 3.21: Distribution of the low-energy index and of its error for the sample $\sigma_\alpha < 0.3$ (time-integrated spectral analysis).

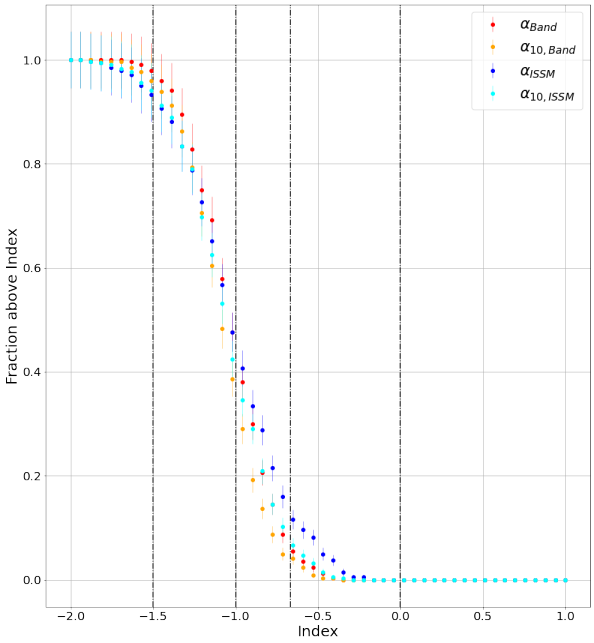

Figure 3.22: Fraction of bursts whose low-energy index is greater than Index (x-axis) at more than 2σ for the sample $\sigma_\alpha < 0.3$ (time-integrated spectral analysis).

	α_{Band}	$\alpha_{10,Band}$	α_{ISSM}	$\alpha_{10,ISSM}$
Fast-cooling limit: $-3/2$				
Bursts with $TS_\beta > 9$	99%	98%	95%	98%
Bursts with $\sigma_\alpha < 0.3$	98%	96%	93%	94%
Marginally fast-cooling limit: -1				
Bursts with $TS_\beta > 9$	54%	43%	60%	54%
Bursts with $\sigma_\alpha < 0.3$	43%	35%	45%	40%
Slow-cooling limit: $-2/3$				
Bursts with $TS_\beta > 9$	7%	5%	19%	10%
Bursts with $\sigma_\alpha < 0.3$	6%	4%	12%	7%

Table 3.4: Probability of the low-energy index to be above the fast-cooling, marginally fast-cooling, slow-cooling limits at more than 2σ for the sample with $TS_\beta > 9$, and $\sigma_\alpha < 0.3$ (time-integrated spectral analysis). The error on each probability is the order of unity (a few percents).

	Band				ISSM			
Par	α	β	E_p	Norm	α	β	E_p	Norm
α	1.000				1.000			
β	**0.133**	1.000			**0.906**	1.000		
E_p	-0.849	-0.385	1.000		0.710	0.928	1.000	
Norm	0.954	0.196	-0.945	1.000	0.498	0.730	0.903	1.000

Table 3.5: Correlation matrix for the fit of Band (left) and ISSM (right) on GRB 090330279.

Figure 3.19 shows the distribution of α and α_{10} before and after the selection cut. The selection reduces the tails of the extremely hard α and α_{10}, and in any case the distribution peaks at a value smaller than the slow-cooling limit of $-2/3$. Five bursts present a value of α_{ISSM} greater than 0, because either their spectral energy distribution peaks at low values, or their *SNR* is small. I exclude them from the following discussion.

- GRB 100609783: $\alpha_{ISSM} = 0.21 \pm 0.12$. The burst *SNR* = 49 and for the BGO the *SNR* = -1 therefore the fit is driven by the three NaIs. The spectrum peaks at the relatively low $E_{p,ISSM} = 147 \pm 4$ keV: this results into a hardening of α_{ISSM} due to the continuous curvature of ISSM.
- GRB 140206304: $\alpha_{ISSM} = 1.37 \pm 0.15$. The global *SNR* is relatively low (78) especially for the BGO (7). $E_{p,ISSM} = 147 \pm 5$ keV, which induces an hard value of $\alpha_{10,ISSM}$ similarly to the previous case.
- GRB 141022087: $\alpha_{ISSM} = 0.98 \pm 0.02$. The burst *SNR* = 28 and the quality of the fit is very poor: the reduced *PG-stat* is 17. The number of bursts with a reduced *PG-stat* greater than 3 and 10 is 83 (24%) and 13 (4%) over the sample of 349 bursts with $\sigma_\alpha < 0.3$. Indeed this GRB fall within the second group which represent a tiny part of the whole sample. Therefore this spectral fit is pathological and an exceptional case.
- GRBs 180125891 and 180427442: $\alpha_{ISSM} = 0.17 \pm 0.19$ (0.10 ± 0.15). Those bursts peak at low energies $E_{p,ISSM} = 59 \pm 1$ (106 ± 3) keV.

Figure 3.20 displays α as a function of TS_β. As TS_β increases, the low-energy index of either model is better measured (smaller errors). The root cause of this apparent correlation is likely to be an increase in the *SNR*, which at the same time improves the fits upon the COMP fits (higher TS_β) and the measurement of the low-energy index. Figure 3.20 also shows that only α_{ISSM} gets slightly harder when TS_β increases. To explain this trend, it is worth recalling that in the Band case, the local photon index $\Gamma(E)$ does not depend on α_{Band} at high energies ($E > E_b$), and not on β_{Band} at low energies ($E < E_b$) (see Equation 1.9). As a consequence α_{Band} and β_{Band} are correlated only through $E_{p,Band}$ and the normalization factor. In the ISSM case the local photon index $\Gamma(E)$ always depends on α_{ISSM} and β_{ISSM} (see Equation 1.4) because there is not break energy. For example, I considered GRB 090330279 which belongs to the sample σ_α <0.3 and for which $TS_\beta > 9$. Table 3.5 presents the correlation matrices for the fits of Band and ISSM. The correlation between α_{Band} and β_{Band} is as small as 0.133 for Band, while it is significantly greater and positive (0.906) for ISSM. The higher correlation between α and β for ISSM explains that when β is better constrained (TS_β greater) and harder than also α is better constrained and harder.

Figure 3.21 shows the distributions of the low-energy indices and of their errors after the selection cut and excluding the outliers previously discussed. The error on α_{ISSM} and $\alpha_{10,ISSM}$ can be very small. As already shown in Figure 3.18, a significant fraction of those cases belong to the spectra which are equally well fitted by ISSM and COMP. In order to compare the spectral fit results with the expectations from the synchrotron theory at low energy (see § 1.3), Figure 3.22 shows the fraction of the bursts whose low-energy index is above a certain threshold (x-axis) at more than 2σ: $\alpha - 2\sigma_\alpha > threshold$. The vertical lines represent the fast-cooling, marginally fast-cooling, slow-cooling values of $-3/2$, -1 and $-2/3$ respectively. Table 3.4 presents the probability at which the low-energy index exceeds these values with a confidence level greater than 2σ. These probabilities have errors of the order of unity (a few percents), therefore they are comparable for α_{10} between Band and ISSM. The majority of bursts present a low-energy index greater than the value of

$-3/2$ expected in the fast-cooling regime. The probability of the low-energy index to be above the marginally fast-cooling value is slightly higher for the sample with $TS_\beta > 9$ than for the sample with $\sigma_\alpha < 0.3$, especially for α_{ISSM}. Apart from that case, the probabilities of these samples are always consistent within their errors of some units. The probability of the low-energy index to be above the slow-cooling value $-2/3$ is low especially for the sample with $\sigma_\alpha < 0.3$. **As a result, the low-energy index α_{10} is softer in more than 90% of the cases than the slow-cooling value of $-2/3$ within 2σ errors**. This conclusion is at odds with past publications claiming for a significant fraction of bursts violating this synchrotron line of death, such as in Preece et al. 1998. In this analysis of CGRO/BATSE bursts, the authors found that 44% of the bursts have a maximum low-energy spectral index $\alpha_{25,max}$ above $-2/3$. Each α_{25} value was computed close to the BATSE detection threshold of 25 keV following Equation 1.9 ($\alpha_{25} = \Gamma_{Band}(25\,keV)$). Then, $\alpha_{25,max}$ was chosen for each burst as the maximum value obtained from a time-resolved analysis, instead of considering all the time intervals analysed (as I will show in § 3.3). This choice might bias the resulting distributions by favoring the positive fluctuations of the low-energy slope within the course of each burst. Besides, the low-energy slope α_{25} might reach its maximum value in time intervals where it is not representative of the non-thermal spectral slope, namely when a quasi-thermal emission contributes to the observed flux (see § 4). Examples of such multi-component spectra can be found in table S2 of Preece et al. 2014 and in table 4 of Guiriec et al. 2015b.

The arithmetic mean and the sample standard deviation of the low-energy indices are presented in Table 3.6. As found by Y20, the ISSM low-energy indices are slightly harder than the Band ones, but all mean values are compatible with realistic models of synchrotron emission from GRB jets (see § 1.3). In the so-called marginally fast-cooling regime [Daigne et al. 2011], specific configurations of the jet such as low-contrast internal shocks can lead to α values as hard as $-2/3$. Moreover, the decay of the magnetic field behind the shock could harden the low-energy part of the synchrotron spectrum (Pe'er et al. 2006; Derishev 2007). In this case, the most energetic electrons would travel in a region where the magnetic field is still high, while a bigger fraction of electrons would see a less intense magnetic field [Bošnjak et al. 2022].

3.2.5 Well characterized bursts

The third sample consists of the bursts whose spectral indices are well measured. I required that both $TS_\beta > 9$ and $\sigma_\alpha < 0.3$. This results into a sample of 134 well characterized bursts. The left panel of Figure 3.23 shows $E_{p,ISSM}$ as a function of the corresponding $E_{p,Band}$. The median value of $E_{p,ISSM}/E_{p,Band}$ is 1.20 consistent with the value of 1.23 for the sample $TS_\beta > 9$ and with the results of Y20. The right panel of the figure shows α as a function of β for Band and ISSM. Two important properties can be underlined from this figure:

- The spread of the ISSM indices is much larger than in the Band case, especially for the high-energy slope β. As discussed in § 3.2.3, this probably reflects the higher flexibility of the ISSM function with respect to the frozen spectral shape of the Band function at high energies. This could also point to a genuine diversity in GRB microphysics in midly relativistic shocks such as internal shocks. In the future, investigating this possibility will need to adapt the spectral analysis procedure to fit directly the physical parameters of the numerical model on which the ISSM proxy function is based.

- Spectra that are found to be soft both at low and high energies with the ISSM model are missing (no blue points in the bottom-left corner of the figure). As discussed in § 3.2.3 (Figure 3.14), this is likely to be due to a selection effect rather than a physical effect. Indeed, bursts which did not pass the $TS_\beta > 9$ cut and are best fitted by the COMP model generally have the smallest SNR and the steepest slope at high energy. In addition, the strong correlation of α and β in the ISSM fits (see § 3.2.4) explains that these bursts are also among the softer ones at low energies.

Table 3.6 presents the mean and the sample standard deviation of the low-energy and high-energy index of Band and ISSM for the three considered samples: the set of bursts with $TS_\beta > 9$ cut, $\sigma_\alpha < 0.3$ cut, and the sample with both cuts applied at the same time. There is a general agreement for the low-energy and high-energy parameters of Band across the three samples. The low-energy index α of ISSM is slightly harder when the cut $TS_\beta > 9$ is applied. This can be explained by the strong correlation between α and β in the

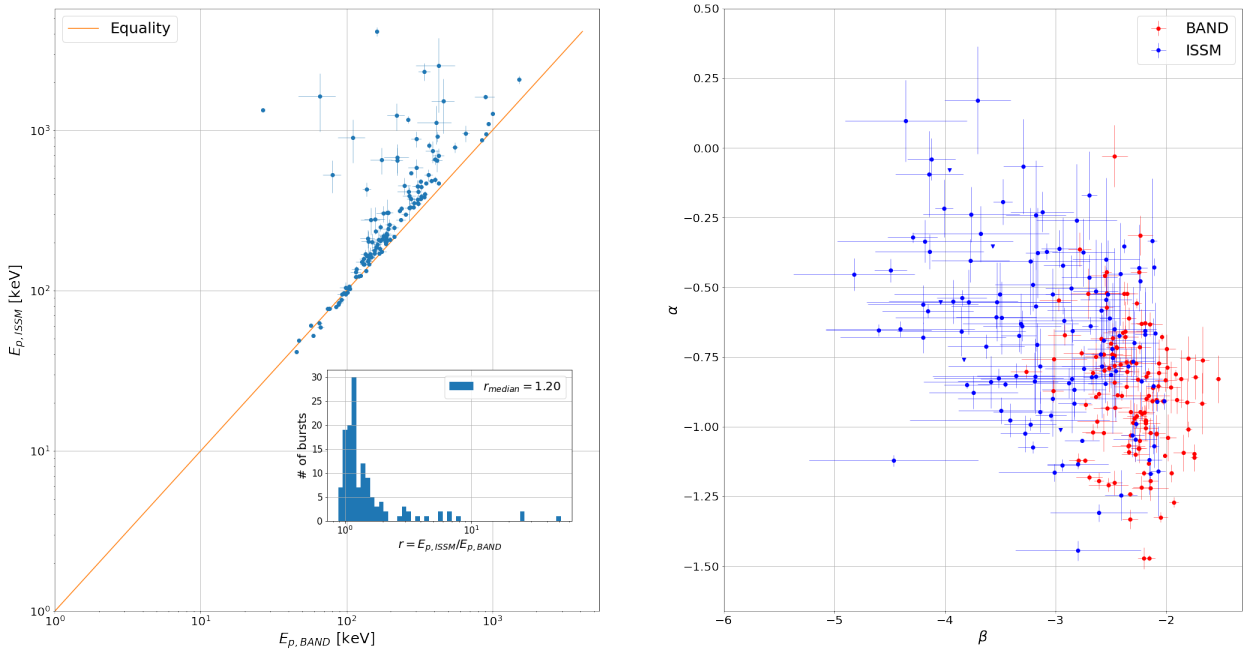

Figure 3.23: Left: $E_{p,ISSM}$ as a function of $E_{p,Band}$ for the well characterized bursts (time-integrated spectral analysis). The median value of the $E_{p,ISSM}/E_{p,Band}$ is 1.20. Right: α as a function of β for Band and ISSM. When the error on β is greater than 1, the value is marked with a triangle.

	Band			ISSM			
	α	α_{10}	β	α	α_{10}	β	β_b
$TS_\beta > 9$	-0.88 ± 0.21	-0.95 ± 0.21	-2.25 ± 0.30	-0.66 ± 0.31	-0.84 ± 0.25	-2.92 ± 0.67	-1.99 ± 0.26
$\sigma_\alpha < 0.3$	-0.93 ± 0.24	-0.99 ± 0.23	-2.34 ± 0.37	-0.83 ± 0.32	-0.93 ± 0.28	-3.20 ± 0.72	-2.05 ± 0.31
Both	-0.88 ± 0.22	-0.95 ± 0.21	-2.30 ± 0.30	-0.69 ± 0.30	-0.84 ± 0.25	-3.08 ± 0.68	-2.03 ± 0.26

Table 3.6: Arithmetic mean and sample standard deviation of the low-energy and high-energy spectral indices of Band and ISSM for the three GRB samples considered in the time-integrated spectral analysis. These samples have been obtained with the cut TS_β >9, σ_α <0.3, and both cuts, respectively.

ISSM fits, namely when β is better constrained with higher values then also α is better constrained with higher values. This effect is not observed for α_{10} index, which is less correlated to beta and mostly driven by the numerous counts close to the GBM detection threshold.
In conclusion the peak energy of ISSM is on average greater than the peak energy of Band. The mean value of $\beta_{b,ISSM}$ is very close to -2, which implies that the ISSM SED often peaks at the break energy of the Band model. As mentioned in § 3.2.3, the consequences on the Amati/Yonetoku relations should be investigated in the future. Moreover the relative error on $E_{p,ISSM}$ is greater than $E_{p,Band}$. This is expected because ISSM is a continuously curved function so its peak energy benefits of a greater freedom in the fit, which translates in greater errors with respect to the Band function. β_{ISSM} is systematically softer than β_{Band} for the same burst, which is a known consequence of the continuous curvature of ISSM.

The mean value of β_{Band} is close to the synchrotron spectral index at high energy which is expected for an electron power-law spectrum with a slope $-p = -2.7$. The mean value of β_{ISSM} is also compatible with theoretical expectations assuming a softer electron spectrum as discussed in § 3.2.3. The low-energy index of ISSM is slightly harder than the one of Band on average. The values of the Band or ISSM low-energy indices, especially the local slopes at 10 keV (α_{10}), are compatible with realistic models of synchrotron emission from GRB jets, as discussed in § 3.2.4. In summary, this study of the most fluent GRBs observed by the GBM support the ISSM model as the most appropriate model to reproduce their time-integrated spectra. I showed that these keV-MeV prompt spectra are well fitted with a single synchrotron component which is consistent with the GRB synchrotron theory.

3.3 Time-resolved spectral analysis

3.3.1 Motivations

The spectral analysis presented in § 3.2 considers the spectra of the selected bursts integrated over their entire duration. The time-integrated spectrum can be the superposition of different emission spectra from different episodes. Therefore, the spectral evolution of each burst is not taken into account, especially for the ones with a high *SNR* in the GBM. A spectral analysis resolved in time is then necessary to properly characterize the GRB spectra. The ISSM model has been built by Y20 against a single-pulse synthetic burst generated by the numerical model presented in § 1.3.4. Y20 also showed that ISSM describes well the spectra in time bins within a pulse. Therefore ISSM is an appropriate model to perform the spectral characterization of the GBM bursts with detailed spectroscopic resolution. In this section I present the results of the spectral analysis conducted on the most significant time bins for the set of the 460 bursts defined in § 3.1. Similarly to the previous section I compare the performance of ISSM and Band in fitting the selected spectra and I investigate the difference between the two models in terms of spectral parameters.

3.3.2 Time intervals selection

I applied the Bayesian block method introduced by Scargle et al. 2013 to obtain the optimal temporal segmentation of each light curve. The Bayesian block method defines the boundaries of the time bins between which a light curve presents a significant rate variation given specific requirement such as the false alarm probability p_0, or the expect number of change points ncp_{prior}. I applied its Python implementation of the *astropy* library called bayesian_blocks. The algorithm uses a fitness function to define the optimal segmentation of the time series: I chose the fitness function *events*, which is adapted for binned data. I considered the light curve between $t_{start} = Flnc\_Spectrum\_Start$ and $t_{stop} = Flnc\_Spectrum\_Stop$, which are the boundaries of the burst duration used for the spectral analysis in the GBM spectral catalog and in § 3.2. I binned each light curve in 500 bins: this choice seems reasonable since even for a long burst with a duration of 100 s each bin lasts 0.2 s. This time scale is still representative of the burst variability. Additionally I set the false alarm probability $p_0 = 0.01$. On top of the optimal temporal segmentation obtained with the Bayesian blocks I selected the blocks which had a $SNR > 5$ in order to have enough signal to weight the response matrix in the spectral data preparation. The blocks with a $SNR < 5$ were merged with other blocks to increase the *SNR*, or simply left alone. Figure 3.24 and Figure 3.25 present four examples of lightcurve with the Bayesian blocks and the cut on $SNR > 5$ (super-blocks) superimposed. The upper panel of Figure 3.25 shows the light curve of GRB 171102107: the 2 blocks at $T - T_0 \sim 30\,s$ are merged together and they are separated from the peak of the following block which has $SNR > 5$. This merger has a negligible impact on the segmentation since $SNR = 5$ is promptly reached and the resulting block is isolated. The definition of the intervals obtained by selecting the Bayesian blocks with a $SNR > 5$ is still a close description of the light curve variability. The upper panel of Figure 3.26 shows the *SNR* distribution obtained for the whole sample of bursts of the time-integrated spectral analysis and all blocks considered for the time-resolved spectral analysis. The *SNR* distribution of the blocks peaks at a lower *SNR* when compared to the distribution of the bursts *SNR*. The *SNR* distribution for the time-integrated analysis starts at $SNR = 20$ because of the selection of the NaIs with a $SNR > 20$ made at § 3.1.5. The block *SNR* distribution has a lower tail extending to negligible values of *SNR* and an upper tail which reaches the highest *SNR*. In order to consider the blocks with a reasonable *SNR* and to be consistent with the time-integrated analysis I selected only the blocks which had a *SNR* greater than 20. This selection comprised 6547 (71%) blocks over a total of 9226. The lower panel of Figure 3.26 shows the number of time bins of each burst as a function of the burst *SNR*. Indeed one expects that when the burst *SNR* increases then the variability of the signal is more pronounced so the number of significant time bins for that burst increases.

3.3.3 Performance of Band and ISSM models

In order to characterize the fitting performance of the Band and ISSM functions I defined three samples as for the time-integrated analysis: the first one comprises the blocks whose spectra are significantly better fitted by Band and ISSM with respect to COMP ($TS_\beta > 9$), the second sample consists of the spectra whose

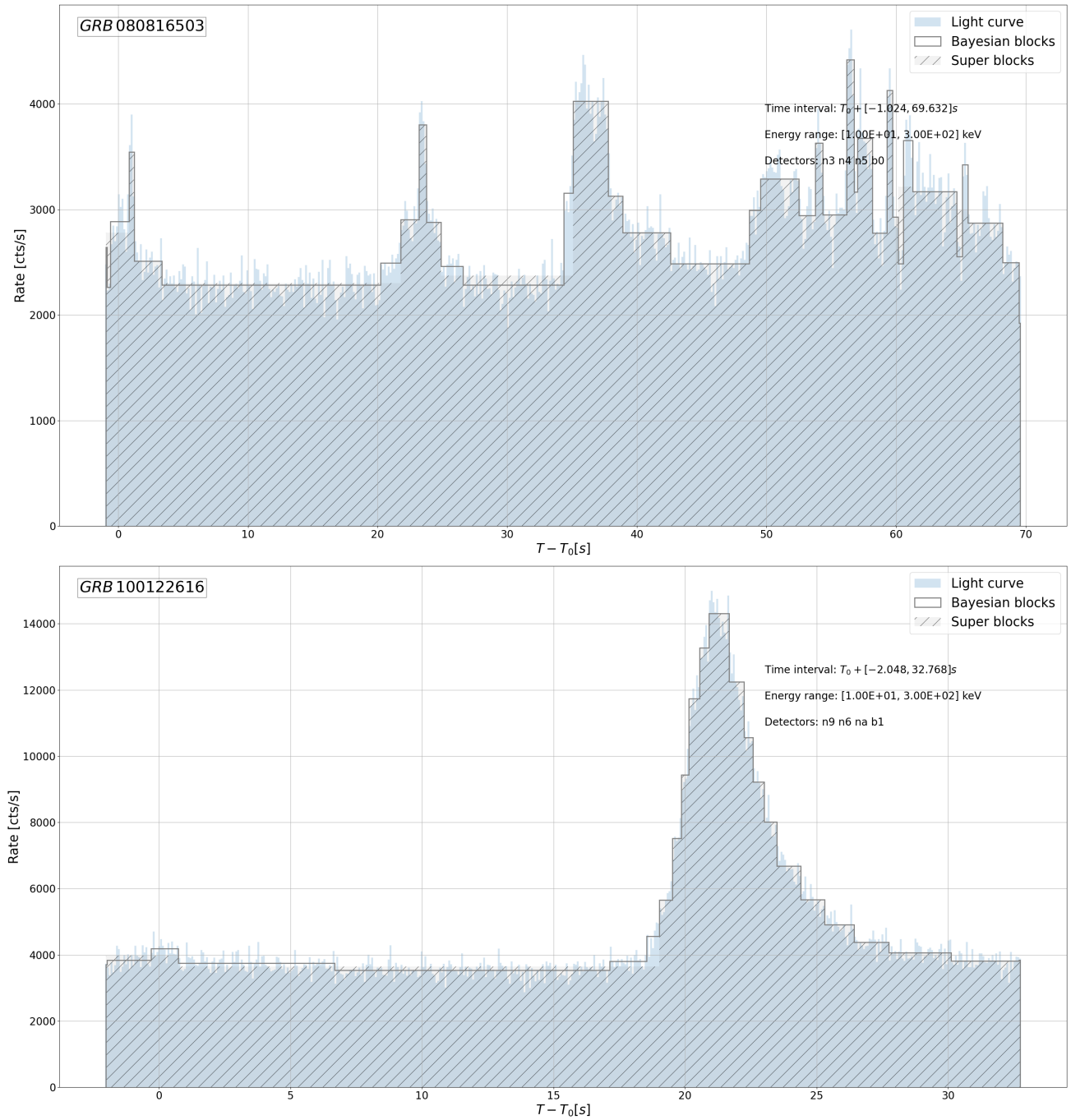

Figure 3.24: Light curves (10-300 keV) of two benchmark bursts, GRBs 080816503 (upper panel) and 100122616 (lower panel). The light curves obtained by applying Bayesian blocks and by selecting the blocks with $SNR > 5$ (super blocks) are superimposed.

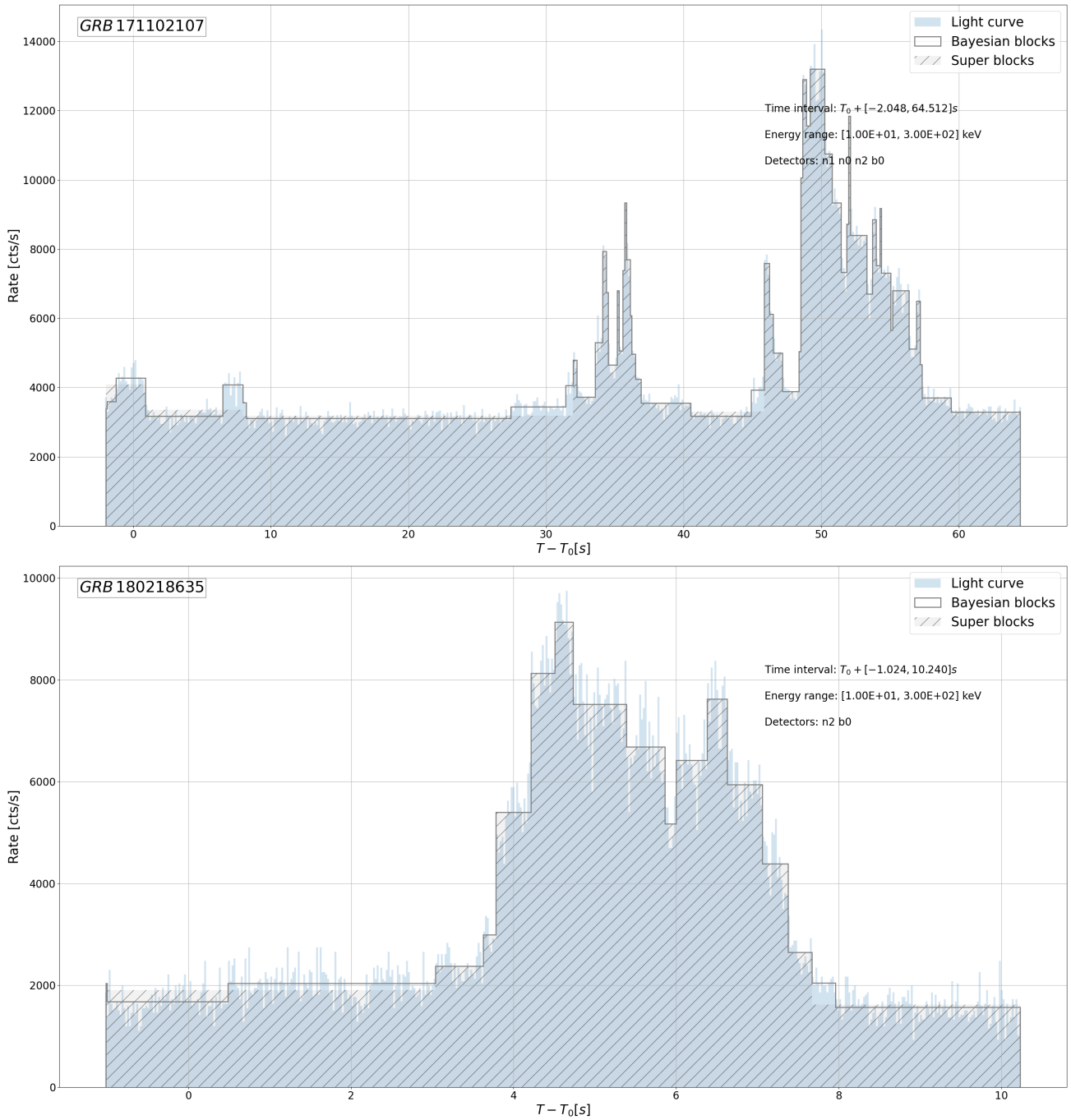

Figure 3.25: Light curves (10-300 keV) of two benchmark bursts, GRBs 171102107 (upper panel) and 180218635 (lower panel). The light curves obtained by applying Bayesian blocks and by selecting the blocks with $SNR > 5$ (super blocks) are superimposed.

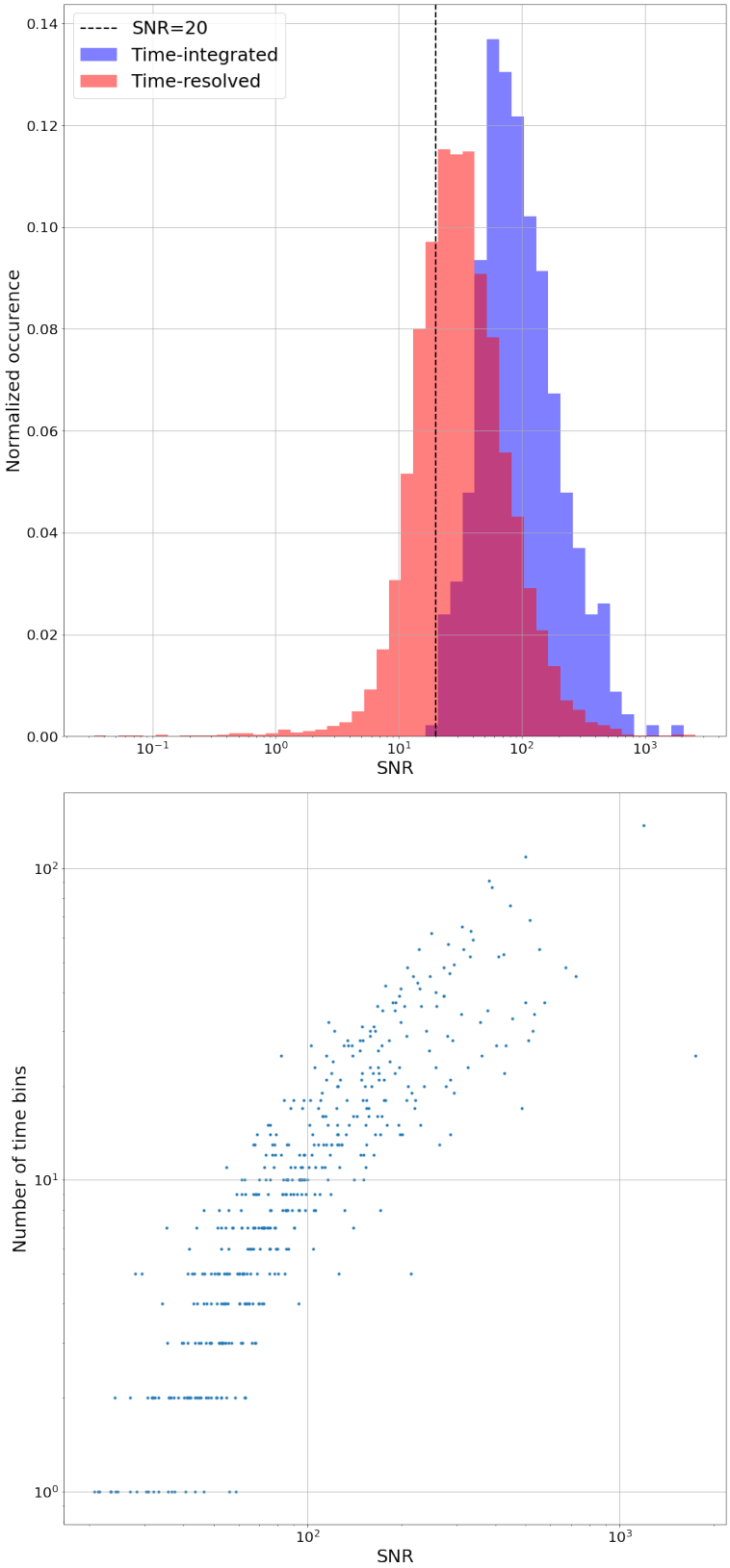

Figure 3.26: Upper panel: *SNR* distributions of the blocks for the time-resolved analysis and of the bursts for the time-integrated analysis. Only the blocks with a *SNR* greater than 20 were chosen for the following discussion. Lower panel: number of time bins per burst as a function of the burst *SNR*.

Selection	COMP	SBPL	Band	ISSM
All bursts (728)	0%	20%	22%	58%
$SNR < 71$ (243)	0%	33%	32%	36%
$71 < SNR < 140$ (242)	0%	22%	21%	57%
$140 < SNR < 1850$ (243)	0%	6%	14%	80%
$196 < SNR < 1752$ (130)	0% (0%)	8% (7%)	15% (13%)	78% (80%)

Table 3.7: Probability of COMP, SBPL, Band, and ISSM to be the reference model for the whole sample of blocks with $TS_\beta > 9$ and for each of the three SNR classes (time-resolved spectral analysis). The last line compares the probability of this analysis to the one of the time-integrated analysis in a common SNR interval. The values between parentheses belong to the time-integrated analysis. All the probabilities are rounded to unity and their errors are of the order of unity.

low-energy index is well constrained ($\sigma_\alpha < 0.3$), and the third sample containts the spectra that are well characterized ($TS_\beta > 9$ and $\sigma_\alpha < 0.3$). The topic of this section will be the first sample.

For each block I performed a spectral analysis for COMP, SBPL, Band, and ISSM. **I performed a total of $\sim$ 37000 spectral fits.** The number of blocks for which $TS_\beta > 9$ is 728 (11%) out of the 6547 blocks with $SNR > 20$. The probability of each model to be the reference model is shown in Table 3.7. **As for the time-integrated analysis ISSM is most frequently the reference model over all the sample and in each of the *SNR* classes, and more often as the *SNR* increases**. The last line of the table presents the values for the common interval $196 < SNR < 1752$ to compare the performance of the time-integrated and -resolved analyses. In that interval the average $SNR = 386$ for the time-integrated and $SNR = 375$ for the time-resolved analysis are similar. The probability of each model to yield the smallest *PG-stat* is similar between the two analyses since its typical error is of the order of unity for the time-integrated analysis and much smaller for the time-resolved analysis owing to the much larger number of fits. Figure 3.27 presents the distribution of $\Delta PGstat$ of COMP, SBPL, Band, and ISSM with respect to the reference model. The blocks are sorted per increasing SNR. Table 3.8 presents the probability of each model to be a good model. **Overall ISSM is a good model more often than Band, especially at the highest *SNR* where it outperforms all other models**. While the fraction of good fits with ISSM is similar for the whole sample of blocks (87%) and the blocks with high SNR (88%), the fraction of good fits with Band is indeed much smaller and limited to 69% and 41% in both cases. Figure 3.28 shows the fraction of blocks which yield a $\Delta PGstat$ smaller than a threshold value. The left panel presents the totality of the blocks, while the right panel focuses on the blocks with the highest SNR. In both cases the fraction of blocks fitted with ISSM is higher than for the other models. The left panel of Figure 3.29 presents the fraction of blocks with a SNR smaller than a threshold value with a strict cut on $\Delta PGstat = 5$ (good fit). The black histogram is the fraction of blocks without any cut. At low SNR all models are equivalent, while from $SNR \sim 200$ onwards the fraction of blocks in which ISSM provides a good fit is significantly greater. ISSM provides the highest cumulative fraction, especially at high SNR where models can be more easily distinguished. The right panel of Figure 3.29 presents the fraction of cases in which the model satisfy the cut on $\Delta PGstat$ as a function of SNR. The total number of bins is divided into 10 classes with the same size (73 time bins) for increasing SNR. The error on each fraction is approximated as $\sqrt{n_g}/n_b$, where n_g is the number of good fits among the n_b time blocks of a given SNR interval. Again, at low SNR the model are not distinguishable, while from $SNR > 100$ up to the highest SNR ISSM yields the highest fraction of time bins in which it is a good model, while the fractions of the Band and SBPL decrease with SNR. The ISSM fraction remains actually close to 80% within errors, regardless of the SNR. Conversely, the Band (resp. SBPL) fraction is 30% (resp. 20%) in the highest SNR bin ($280 < SNR < 1850$).

Figure 3.30 compares the goodness of the Band or ISSM fits between the two spectral analyses for the common interval of SNR ($196 < SNR < 1752$). The median value of the ISSM reduced *PG-stat* decreases from 2.20 for the time-integrated analysis (blue) to 1.16 for the time-resolved (red) analyses. A bigger im-

Selection	$\Delta PGstat < 5$	$\Delta PGstat < 10$
All bursts (728)		
COMP	0%	2%
SBPL	64%	78%
Band	69%	84%
ISSM	87%	93%
$\boldsymbol{SNR < 71}$ **(243)**		
COMP	0%	3%
SBPL	93%	100%
Band	81%	98%
ISSM	86%	95%
$\mathbf{71 < SNR < 140}$ **(242)**		
COMP	0%	1%
SBPL	74%	88%
Band	74%	93%
ISSM	89%	94%
$\mathbf{140 < SNR < 1850}$ **(243)**		
COMP	0%	0%
SBPL	25%	45%
Band	41%	60%
ISSM	88%	91%
$\mathbf{196 < SNR < 1752}$ **(130)**		
COMP	0% (0%)	0% (0%)
SBPL	19% (12%)	32% (18%)
Band	32% (23%)	48% (27%)
ISSM	82% (85%)	85% (90%)

Table 3.8: Probability of COMP, SBPL, Band, and ISSM to yield a $\Delta PGstat$ smaller than 5 and 10 with respect to the reference model for the sample of spectra with $TS_\beta > 9$ (time-resolved spectral analysis). I divided the sample in three classes for increasing *SNR* and add a *SNR* interval common with the time-integrated analysis for a proper comparison between the two analyses. The values between parentheses belong to the time-integrated analysis. All the probabilities are approximated to the unity and their errors are order of some units.

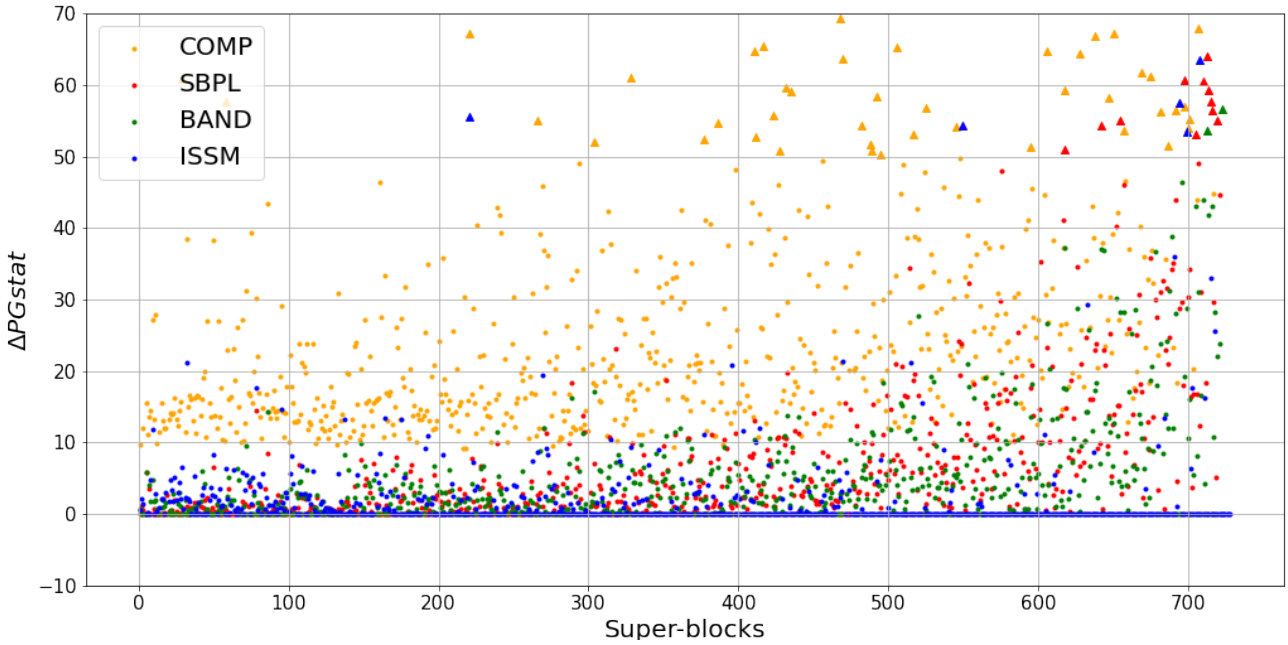

Figure 3.27: Distribution of $\Delta PGstat$ of COMP, SBPL, Band and ISSM with respect to the reference model for the sample of spectra with $TS_\beta > 9$ (time-resolved spectral analysis). The blocks indices are ordered per increasing SNR.

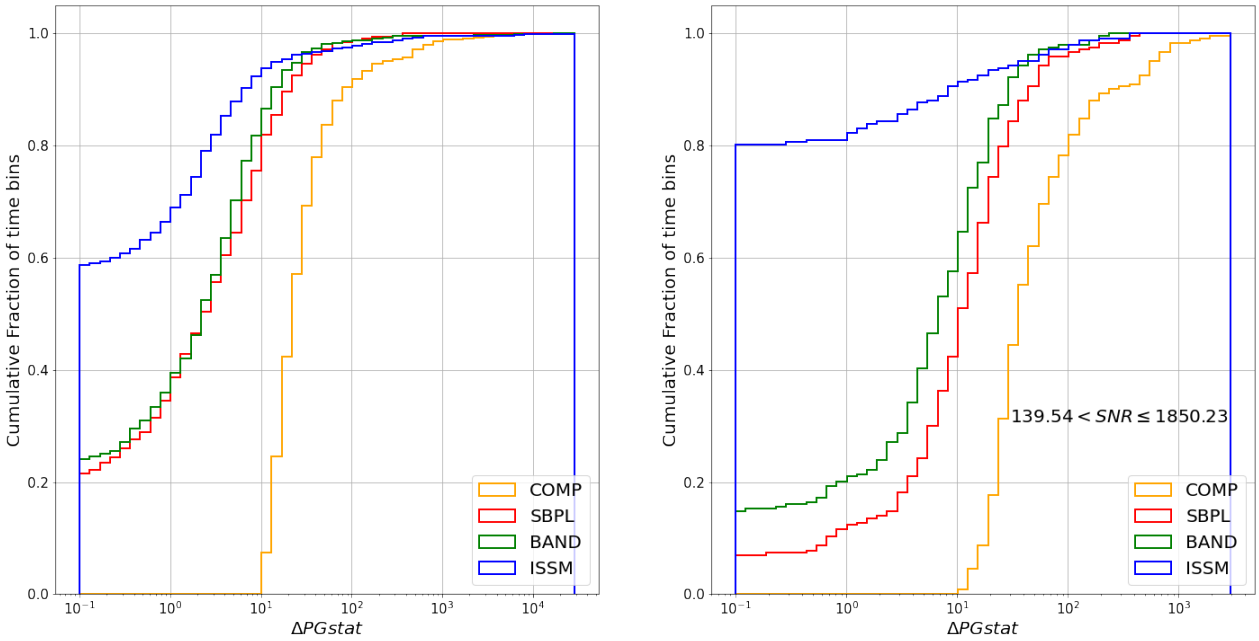

Figure 3.28: Left: cumulative distribution of $\Delta PGstat$ per each model for the whole sample of spectra with $TS_\beta > 9$ (time-resolved spectral analysis). Right: cumulative distribution for the class with the highest SNR.

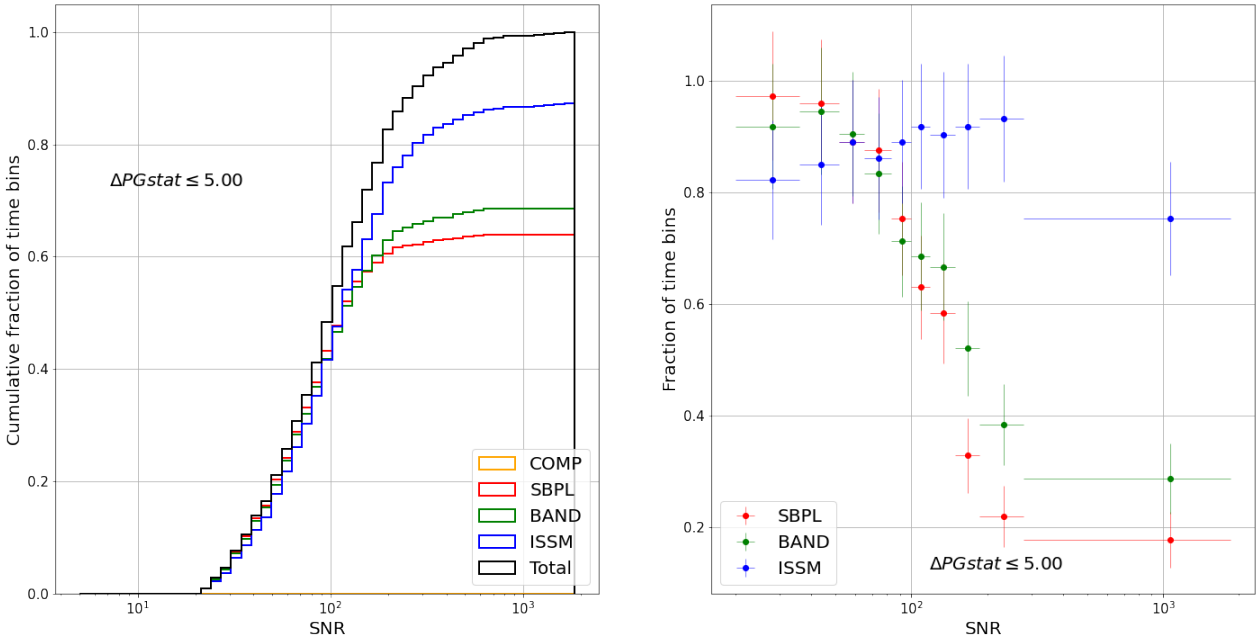

Figure 3.29: Left: cumulative distribution of SNR per each model when the corresponding $\Delta PGstat$ with respect to the reference model is smaller than 5 (time-resolved spectral analysis). The black histogram is the cumulative distribution over the whole sample with $TS_\beta > 9$. Right: fraction of bursts with the same cut on $\Delta PGstat$ as function of SNR.

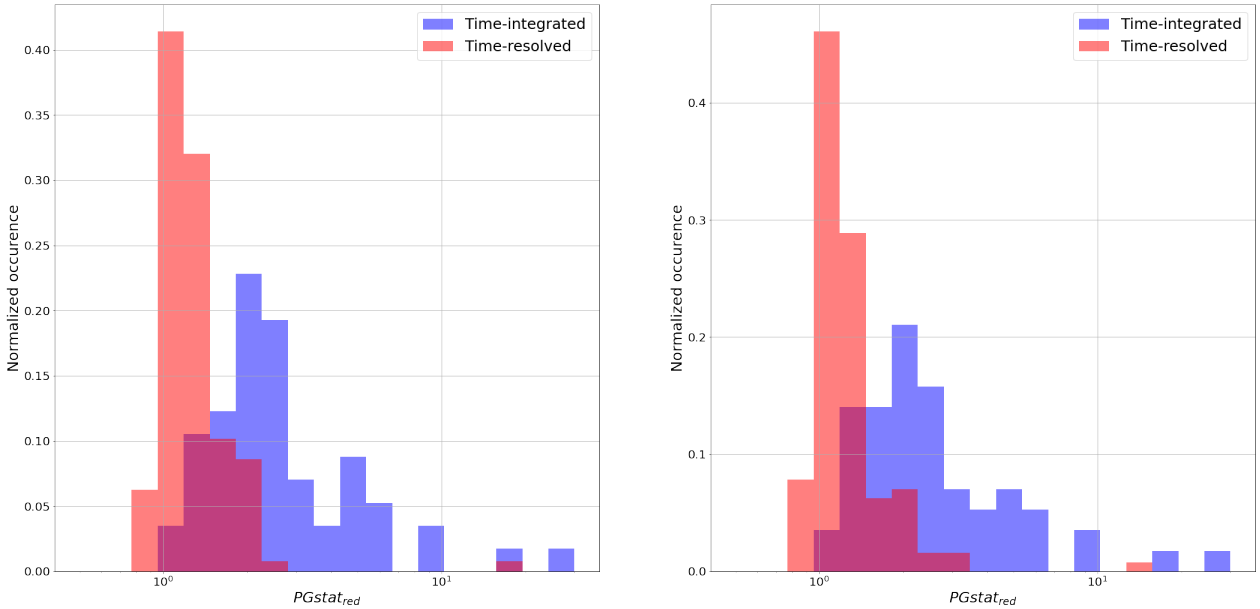

Figure 3.30: Left: distributions of the Band reduced PG-$stat$ in the common interval $196 < SNR < 1752$ of the time-integrated (blue) and time-resolved (red) analyses. Right: same as left panel for the ISSM model.

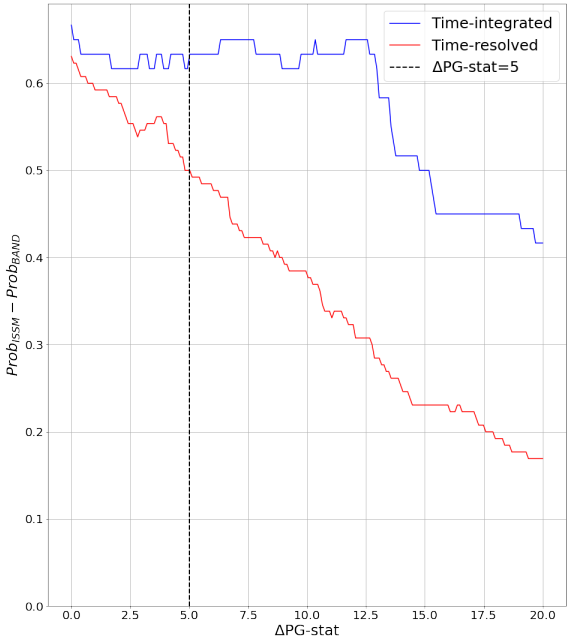

Figure 3.31: Difference $Prob_{ISSM} - Prob_{Band}$ between the probabilities of the ISSM and Band models to approach the reference model within a given $\Delta PGstat$ value shown in the horizontal axis, in the time-integrated and time-resolved analyses for the common interval of SNR ($196 < SNR < 1752$).

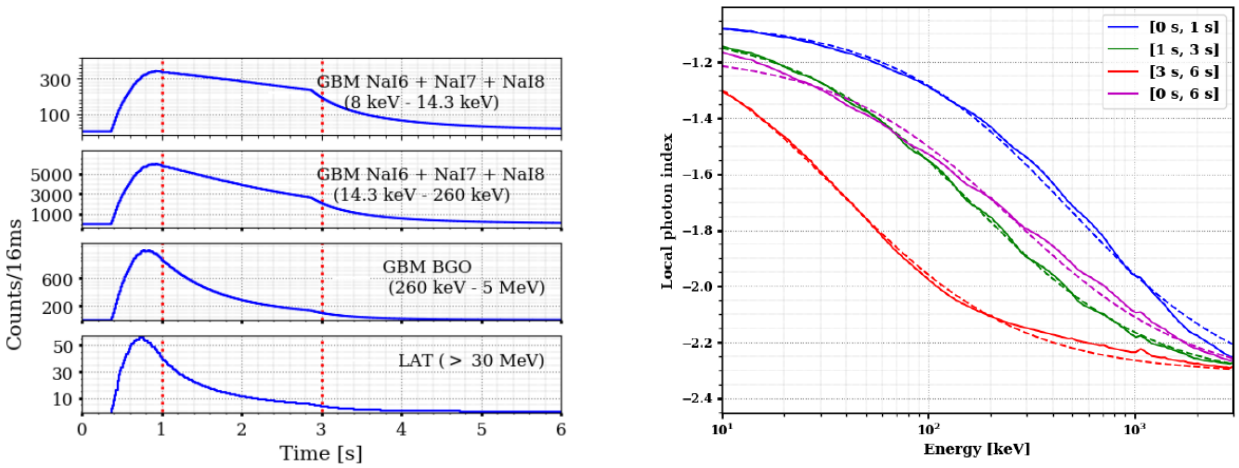

Figure 3.32: Left: light curve of the synthetic burst named "case B" in Figure 1.11, simulated with the internal-shock numerical model and folded through the response of the GBM and LAT instruments (credit Y20). Right: least-square fit (dashed lines) of the $\Gamma_{ISSM}(E)$ function to the true local photon index (solid lines) of the same synthetic burst, for the time intervals shown in the left panel: rising phase (blue), decaying phase (green), tail (red). The magenta curves correspond to the time-integrated synthetic spectrum.

provement is obtained for the Band model, with median values of 2.31 and 1.19, respectively. This decrease in reduced *PG-stat* in the Band case (-1.12) is indeed larger than in the ISSM case (-1.04), which is a significant difference since a variation of 0.1 in reduced *PG-stat* corresponds roughly to a variation of 45 units in the fit statistics (for $\sim$ 450 degrees of freedom, typically). Therefore, **time-resolved spectra are better fitted by both models than time-integrated spectra for the same level of *SNR*, and this improvement of the goodness of fit is bigger for the Band model which seems much less appropriate in the time-integrated analysis**.

This important result is confirmed in Figure 3.31, which is based on the proper statistical test that has been used so far to classify a fit as good, namely when its *PG-stat* is close to the one of the reference model (see § 3.3.3). The figure compares the fitting performance of the Band and ISSM models in the time-integrated and time-resolved analyses for the common interval of *SNR* ($196 < SNR < 1752$). Specifically, it displays the difference $\Delta Prob = Prob_{ISSM} - Prob_{Band}$ between the probabilities of the ISSM and Band models to approach the reference model within a given $\Delta PGstat$ value shown in the horizontal axis. $\Delta Prob$ is found to be always positive, and it quantifies the increase in the probability to obtain a good spectral fit when switching from the Band model to the ISSM model, as a function of the $\Delta PGstat$ threshold value that determines whether a fit is considered good or not. In the time-integrated analysis, $\Delta Prob$ remains close to $\sim$65% in the range of $\Delta PGstat$ values that correspond to a $\sim 5\sigma$ threshold (see § 3.3.3 and Y20). Namely, ISSM is decisively more often a good model than Band. Beyond $\Delta PGstat \sim 12$, $\Delta Prob$ decreases rapidly as the criterion defining a good model is more and more relaxed, i.e. the models become less distinguishable and are more likely to be considered equivalently good. Conversely, Figure 3.31 reveals a different behaviour in the time-resolved analysis, where $\Delta Prob$ decreases steadily as the $\Delta PGstat$ threshold increases. Moreover, $\Delta Prob$ remains always smaller than in the time-integrated analysis. **These results are strong evidence that the benefit of switching to the ISSM model is significant in the time-resolved analysis, and even higher in the time-integrated analysis.**

The forward-folding technique that is used to fit the GBM data assumes a spectral law in the first place, then it varies the model parameters to maximize the likelihood of obtaining the observed data set under this hypothesis. Therefore, this technique estimates the capability of the assumed model to reproduce the data, yet it does not inform about the true spectrum. The results of the hypothesis testing reported so far clearly favour the ISSM physical model over phenomenological models such as the Band function. As long as alternative physical models do not prove to reproduce GRB prompt spectra better than the ISSM model, the GRB internal-shock synchrotron model can be considered as a good explanation for the observed prompt emission of GRBs in the keV-MeV energy domain. Under this plausible hypothesis, the benefit of using the ISSM model, especially in time-integrated spectral analyses, has been also illustrated by Y20 who studied one synthetic burst generated by the numerical model described in § 1.3.4. The light curve of this synthetic burst consisted of a single pulse, as shown in the left panel of Figure 3.32, with a rising phase (blue), a decaying phase (green) and a tail (red). The right panel of Figure 3.32 shows that the $\Gamma_{ISSM}(E)$ function can follow adequately the variation of the local photon index $\Gamma(E)$ as a function of energy in each of the three time intervals. This panel also shows that the true SED peak energy E_p, which is defined as $\Gamma(E_p) = -2$, decreases rapidly from $\sim$ 1 MeV to $\sim$ 100 keV during the burst duration. Despite this strong hard-to-soft spectral evolution, the natural curvature of the ISSM spectral shape offers enough flexibility to reproduce the time-integrated spectrum reasonably well too (see the magenta curves in the panel), even if it results from the superposition of three very different spectra. This is not the case of the Band function, which consists of two (smoothly-connected) power laws, since the sum of two power-law functions can be hardly described by another power-law function. Quantitatively, Y20 simulated the response of the Fermi instruments to the synthetic burst and performed a spectral analysis with the Band and ISSM models. In table 1 of this article, they found that the increase in the fit statistic from the time-resolved analysis to the time-integrated analysis is either moderate or negligible with the ISSM model, while it is significantly larger with the Band model owing to its spectral rigidity. **These considerations, along with the results from the spectral analyses that I reported on in this chapter, demonstrate conclusively that the Internal-Shock Synchrotron Model is appropriate to describe the high-energy prompt emission spectra of GRBs, and that it should be always preferred to the Band model, especially in (long) time intervals with a strong spectral evolution.**

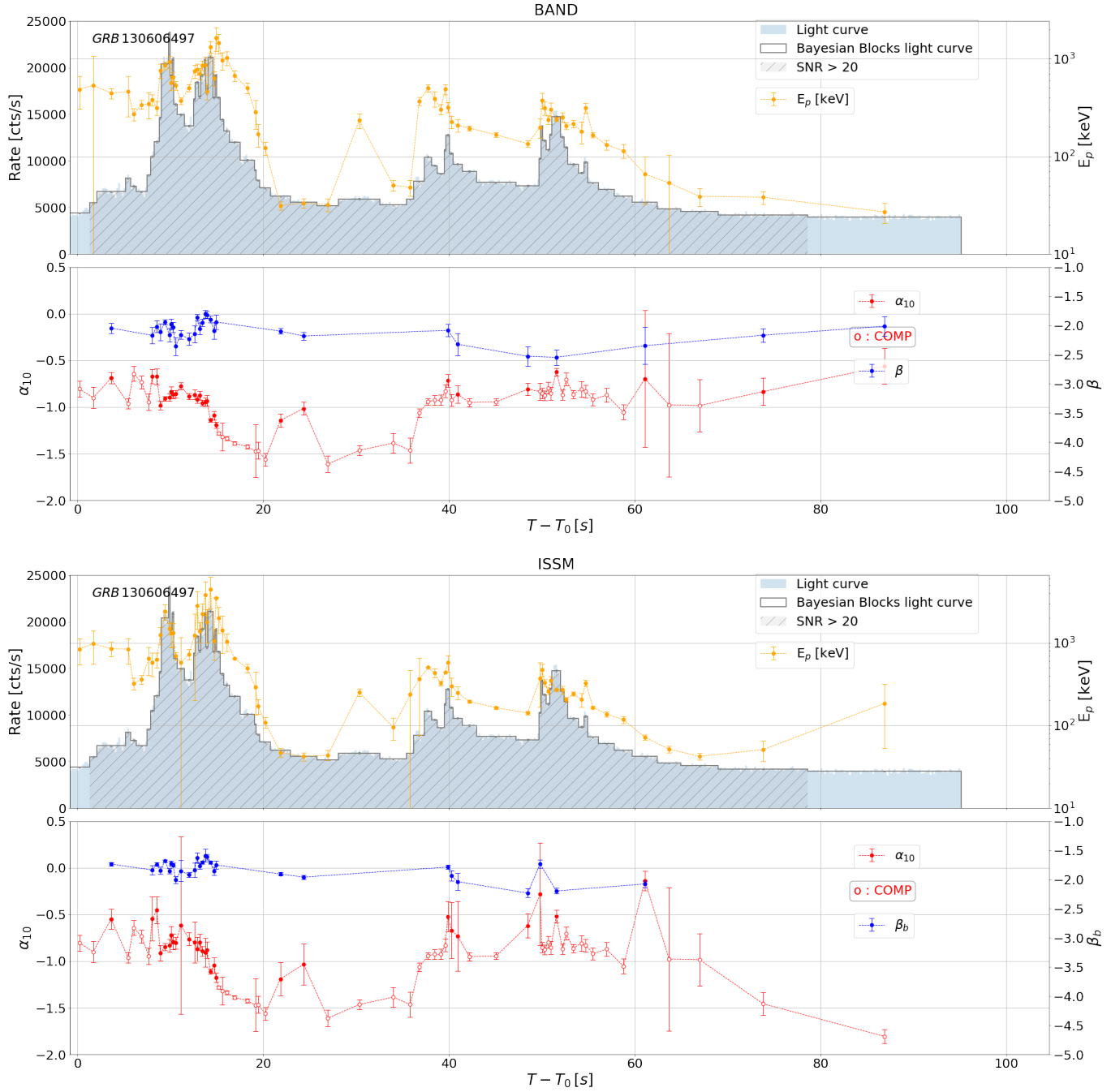

Figure 3.33: GRB 130606497. Upper (lower) panel: Band (ISSM) fit of the time-resolved spectrum. For each panel, the upper sub-panel presents the light curve (10-300 keV) of the burst, the distribution of the blocks, and highlights the blocks with a *SNR* greater than 20. Moreover it presents the time evolution of the peak energy E_p. The lower sub-panels present the temporal evolution of the low- and high-energy spectral indices.

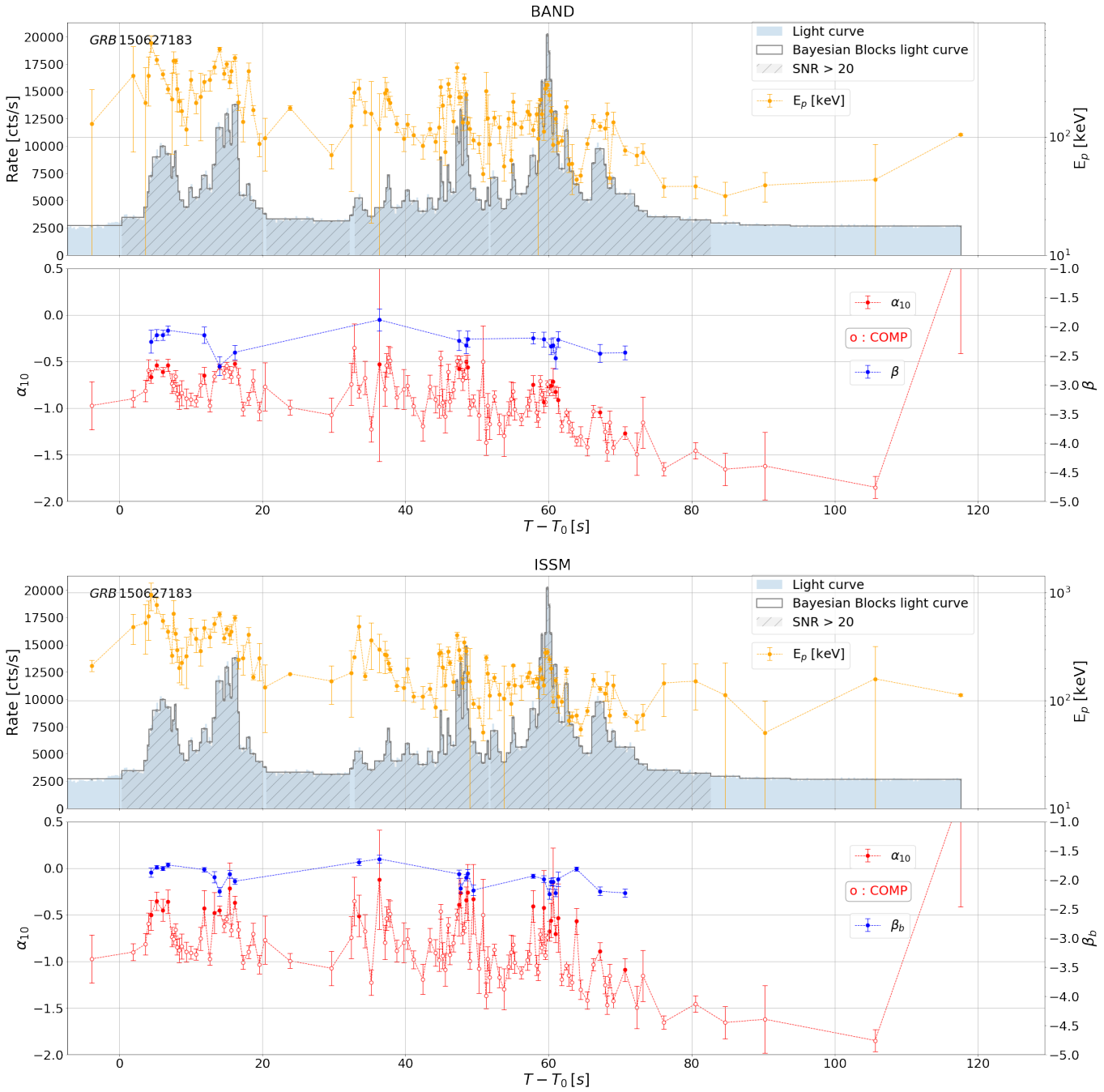

Figure 3.34: Same figure as Figure 3.33 for GRB 150627183.

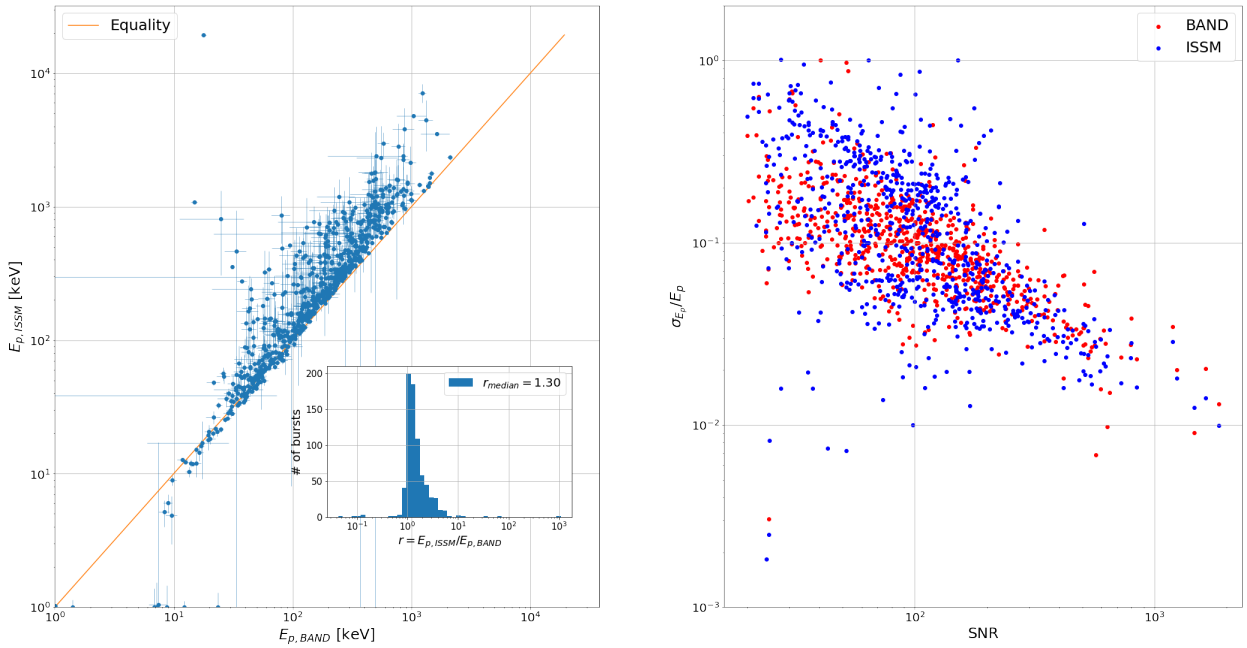

Figure 3.35: Left: $E_{p,ISSM}$ as a function of $E_{p,Band}$ for the sample of spectra with $TS_\beta > 9$ (time-resolved spectral analysis). The median value of the ratio $E_{p,ISSM}/E_{p,Band}$ is 1.30. Right: relative error on E_p for Band and ISSM as a function the block *SNR*.

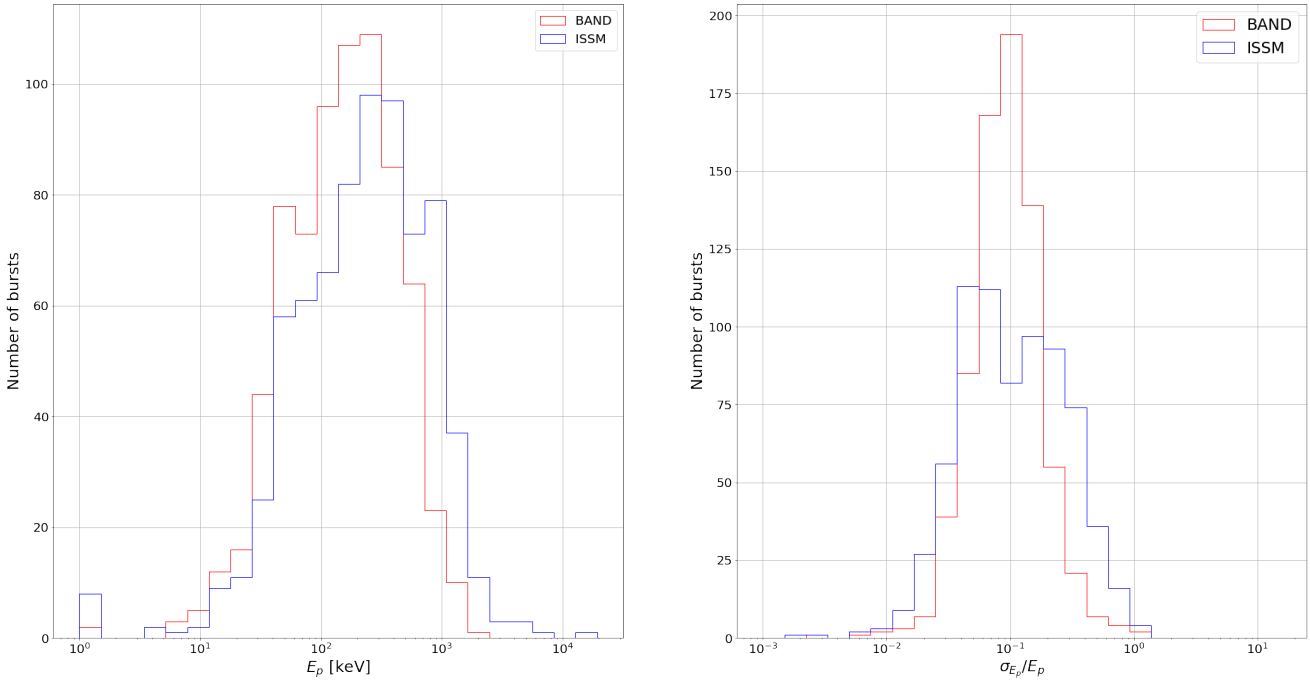

Figure 3.36: Left: distribution of E_p for ISSM and Band for the sample of spectra with $TS_\beta > 9$ (time-resolved spectral analysis). On average $E_{p,ISSM}$ is greater than $E_{p,Band}$. Right: distribution of their relative errors. As for the peak energy, the distribution of its relative error has a tail extending to higher values in the ISSM case.

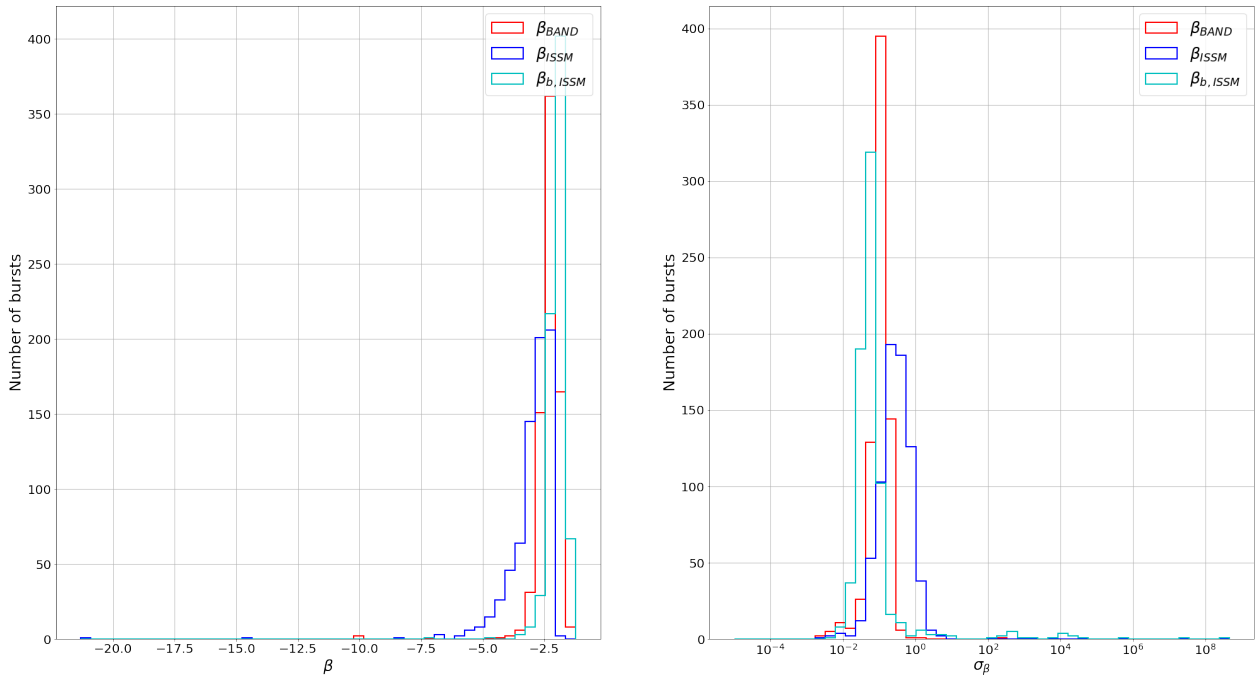

Figure 3.37: Distribution of $\beta_{b,ISSM}$, β_{Band}, β_{ISSM}, and of their errors for the sample of spectra with $TS_\beta > 9$ (time-resolved spectral analysis).

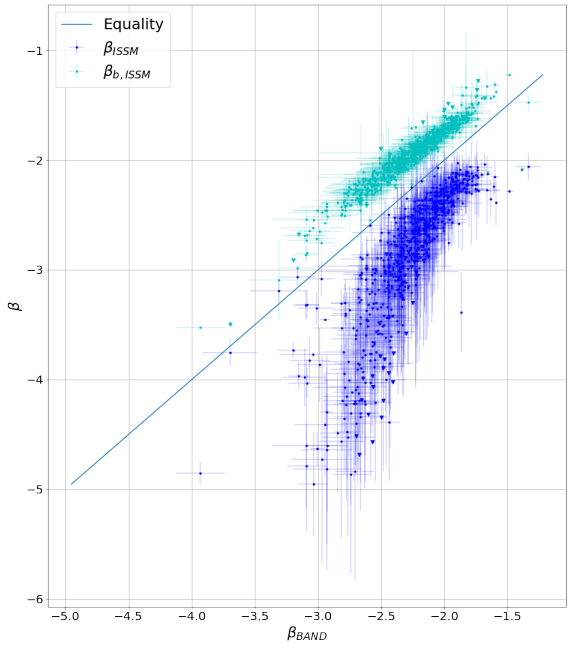

Figure 3.38: β_{ISSM} and $\beta_{b,ISSM}$ as a function of β_{Band} for the sample of spectra with $TS_\beta > 9$ (time-resolved spectral analysis). The figure shows that $\beta_{b,ISSM} > \beta_{Band} > \beta_{ISSM}$. The marker is a triangle when the error on β_{ISSM} or $\beta_{b,ISSM}$ is greater than 1. From this figure I excluded the cases with $\beta_{ISSM} < -5$ that are discussed in the text.

3.3.4 High-energy spectral parameters

Figure 3.33 and Figure 3.34 present the case of GRBs 130606497 and 150627183 whose high-energy spectral index is constrained in a significant number of blocks. In those figures, the upper panels present the results for Band and the lower panels for ISSM. For each panel, the light curve of the burst is plotted in the upper sub-panel, with superimposed the Bayesian blocks distribution with a $SNR > 5$. I highlighted with dashed lines the blocks with a $SNR > 20$, where the signal is more significant. The lower sub-panels present the temporal evolution of the low- and high-energy indices. The void red circles correspond to the blocks where the spectrum is better fitted by COMP ($TS_\beta < 9$). In those cases only the low-energy index is displayed. The red and blue filled circles correspond to the blocks where $TS_\beta > 9$. The peak energy follow the intensity of the light curves in the energy range $(10 - 300)$ keV. This hardness-intensity correlation is a well-known property of the GRB prompt emission [Ryde et al. 2000]. Additionally the high-energy index is typically constrained at the peaks of the light curve. In those blocks the high-energy channels of the count spectra are indeed populated, hence this spectral index can be constrained.

I compared the high-energy spectral parameters of ISSM and Band for the sample $TS_\beta > 9$. The left panel of Figure 3.35 shows the peak energy of ISSM as a function of the peak energy of the Band model for the same block. The ratio between the peak energy of ISSM over Band has a median of 1.30 which is close to the value of 1.23 found in the time-integrated analysis, and it has a tail extending to higher values. This means that the ISSM SED peaks at higher energies than the Band SED for the vast majority of the time intervals in the light curve. The right panel of Figure 3.35 shows that the relative error on E_p decreases as the block SNR increases, like in the time-integrated spectral analysis.

Figure 3.36 shows the distribution of the peak energy and of its relative error for ISSM and Band. ISSM yields greater relative errors than Band also in the time-resolved analysis because of its continuous curvature (see § 3.2.3). In 8 blocks $E_{p,ISSM}$ is smaller than 2. In those cases the SNR is too low to constrain the parameters (GRB 130815420 with $SNR = 27$ in the block 1 and $SNR = 28$ in the block 2, GRB 140104731 with $SNR = 32$ in block 6 and $SNR = 31$ in block 7, GRB 150127398 with $SNR = 25$ in block 7, and GRB 160216801 with $SNR = 20$ in block 16) or the fit is of very poor quality (GRB 110426629 in blocks 6 and 9). The relative error on $E_{p,ISSM}$ is greater than 1 in 7 blocks where either the quality of the fit is very poor (GRB 130121835 with block 5, GRB 160509374 with block 13), either the correlation among the spectral parameters is high and the relative errors are also high (GRB 110328520 with block 2, GRB 130606497 with blocks 16 and 18, GRB 140818229 with block 5, and GRB 160216801 with block 16).

The hierarchy of the spectral indices is the same as in the time-integrated analysis: $\beta_{b,ISSM} > \beta_{Band} > \beta_{ISSM}$ as shown in the left panel of Figure 3.37 and in Figure 3.38. β_{ISSM} is expected to be softer than the other two indices because it is an asymptotic limit. The distribution of β_{ISSM} presents 22 cases (3%) with a value smaller than -5, which mostly correspond to blocks with a high $SNR > 100$ for which the high-energy part of the counts spectrum is so populated that softer β_{ISSM} can be constrained. The distribution of β_{Band} presents 2 cases (0.3%) with a value smaller than -5, block 24 of GRB 081009140 and block 7 of GRB 150127398. Those blocks have a low SNR (28 and 25, respectively) and their SEDs peak at low energies. The right panel of Figure 3.37 shows the distributions of the errors on the high-energy indices. $\beta_{b,ISSM}$ is better constrained than β_{Band} and β_{ISSM} apart from 29 cases (4%) in which the error on $\beta_{b,ISSM}$ is greater than 2. The error on β_{Band} is greater than 2 in one case: block 24 of GRB 081009140. In that case the $SNR = 28$ so β_{Band} is poorly constrained. The mean values of β and the sample standard deviations are presented in Table 3.10. The high-energy slopes in the time-resolved analysis are slightly softer than the corresponding values of the time-integrated analysis presented in Table 3.6. This can be explained as follows: the time-integrated spectra result from an average of time-resolved spectra with different peak energies. This superposition effect flattens and widens the time-integrated SED around their peak energy, and smoothen their spectral slopes (softening of the low-energy index and hardening of the high-energy index in the time-integrated analysis with respect to the time-resolved analysis).

3.3.5 Low-energy spectral parameters

The second sample is defined by the condition $\sigma_\alpha < 0.3$. This requirement selects 2852 (43%) blocks from the initial selection of 6547 blocks with $SNR > 20$. Figure 3.39 shows the distribution of the error on the low-energy index before and after the selection cut $\sigma_\alpha < 0.3$. The distribution of the error on $\alpha_{10,ISSM}$

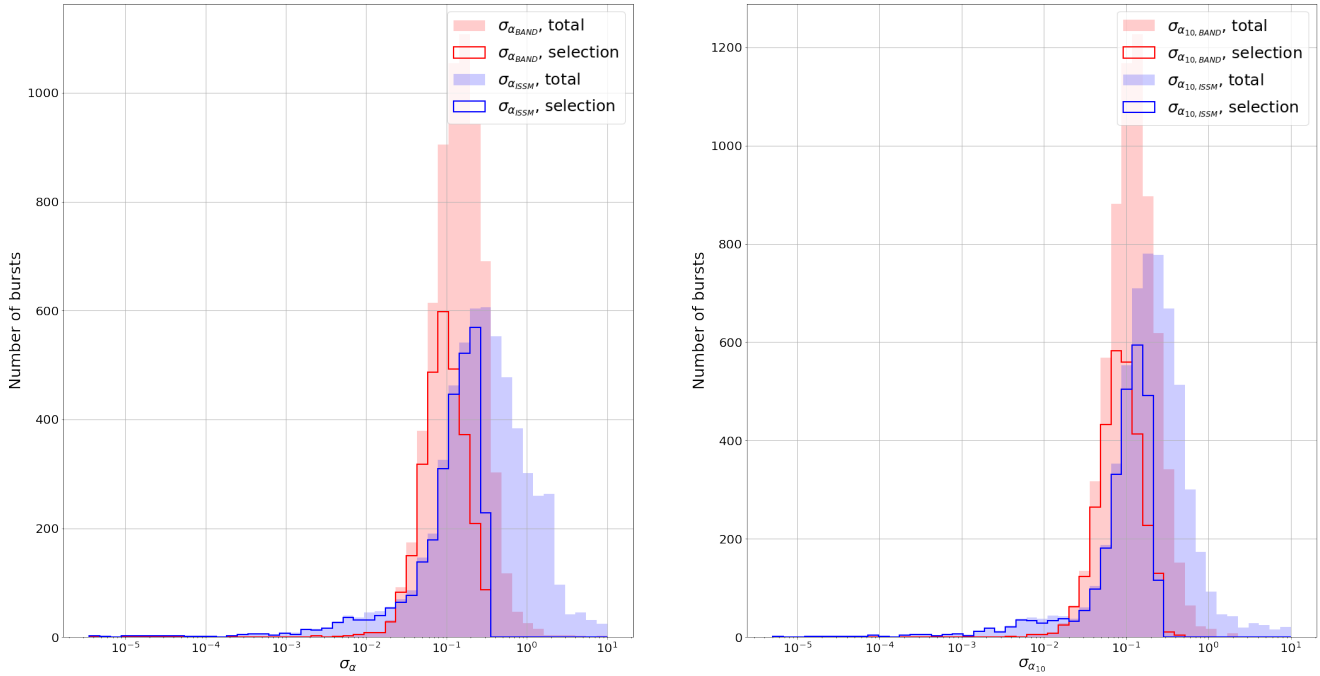

Figure 3.39: Distribution of the error on α (left) and α_{10} (right) for Band and ISSM before and after the selection cut $\sigma_\alpha < 0.3$ (time-resolved spectral analysis).

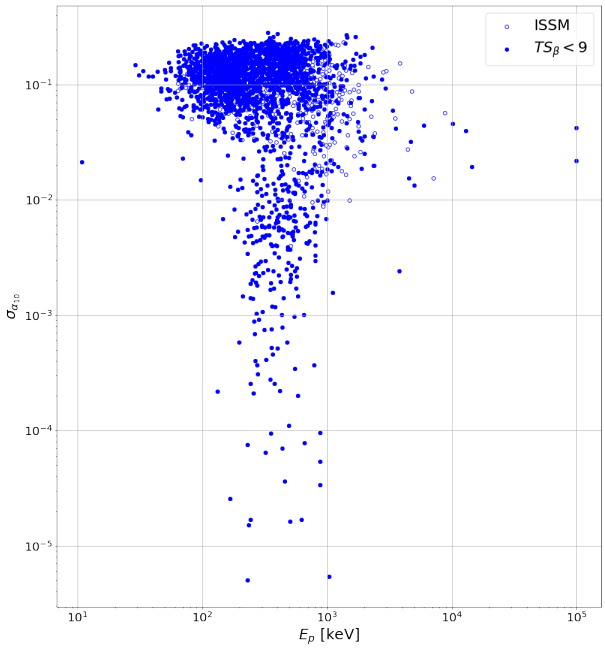

Figure 3.40: Error on $\alpha_{10,ISSM}$ as a function of $E_{p,ISSM}$ for the sample of spectra with $\sigma_\alpha < 0.3$ (time-resolved spectral analysis). The filled circles correspond to the spectra that are best fitted by a COMP model ($TS_\beta < 9$). Their fit can reach very small errors for moderate values of the peak energy.

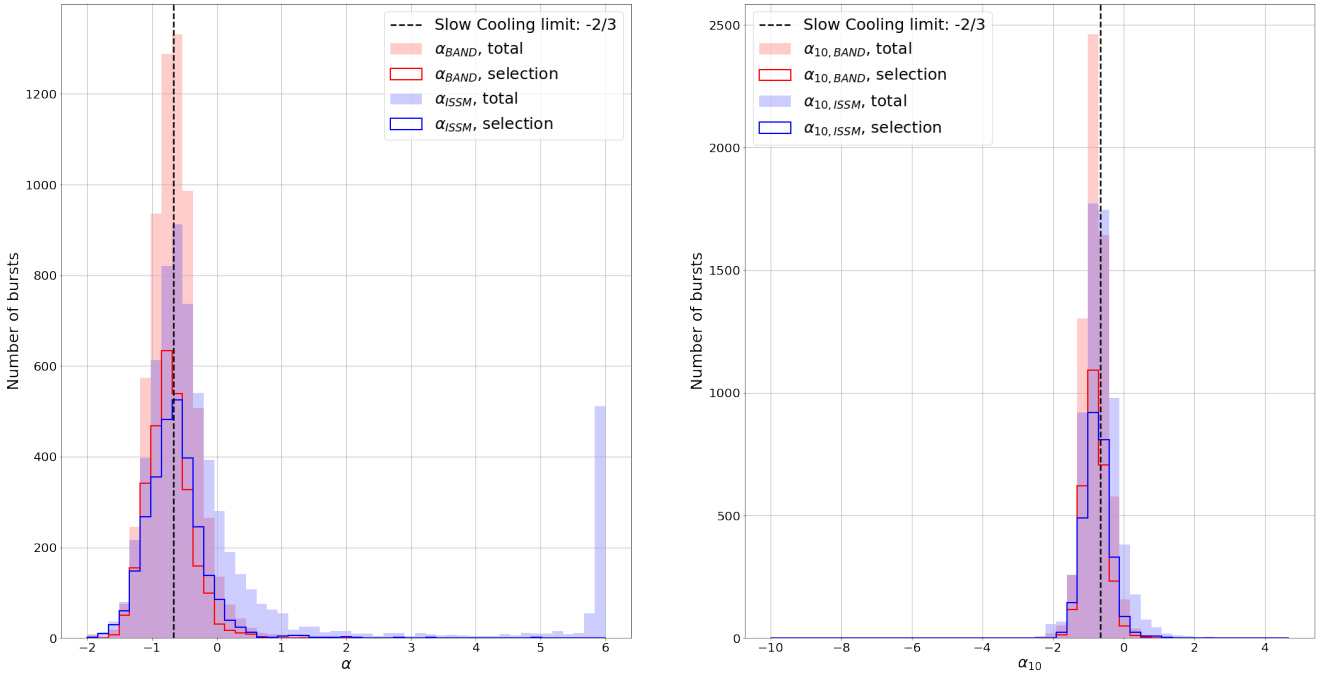

Figure 3.41: Distribution of α (left) and α_{10} (right) for Band and ISSM before and after the selection $\sigma_\alpha < 0.3$ (time-resolved spectral analysis).

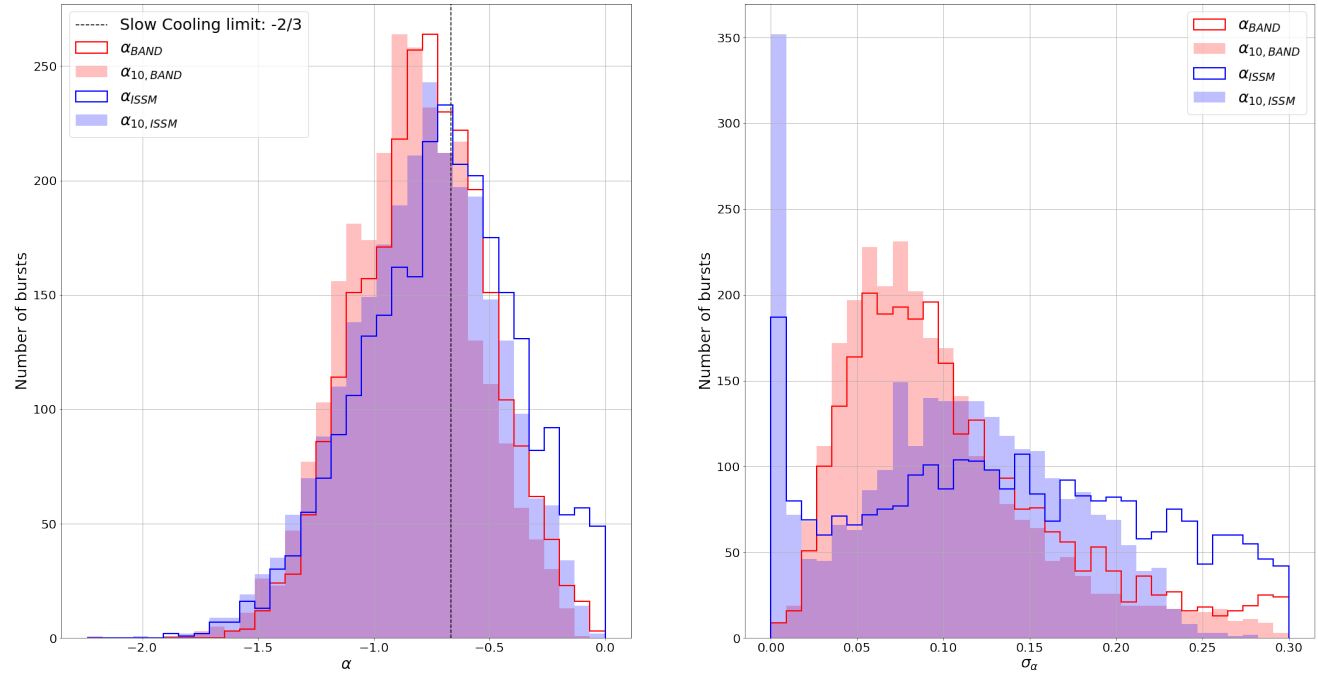

Figure 3.42: Distribution of the low-energy index and of its error for the sample of spectra with $\sigma_\alpha < 0.3$ (time-resolved spectral analysis).

	α_{Band}	$\alpha_{10,Band}$	α_{ISSM}	$\alpha_{10,ISSM}$
Fast-cooling limit: $-3/2$				
Bursts with $TS_\beta > 9$	99%	99%	96%	98%
Bursts with $\sigma_\alpha < 0.3$	95%	94%	92%	92%
Marginally fast-cooling limit: -1				
Bursts with $TS_\beta > 9$	83%	78%	78%	78%
Bursts with $\sigma_\alpha < 0.3$	52%	47%	53%	51%
Slow-cooling limit: $-2/3$				
Bursts with $TS_\beta > 9$	19%	12%	31%	23%
Bursts with $\sigma_\alpha < 0.3$	14%	11%	20%	17%

Table 3.9: Probability of the low-energy index to be above the fast-cooling, marginally fast-cooling, slow-cooling limits at more than 2σ for the sample with $TS_\beta > 9$, and $\sigma_\alpha < 0.3$ (time-integrated spectral analysis). The error on each probability is the order of unity or less: it is more accurate than a few percents of the corresponding error in the time-integrated analysis because of the greater number of fits.

presents a tail extending to very low values, similarly to the time-integrated analysis. Those extremely low errors corresponds to the blocks whose spectra are better fitted by COMP and have moderate/high $E_{p,ISSM}$ values. As shown in Figure 3.40, the tiny errors on α at moderate/high $E_{p,ISSM}$ belong to the spectra that are better fitted by COMP than ISSM ($TS_\beta < 9$). Figure 3.41 shows the distribution of α and α_{10} before and after the selection cut. The selection reduces the tails of the extremely hard α and α_{10}. 167 (6%) fits yield an $\alpha_{ISSM} > 0$. More than half of them (99) have a low/medium $SNR < 100$, and the half of the remaining 68 spectra peak at relatively low energies below $E_{p,ISSM} = 200$ keV. In 1 case $\alpha_{10,ISSM}$ is smaller than -2 (-7.11 ± 0.01): the block belongs to GRB 150127398, its fit quality is poor ($PG\text{-}stat/\mathrm{dof} = 3926/474$) and it has a low $SNR = 25$. In 8 blocks the error on $\alpha_{10,Band}$ is greater than 0.3. In those cases the spectrum peaks below 30 keV. I exclude the mentioned outliers from the following discussion. Figure 3.42 shows the distributions of the low-energy indices and of their errors after the selection cut and excluding the outliers previously discussed. The distribution of the error on α_{ISSM} and $\alpha_{10,ISSM}$ peaks at low values, a significant fraction of those cases belong to the spectra with a $TS_\beta < 9$, as explained above.

Table 3.9 presents the probability at which the low-energy index exceeds the fast-cooling, marginally fast-cooling, and slow-cooling values with a confidence level greater than 2σ. The majority of blocks present a low-energy index greater than the fast-cooling value of $-3/2$. Remarkably the probability of the low-energy index to be above the slow-cooling limit $-2/3$ is relatively low especially for the sample with $\sigma_\alpha < 0.3$, yet nearly twice higher than in the time-integrated analysis (see Table 3.4). **As a result, the low-energy index α_{10} is softer in more than 83% of the cases than the slow-cooling value of $-2/3$ within 2σ errors**. The arithmetic mean and the sample standard deviation of the low-energy indices are presented in Table 3.10. Their mean values are harder than in the time-integrated analysis (see Table 3.4) because of the spectral superposition effect discussed in § 3.3.4.

3.3.6 Well characterized spectra

I considered the spectra whose indices are well measured as for the time-integrated analysis. I required $TS_\beta > 9$ and $\sigma_\alpha < 0.3$. This resulted into a sample of 372 well characterized spectra. The left panel of Figure 3.43 shows $E_{p,ISSM}$ as a function of the corresponding $E_{p,Band}$. The median value of $E_{p,ISSM}/E_{p,Band}$ is 1.26 which is consistent with the value of 1.30 for the sample $TS_\beta > 9$, and also with the values of the time-integrated analysis. The right panel of the figure shows the regions of α and β for Band and ISSM for the well-characterized spectra of the time-resolved analysis. Like in the time-integrated analysis, one can notice the larger spread of the ISSM indices, especially for the high-energy slope β. As discussed in § 3.2.5, this likely results from the higher flexibility of the ISSM function with respect to the frozen spectral shape of the Band function at high energies. Also visible is the lack of soft spectra with the ISSM model, which did not pass the $TS_\beta > 9$ cut (see § 3.2.5).

Table 3.10 presents the mean and the sample standard deviation of the low-energy and high-energy index

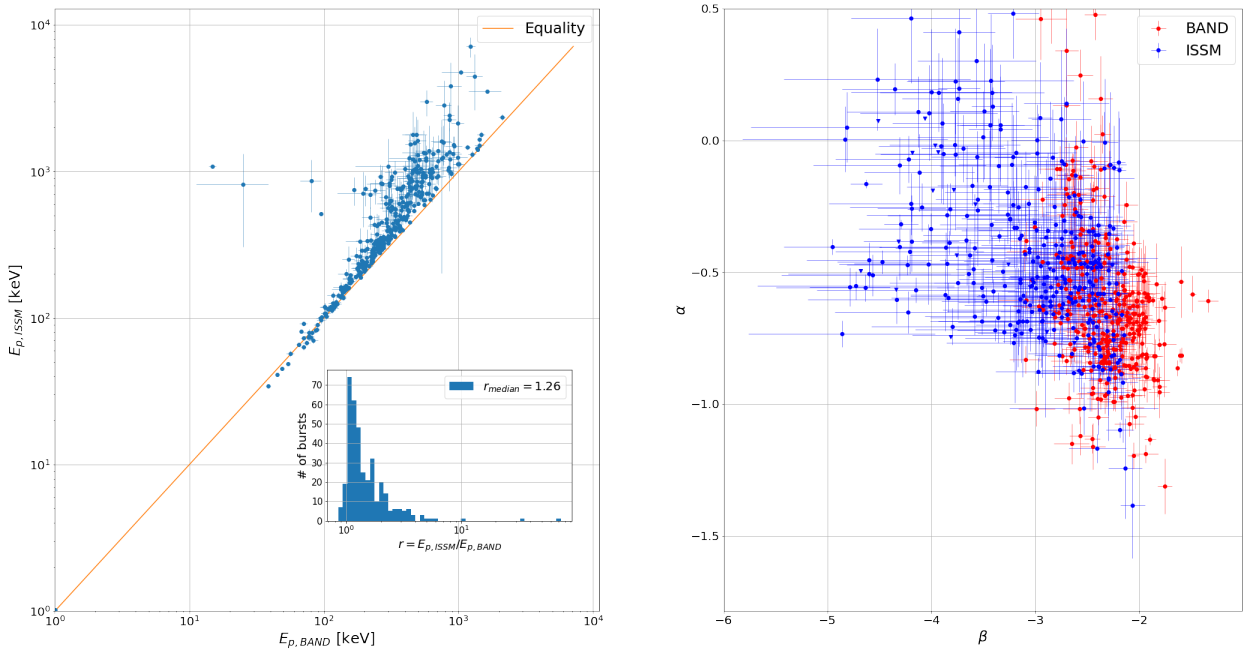

Figure 3.43: Left: $E_{p,ISSM}$ as a function of $E_{p,Band}$ for the well characterized spectra sample (time-resolved spectral analysis). The median value of the $E_{p,ISSM}/E_{p,Band}$ is 1.26. Right: α as a function of β for Band and ISSM. When the error on β is greater than 1, the value is marked with a triangle.

	Band			ISSM			
	α	α_{10}	β	α	α_{10}	β	β_b
$TS_\beta > 9$	-0.69 ± 0.19	-0.75 ± 0.19	-2.40 ± 0.26	-0.46 ± 0.25	-0.60 ± 0.22	-3.18 ± 0.67	-2.06 ± 0.22
$\sigma_\alpha < 0.3$	-0.78 ± 0.28	-0.85 ± 0.28	-2.41 ± 0.41	-0.71 ± 0.33	-0.80 ± 0.32	-3.45 ± 0.76	-2.08 ± 0.34
Both	-0.69 ± 0.19	-0.74 ± 0.19	-2.28 ± 0.29	-0.50 ± 0.24	-0.61 ± 0.21	-3.00 ± 0.65	-1.95 ± 0.25

Table 3.10: Arithmetic mean and sample standard deviation of the low-energy and high-energy spectral indices of Band and ISSM for the three time block samples considered in the time-resolved spectral analysis. These samples have been obtained with the cut $TS_\beta > 9$, $\sigma_\alpha < 0.3$, and both cuts, respectively.

of Band and ISSM for the three considered samples: the set of spectra with $TS_\beta > 9$ cut, $\sigma_\alpha < 0.3$ cut, and the sample with both cuts applied at the same time. As for the time-integrated analysis there is a general agreement for the low-energy and high-energy parameters of Band across the three samples. Moreover the low-energy index α of ISSM is slightly harder when the cut $TS_\beta > 9$ is applied. As for the time-integrated analysis this is due to the high positive correlation between α and β for ISSM: when β is better constrained with higher values, also α is higher.

In conclusion the peak energy of ISSM is on average greater than the peak energy of Band also for the sample of time-resolved spectra, with a relative error on $E_{p,ISSM}$ greater than $E_{p,Band}$. As for the time-integrated analysis the continuous curvature of ISSM opens a greater parameter space for $E_{p,ISSM}$ than $E_{p,Band}$, and this greater freedom translates into a greater uncertainty on the parameter. The mean value of $\beta_{b,ISSM}$ is again very close to -2, which implies that the ISSM time-resolved SED often peaks at the break energy of the Band model. The consequences of the higher $E_{p,ISSM}$ and its relative error on the Amati/Yonetoku relations should be investigated in the future. Similarly to the time-integrated analysis, the low-energy index of ISSM is harder than the low-energy index of Band, and the high-energy index of ISSM is softer than the high-energy index of Band. Again one expects this because of the continuous curvature of the ISSM model. The mean values of the low-energy index and of the high-energy index are respectively harder and softer in this analysis than in the time-integrated spectral analysis, for both models. As explained before, this is caused by the superposition of different spectra when averaging over the duration of the burst. This tends to flatten and to widen the time-averaged SED around its peak energy, and to smoothen its spectral

slopes (softening of the low-energy index and hardening of the high-energy index).

Chapter 4

Photospheric emission in *Fermi* GRB prompt spectra

4.1 Introduction

The study conducted in the previous chapter showed that synchrotron radiation can explain the bulk of the prompt keV-MeV emission of most GRBs. Additional physical processes occur in GRB jets as discussed in § 1, in particular a quasi-thermal emission is expected during the prompt phase in the standard fireball model. The most extreme case is GRB 090902B, whose spectrum likely consists of a single dominant thermal component, which suffices to describe the entire prompt keV-MeV emission [Abdo et al. 2009a]. Moreover, a thermal sub-dominant component has been found in addition to the main non-thermal component in GRB 100724B, GRB 120323A, and GRB 131014A (Guiriec et al. 2011, Guiriec et al. 2013, Guiriec et al. 2015a, respectively). The presence of an additional thermal component has implications on the spectral features of the non-thermal component. In the case of GRB 100724B Guiriec et al. 2011 found that the low-energy index and the high-energy index of the Band spectrum are smaller (softer) when a black-body component is added. If multi-component spectral models turn out to be necessary for other bursts, then the violation of the synchrotron line of death (see § 1.3.2) would be less severe, which would reinforce the synchrotron interpretation of the main bulk component of the GRB spectra. Therefore, assessing the presence and the significance of an additional thermal component is of paramount importance. However, the analyses performed so far assumed that the non thermal component of the GRB spectra is described by the phenomenological Band function, which is purely a mathematical tool and does not rely on physical grounds. The analysis of the GRB spectra with a realistic synchrotron model is indeed a prerequisite before looking for any deviation from this dominant non thermal component.

In this chapter I revisit the spectral analysis of the three GRBs 100724B, 120323A, and 131014A. Firstly I test my analysis procedure by recovering the results published in the literature. Secondly I perform the spectral data preparation following the same procedure I adopted in § 3, and I perform a time-integrated and time-resolved spectral analyses by fitting Band, ISSM, with and without an additional thermal component modeled as a black body. Finally I test and discuss whether the additional thermal component is still statistically required when adopting the ISSM physical model to fit the non-thermal component of the three GRB spectra.

4.2 Observations

GRB 100724B triggered the GBM on 2010 July 24 at T_0 = 00:42:05.992 UT [Bhat 2010], and it was detected at high energies also by the LAT [Tanaka et al. 2010]. The burst was bright enough to prompt an Autonomous Repoint Request (ARR) to maintain its localization within the LAT field of view. The most precise localization of the burst was given by the Inter-Planetary Network (IPN) at R.A. = 118.8°, decl. = 75.8° [Guiriec et al. 2011]. GRB 100724B is a long GRB with a T_{90} = 112 s in the 50-300 keV energy band. Figure 4.1 shows the GBM light curves in three energy bands ranging from 8 keV to 40 MeV. The light

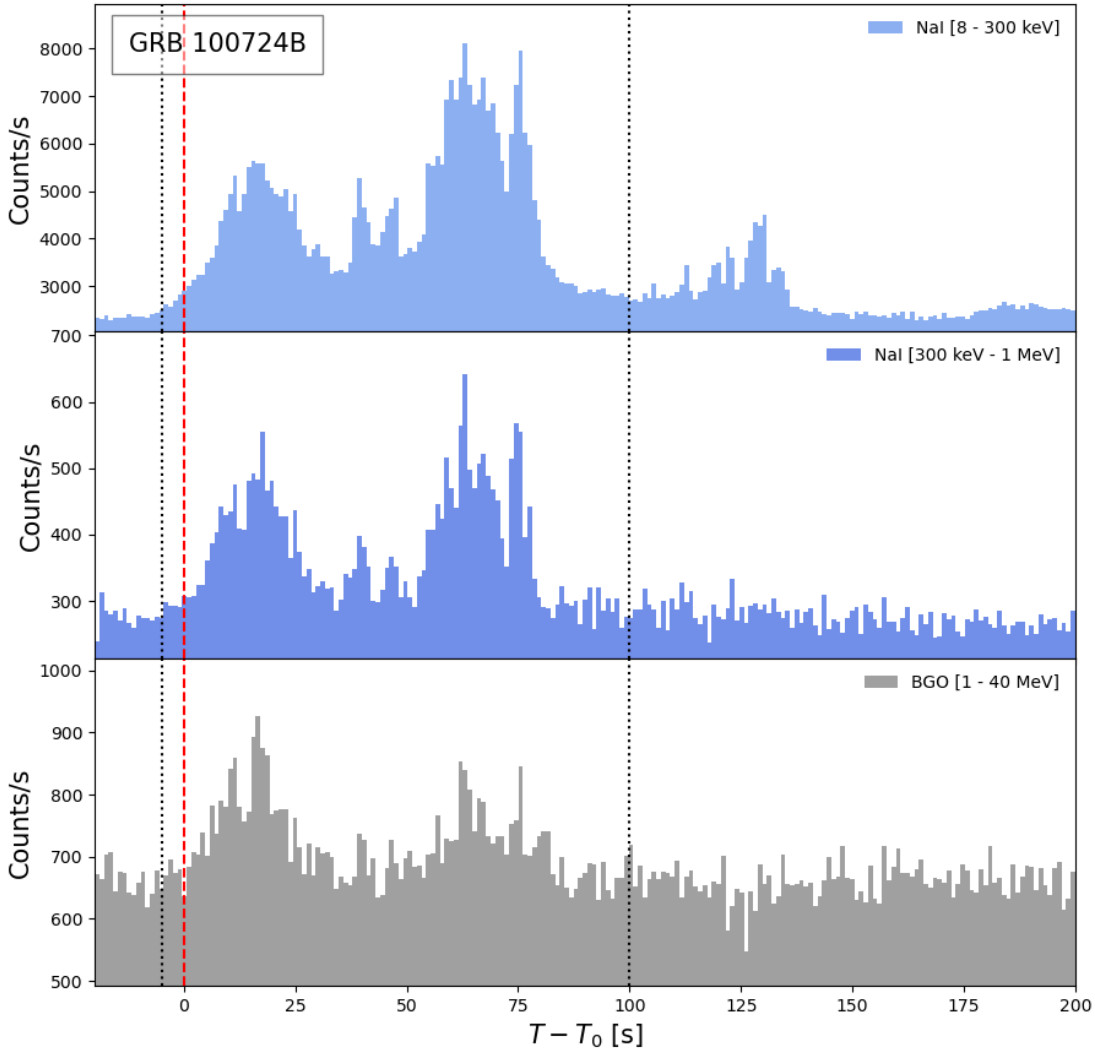

Figure 4.1: Composite light curve of GRB 100724B as seen by the NaIs 0, 1, 5 and the BGO 0.

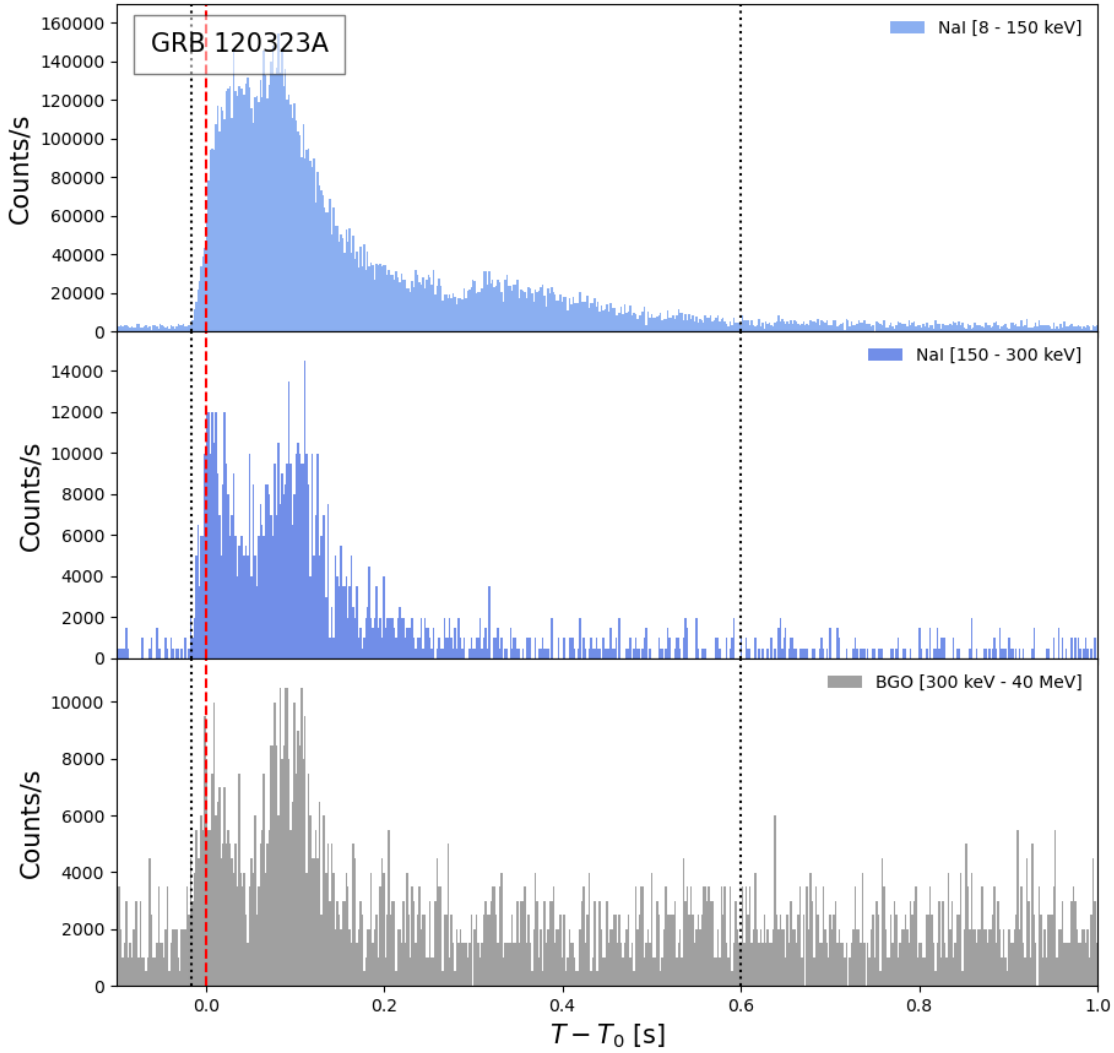

Figure 4.2: Composite light curve of GRB 120323A as seen by the NaIs 0, 3, 4 and the BGO 0.

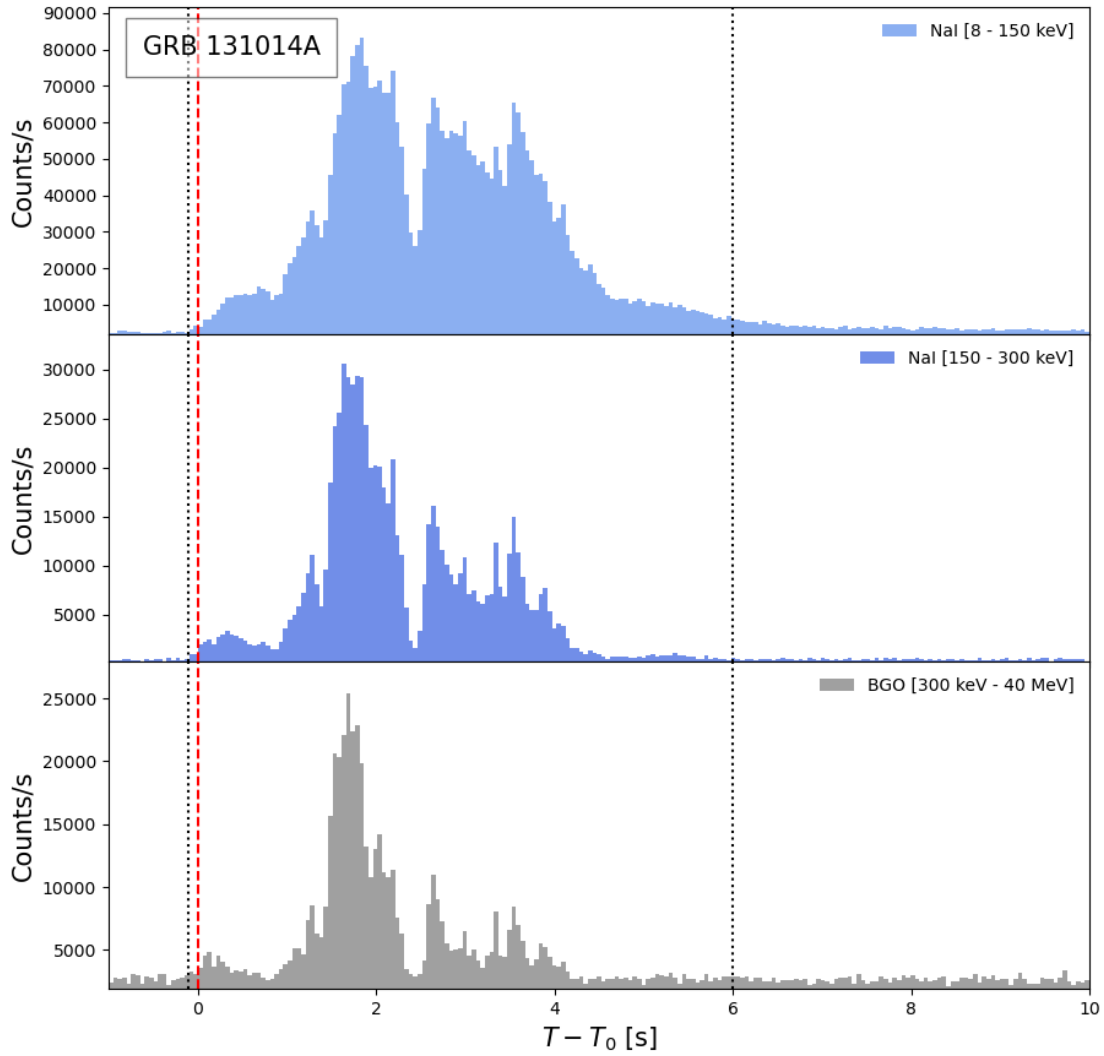

Figure 4.3: Composite light curve of GRB 131014A as seen by the NaIs 9, a, b and the BGO 1.

curves present multiple episodes in each energy band. This burst presents a remarkable spectral evolution at $T_0 + 125$ s, where gamma-ray emission is observed in the 8-300 keV energy band, and not at higher energies. The analysis performed by Guiriec et al. 2011 identifies an additional thermal component with a temperature $kT = 38 \pm 1$ keV in the main emission episode between $T_0 - 1.024$ s and $T_0 + 83.969$ s.

GRB 120323A triggered the GBM on 2012 March 23 at T_0 = 12:10:19.72 s UT [Gruber et al. 2012]. It is a short burst with a $T_{90} = 0.45$ s between 50 and 300 keV. GRB 120323A was bright enough to trigger an ARR but it was not detected at high-energy by the LAT in the standard data neither with the LAT Low-Energy data cut [Pelassa et al. 2010]. The best localization of the event was provided by IPN at R.A. = 340.4°, decl. = 29.7° [Golenetskii et al. 2012]. Figure 4.2 presents the light curves of the bursts in different GBM energy ranges. It appears an initial double peaked structure which is visible from the low energies 8-150 keV up to higher energies 300 keV-40 MeV. The analysis performed by Guiriec et al. 2013 reports the detection of an additional thermal component with a temperature $kT = 11 \pm 1$ keV in the time interval between $T_0 - 0.016$ s and $T_0 + 0.548$ s.

GRB 131014A was detected by the GBM on 2013 October 14 at T_0 = 05:09:00 s UT [Fitzpatrick et al. 2013]. It is a long burst with a moderate duration $T_{90} = 3.2$ s from 50 to 300 keV. The burst was hard and bright enough to trigger an ARR and to be detected by the LAT at high energies [Desiante et al. 2013]. The highest energy photon was detected 15 s after the GBM trigger at 1.8 GeV. The best localization of the burst was given by the Swift-XRT at R.A. = 100.303°, decl. = -19.097° [Evans et al. 2013]. Figure 4.3 shows the light curves of the bursts in three different energy bands. A multi-episode emission is seen by both NaIs and the BGO detectors. The analysis performed by Guiriec et al. 2015a reports the detection of an additional thermal component with an initial temperature $kT \sim 100$ keV. The temperature decreases in the first second, increases at $T_0 + 1.6$ s, and then cools down until the end of the burst emission.

In all the presented light curves the vertical dashed black lines delimit the on-source intervals that I chose for the analysis.

4.3 Comparison with literature results

I tested the accuracy of my spectral analysis procedure by recovering the spectral results presented in Guiriec et al. 2011, Guiriec et al. 2013, and Guiriec et al. 2015a. I selected the same detectors and chose the same on-source intervals. Since the off-source intervals were not defined in the references I manually chose them. Moreover, in the references the fit statistic is the *Castor* C-stat, which is implemented in *XSPEC* as *C-stat* (see Appendix § A). I recall that *C-stat* is not recommended in the case of a background estimated prior to the spectral fit, while *PG-stat* is the adequate fit statistic. However, for the purpose of comparing my results with the literature I used *C-stat* in this section. For GRBs 100724B and 120323A I considered the time-integrated data. For GRB 131014A the time-integrated analysis is not available in Guiriec et al. 2015a, thus I chose one of the brightest time bins (41th, $T_0 + [1.80, 1.82]$ s, see Figure 4.3) of the fine time-resolved analysis of the reference. Table 4.1, Table 4.2, and Table 4.3 compare my results with the reference ones. In all cases the results are in agreement. I conclude that my spectral analysis procedure is accurate enough and then I will adopt it for the following discussion.

4.4 Time-integrated spectral analysis

Similarly to the previous chapter (see § 3.1), I selected the spectral data as follows: a maximum of 3 NaIs detectors are chosen with a good background fit and with the highest *SNR*. I performed a spectral analysis integrated for the duration of each burst. I manually defined the duration as long enough to contain as much signal as possible and short enough to exclude background contamination. The on source intervals are:

- GRB 100724B: $T_0 + [-5, 100]$ s. It corresponds to the main emission episode of the burst. I excluded the following episode because the resulting time-integrated spectrum could not be adequately fitted by any models due to the strong spectral evolution of the burst.

	Band		Band+BB	
GRB 100724B	This analysis	Literature	This analysis	Literature
C-stat/dof	1099/704	1133/704	1055/702	1038/702
α	-0.69 ± 0.01	-0.67 ± 0.01	-0.85 ± 0.03	-0.90 ± 0.02
β	-1.98 ± 0.02	-1.99 ± 0.01	-2.08 ± 0.04	-2.11 ± 0.02
E_p (keV)	370 ± 8	352 ± 6	570^{+37}_{-55}	615 ± 29
Band norm (10^{-2})	4.1 ± 0.1	-	2.9 ± 0.1	-
kT (keV)	-	-	35^{+2}_{-1}	38 ± 1
Th norm	-	-	1.65 ± 0.20	-
$TS_{BB}(\sigma)$	-	-	44 (6.3)	95 (>8)

Table 4.1: Comparison of my results with the time-integrated analysis of Guiriec et al. 2011 on GRB 100724B. The results are in excellent agreement, and the additional thermal component is statistically required in both cases at $kT \sim 35$ keV. The units of the normalizations are $cm^{-2}s^{-1}keV^{-1}$.

	Band		Band+BB	
GRB 120323A	This analysis	Literature	This analysis	Literature
C-stat/dof	488/470	600/470	441/468	568/468
α	-0.96 ± 0.05	-0.92 ± 0.07	-1.42 ± 0.04	$-1.44^{+0.05}_{-0.07}$
β	-2.09 ± 0.02	-2.06 ± 0.02	-7.8^{+9}_{-7}	< -2.36
E_p (keV)	74^{+6}_{-4}	71 ± 5	255 ± 22	263^{80}_{-44}
Band norm (10^{-2})	1.2 ± 0.4	-	0.35 ± 0.02	-
kT (keV)	-	-	11 ± 2	11 ± 1
Th norm	-	-	23 ± 2	-
$TS_{BB}(\sigma)$	-	-	47 (6.5)	32 (5.3)

Table 4.2: Comparison of my results with the time-integrated analysis of Guiriec et al. 2013 on GRB 120323A. The results are in excellent agreement, and the additional thermal component is statistically required in both cases at $kT \sim 11$ keV. The units of the normalizations are $cm^{-2}s^{-1}keV^{-1}$.

	Band		Band+BB	
GRB 131014A	This analysis	Literature	This analysis	Literature
C-stat/dof	390/450	431/443	379/448	423/441
α	-0.01 ± 0.09	-0.01 ± 0.08	-0.31 ± 0.11	-0.43 ± 0.10
β	-2.88 ± 0.30	-2.41 ± 0.12	< -10	-2.93 ± 0.35
E_p (keV)	490 ± 36	485 ± 33	805 ± 110	982 ± 163
Band norm (10^{-2})	1.9 ± 0.1	-	0.94 ± 0.15	-
kT (keV)	-	-	65.5 ± 0.3	65.2 ± 6.7
Th norm	-	-	439 ± 132	-
$TS_{BB}(\sigma)$	-	-	11 (2.9)	8 (2.4)

Table 4.3: Comparison with Guiriec et al. 2015a on GRB 131014A. I considered the results on the bright 41th time bin of the time-resolved analysis because no results for the time-integrated analysis are reported in the article. The two analyses are in excellent agreement, and the additional thermal component is marginally required at $kT \sim 65$ keV. The units of the normalizations are $cm^{-2}s^{-1}keV^{-1}$.

- GRB 120323A: $T_0 + [-0.016, 0.6]$ s.
- GRB 131014A: $T_0 + [-0.1, 6.0]$ s.

Their boundaries are highlighted as black dashed lines in Figure 4.1, Figure 4.2, and Figure 4.3. I fitted each spectrum with the following four models: Band, ISSM, Band+black body (BB), ISSM+BB. I compared the performance of Band and ISSM, and I computed the significance of the additional thermal component in terms of Gaussian standard deviations corresponding to the test statistic $TS_{BB} = PG_{NT} - PG_{NT+BB}$ which behaves as a χ^2 with 2 degrees of freedom (in the large sample limit). As in the analyses presented in § 3 I used the *PG-stat* fit statistic. As shown in Figure 3.9, a minimum burst $SNR \sim 200$ is necessary to distinguish between Band and ISSM. Indeed, this condition is satisfied for the three considered bursts: GRBs 100724B has a $SNR = 491$, 120323A has a $SNR = 599$, and 131014A has a $SNR = 1637$. Therefore the signal statistics is high enough to compare the performance of the Band and ISSM models.

Table 4.4 presents the results for the time-integrated analysis of **GRB 100724B**. All the four fits are of acceptable quality (reduced *PG-stat* < 3). However, the reduced *PG-stat* values are somehow greater than the reduced *C-stat* values obtained when comparing with literature. This could be explained by a different background estimation, or by a stronger spectral evolution in the time-integrated GRB window used here, or by the different nature of the two fit statistics. Since the large sample limit is not fully reached (especially in the high-energy channels where the number of counts is the smallest), one should be cautious when using the reduced fit statistics as goodness of fits as they might not be χ^2 behaved. Nonetheless, both statistics are based on log-likelihood expressions and can be used relatively safely for hypothesis testing to look for an additional BB component, as discussed in the following. When I use *C-stat* I obtain *C-stat*/dof = 802/474 for Band and *C-stat*/dof = 780/472 for Band+BB, with a thermal component at kT $= 31 \pm 3$ keV detected with a significance of 4.3σ (vs. 5.5σ using *PG-stat*); I obtain *C-stat*/dof = 771/474 for ISSM and *C-stat*/dof = 761/472 for ISSM+BB, with a thermal component at kT $= 47 \pm 6$ keV not required by the data (0 vs. 3.0σ using *PG-stat*). In the analysis based on *PG-stat*, ISSM yields a fit statistic smaller than Band ($\Delta PGstat$ =54) and Band+BB ($\Delta PGstat$ =20). **The additional thermal component is significant when the non thermal component is Band ($\sigma_{\mathbf{BB}} = 5.5$), while it is less significant in the case of ISSM ($\sigma_{\mathbf{BB}} = 3.0$). This likely results from the continuously curved shape of ISSM, which accounts for the low-energy excess that the Band fit attributes to the BB component**. When the thermal component is significant it accounts for part of the flux at low energies and the non thermal component peaks at higher energies with a slightly softer α. The low-energy index of ISSM is harder than Band, its high-energy index is softer, and its peak energy is greater. This is consistent with the results presented in § 3. The lower two panels of Figure 4.4 show the spectral energy distribution (SED) for Band+BB (lower left panel) and ISSM+BB (lower right panel). The contribution of BB to the SED is greater for Band+BB than ISSM+BB. **I conclude that the thermal component is detected also in my time integrated spectral analysis, but with a lower significance when the non thermal component is ISSM**.

Table 4.5 presents the spectral results of the time-integrated analysis of **GRB 120323A**. All four fits are of excellent quality (reduced *PG-stat* < 1.2). ISSM is preferred over Band ($\Delta PGstat = 22$), while the composite models are equivalently good. **The additional thermal component is detected at kT $\sim$ 10 keV and it is more significant in the case of Band+BB ($\sigma_{\mathbf{BB}} = 5.9$) than ISSM+BB ($\sigma_{\mathbf{BB}} = 4.4$)**. Again, the ISSM curved shape accounts for at least part of the low-energy excess that the Band fit attributes to the BB component. Like for the previous GRB 100724B, the low-energy index softens and the peak energy increases when the BB component is added to the fit model. One expects that the thermal component contributes partially to the spectrum flux at low energies, and consequently the non thermal component peaks at higher energies. **More interestingly, the value of α decreases from -0.40 ± 0.27, which is harder than the slow-cooling value of $-2/3$, to -1.35 ± 0.05, which is compatible with the expected value in the fast-cooling regime**. Figure 4.5 shows the residuals and the SEDs for Band+BB and ISSM+BB. In both cases the contribution from the BB component is significant.

Table 4.6 presents the results of the time-integrated analysis of **GRB 131014A**. The quality of all four fits is acceptable (reduced *PG-stat* < 3). However, the reduced *PG-stat* values are somehow greater than

the reduced *C-stat* values obtained when comparing with the literature, like in the case of GRB 100724B. When I use *C-stat*, I obtain *C-stat*/dof = 1081/474 for Band and Cstat/dof = 906/472 for Band+BB, with a thermal component detected at kT = 32 ± 1 keV with a significance larger than σ; I obtain *C-stat*/dof = 855/474 for ISSM and *C-stat*/dof = 855/472, with a thermal component at kT = 37 ± 8 keV not required by the data. The BB is significantly detected at kT = 35 keV with a confidence level greater than 8σ when the non thermal component is Band, while it is not detected when the non thermal component is ISSM. In the analysis based on *PG-stat*, ISSM is preferred over both Band and Band+BB ($PG_{Band} - PG_{ISSM} = 281, PG_{Band+BB} - PG_{ISSM} = 59$, respectively), and it is as good as ISSM+BB. For this burst, the ISSM curved shape accounts for the entire low-energy excess that the Band fit attributes to the BB component. Figure 4.6 shows the residuals and SEDs for Band+BB and ISSM+BB. The residual are comparable between the two models. The contribution of BB to ISSM+BB is negligible, whereas it is more visible in Band+BB. **I conclude that the additional thermal component is not required by the time-integrated spectrum of GRB 131014A when the non thermal component is ISSM**. The usual remarks when comparing Band and ISSM are valid: in the case of ISSM the low-energy index is harder, the high-energy index is softer, and the peak energy is greater.

The additional thermal component is statistically required for each burst when the non thermal component is Band. The thermal component is still detected in the time-integrated spectra of GRBs 100724B and 120323A when using the ISSM physical model to fit their non-thermal component. However in this case the additional thermal component is less significant and becomes marginal ($<5\sigma$). In the case of GRB 131014A, the significance drops to zero.

4.5 Time-resolved spectral analysis

I determined the temporal segmentation of each burst light curve following the same procedure presented in § 3.3.2. In particular I applied the Bayesian blocks algorithm with a false alarm probability $p_0 = 0.01$ on the light curve summed over the NaI detectors in the energy range 10-300 keV. Similarly, I selected the time bins with a $SNR > 5$. As a matter of fact the *SNR* in most of time bins is greater than the threshold value of 20 that I considered in the previous chapter (to ensure that the signal is high enough to constrain the model spectral parameters) since the bursts considered here are particularly bright and fluent. Figure 4.7 shows the *SNR* distribution in each time bin of the three bursts. The vertical dashed lines correspond to the *SNR* threshold value of 200 above which Band and ISSM can be distinguished, as shown in Figure 3.9. The majority of time bins of GRB 131014A have a *SNR* close or greater than 200, while only a null and smaller fraction of time bins of GRBs 100724B and 120323A respectively satisfy this condition.

I performed a time-resolved spectral analysis for each burst fitting the four models Band, Band+BB, ISSM, and ISSM+BB. I compared Band+BB and ISSM+BB with Band and ISSM respectively, and I considered the additional thermal component marginally and firmly detected when it is required with a confidence level greater than 3σ and 5σ respectively. Since the composite models have 2 more parameters, these significances translate in $TS_{BB} > 11.8$ and 28.7. It should be noted that a 3σ excess should not be considered as a firm detection given the possible systematic effects arising from the background estimation (whose temporal evolution might not exactly behave like a polynomial function of time) or from the mis-calibration of the detector. In particular, the response of the GBM accounts for the scattering of photons on the Earth atmosphere, which indirectly increases the effective area. As noted by Palit et al. 2021, not accounting for this effect or underestimating it can generate count excesses in the $30 - 300$ keV energy range (see Figure 4.8). Such a low-energy excess can then be mis-interpreted as an additional thermal component, or enhances it artificially if it already exists. For these reasons, a 5σ threshold is highly recommanded to claim for a firm detection.

For each burst I present two figures. The first one shows the $\Delta PGstat$ between Band and ISSM, Band and Band+BB, ISSM and ISSM+BB, Band+BB and ISSM+BB over the temporal evolution of the burst. In this first figure it is possible to discerne the time bins where the BB significance exceeds 3σ (red horizontal line), and it is possible to compare the fit performance of the various model combinations. The second figure shows the temporal variation of the spectral parameters of Band+BB and ISSM+BB, respectively. Those

GRB 100724B	Band	Band+BB	ISSM	ISSM+BB
PG-stat/dof	1284/474	1250/472	1230/474	1218/472
$TS_{BB}(\sigma)$	-	34 (5.5)	-	12 (3.0)
α	-0.74 ± 0.01	-0.84 ± 0.02	-0.56 ± 0.02	-0.62 ± 0.02
β	-1.98 ± 0.02	-2.05 ± 0.03	-2.30 ± 0.03	-2.27 ± 0.02
E_p (keV)	388 ± 9	522 ± 37	966 ± 41	1109 ± 46
nTh norm (10^{-2})	3.39 ± 0.05	2.71 ± 0.13	0.230 ± 0.002	0.224 ± 0.002
kT (keV)	-	30 ± 2	-	49 ± 5
Th norm	-	0.88 ± 0.21	-	0.64 ± 0.16

Table 4.4: Time-integrated analysis of GRB 100724B. The units of the normalizations are $cm^{-2}s^{-1}keV^{-1}$.

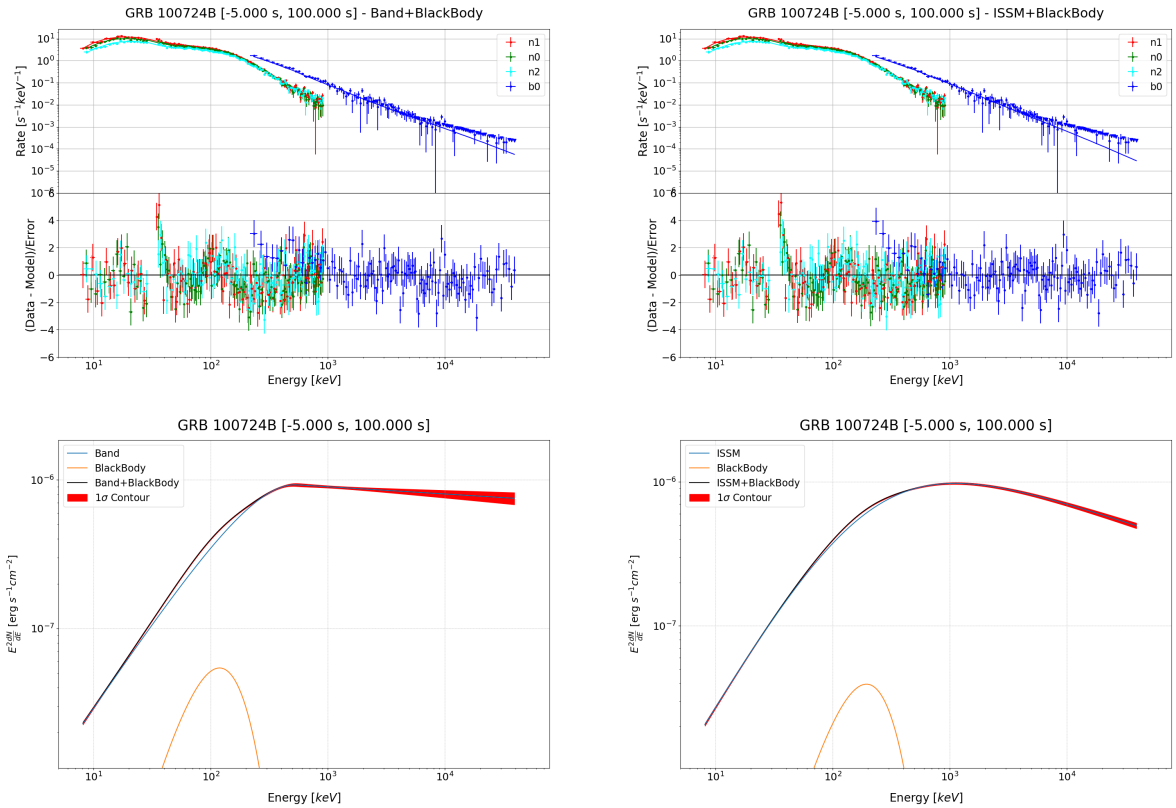

Figure 4.4: GRB 100724B: residuals and SEDs for Band+BB and ISSM+BB. The contribution of the BB is minor in the case of ISSM+BB.

GRB 120323A	Band	Band+BB	ISSM	ISSM+BB
PG-stat/dof	571/474	532/472	549/474	526/472
$TS_{BB}(\sigma)$	-	39 (5.9)	-	23 (4.4)
α	-1.04 ± 0.06	-1.45 ± 0.03	-0.40 ± 0.27	-1.35 ± 0.05
β	-2.06 ± 0.02	-2.64 ± 0.25	-2.27 ± 0.04	-3.00 ± 0.47
E_p (keV)	79 ± 6	269 ± 28	132 ± 7	236 ± 20
nTh norm (10^{-2})	95 ± 12	32 ± 2	1.02 ± 0.03	1.09 ± 0.03
kT (keV)	-	11 ± 1	-	10 ± 1
Th norm	-	20 ± 2	-	17 ± 2

Table 4.5: Time-integrated analysis of GRB 120323A. The units of the normalizations are $cm^{-2}s^{-1}keV^{-1}$.

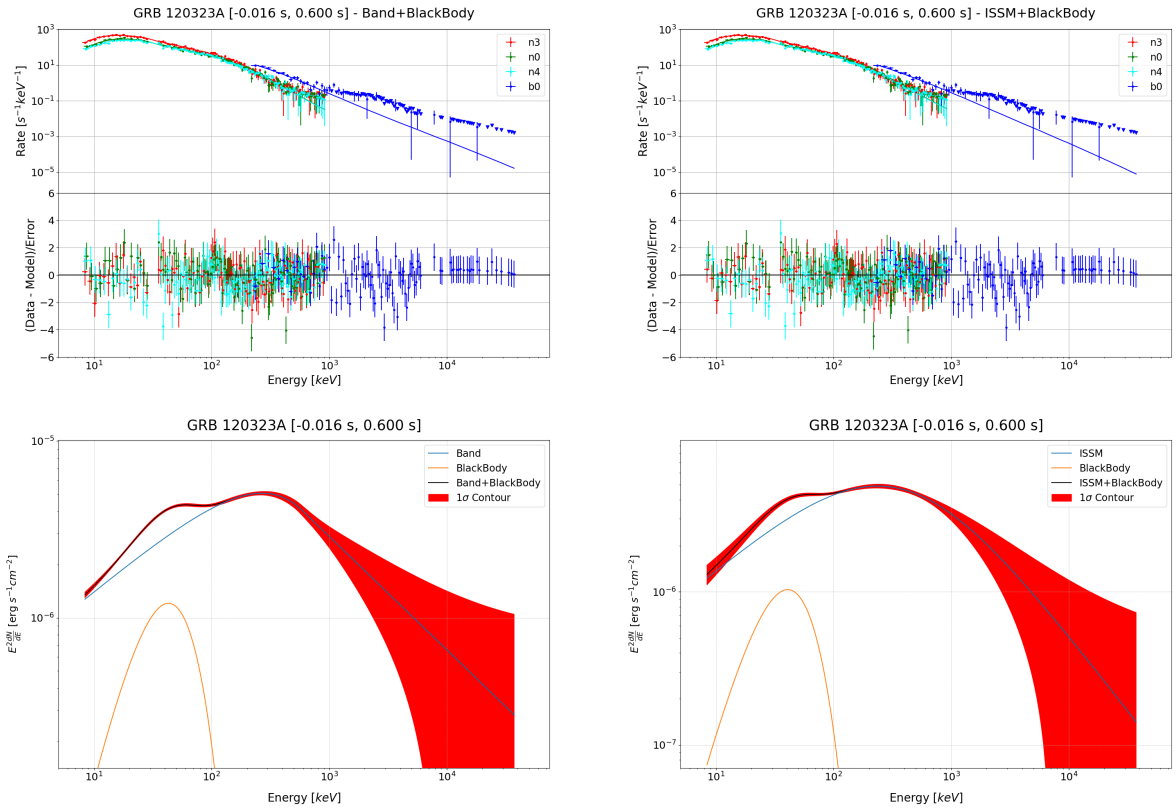

Figure 4.5: GRB 120323A: residuals and SEDs for Band+BB and ISSM+BB. The contribution of the BB is significant in both cases.

GRB 131014A	Band	Band+BB	ISSM	ISSM+BB
PG-stat/dof	1278/474	1056/472	997/474	998/472
$TS_{BB}(\sigma)$	-	222 (>8)	-	-1 (0)
α	-0.37 ± 0.01	-0.49 ± 0.01	-0.17 ± 0.02	-0.20 ± 0.06
β	-2.58 ± 0.02	-2.90 ± 0.05	-3.85 ± 0.10	-3.91 ± 0.27
E_p (keV)	322 ± 2	412 ± 8	371 ± 3	378 ± 10
nTh norm (10^{-2})	69.7 ± 0.4	49.7 ± 1.3	3.44 ± 0.02	3.45 ± 0.03
kT (keV)	-	32 ± 1	-	35 ± 9
Th norm	-	25.4 ± 2.2	-	2.7 ± 3.4

Table 4.6: Time-integrated analysis of GRB 131014A. The units of the normalizations are $cm^{-2}s^{-1}keV^{-1}$.

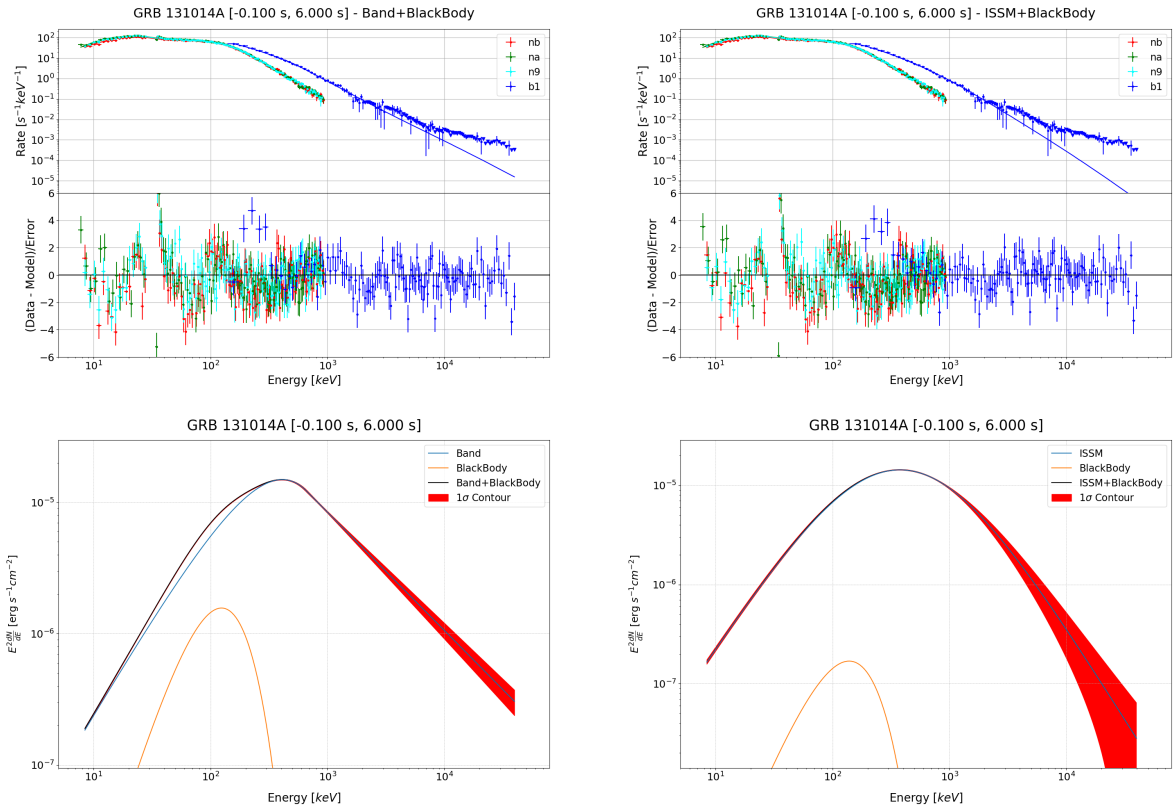

Figure 4.6: GRB 131014A: residuals and SEDs for Band+BB and ISSM+BB. The contribution of the BB is negligible in the case of ISSM+BB.

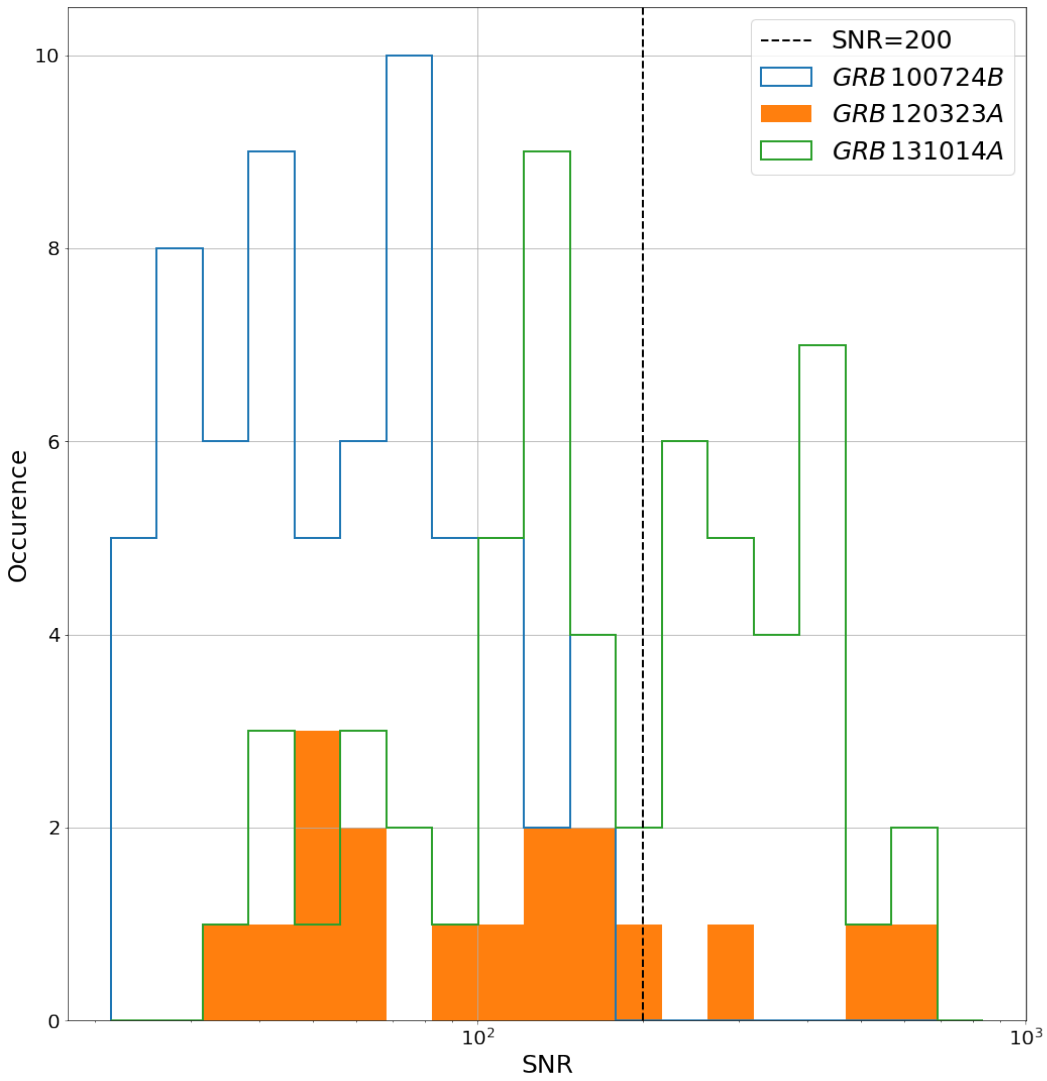

Figure 4.7: Distribution of *SNR* in the time-resolved analysis of GRBs 100724B, 120323A, and 131014A.

parameters are the low-energy index, the peak energy of the non thermal component, and the temperature kT of the additional thermal component. The latter parameter is shown only when BB is at least marginally detected with a confidence greater than 3σ. The peak energy of the non thermal component is superimposed to the burst light curve, and the time bins with a $SNR > 20$ are highlighted with dashed lines. Table 4.7 collects the spectral results for each time bin where the thermal component is at least marginally detected, when the non thermal component is either Band or ISSM. The table presents the fit statistic obtained by the fit of each model, the significance of the additional thermal component, and its temperature.

In the following discussion I claim for a BB detection only if the following criterion is fulfilled : I require the *PG-stat* of the NT+BB fit (where NT stands for the non-thermal component, resp. Band or ISSM) where $\sigma_{BB} > 5$ is found, to be also smaller (decrease greater than the 3 or 5σ thresholds of 11.8 or 28.7 for marginal or significant detections) than the alternative single NT component fit (resp. ISSM only or Band only). Otherwise, one should prefer the best of the latter two fits as it has 2 parameters less, or the two-component model based on the alternative NT component if it further improves the results. For example, if BB is detected in Band+BB with a *PG-stat* greater than ISSM, then this BB detection would be spurious, since ISSM fits better both of Band and Band+BB. Similarly, if BB is detected in ISSM+BB with a *PG-stat* greater than Band, then this BB detection would be spurious too, since Band fits better both of ISSM and ISSM+BB. **In other words, the BB component must be searched only as an additional component to the single NT component fit (Band only or ISSM only) that has the lowest PGstat, since it best reproduces the bulk of the emission.** This condition prevents a spurious

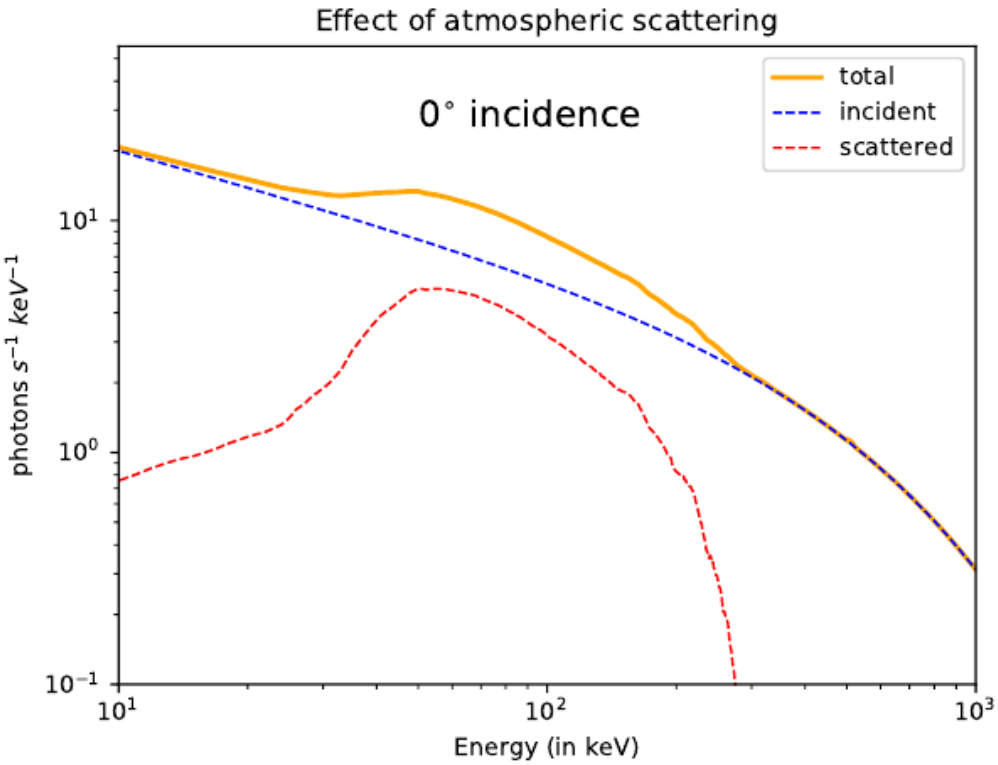

Figure 4.8: Simulations of reflected spectra for a short GRB with Band parameters $\alpha = -0.5$, $\beta = -2.25$, and $E_p = 800$ keV, which is incident at 0° and detected directly. The dashed red line shows the scattered spectrum. The solid orange line denotes the net spectrum incident on the detector. Credit Palit et al. 2021.

BB detection in the following situations:

- Case S1 (spurious BB detection when fitting ISSM+BB): a BB significance $\sigma_{BB,ISSM} > 3$ (5) is found, but the ISSM-only fit is (much) worse than the Band-only fit. This BB detection is considered spurious, as it results from a bad model choice for the non thermal component rather than from the addition of the BB component to it. In addition, the ISSM+BB fit is not better than the Band or Band+BB fits. Therefore, the best of the latter must be preferred.
- Case S2 (spurious BB detection when fitting Band+BB): a BB significance $\sigma_{BB,Band} > 3$ (5) is found, but the Band-only fit is (much) worse than the ISSM-only fit. This BB detection is considered spurious, as it results from a bad model choice for the non thermal component rather than from the addition of the BB component to it. In addition, the Band+BB fit is not better than the ISSM or ISSM+BB fits. Therefore, the best of the latter must be preferred.

This second case corresponds to the situation previously discussed, where the natural curvature of the ISSM function absorbs (part of) the fake low-energy excess that results from a bad description of the non-thermal component by the Band model. **The BB detections found with the Band+BB model in the time-integrated analyses presented in section § 4.4 are artefacts, while the BB detections with the ISSM+BB model are marginal for GRBs 100724B and 120323A, and null for GRB 131014A**.

Figure 4.9 shows the temporal evolution of $\Delta PGstat$ between Band and ISSM, Band and Band+BB, ISSM and ISSM+BB, and Band+BB and ISSM+BB for **GRB 100724B**. The time bin spectra are equivalently or better fitted by Band with respect to ISSM (1st panel): $PG_{Band} - PG_{ISSM} < 10$ always. The thermal component is not detected in Band+BB (2nd panel), except for the time bin centered at $T_0 + 108.7$ s, whose significance reaches almost 3σ. On the other hand the thermal component is demanded in 3 time bins for ISSM+BB (3rd panel): these time bins are 15, 36, and 55 and are centered at $T_0 + 26.2, 64.3, 108.7$ s. However, σ_{BB} is greater than 5 only for the first of these time bins. All of these three time bins correspond to spurious detections of type S1, where Band is preferred over ISSM ($\Delta PGstat = -60.2$, -8.9, and -13.5

respectively). In the latter time bin 55 the BB component accounts completely for the observed emission and no non-thermal component is required by the fit as indicated by the shift of $E_{p,ISSM}$ to an unrealistic value of ~ 100 MeV, which is the maximum value allowed in the fit. Moreover, ISSM fit is of poorer quality than Band ($\Delta PGstat \leq 10$), especially for the time bin centered at $T_0+26.2$ s (see also Table 4.7). Band+BB and ISSM+BB are equivalently good (4th panel and Table 4.7). **I conclude that the thermal component is not strongly required in the time-resolved analysis of GRB 100724B**. Figure 4.10 presents the temporal evolution of the spectral parameters of Band+BB (upper panel) and ISSM+BB (lower panel). In both cases the temporal evolution of the peak energy follows the evolution of the light curve. The values of the low-energy index are hard and they are equally distributed around -0.5 for the temporal evolution of the burst.

Figure 4.11 shows the $\Delta PGstat$ between Band and ISSM, Band and Band+BB, ISSM and ISSM+BB, Band+BB and ISSM+BB as a function of the time for **GRB 120323A**. Over the temporal evolution of the burst Band and ISSM fits the data equally well (1st panel): in 10 time bins $|\Delta PGstat| < 10$, in 2 time bins $\Delta PGstat < -10$, and in 4 time bins $\Delta PGstat > 10$. The time bins 5 and 6 correspond to spurious detections of type S1, where Band is preferred over ISSM ($\Delta PGstat = -12.3, -12.4$ respectively). **The time bin 7 is a solid detection. The ISSM model is more appropriate than the Band function to describe the non-thermal emission ($\Delta PGstat = 25.2$). Adding the BB component improves clearly upon the ISSM-only fit with a significance $\sigma_{BB,ISSM} = 6.1$. The additional thermal component has a temperature kT $= 8.5 \pm 0.3$ keV and a peak energy $E_{p,BB} = 33.3 \pm 1.2$ keV**. The 4 fits of this time bin are shown in Figure 4.12. Surprisingly, adding the BB component moves the non-thermal peak energy to lower values (625 keV to 552 keV) and hardens the low-energy index from a value typical of the fast-cooling regime (-1.48 ± 0.05) to a value typical of the marginally fast-cooling regime (-0.95 ± 0.09). The $SNR = 300$ of this time bin is well above the threshold ~ 200 for a good spectroscopic precision in order to distinguish between Band and ISSM, and also to discerne the presence of the detected additional thermal component. The time bins 8, 16 correspond to spurious detections of type S2, where ISSM is preferred over Band. Time bin 10 is a spurious marginal detection of type S2. Figure 4.13 presents the temporal evolution of the spectral parameters of Band+BB (upper panel) and ISSM+BB (lower panel).

Figure 4.14 shows the $\Delta PGstat$ between Band and ISSM, Band and Band+BB, ISSM and ISSM+BB, Band+BB and ISSM+BB as a function of the time for **GRB 131014A**. ISSM is preferred over Band (1st panel, $\Delta PGstat > 10$) in 13 time bins; Band is preferred over ISSM ($\Delta PGstat < -10$) in 1 time bin; no preferred model ($|\Delta PGstat| < 10$) is found in the remaining 45 time bins. Time bin 16 corresponds to a spurious detection of type S1, where Band is preferred over ISSM ($\Delta PGstat = 156$). Time bins 7, 17, 18, 19, 20, 22, 33, 37, 38, 45, 55 correspond to spurious detections of type S2, where ISSM is preferred over Band. Specifically in time bins 17, 18, and 19 the BB detection on top of the non-thermal emission fitted by Band is artificial due to very bad Band fits. The ISSM model is preferred since it is alone able to reproduce the spectra. Figure 4.15 presents the temporal evolution of the spectral parameters of Band+BB (upper panel) and ISSM+BB (lower panel).

Table 4.7 presents all the time bins where the additional thermal component is required at more than 3σ for either Band or ISSM. When the non thermal component is Band, $\sigma_{BB} > 3$ in 14 time bins, 3 of which belong to GRB 120323A, and 11 to GRB 131014A, but all of them are are either spurious detections (case S2) or unrealistic (bins 17 to 19) as discussed above. When the non thermal component is ISSM, $\sigma_{BB} > 3$ in 7 time bins: 3 belong to GRB 100724B, 3 to GRB 120323A, and only 1 to GRB 131014A, but they are all spurious detections (case S1) as discussed above, except for one time bin in GRB 120323A (shown in red in Table 4.7). For the three bursts considered an additional thermal component is required two times more when the non thermal component is Band with respect to ISSM, but the former are all spurious detections. In this S2 case, the continuously curved shape of ISSM fully accounts for the fake low-energy excess that results from a bad description of the non-thermal component by the Band model.

To conclude, in the time-integrated analysis I found that the detections of an additional thermal component for GRBs 100724B and 120323A are marginal detections. These detections are of type S2, where the synchrotron ISSM model is preferred over the ad-hoc phenomenological Band function. The additional

Bin	$T-T_0$ [s]	*SNR*	PG_B	PG_{B+BB}	σ_{BB}	kT [keV]	PG_I	PG_{I+BB}	σ_{BB}	kT [keV]	Case
GRB 100427B											
15	26.2	49	525.4	525.3	0.1	3.1 ± 2.2	585.6	526.4	7.4	3.5 ± 1.1	S1
36	64.3	119	496.4	488.8	2.3	8.9 ± 0.9	505.3	492.5	3.1	8.5 ± 0.7	S1
55	108.7	32	700.8	689.2	2.96	27.5 ± 2.8	714.3	689.0	4.7	26.9 ± 2.9	S1
GRB 120323A											
5	0.04	574	429.7	426.6	1.2	10.7 ± 0.8	442.0	423.1	3.9	13.3 ± 1.0	S1
6	0.08	500	522.5	522.4	0.1	8.7 ± 0.5	534.9	517.3	3.8	8.9 ± 0.5	S1
7	0.11	300	456.3	456.5	0	7.3 ± 0.9	431.0	389.1	**6.1**	8.5 ± 0.3	Detection
8	0.12	204	417.5	374.5	6.2	6.1 ± 4.6	384.4	385.1	0	98.3 ± 27.9	S2
10	0.15	159	458.0	442.2	3.6	5.3 ± 2.6	444.2	440.2	1.5	5.7 ± 1.1	S2
16	0.42	55	445.6	403.8	6.1	7.8 ± 5.8	404.2	414.0	0	5.0 ± 0.8	S2
GRB 131014A											
7	1.05	135	466.8	452.5	3.4	25.6 ± 3.6	456.4	452.1	1.6	23.3 ± 3.2	S2
16	1.59	382	431.6	422.5	2.6	53.1 ± 9.2	587.5	424.7	>8	8.8 ± 2.0	S1
17	1.67	667	6856.4	1271.8	>8	112.2 ± 1.5	491.1	482.6	2.5	8.4 ± 2.0	S2
18	1.79	836	9200.0	556.8	>8	50.9 ± 3.9	565.5	558.5	2.2	2.7 ± 1.0	S2
19	1.89	414	3185.6	472.0	>8	4996 ± 2	471.7	471.6	2.2	12 ± 11	S2
20	2.00	680	512.3	493.4	3.9	40.3 ± 4.5	499.7	499.7	0	46 ± 571	S2
22	2.18	446	517.0	499.6	3.8	29.0 ± 4.4	505.4	501.0	1.6	24.2 ± 5.9	S2
33	2.64	498	488.9	438.2	6.8	35.8 ± 2.3	444.7	444.7	0	31.2 ± 1.9	S2
37	3.07	298	523.0	499.4	4.5	19.0 ± 2.3	503.5	497.8	1.9	12.7 ± 2.1	S2
38	3.21	410	543.4	531.0	3.1	13.3 ± 1.7	532.7	524.0	2.5	10.1 ± 0.9	S2
45	3.71	291	513.5	500.7	3.2	14.7 ± 3.2	501.5	498.1	1.3	11.4 ± 2.2	S2
55	5.26	92	530.2	516.4	3.3	8.0 ± 1.4	523.1	517.2	1.9	7.7 ± 0.8	S2

Table 4.7: Resume of the time bins where BB is detected at more than 3σ when the non thermal component is Band or ISSM. Legend: $T-T_0$ is evaluated at the center of the time bin; B stands for Band, I for ISSM, and BB for black body; "Type" specifies the type of detection: S1 stands for a spurious detection when Band is preferred over ISSM; S2 stands for a spurious detection when ISSM is preferred over Band. The green color denotes the *PG-stat* of the preferred NT component. The red line corresponds to a firm BB detection.

BB is found with a statistical significance of 3σ at a temperature $kT = 49 \pm 5$ keV and at a peak energy of $E_{p,BB} = 192 \pm 20$ keV for GRB 100724B. BB is found with a statistical significance of 4.4σ at a temperature $kT = 10 \pm 1$ keV and an energy peak $E_{p,BB} = 39.2 \pm 3.9$ keV for GRB 120323A. The softening of the low-energy index is significant, from a hard value of -0.40 to a value of -1.35 which is compatible with its expected value in the fast-cooling regime. On the other hand no thermal component is detected in GRB 131014A. A systematic search for an additional thermal component over the sample defined in the previous chapter § 3 might result into other detections. However, I have shown in Table 3.4 of the previous chapter that such possibility, if real, could be limited to the small number of bursts with a low-energy index that is harder than the $-2/3$ slow-cooling value. **Such an analysis should fit the non-thermal component with the ISSM physical model rather than the Band phenomenological function to avoid the frequent BB detections caused by the limited flexibility of the Band spectral shape**.

In the time-resolved analysis each time BB is detected along with the Band model as non thermal component, the ISSM model is preferred. In this spurious detection of type S2 ISSM absorbs the fake low-energy excess. Similarly, each time the BB component is detected along with the ISSM model as non thermal component, the Band model is preferred, which corresponds to a spurious detection of type S1, except in time bin 7 of GRB 120323A. In this case the ISSM+BB model clearly outperforms all of the other models and the thermal component is firmly detected at $kT = 8.5 \pm 0.3$ keV and $E_{p,BB} = 33.3 \pm 1.2$ keV with a statistical sig-

nificance of 6.1σ. The fact that I find only only one firm detection of the BB component while it is marginally detected in the time-integrated analyses of GRBs 100724B and 120323A may be due to the insufficient *SNR* in the time-resolved analysis of these two bursts as shown in Figure 4.7. Especially for GRB 100724B the *SNR* in the time-resolved analysis is always smaller than the threshold 200 necessary to distinguish among the Band and ISSM models. For the case of GRB 131014A the *SNR* is greater than 200 in 28 (50%) time bins over a total of 57 time bins. For each spurious detection of type S2 for this GRB the *SNR* is greater than 200, except for time bin 55. When the signal is high enough to distinguish between Band and ISSM, and an additional BB component is at least marginally detected on top of Band, ISSM is preferred and no additional BB component is firmly detected. **This strengthens the conclusion that a physical synchrotron model such as ISSM is able to satisfactory describe GRB prompt emission spectra in most cases**.

In the same spirit of the conclusions drawn by Guiriec et al. 2011, the marginal detections of the additional thermal component in the time-integrated spectra of GRBs 100724B and 120323A, and the firm detection in time bin 7 of GRB 120323A, suggest that not all the energy budget of the burst jet is transported by Poynting flux, but at least a part of it is carried by thermal flux (see § 1.3.3). In the future, grouping the blocks together should improve the sensitivity of the spectral analysis to the photospheric emission that is expected in this scenario. For instance, a pulse-resolved spectral analysis should be envisaged at least for the GRB light curves whose pulses can be separated and don't overlap too much, and a systematic search for a firm BB detection should be performed in such a pulse-resolved analysis, which should be extended to the 460 bursts selected in the previous chapter.

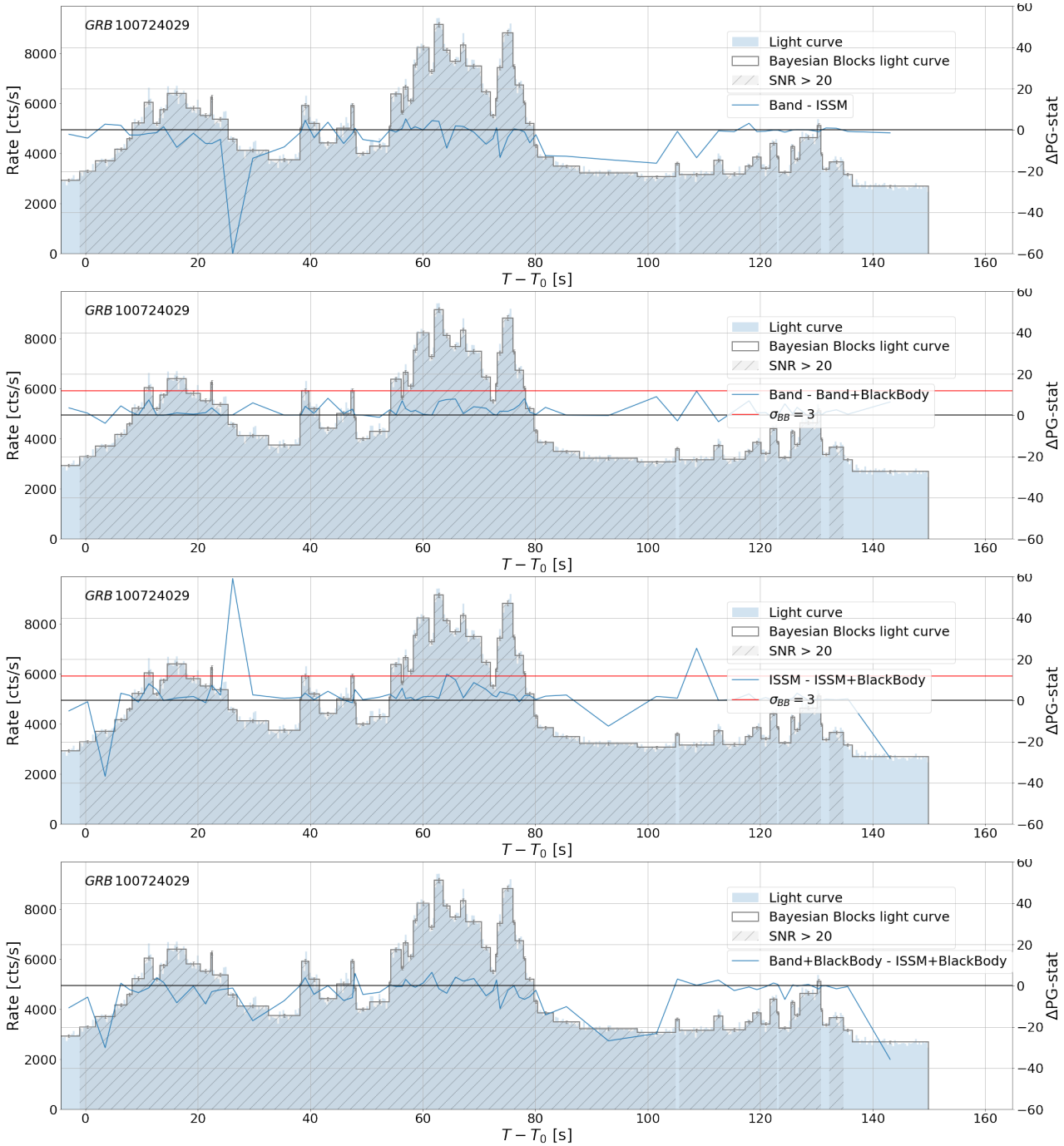

Figure 4.9: **GRB 100724B**: difference of *PG-stat* between Band and ISSM (1st panel), Band and Band+BB (2nd panel), ISSM and ISSM+BB (3rd panel), and Band+BB and ISSM+BB (4th panel).

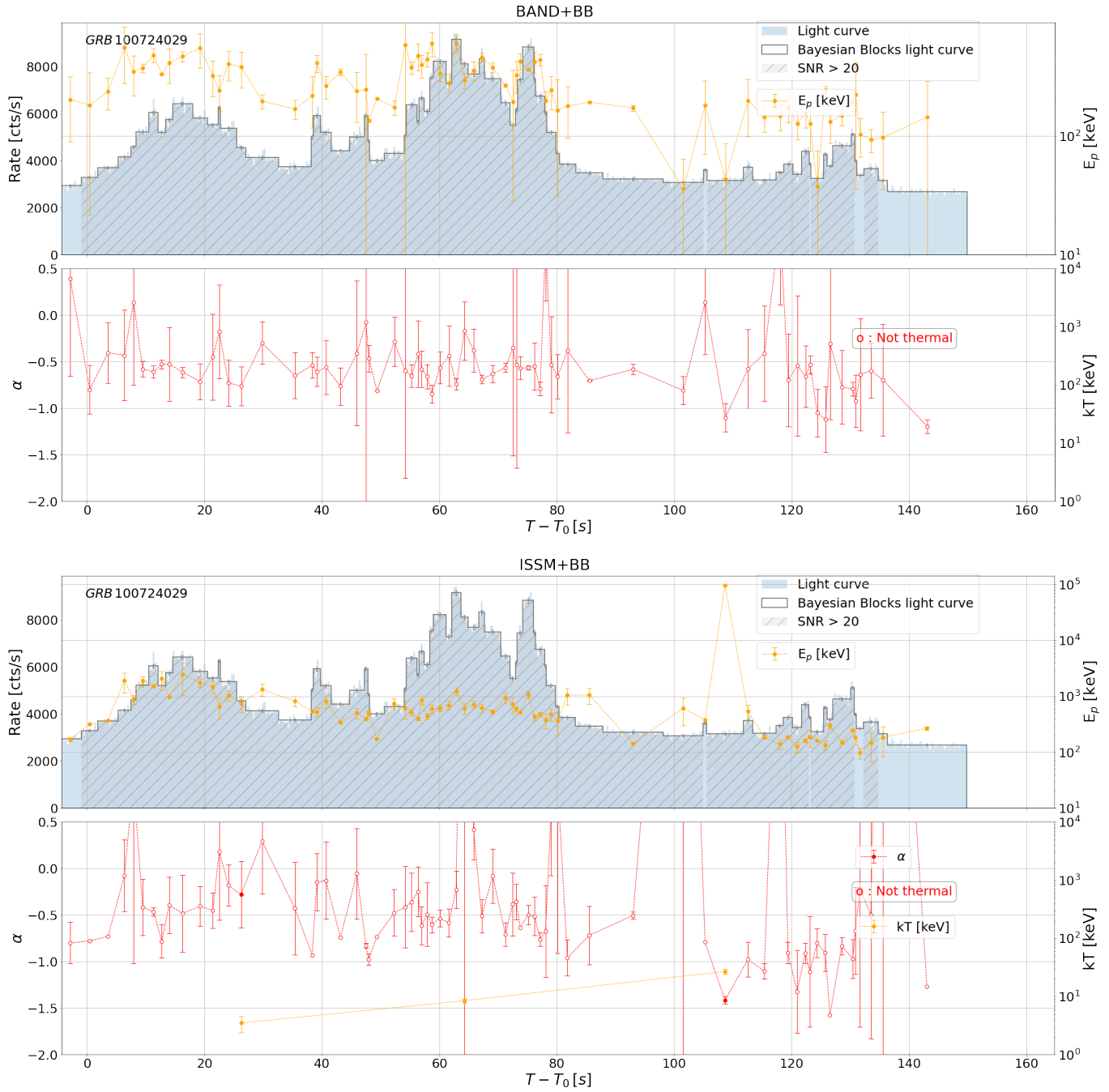

Figure 4.10: **GRB 100724B**: temporal evolution of Band+BB (upper panel) and ISSM+BB (lower panel) spectral parameters. The temperature kT is shown only when the thermal component is detected at more than 3σ.

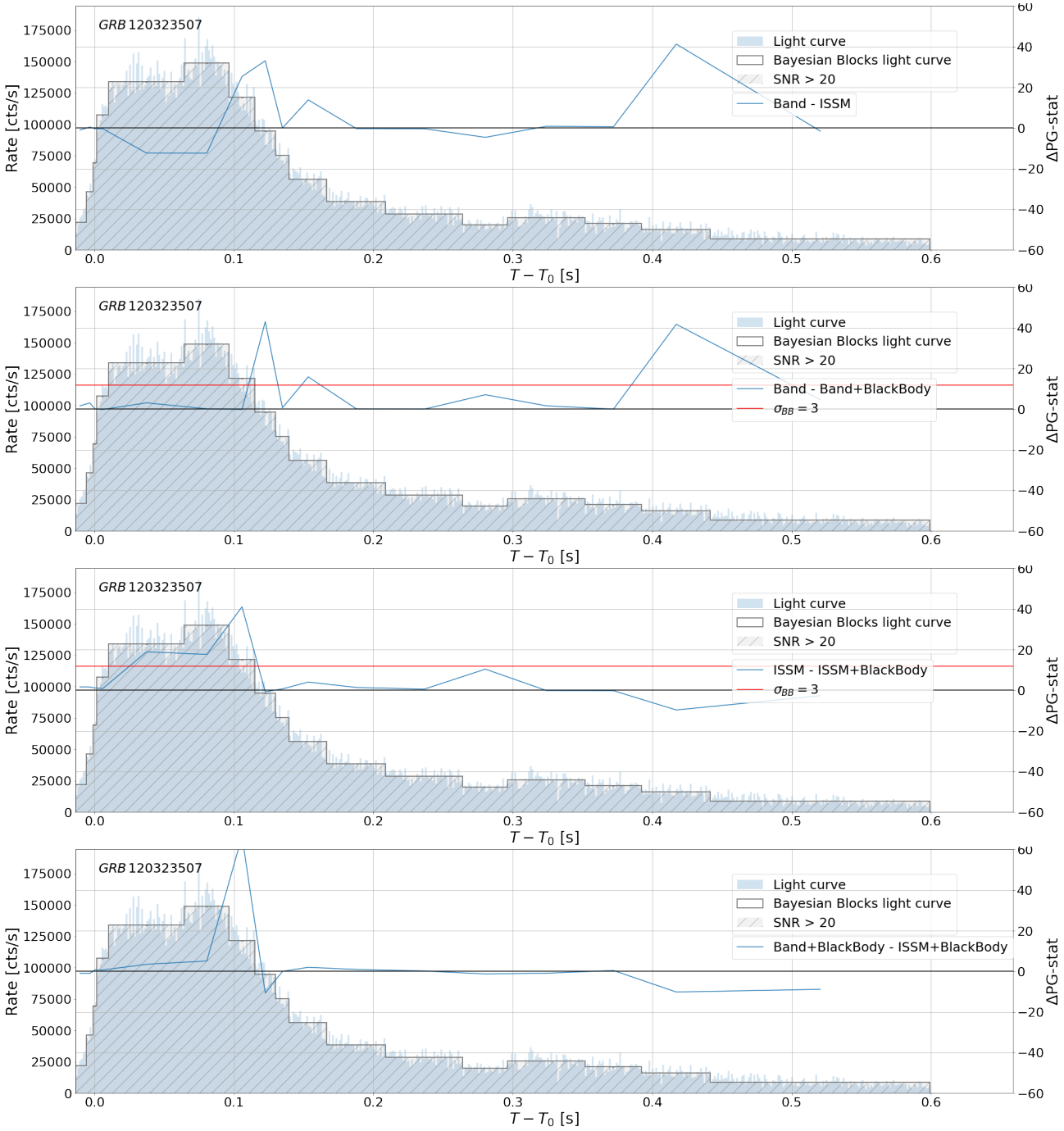

Figure 4.11: **GRB 120323A**: difference of *PG-stat* between Band and ISSM (1st panel), Band and Band+BB (2nd panel), ISSM and ISSM+BB (3rd panel), and Band+BB and ISSM+BB (4th panel).

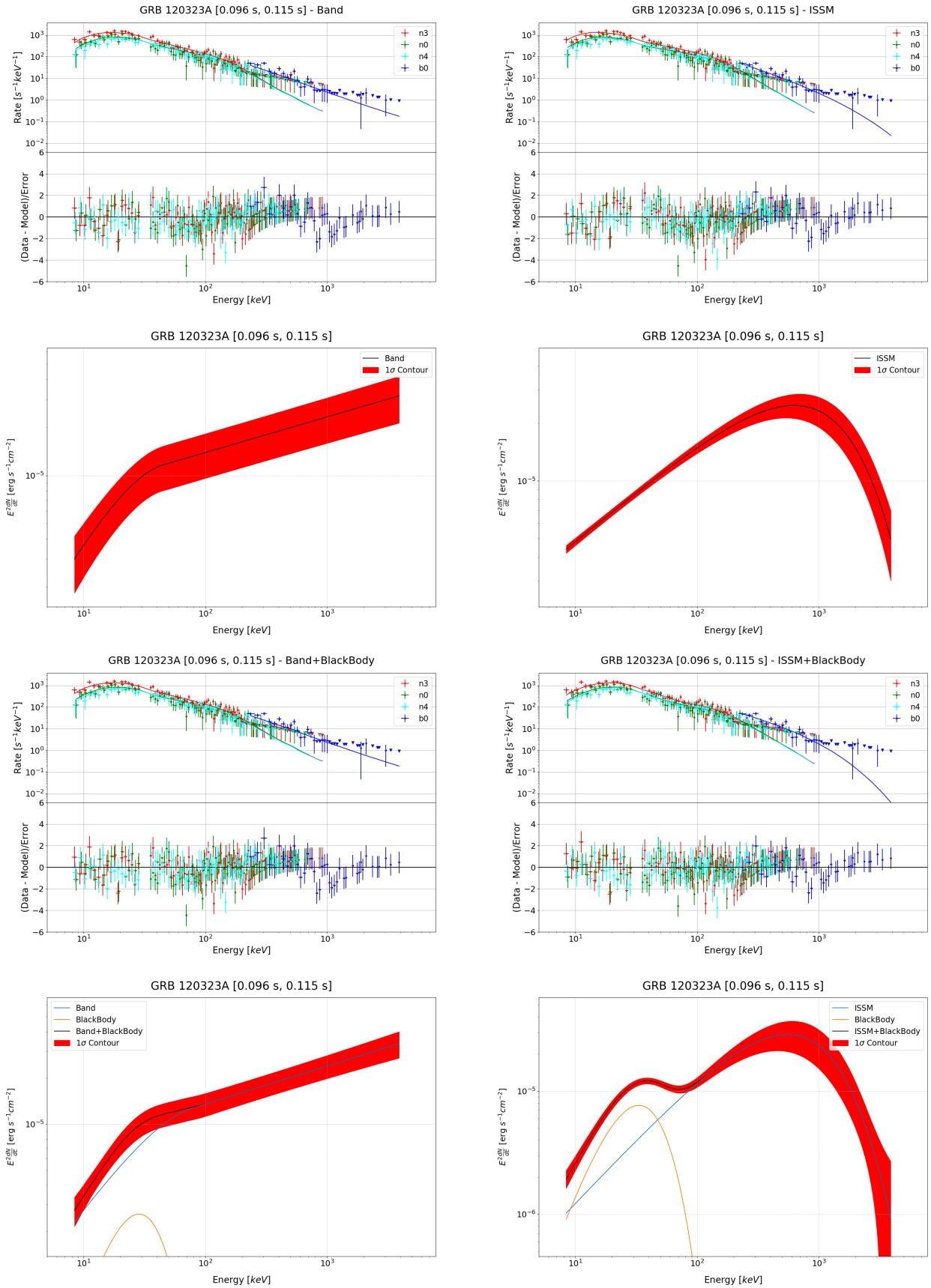

Figure 4.12: **GRB 120323A**, time bin 7: residuals and spectral energy distributions for different model combinations.

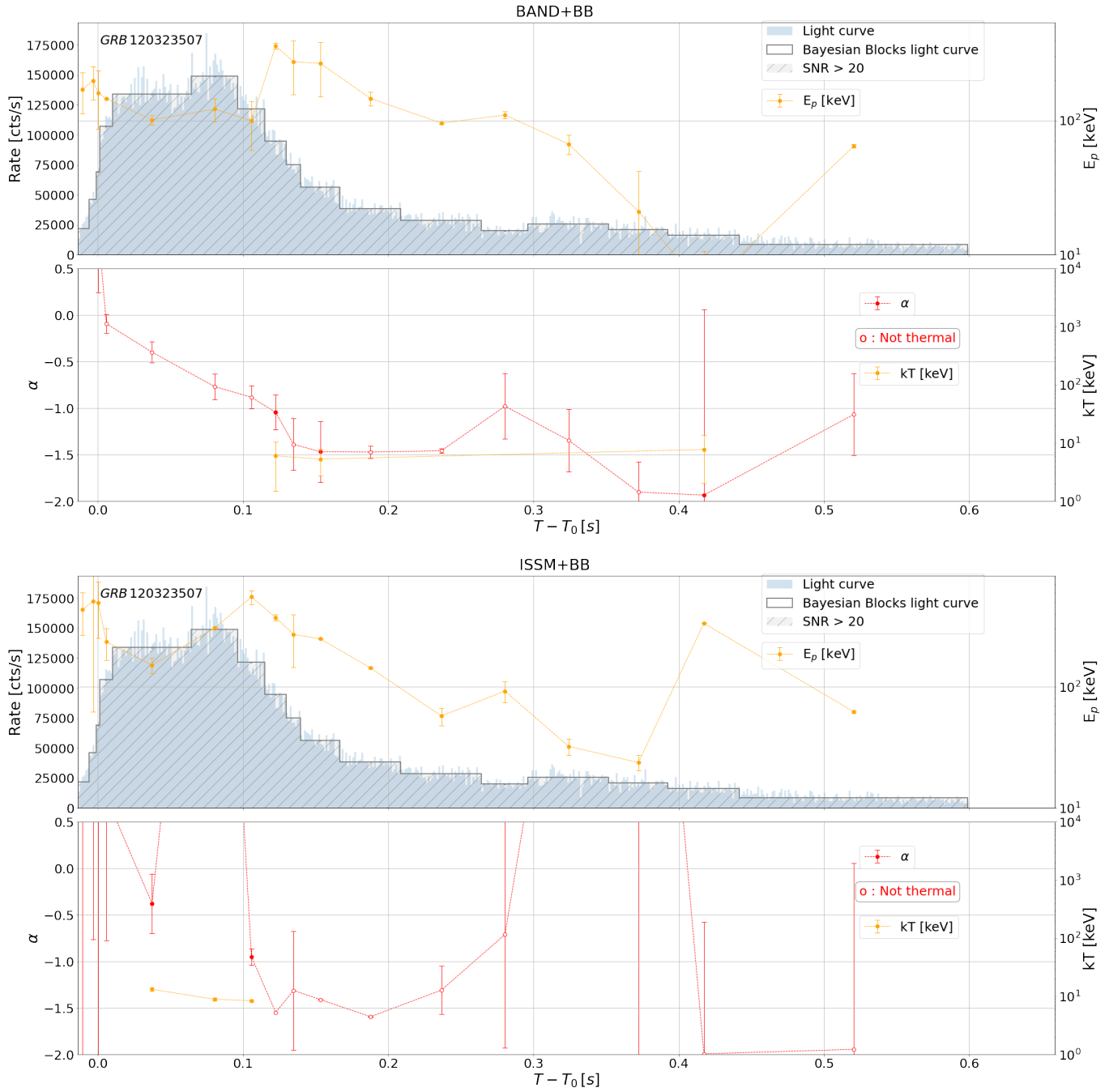

Figure 4.13: **GRB 120323A**: temporal evolution of Band+BB (upper panel) and ISSM+BB (lower panel) spectral parameters. The temperature kT is shown only when the thermal component is detected at more than 3σ.

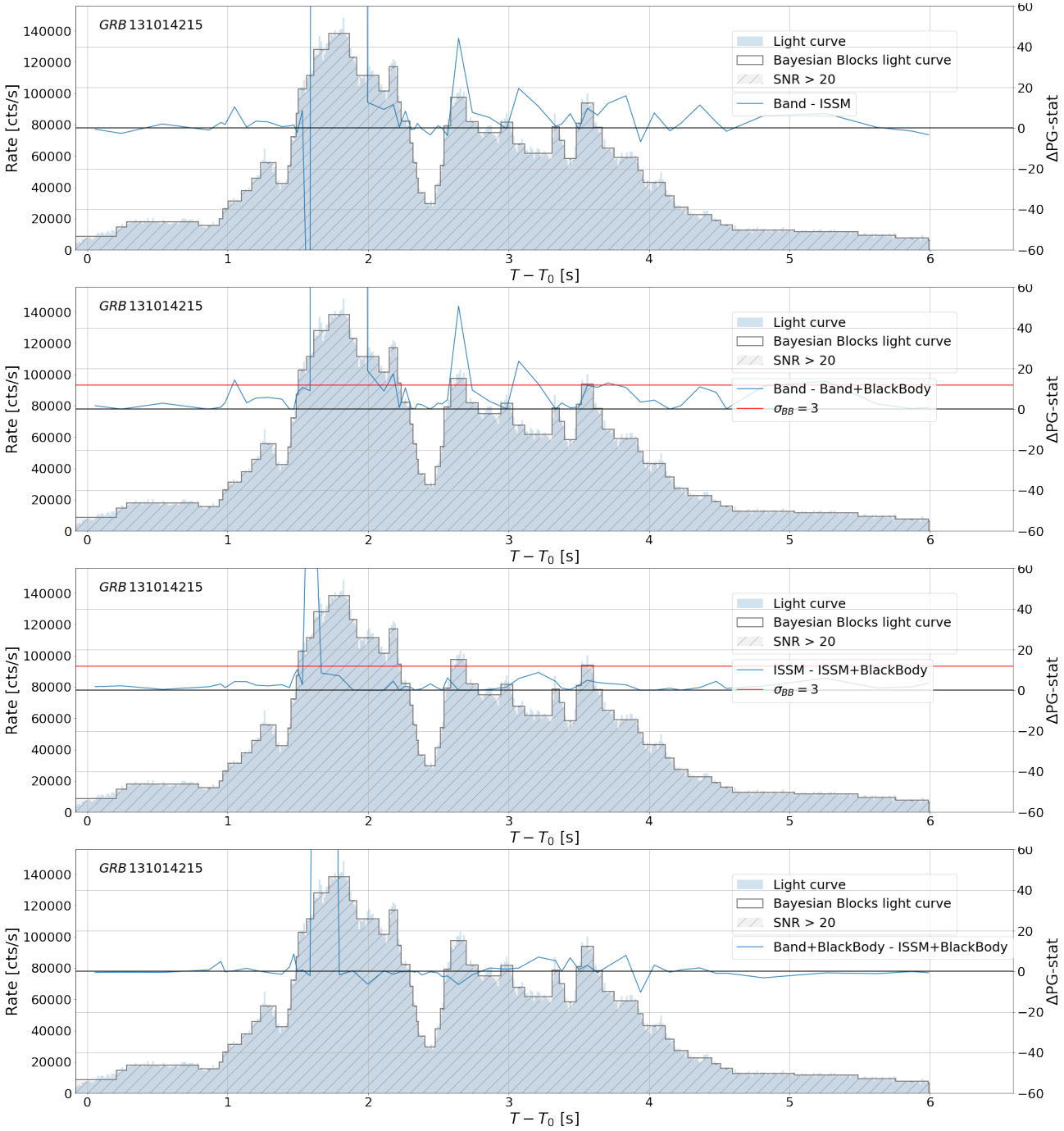

Figure 4.14: **GRB 131014A**: difference of *PG-stat* between Band and ISSM (1st panel), Band and Band+BB (2nd panel), ISSM and ISSM+BB (3rd panel), and Band+BB and ISSM+BB (4th panel).

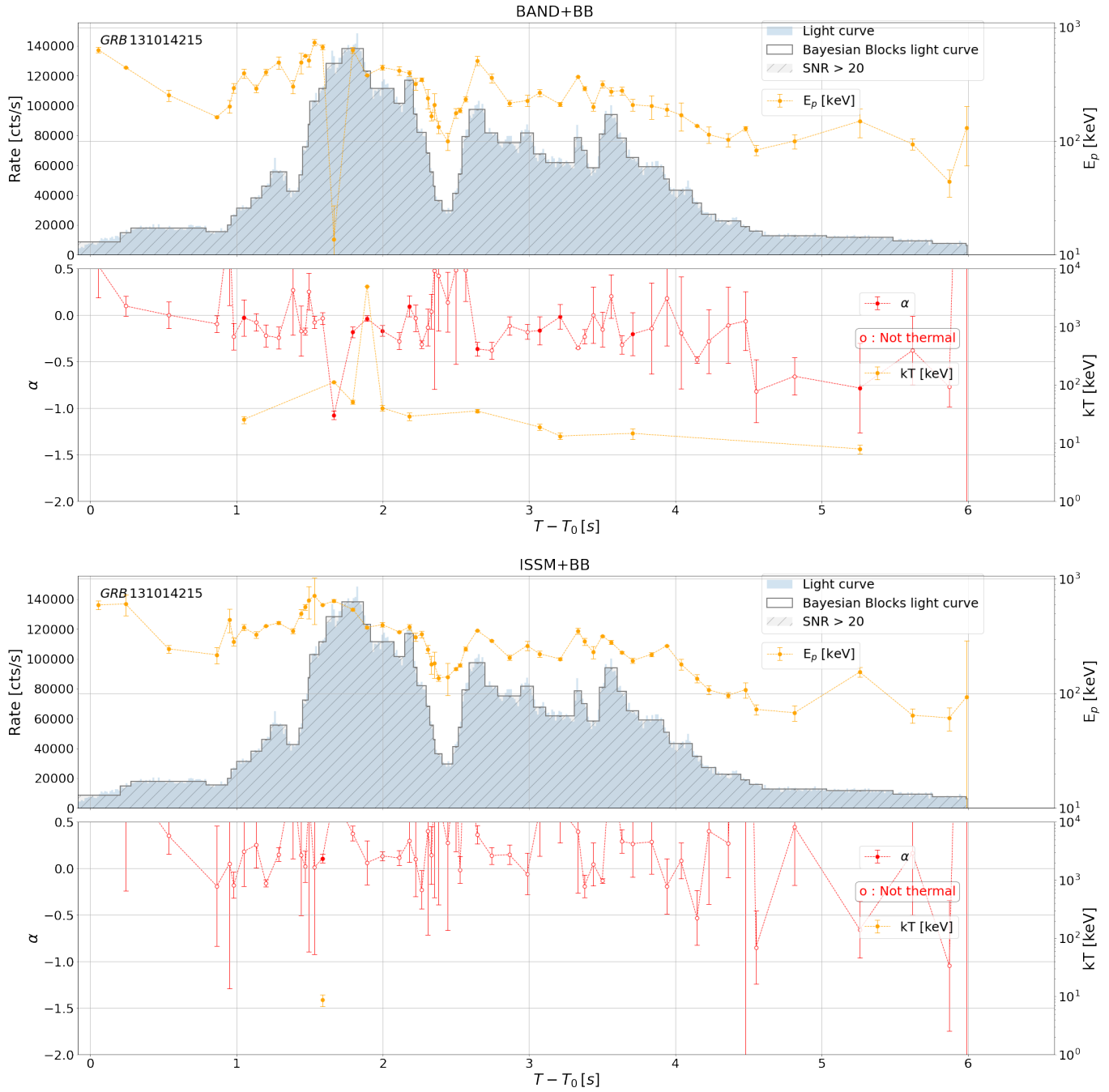

Figure 4.15: **GRB 131014A**: temporal evolution of Band+BB (upper panel) and ISSM+BB (lower panel) spectral parameters. The temperature kT is shown only when the thermal component is detected at more than 3σ.

Chapter 5

GRB 220101A: the most distant *Fermi* gamma-ray burst

In this chapter I analyse GRB 220101A, a burst which occured during one of my BA shifts. It is the most distant gamma-ray burst detected by the LAT to date ($z = 4.618$) as well as a very energetic event, with an equivalent isotropic energy $E_{iso} \sim 3.3 \times 10^{54}$ erg. In this chapter I perform a spectral analysis from keV to GeV energies adopting two independent analysis chains: the one I have been using for all the spectral analyses presented in this Thesis, which is based on the spectral data preparation of *GBMToolkit* and on the spectral fitting engine of *pyXSPEC*; the other one is *3ML*. The agreement between the two analysis chains reinforces the detection of a high-energy spectral cutoff below 100 MeV in the prompt emission. Secondly, I estimate the variability of the observed high-energy emission and determine the bulk Lorentz factor Γ_{bulk} of the jet and the radius at which the observed emission took place in the assumption that the attenuation at high energies is due to opacity to pair creation. To conclude I compare GRB 220101A with other LAT detected GRBs which present similar features.

5.1 Observations

GRB 220101A was detected and observed in a broad multi-wavelength range. The prompt emission has been observed from hard X-rays to high-energy gamma-rays, and the afterglow has been observed via radio few days after the event [Laskar 2022]. The first detection of GRB 220101A was provided by Swift-BAT which allowed the follow-up with XRT in the hard X-rays and with UVOT in the visible domain [Tohuvavohu et al. 2022]. The most precise localization of the event was estimated by Swift-UVOT at RA, Dec = 1.35340°, 31.76903°, with a 90% confidence error radius of about 0.61 arcsec. Given the brightness of the optical afterglow, a prompt photometric estimate of GRB 220101A redshift could be performed. The Xinglong-2.16m telescope estimated the redshift $z = 4.618$ [Fu et al. 2022], in accord with following estimation of the Liverpool telescope [Perley 2022], and of the Nordic Optical Telescope [Fynbo et al. 2022].

On 2022 January 1 at 05:10:11.51 UT the GBM [Lesage et al. 2022] triggered on GRB 220101A, which was also detected by the LAT at high energies [Arimoto et al. 2022]. The best LAT on-ground localization of the event is RA, Dec = 1.52°, 31.75° with an error radius of 0.46°, which is consistent with the Swift-XRT localization. This was 18° from the LAT boresight at the time of the *Fermi* trigger, which was a favourable condition to observe the burst because not far from normal incidence where the LAT effective detection area is maximal. Figure 5.1 shows the multi-detector light curve of GRB 220101A. The red-dashed vertical line denotes the time of the trigger T_0 and the black-dashed lines define the time bins that are used in the time-resolved spectral analysis. Most of the emission recorded by the GBM is observed in the time interval $T_0 + [65, 134]$ s, while most of the LAT Low-Energy events (LLE events, see § 2.2.1) are recorded in the time interval $T_0 + [95, 107]$ s (time bin B+C). In coincidence with the main episode observed by the NaIs and the LAT around $T_0 + 100$ s there is a depletion of high-energy events recorded by the LAT at energies greater than ∼100 MeV. The highest energy photon is detected at $T_0 + 152$ s with an energy $E_{max} = 927$ MeV and with a probability of association to the GRB greater than 0.99.

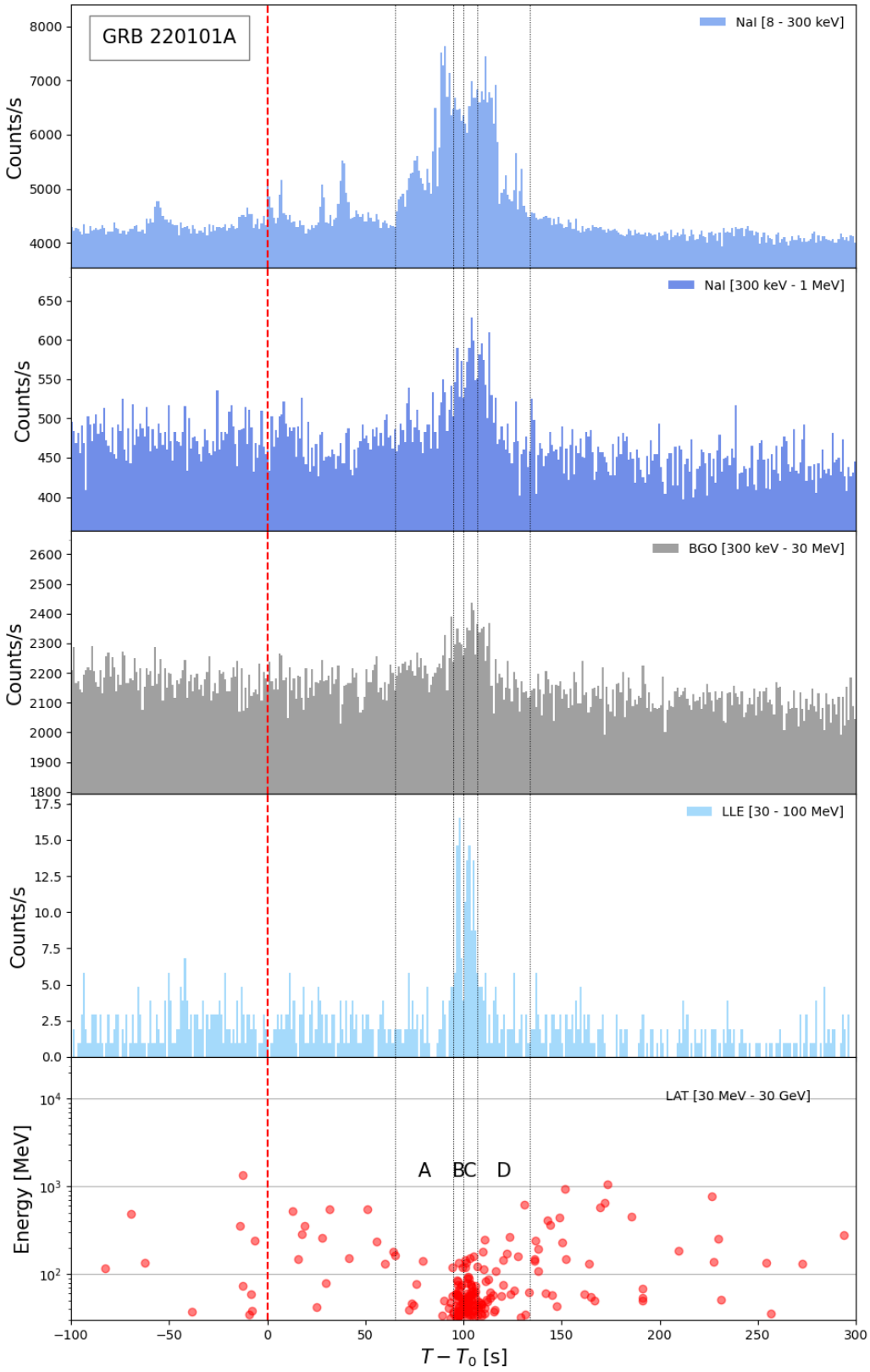

Figure 5.1: Multi-detector light curve for GRB 220101A in increasing energy bands from the top panel to the bottom panel. The red dashed vertical line denotes the time of the trigger, while the black dashed vertical lines delimitate the time intervals that I chose for the time-resolved spectral analysis on the main emission episode observed by the LAT.

Band	This analysis	GBM Team
α	-1.09 ± 0.03	-1.06 ± 0.02
β	-2.21 ± 0.16	-2.32 ± 0.17
E_p (keV)	297 ± 26	292 ± 18
norm (10^{-2})	0.67 ± 0.03	-
C-stat/dof	975/592	1941/599

Table 5.1: Comparison of my results when fitting Band to the time-integrated interval between $T_0 - 65$ s and $T_0 + 179$ s with Lesage et al. 2022. The units of the normalizations are $cm^{-2}s^{-1}keV^{-1}$.

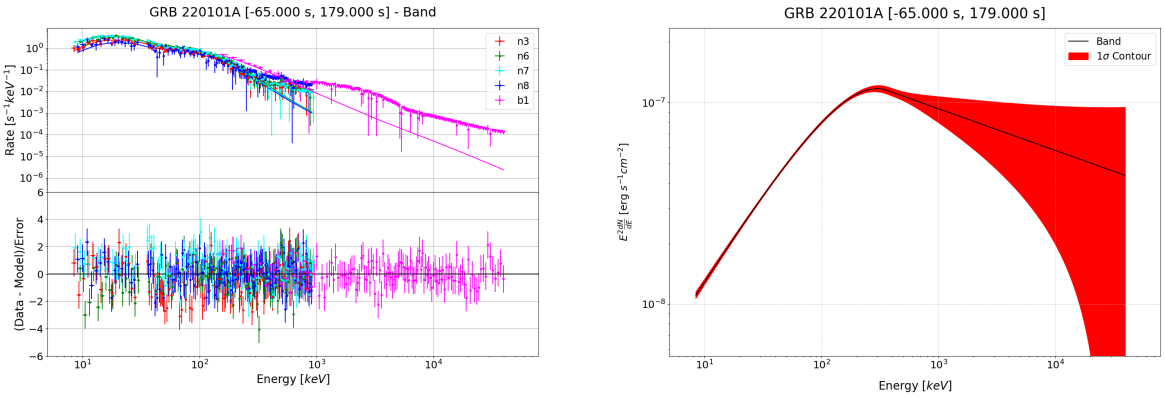

Figure 5.2: Residuals (left panel) and spectral energy distribution (right panel) of my analysis.

5.2 Spectral analysis

I performed a time-integrated and time-resolved analyses in the main LAT emission episode at $T_0 + [65, 134]$ s. I compared the phenomenological Band function and the ISSM model with and without an additional cutoff at high energies to account for the attenuated flux above $\sim$ 100 MeV at $T_0 + 100$ s. As first step I recovered the results published by the GBM Team [Lesage et al. 2022]. As second step I analysed the LAT data in the main emission episode, and in the time intervals before and after it. Since the LAT data alone didn't yield a detection of a cutoff I increased the data leverage at lower energies adding the GBM data. As third step, I performed a joint analysis on GBM data and the LAT Low Energy data (LLE, see § 2.2.1), which extends the LAT energy range down to 20 MeV. I analysed this data set with two independent analysis chains based respectively on *pyXSPEC* and *3ML*.

5.2.1 Spectral analysis on GBM data

As a sanity check, I first compared my spectral analysis with the results reported by the GBM Team [Lesage et al. 2022]. I considered the same data set used by the GBM Team, which are the CSPEC data for the NaIs detectors 3, 6, 7, 8 and the BGO detector 1, between $T_0 - 65$ s and $T_0 + 179$ s. Table 5.1 presents the spectral analysis results of mine and of the GBM Team when fitting the Band function to the data. The two sets of results are in perfect agreement. Figure 5.2 presents the spectral residuals and the spectral energy distribution of my analysis. The model well adapts to the data as the residuals are well contained within $+3$ and -3, especially at high energies. The fluence of the burst in the energy range $(10 - 1000)$ keV is $(8.06 \pm 0.19)10^{-5}\, erg/cm^2$ and with $SNR = 161$. These values define GRB 220101A as a fluent burst (energy fluence greater than $10^{-5}\, erg/cm^2$, see § 3.1) with a moderate SNR, which is high enough to distinguish the ISSM and Band spectral models (see right panel of Figure 3.9).

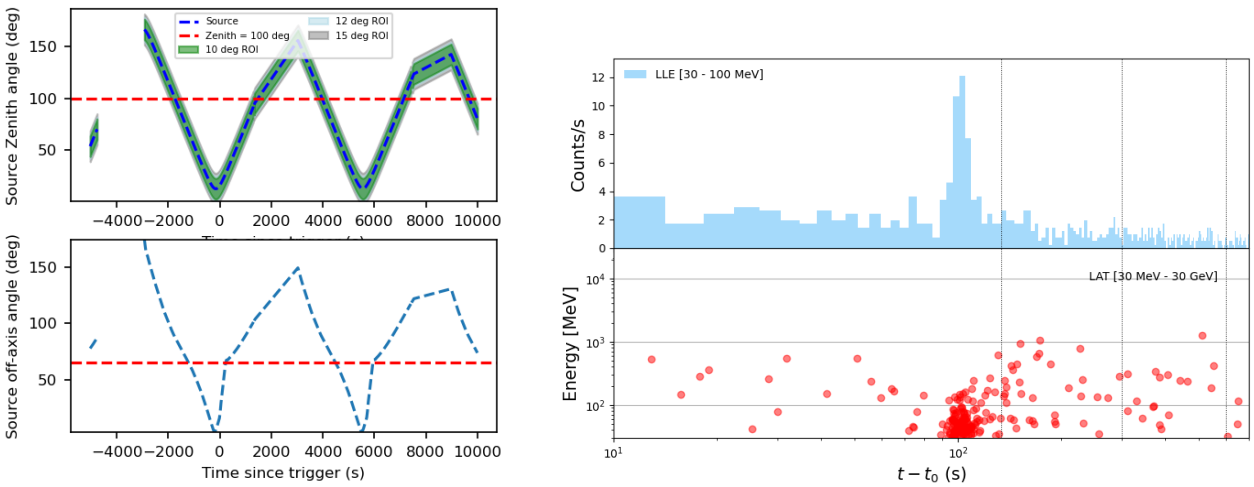

Figure 5.3: Left: the lower panel shows the temporal evolution of the angle under which the LAT observed the source. The red horizontal line corresponds to the edge of the LAT field of view. The source was within the LAT field of view up to roughly ~ 600 s from the time of the trigger, and again between $T_0 + 4500$ s and $T_0 + 6000$s. Right: LAT light curve between 10 s to 700 s after the time of the trigger. The vertical pointed lines denote the edges of the time intervals over which I analysed LAT data.

5.2.2 Spectral analysis on LAT data

I analysed LAT standard data at energies greater than 100 MeV to look for a significant excess at high energies, and to test whether a spectral cutoff is statistically required. Since there is a depletion of high energy gamma-rays above ~ 100 MeV at $\sim T_0 + 100$ s I considered also the LAT data at energies down to 30 MeV to increase the available statistics in the interested energy range. The LAT data employed in the analysis are the standard LAT P8R3_TRANSIENT020E_V2 data in a region of interest centered at the Swift position with a 12° radius. I considered $T_0 + [0, 600]$ s as the time interval in which the burst position was in the LAT field of view (see left panel of Figure 5.3). Moreover I focused on the main emission interval $T_0 + [65, 134]$ s, and on the time intervals $T_0 + [0, 65]$ s, $T_0 + [134, 300]$ s, and $T_0 + [300, 600]$ s. For each interval I determined the likelihood of the model in which the point source is modeled by a power law (PL), and the likelihood of the model in which the point source is modeled by a power law with an exponential cutoff (CUTPL). I computed the difference of the likelihood between the two models as $TS_{cut} = TS_{PL} - TS_{CUTPL}$. As the two models differ by only 1 parameter, the cutoff energy, I determined the corresponding Gaussian significance of the additional cutoff as $\sigma_{cut} = \sqrt{TS_{cut}}$.

Table 5.2 presents the spectral results. High-energy emission from the point source is detected ($TS > 25$) over the whole time interval $T_0 + [0, 600]$ s, and more specifically in the main emission episode $T_0 + [65, 134]$ s and in $T_0 + [134, 300]$ s. No high-energy emission is detected before $T_0 + 65$ s and after $T_0 + 300$ s, neither in the time window when the burst re-entered the LAT field of view, i.e. $4500 \text{ s} < T - T_0 < 6000$ s (see left panel of Figure 5.3). In the main emission interval $T_0 + [65, 134]$ s its spectral index is very steep and significantly softer than -3. This is consistent with the depletion seen at $\sim T_0 + 100$ s. However, no cutoff is required by the data in any time intervals. For this reason I considered also GBM data to increase the data leverage at lower energies.

5.2.3 Joint spectral analysis on GBM and LAT data

I considered the LAT standard data above 30 MeV and the Time Tagged Events (TTE) data of the GBM detectors NaI 3, 6, 7, 9, which observed the burst at an angle smaller than 60°. Moreover I considered the BGO detector 1, which observed the burst with the smallest angle. Firstly I performed a GBM+LAT joint spectral analysis over the interval $T_0 + [65, 134]$ s where the burst high-energy emission is detected. I fitted the Band function and Band multiplied by an exponential cutoff, which I label "BandExpCut". Since the cutoff introduces one degree of freedom in the fit, I determined its significance as $\sigma_{cut} = \sqrt{PG_{Band} - PG_{BandExpCut}}$. Secondly, I considered the two main peaks observed in the LLE data between $T_0 + 95$ s and $T_0 + 107$ s, and I

$T - T_0$ [s]	Range [MeV]	PL		CUTPL			
		Index	TS	Index	E_{cut} [MeV]	TS	σ_{cut}
$0 - 600$	> 100	-2.48 ± 0.23	**104.1**	-1.97 ± 0.58	939 ± 1129	**105.3**	1.1
	> 30	-2.93 ± 0.13	**170.0**	-2.93 ± 0.13	$(2.9 \pm 7.9) \times 10^5$	**170.0**	0
$0 - 65$	> 100	-2.33 ± 0.74	10.6	-1.01 ± 0.37	321 ± 321	1.1	0.7
	> 30	-1.73 ± 0.39	12.7	-1.00 ± 0.02	458 ± 434	14.6	1.4
$65 - 134$	> 100	-3.41 ± 0.52	**45.7**	-2.97 ± 1.32	607 ± 1816	**45.8**	0.3
	> 30	-3.48 ± 0.17	**129.1**	-3.45 ± 0.28	3167 ± 21570	**129.1**	0
$134 - 300$	> 100	-2.18 ± 0.31	**47.3**	-1.00 ± 0.08	427 ± 193	**50.0**	1.6
	> 30	-1.98 ± 0.21	**56.8**	-1.0 ± 2.3	439 ± 1568	**60.7**	2.0
$300 - 600$	> 100	-1.81 ± 0.51	11.1	-1.00 ± 0.08	945 ± 931	12.1	1.0
	> 30	-1.76 ± 0.50	9.9	-1.00 ± 0.01	1045 ± 1143	10.7	0.9

Table 5.2: Results of the spectral analysis of PL and CUTPL on LAT data in different time windows. The units of the normalization are $10^{-7} cm^{-2} s^{-1} MeV^{-1}$.

Parameter	Band	BandExpCut
α	-0.86 ± 0.02	-0.84 ± 0.02
β	-2.51 ± 0.02	-2.30 ± 0.04
E_p [keV]	300 ± 9	288 ± 10
E_{cut} [MeV]	-	$\mathbf{89 \pm 23}$
Norm (10^{-2})	2.01 ± 0.05	2.06 ± 0.06
PG-stat/dof	1050.8/642	1015.8/641
σ_{cut}	-	**5.9**

Parameter	Band	BandExpCut
α	-0.86 ± 0.03	-0.83 ± 0.04
β	-2.40 ± 0.03	-1.97 ± 0.07
E_p [keV]	417 ± 27	367 ± 28
E_{cut} [MeV]	-	$\mathbf{36 \pm 7}$
Norm (10^{-2})	2.57 ± 0.09	2.72 ± 0.12
PG-stat/dof	835.7/642	776.7/641
σ_{cut}	-	**7.7**

Table 5.3: Results of the joint spectral analysis of Band with and without a cutoff on GBM+LAT data in the time intervals $T_0 + [65, 134]$ s (left table), and $T_0 + [95, 107]$ s (B+C, right table). The units of the normalization are $cm^{-2} s^{-1} keV^{-1}$.

performed a joint spectral analysis in this time interval. Finally, I divided the whole time interval $T_0 + [65, 134]$ s in four sub-intervals, which I label "A, B, C, D". The two main LLE peaks fall in time bins B and C respectively. I performed a joint spectral analysis over the four sub-intervals testing the statistical significance of an additional cutoff at high energies.

The left side of Table 5.3 presents the results for the time-integrated analysis. An high-energy cutoff at 89 ± 23 MeV is detected with a significance of 5.9σ. The right side of Table 5.3 presents the results of the joint analysis over the main LLE peaks (B+C). An high-energy cutoff is detected at 36 ± 7 MeV with a confidence level of 7.7σ. Figure 5.4 presents the residuals plot (upper panel) and the spectral energy distribution (lower panel) of Band and BandExpCut, respectively. The additional cutoff at high energies stabilises the residuals in the LAT energy range. Moreover the quality of the fit and the constraints on the spectral parameters are excellent. Table 5.4 presents the results for the time-resolved analysis. An high-energy cutoff is detected in time bins B and C at 25 ± 10 MeV and 46 ± 16 MeV with a confidence level of 5.1σ and 5.4σ, respectively. One expects that the peak energy of Band decreases and the high-energy index hardens when the cutoff is detected. In particular the additional high-energy cut accounts for the soft spectrum at high energies. I conclude that an high-energy cutoff is significantly detected when extending the energy leverage to the GBM energy range between tens of keV and tens of MeV. In order to improve on my analysis I considered the LLE data down to 20 MeV. In fact the LLE data provides higher photon statistics than the LAT standard data especially below 100 MeV.

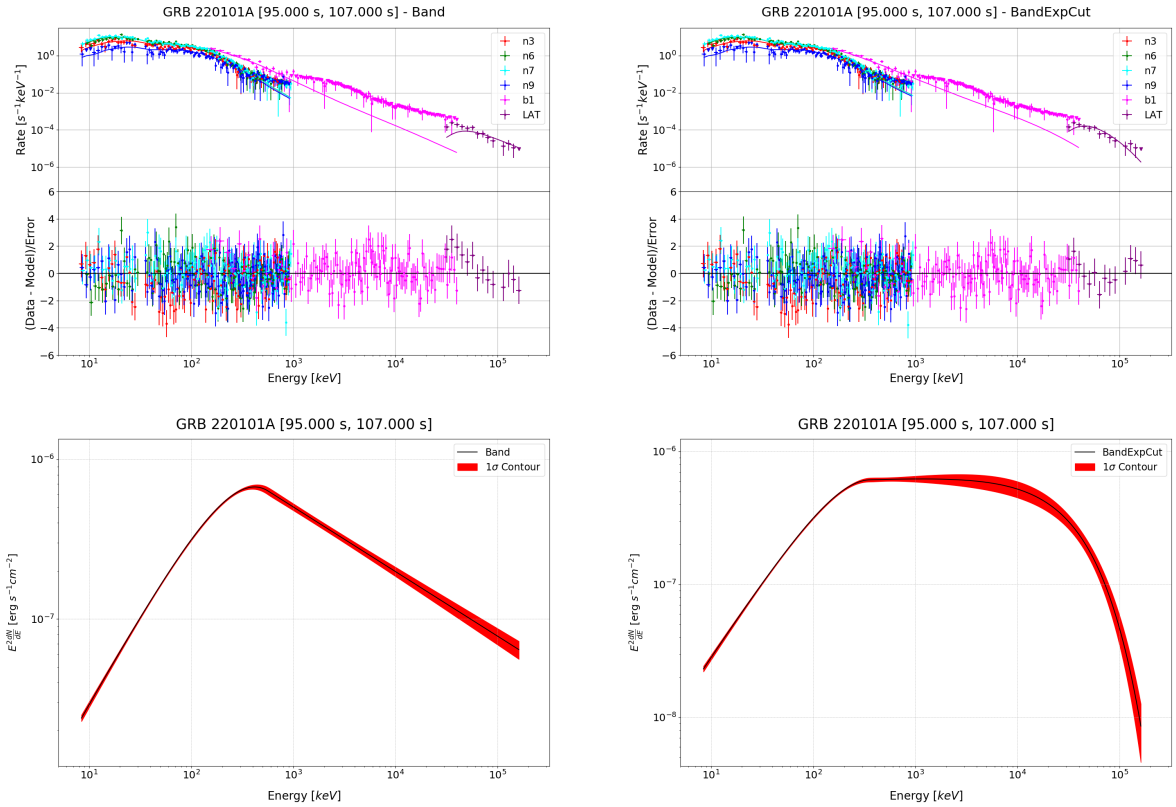

Figure 5.4: Left: residuals and spectral energy distribution of Band on GBM+LAT data for the time interval comprising the two main LLE peaks $T_0 + [95, 107]$ s (B+C). Right: residuals and spectral energy distribution of BandExpCut for the same data selection.

Parameter	A: $T_0 + [65, 95]$ s		B: $T_0 + [95, 100]$ s	
	Band	BandExpCut	Band	BandExpCut
α	-0.77 ± 0.03	-0.73 ± 0.04	-0.87 ± 0.05	-0.83 ± 0.05
β	-2.70 ± 0.06	-2.22 ± 0.14	-2.46 ± 0.05	-1.87 ± 0.16
E_p [keV]	241 ± 11	222 ± 14	389 ± 37	336 ± 43
E_{cut} [MeV]	-	25 ± 11	-	$\mathbf{25 \pm 10}$
Norm (10^{-2})	2.11 ± 0.10	2.25 ± 0.14	2.57 ± 0.15	2.73 ± 0.21
PG-stat/dof	776.2/642	764.3/641	756.1/642	730.2/641
σ_{cut}	-	3.4	-	**5.1**
	C: $T_0 + [100, 107]$ s		D: $T_0 + [107, 134]$ s	
	Band	BandExpCut	Band	BandExpCut
α	-0.86 ± 0.04	-0.83 ± 0.04	-0.93 ± 0.03	-0.93 ± 0.02
β	-2.41 ± 0.03	-2.04 ± 0.10	-2.57 ± 0.04	-2.57 ± 0.03
E_p [keV]	437 ± 37	393 ± 39	306 ± 17	306 ± 2
E_{cut} [MeV]	-	$\mathbf{46 \pm 16}$	-	$> 10^9$
Norm (10^{-2})	2.57 ± 0.12	2.70 ± 0.12	1.78 ± 0.07	1.78 ± 0.02
PG-stat/dof	681.8/642	652.7/641	696.8/642	696.8/641
σ_{cut}	-	**5.4**	-	0

Table 5.4: Results of the joint spectral analysis of Band with and without a cutoff on GBM+LAT data in time intervals A, B, C, and D. The units of the normalization are $cm^{-2}s^{-1}keV^{-1}$.

Parameter	Band	BandExpCut	ISSM	ISSMExpCut
α	-0.85 ± 0.02	-0.85 ± 0.01	-0.69 ± 0.04	-0.69 ± 0.03
β	-2.43 ± 0.02	-2.28 ± 0.22	-2.62 ± 0.03	-2.62 ± 0.03
E_p [keV]	296 ± 10	289 ± 2	441 ± 17	440 ± 14
E_{cut} [MeV]	-	$\mathbf{96 \pm 11}$	-	$> 10^6$
Norm (10^{-2})	2.03 ± 0.05	2.05 ± 0.01	13.93 ± 0.44	12.95 ± 0.36
PG-stat/dof	1010.9/637	986.3/636	1031.0/637	1031.0/636
σ_{cut}	-	**5.0**	-	0

Table 5.5: Results of the joint spectral analysis of Band and ISSM with and without a cutoff on GBM+LLE data in the time interval $T_0 + [65, 134]$. The units of the normalization are $cm^{-2}s^{-1}keV^{-1}$.

Parameter	Band	BandExpCut	ISSM	ISSMExpCut
α	-0.86 ± 0.03	-0.83 ± 0.04	-0.75 ± 0.04	-0.68 ± 0.05
β	-2.31 ± 0.02	-2.00 ± 0.06	-2.50 ± 0.03	-2.23 ± 0.04
E_p [keV]	416 ± 29	370 ± 28	746 ± 41	1076 ± 142
E_{cut} [MeV]	-	$\mathbf{41 \pm 12}$	-	$\mathbf{64 \pm 15}$
Norm (10^{-2})	2.57 ± 0.10	2.71 ± 0.13	17.24 ± 0.79	16.53 ± 0.82
PG-stat/dof	834.2/637	773.2/636	823.1/637	790.7/636
σ_{cut}	-	**7.8**	-	**5.7**

Table 5.6: Results of the joint spectral analysis of Band and ISSM with and without a cutoff on GBM+LLE data in the time interval $T_0 + [95, 107]$ s (B+C). The units of the normalization are $cm^{-2}s^{-1}keV^{-1}$.

5.2.4 Joint spectral analysis on GBM and LLE data

I considered the same GBM data selection, namely the NaI detectors 3, 6, 7, 9 and the BGO detector 1. Morever, I considered the LLE data down to 20 MeV. I performed a joint spectral analysis on GBM+LLE data in the same time intervals defined in the previous § 5.2.3. I tested whether the high-energy cutoff is statistically required when the baseline spectral function is either Band or ISSM. Testing two different spectral functions makes the analysis more robust and highlights possible systematics on the value of the spectral cutoff that may arise from considering a specific spectral model. Table 5.5 presents the results for the time-integrated analysis. An high-energy cutoff at 96 ± 11 MeV is detected with a significance of 5.0σ in the case of Band. These results are consistent with those from the GBM+LAT joint fits (left side of Table 5.3), with a better goodness of fit (decrease of 30 to 50 units in the fit statistics). On the other hand, no high-energy cutoff is statistically required in the case of ISSM. One expects that the significance of the high-energy cutoff decreases in the latter case because ISSM is continuously curved and naturally better adapts to soft spectra. However, the BandExpCut model should be preferred over the ISSMExpCut model in the present case as both ISSM fits are of poorer quality than the Band ones ($\Delta PGstat$ at least smaller than -20). Table 5.6 presents the results for the joint analysis over the main LLE peaks. An high-energy cutoff is detected at 41 ± 12 MeV and 64 ± 15 MeV with a confidence level of 7.8σ and 5.7σ for Band and ISSM, respectively. Again, the BandExpCut model shall be preferred over the ISSMExpCut model, and the Band fits are fully consistent with those from the GBM+LAT joint fits (right side of Table 5.3). Figure 5.5 presents the residuals plot (upper panel) and the spectral energy distribution (lower panel) of Band and BandExpCut, respectively on GBM+LLE data. Figure 5.6 presents the same plots in the ISSM case. The additional cutoff at high energies stabilises the residuals in the LLE energy range for both Band and ISSM. Moreover the quality of the fit and the constraints on the spectral parameters are very good, especially with the BandExpCut model.

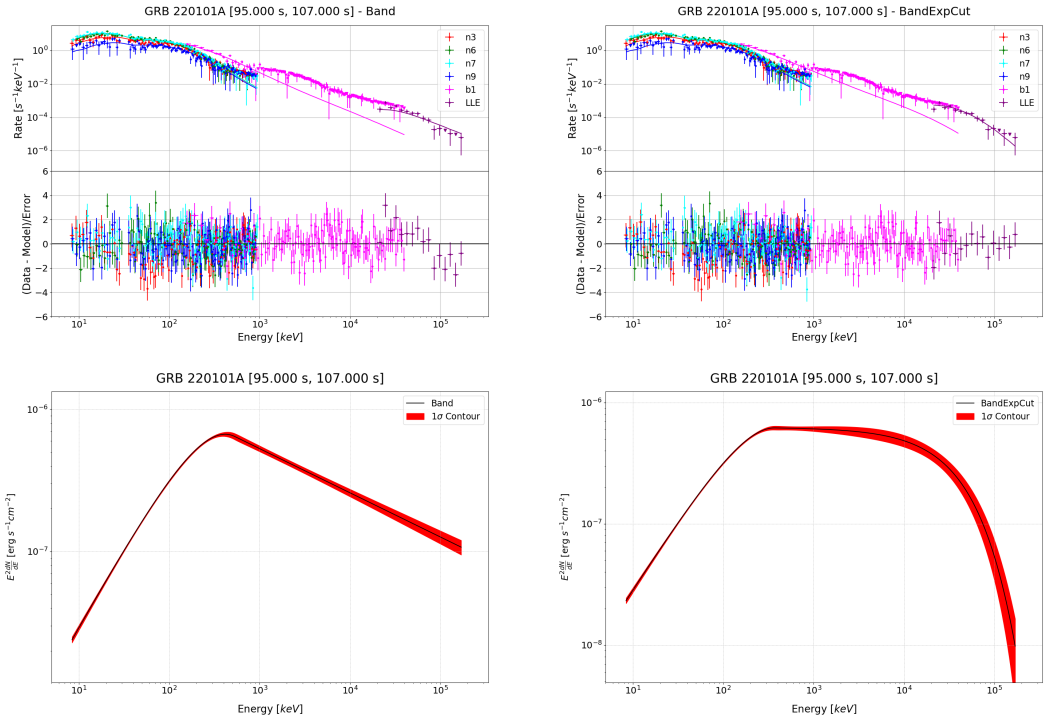

Figure 5.5: Left: residuals and spectral energy distribution of Band on GBM+LLE data for the time interval comprising the two main LLE peaks $T_0 + [95, 107]$ s (B+C). Right: residuals and spectral energy distribution of BandExpCut for the same data selection.

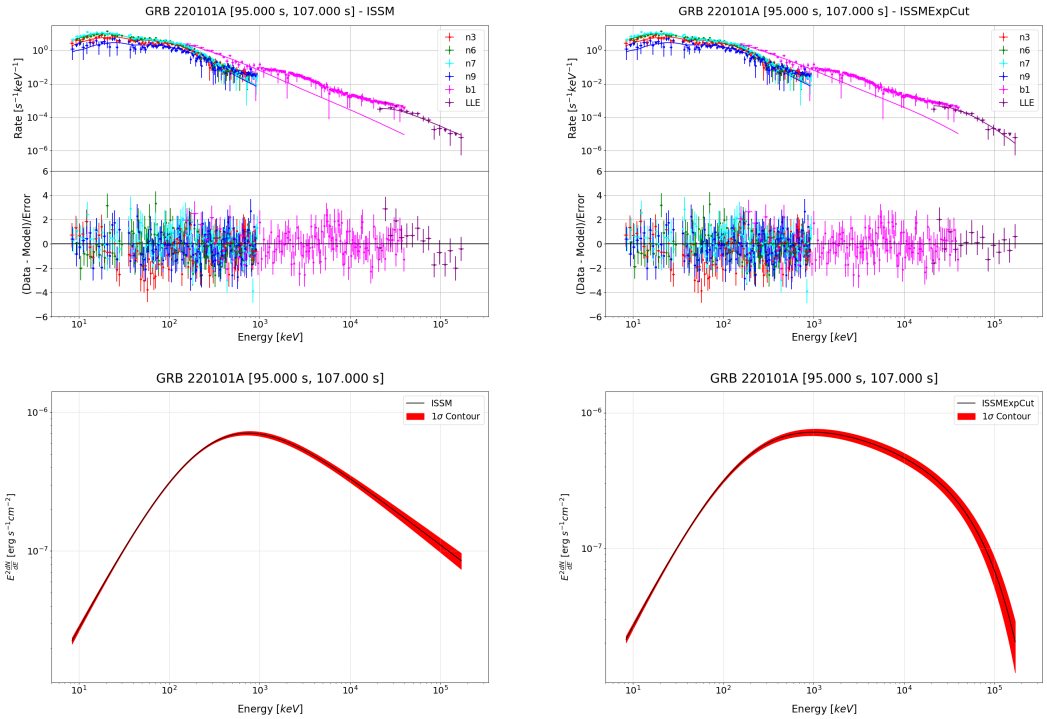

Figure 5.6: Left: residuals and spectral energy distribution of ISSM on GBM+LLE data for the time interval comprising the two main LLE peaks $T_0 + [95, 107]$ s (B+C). Right: residuals and spectral energy distribution of ISSMExpCut for the same data selection.

Parameter	A: $T_0 + [65, 95]$ s		B: $T_0 + [95, 100]$ s	
	Band	BandExpCut	Band	BandExpCut
α	-0.75 ± 0.04	-0.73 ± 0.01	-0.87 ± 0.05	-0.83 ± 0.06
β	-2.54 ± 0.05	-2.57 ± 0.06	-2.32 ± 0.04	-1.86 ± 0.11
E_p [keV]	235 ± 11	226 ± 3	393 ± 41	334 ± 41
E_{cut} [MeV]	-	$> 10^6$	-	$\mathbf{22 \pm 8}$
Norm (10^{-2})	2.14 ± 0.11	2.24 ± 0.02	2.55 ± 0.16	2.74 ± 0.21
PG-stat/dof	793.2/637	795.5/636	771.6/637	730.6/636
σ_{cut}	-	0	-	**6.4**
	C: $T_0 + [100, 107]$ s		D: $T_0 + [107, 134]$ s	
	Band	BandExpCut	Band	BandExpCut
α	-0.85 ± 0.04	-0.83 ± 0.04	-0.92 ± 0.03	-0.92 ± 0.02
β	-2.31 ± 0.03	-2.09 ± 0.06	-2.51 ± 0.05	-2.52 ± 0.05
E_p [keV]	433 ± 38	394 ± 37	303 ± 18	304 ± 17
E_{cut} [MeV]	-	$\mathbf{70 \pm 24}$	-	$> 10^6$
Norm (10^{-2})	2.58 ± 0.13	2.70 ± 0.15	1.78 ± 0.07	1.78 ± 0.07
PG-stat/dof	673.4/637	647.4/636	687.3/637	687.3/636
σ_{cut}	-	**5.1**	-	0

Table 5.7: Results of the joint spectral analysis of Band with and without the cutoff on GBM+LLE data in time intervals A, B, C, and D. The units of the normalization are $cm^{-2}s^{-1}keV^{-1}$.

Parameter	A: $T_0 + [65, 95]$ s		B: $T_0 + [95, 100]$ s	
	ISSM	ISSMExpCut	ISSM	ISSMExpCut
α	-0.54 ± 0.08	-0.54 ± 0.07	-0.78 ± 0.09	-0.67 ± 0.08
β	-2.79 ± 0.09	-2.79 ± 0.08	-2.51 ± 0.06	-2.16 ± 0.05
E_p [keV]	315 ± 18	315 ± 17	704 ± 79	1324 ± 337
E_{cut} [MeV]	-	$> 10^6$	-	$\mathbf{40 \pm 10}$
Norm (10^{-2})	10.63 ± 0.66	10.64 ± 0.57	17.77 ± 1.61	16.85 ± 1.18
PG-stat/dof	807.5/637	807.5/636	766.0/637	742.9/636
σ_{cut}	-	0	-	**4.8**
	C: $T_0 + [100, 107]$ s		D: $T_0 + [107, 134]$ s	
	ISSM	ISSMExpCut	ISSM	ISSMExpCut
α	-0.73 ± 0.06	-0.74 ± 0.09	-0.79 ± 0.06	-0.79 ± 0.05
β	-2.49 ± 0.04	-2.49 ± 0.05	-2.74 ± 0.07	-2.74 ± 0.07
E_p [keV]	772 ± 57	774 ± 71	410 ± 31	410 ± 24
E_{cut} [MeV]	-	$> 10^6$	-	$> 10^6$
Norm (10^{-2})	16.84 ± 1.07	16.92 ± 1.50	13.63 ± 0.76	13.62 ± 0.58
PG-stat/dof	668.5/637	668.5/636	703.0/637	703.0/636
σ_{cut}	-	0	-	0

Table 5.8: Results of the joint spectral analysis of ISSM with and without a cutoff on GBM+LLE data in time intervals A, B, C, and D. The units of the normalization are $cm^{-2}s^{-1}keV^{-1}$.

		B	C	B+C
BandExpCut	E_{cut} [MeV]	22 ± 8	70 ± 24	41 ± 12
	σ_{cut}	6.4	5.1	7.8
ISSMExpCut	E_{cut} [MeV]	40 ± 10	-	64 ± 15
	σ_{cut}	4.8	-	5.7

Table 5.9: Spectral cutoff energy E_{cut} and its detection significance from *pyXSPEC* fits of BandExpCut and ISSMExpCut on GBM+LLE data for the intervals B, C, and B+C.

Table 5.7 presents the results for the time-resolved analysis of Band. An high-energy cutoff is detected in time bins B and C at 22 ± 8 MeV and 70 ± 24 MeV with a confidence level of 6.4σ and 5.1σ, respectively. As before, the peak energy of Band decreases and the high-energy index hardens when the cutoff is detected. Table 5.8 presents the results for the time-resolved analysis of ISSM. An high-energy cutoff is detected only in time bin B at 40 ± 10 MeV with a confidence level of 4.8σ. Table 5.9 summarizes the results on the spectral cutoff energies and their detection significances when fitting BandExpCut and ISSMExpCut to GBM+LLE data on the time intervals B, C, and B+C. The reduced significance of the high-energy cutoff, which is detected in only one time bin may be explained recalling that ISSM is continuously curved, fact that naturally accounts for part of the soft spectrum at high energies. However, as mentioned before ISSM fits are systematically worse than Band fits, though their reduced *PG-stat* are acceptable. This might result from the fact that the ISSM spectral curvature is determined by the counts at all energies, while the β index of the Band model can be varied more freely about the break energy without affecting much the spectral fit at lower energies. As a result, the Band (resp. BandExpCut) fits have the smallest fit statistic among all 4 fits in the cases where the cutoff is not detected (resp. detected). Therefore, I conclude that the non-thermal emission of GRB 220101A during the LAT main emission episode is best fitted by the Band function, and that an high-energy cutoff is significantly detected when extending the energy leverage to the GBM energy range and combining it with the LLE data selection.

5.2.5 3ML analysis

In order to exclude possible systematics due to the specific spectral analysis chain I also performed a joint spectral analysis using the *3ML* software ("Multi-Mission Maximum Likelihood", see § 2.4.2), and I compared the outcome of the two spectral analysis procedures. As first step, I compared the two analysis chains on the same GBM+LLE data set used in § 5.2.4. Table 5.10 and Table 5.11 presents the *3ML* spectral results when fitting Band and ISSM, respectively, with and without an additional high-energy cutoff. The *3ML* analysis yields fully consistent results with the *pyXSPEC* analysis: the high-energy cutoff is required in time bin B and C with a statistical confidence of 6.0σ and 4.5σ when fitting BandExpCut; the high-energy cutoff is required in time bin B with a significance of 4.6σ and marginally in time bin C with a significance of 3.2σ when fitting ISSMExpCut. The spectral parameters are in excellent agreement between the two analysis chains, so I confirm the detection of an high-energy cutoff and exclude possible systematics due to the specific spectral analysis chain adopted.

As mentioned in § 2.4.2, *3ML* allows to employ the full accuracy of the unbinned likelihood for the LAT standard data, which on the other hand is lost during the binning in space and energy that is required by *pyXSPEC*. Therefore, I performed a *3ML* analysis limiting the LLE data below 100 MeV, and I considered the LAT standard data from 100 MeV onwards. In this analysis, GBM and LLE (<100 MeV) data are thus treated in the same way as in *pyXSPEC*, while the LAT standard data above 100 MeV contribute to the joint fit through the actual LAT native likelihood. Table 5.12 and Table 5.13 presents the *3ML* results of the joint spectral analysis of Band and ISSM. Unlike the previous GBM+LLE analysis with *pyXSPEC*, where ISSM fits were systematically worse than Band fits, the quality of the fits are remarkably equivalent with *3ML*, both within the GBM+LLE and within the GBM+LLE(<100MeV)+LAT(>100MeV) analyses. According to *3ML*, both Band and ISSM are thus able to describe the non-thermal spectrum. Spectral cutoffs at 31 ± 8 MeV and 68 ± 18 MeV are detected with a confidence level of 6.3σ and 5.8σ in time bins B and C when fitting

Parameter	A: $T_0 + [65, 95]$ s		B: $T_0 + [95, 100]$ s	
	Band	BandExpCut	Band	BandExpCut
α	-0.73 ± 0.04	-0.73 ± 0.04	-0.85 ± 0.05	-0.81 ± 0.06
β	-2.54 ± 0.05	-2.53 ± 0.05	-2.30 ± 0.04	-1.86 ± 0.08
E_p [keV]	227 ± 11	227 ± 11	380 ± 40	320 ± 40
E_{cut} [MeV]	-	$(2.42 \pm 0.32) \times 10^4$	-	$\mathbf{22 \pm 6}$
Norm (10^{-2})	2.19 ± 0.12	2.19 ± 0.12	2.54 ± 0.16	2.74 ± 0.22
-log(like)	4217.74	4217.76	2652.08	2634.00
σ_{cut}	-	0	-	**6.0**
	C: $T_0 + [100, 107]$ s		D: $T_0 + [107, 134]$ s	
	Band	BandExpCut	Band	BandExpCut
α	-0.85 ± 0.04	-0.82 ± 0.04	-0.92 ± 0.03	-0.92 ± 0.03
β	-2.29 ± 0.03	-2.09 ± 0.06	-2.53 ± 0.05	-2.50 ± 0.05
E_p [keV]	423 ± 35	392 ± 34	298 ± 18	297 ± 18
E_{cut} [MeV]	-	$\mathbf{72 \pm 25}$	-	730 ± 220
Norm (10^{-2})	2.59 ± 0.12	2.68 ± 0.14	1.78 ± 0.08	1.78 ± 0.08
-log(like)	2923.17	2913.07	4025.88	4025.79
σ_{cut}	-	**4.5**	-	0.4

Table 5.10: Results of the *3ML* spectral analysis when fitting Band with and without a cutoff on GBM+LLE data in time intervals A, B, C, and D. The units of the normalization are $cm^{-2}s^{-1}keV^{-1}$.

Parameter	A: $T_0 + [65, 95]$ s		B: $T_0 + [95, 100]$ s	
	ISSM	ISSMExpCut	ISSM	ISSMExpCut
α	-0.49 ± 0.08	-0.49 ± 0.08	-0.74 ± 0.08	-0.62 ± 0.11
β	-2.78 ± 0.08	-2.78 ± 0.08	-2.49 ± 0.06	-2.11 ± 0.08
E_p [keV]	303 ± 17	303 ± 17	680 ± 70	1700 ± 1000
E_{cut} [MeV]	-	$> 10^6$	-	$\mathbf{36 \pm 10}$
Norm (10^{-2})	1.22 ± 0.02	1.22 ± 0.02	1.85 ± 0.04	1.86 ± 0.04
-log(like)	4223.01	4223.01	2650.17	2639.51
σ_{cut}	-	0	-	**4.6**
	C: $T_0 + [100, 107]$ s		D: $T_0 + [107, 134]$ s	
	ISSM	ISSMExpCut	ISSM	ISSMExpCut
α	-0.71 ± 0.07	-0.65 ± 0.08	-0.77 ± 0.06	-0.78 ± 0.06
β	-2.46 ± 0.04	-2.28 ± 0.07	-2.76 ± 0.09	-2.76 ± 0.09
E_p [keV]	760 ± 60	950 ± 140	395 ± 26	395 ± 26
E_{cut} [MeV]	-	100 ± 40	-	$(3.1 \pm 0.4) \times 10^5$
Norm (10^{-2})	1.97 ± 0.04	1.98 ± 0.04	1.22 ± 0.02	1.22 ± 0.02
-log(like)	2916.08	2916.08	4031.44	4031.44
σ_{cut}	-	3.2	-	0

Table 5.11: Results of the *3ML* spectral analysis when fitting ISSM with and without a cutoff on GBM+LLE data in time intervals A, B, C, and D. The units of the normalization are $cm^{-2}s^{-1}keV^{-1}$.

Parameter	A: $T_0 + [65, 95]$ s		B: $T_0 + [95, 100]$ s	
	Band	BandExpCut	Band	BandExpCut
α	-0.74 ± 0.04	-0.69 ± 0.03	-0.86 ± 0.05	-0.82 ± 0.05
β	-2.69 ± 0.09	-2.05 ± 0.16	-2.34 ± 0.04	-1.93 ± 0.07
E_p [keV]	233 ± 12	215 ± 31	380 ± 40	330 ± 40
E_{cut} [MeV]	-	5 ± 16	-	$\mathbf{31 \pm 8}$
Norm (10^{-2})	2.15 ± 0.12	2.34 ± 0.09	2.52 ± 0.16	2.72 ± 0.20
-log(like)	4216.27	4214.33	2672.58	2652.63
σ_{cut}	-	2.0	-	**6.3**
	C: $T_0 + [100, 107]$ s		D: $T_0 + [107, 134]$ s	
	Band	BandExpCut	Band	BandExpCut
α	-0.85 ± 0.04	-0.82 ± 0.04	-0.92 ± 0.03	-0.92 ± 0.03
β	-2.34 ± 0.03	-2.09 ± 0.05	-2.54 ± 0.04	-2.52 ± 0.04
E_p [keV]	430 ± 40	391 ± 34	298 ± 18	298 ± 18
E_{cut} [MeV]	-	$\mathbf{68 \pm 18}$	-	1950 ± 270
Norm (10^{-2})	2.55 ± 0.12	2.68 ± 0.14	1.78 ± 0.08	1.78 ± 0.08
-log(like)	2959.45	2942.45	4070.01	4069.89
σ_{cut}	-	**5.8**	-	0.5

Table 5.12: Results of the *3ML* joint spectral analysis when fitting Band with and without the cutoff on the GBM+LLE+LAT data set in time intervals A, B, C, and D. The units of the normalization are $cm^{-2}s^{-1}keV^{-1}$.

Parameter	A: $T_0 + [65, 95]$ s		B: $T_0 + [95, 100]$ s	
	ISSM	ISSMExpCut	ISSM	ISSMExpCut
α	-0.54 ± 0.07	-0.53 ± 0.07	-0.76 ± 0.08	-0.62 ± 0.12
β	-3.04 ± 0.17	-2.97 ± 0.17	-2.53 ± 0.06	-2.11 ± 0.09
E_p [keV]	286 ± 17	290 ± 18	670 ± 70	1700 ± 1100
E_{cut} [MeV]	-	> 350	-	$\mathbf{40 \pm 12}$
Norm (10^{-2})	1.22 ± 0.02	1.22 ± 0.02	1.85 ± 0.04	1.86 ± 0.04
-log(like)	4217.77	4217.72	2669.35	2657.27
σ_{cut}	-	0.3	-	**4.9**
	C: $T_0 + [100, 107]$ s		D: $T_0 + [107, 134]$ s	
	ISSM	ISSMExpCut	ISSM	ISSMExpCut
α	-0.73 ± 0.06	-0.65 ± 0.08	-0.77 ± 0.06	-0.76 ± 0.06
β	-2.51 ± 0.04	-2.27 ± 0.06	-2.73 ± 0.06	-2.71 ± 0.06
E_p [keV]	740 ± 60	970 ± 130	398 ± 25	402 ± 26
E_{cut} [MeV]	-	$\mathbf{89 \pm 26}$	-	> 990
Norm (10^{-2})	1.96 ± 0.04	1.98 ± 0.04	1.22 ± 0.02	1.22 ± 0.02
-log(like)	2955.06	2945.55	4075.85	4076.41
σ_{cut}	-	**4.4**	-	0

Table 5.13: Results of the *3ML* joint spectral analysis when fitting ISSM with and without a cutoff on the GBM+LLE+LAT data set in time intervals A, B, C, and D. The units of the normalization are $cm^{-2}s^{-1}keV^{-1}$.

		B: $T_0 + [95, 100]$ s		C: $T_0 + [100, 107]$ s	
		GBM+LLE	GBM+LLE+LAT	GBM+LLE	GBM+LLE+LAT
BandExpCut	E_{cut} [MeV]	22 ± 6	31 ± 8	72 ± 25	68 ± 18
	σ_{cut}	6.0	6.3	4.5	5.8
ISSMExpCut	E_{cut} [MeV]	36 ± 10	40 ± 12	100 ± 40	89 ± 26
	σ_{cut}	4.6	4.9	3.2	4.4

Table 5.14: Spectral cutoff energy E_{cut} and it detection significance from *3ML* fits of BandExpCut and ISSMExpCut on the GBM+LLE and GBM+LLE(<100 MeV)+LAT data sets.

BandExpCut. High-energy cuts at 40 ± 12 MeV and 89 ± 26 MeV are detected with a confidence level of 4.9σ and 4.4σ in time bins B and C when fitting ISSMExpCut. The significance of the cutoff decreases slightly from the Band case to the ISSM case due to the continuous curvature of the latter function. Table 5.14 summarizes the results on the spectral cutoff energies and their detection significances in time bins B and C when performing a *3ML* joint spectral analysis on the two data sets: GBM+LLE and GBM+LLE(<100 MeV)+LAT(>100 MeV). For the GBM+LLE data the cutoff is significantly detected in both time bins when fitting BandExpCut, while only in time bin B when fitting ISSMExpCut. When I restrain the LLE data below 100 MeV and employ the LAT standard data above 100 MeV, the high-energy cutoff detections are slightly reinforced, especially in time bin C. This can be explained by the better sensitivity of the LAT native likelihood, which manifests more in time bin C since the cutoff energy is closer to the 100 MeV threshold of the LAT standard data set. The spectral cutoff values found when fitting the two different non thermal (NT) models Band and ISSM are different, so the systematic effect on the estimation of the spectral cutoff energies must be taken into account. In order to estimate them I consider only solid detections, where $\sigma_{cut} > 4\sigma$. I discard the ISSM fits in the *pyXSPEC* analysis because they are worse fits, but not in the *3ML* analysis, where the ISSM fits are as good as the Band ones. **I choose as final values the spectral cutoff energies obtained with the *pyXSPEC* fit of BandExpCut on GBM+LLE data (see Table 5.9), and I estimate the systematics from the absolute variations of the other analyses around these results, ignoring the statistical errors**.

- For time bin B the central value that I will use in the $\Gamma_{\gamma\gamma}$ opacity computation in § 5.4 is $E_{cut,Band} = 22 \pm 8$ MeV determined by the *pyXSPEC* analysis. The lowest cutoff value is $E_{cut,Band} = 22$ MeV, from both *pyXSPEC* and *3ML* analyses. The highest cutoff value is $E_{cut,ISSM} = 40$ MeV in the *3ML* analysis on GBM+LLE+LAT data. Thus I estimate the value of the spectral cutoff as $E_{cut} = 22 \pm 8\,(\text{stat}) + 18/-0\,(\text{syst})$ MeV in this time bin.

- For time bin C the central value used for opacity computation is $E_{cut,Band} = 70 \pm 24$ MeV determined as well by the *pyXSPEC* analysis. The lowest cutoff value is $E_{cut,Band} = 68$ MeV and the highest cutoff value is $E_{cut,Band} = 89$ MeV, both determined in the *3ML* analysis on GBM+LLE+LAT data. I estimate the cutoff value as $E_{cut} = 70 \pm 24\,(\text{stat}) + 19/-2\,(\text{syst})$ MeV in this time bin.

- In the joint time bin B+C the central value used for opacity computation is $E_{cut,Band} = 41 \pm 12$ MeV in the *pyXSPEC* analysis. There is no other fit in the *3ML* analysis. Since the systematics are similar for B and C, I use the same for B, C, and B+C, i.e. $+19/-2$ MeV (syst), which is the most conservative one.

5.3 Minimum variability time scale

The fast variability of the observed high-energy emission suggests that the detected high-energy cutoff is due to opacity to pair creation (see § 1.1.2 for a detailed discussion). In this section I quantify the minimum variability time scale of the observed high-energy emission. Specifically, I consider the LLE data selection

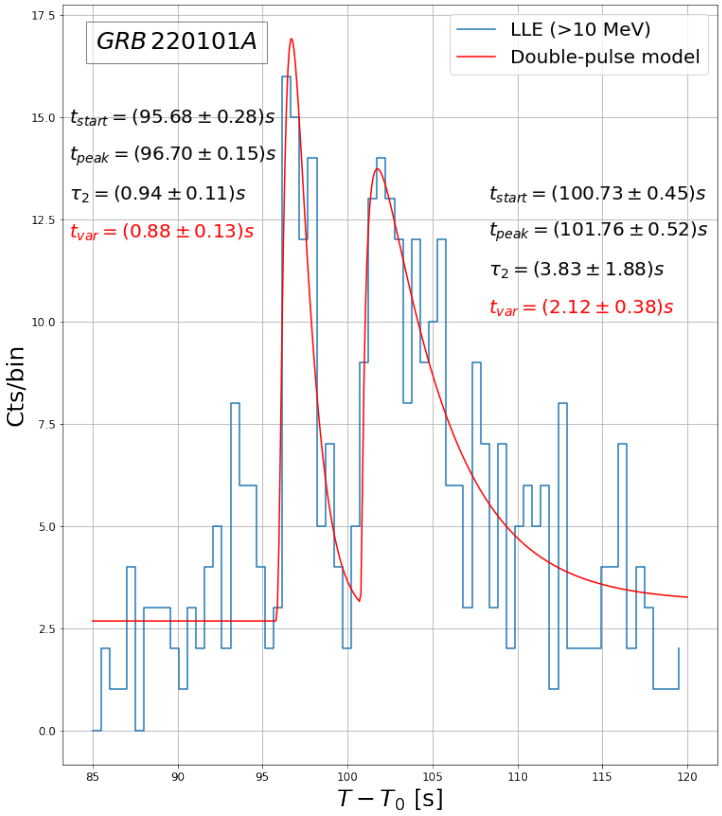

Figure 5.7: Light curve of the two main LLE peak and the best-fit FRED2P function.

at energies greater than 10 MeV in the time interval $T_0 + [85, 120]$ s, which comprises the two observed LLE peaks. I modeled the two-peak light curve with the following FRED2P function, which is an extension of the Fast Rise Exponential Decay function (FRED, Yassine et al. 2017, Norris et al. 2005):

$$I(t) = \begin{cases} B_x, & \text{if } t \leq t_{start,x} \\ A_x \times \exp\left\{-\frac{1}{\tau_{2x}}\left[\frac{(t_{peak,x} - t_{start,x})^2}{t - t_{start,x}} + (t - t_{start,x})\right]\right\} + B_x, & \text{if } t_{start,x} < t \leq t_{start,y} \\ A_y \times \exp\left\{-\frac{1}{\tau_{2y}}\left[\frac{(t_{peak,y} - t_{start,y})^2}{t - t_{start,y}} + (t - t_{start,y})\right]\right\} + B_y, & \text{if } t > t_{start,y} \end{cases} \tag{5.1}$$

with

$$B_y = I(t_{start,y}) \tag{5.2}$$

The labels x and y correspond to the first and second LLE peak, respectively. FRED2P is parameterized on each peak as the normalization A, the off-set B, the start of the pulse t_{start}, the peak time of the pulse t_{peak}, and the decay index τ_2. Figure 5.7 presents the two LLE peaks superimposed to the best-fit FRED2P function. For each pulse I determined the minimum variability time scale as half-width at half-maximum:

$$t_{var} = \frac{\tau_2}{2} \times \sqrt{\left(\log(2) + 2\frac{t_{peak} - t_{start}}{\tau_2}\right)^2 - 4\left(\frac{t_{peak} - t_{start}}{\tau_2}\right)^2} \tag{5.3}$$

The minimum variability time scale is $t_{var,x} = 0.88 \pm 0.13$ s for the first peak, and $t_{var,y} = 2.12 \pm 0.38$ s for the second peak.

Time bin	B: $T_0 + [95, 100]s$	C: $T_0 + [100, 107]s$	B+C: $T_0 + [95, 107]s$
t_{var} $[s]$	0.88 ± 0.13	2.12 ± 0.38	1.5 ± 0.5
s	-1.90 ± 0.11	-2.10 ± 0.06	-2.03 ± 0.05
$\Phi(s)$	0.48 ± 0.02	0.469 ± 0.007	0.473 ± 0.006
E_{cut} $[MeV]$	22 ± 8	70 ± 24	41 ± 12
E_* $[MeV]$	1	1	1
$F(E_*)$ $[cm^{-2}MeV^{-1}]$	0.341 ± 0.002	0.803 ± 0.002	0.57 ± 0.03
L $[10^{53}erg/s]$	7.56 ± 0.66	7.55 ± 0.40	7.55 ± 0.34
R_{LE} $[10^{14}cm]$	1.27 ± 0.29	2.43 ± 0.61	1.76 ± 0.73
$\Gamma_{\gamma\gamma}(R_{LE} = R_{HE})$	116 ± 10	104 ± 9	105 ± 13

Table 5.15: Resume of the parameters employed in the computation of Γ_{bulk}, and the observed energy emission radius in the time bins B, C, and B+C. The luminosity is computed in the observer frame energy range 10 keV - 1 GeV.

Time bin	B: $T_0 + [95, 100]s$	C: $T_0 + [100, 107]s$	B+C: $T_0 + [95, 107]s$
R_{LE} $[10^{14}cm]$	1.27 ± 0.29	2.43 ± 0.61	1.76 ± 0.73
R_{ph} $[10^{14}cm]$	1.81 ± 0.51	2.55 ± 0.68	2.46 ± 0.91
$\Gamma_{\gamma\gamma}$	116 ± 10	104 ± 9	105 ± 13
Γ_{Tr}	125 ± 4	105 ± 4	112 ± 8

Table 5.16: Resume of the radius at which the low-energy emission took place R_{LE}, the photospheric radius R_{ph}, $\Gamma_{\gamma\gamma}$, and Γ_{Tr} in the time bins B, C, and B+C.

5.4 Constraints on the bulk Lorentz factor and the region of emission

The bulk Lorentz factor Γ_{bulk} is obtained as in Yassine et al. 2017 assuming that the observed spectral cutoff is due to opacity to gamma-gamma annihilation in the GRB jet, and that the prompt emission is produced near or above the photosphere at a radius R_{LE} for the low-energy (MeV) emission and R_{HE} for the high-energy (tens of MeV) emission. This opacity model has been proposed by Hascoët et al. 2012 and it has been applied by Yassine et al. 2017 to determine Γ_{bulk} and the emission radii of GRB 090926A. The radius at which the low-energy emission is produced is obtained from the estimated variability as:

$$R_{LE} = 2c\Gamma^2 \frac{t_{var}}{1+z} \tag{5.4}$$

The bulk Lorentz factor Γ_{bulk} is given by:

$$\Gamma_{\gamma\gamma} = \frac{K\Phi(s)}{\left[\frac{1}{2}(1+\frac{R_{HE}}{R_{LE}})(\frac{R_{HE}}{R_{LE}})\right]^{1/2}}(1+z)^{-(1+s)/(1-s)} \times \left\{\sigma_T \left[\frac{D_L(z)}{ct_{var}}\right]^2 E_* F(E_*)\right\}^{1/2(1-s)} \left[\frac{E_* E_{cut}}{(m_e c^2)^2}\right]^{(s+1)/2(s-1)} \tag{5.5}$$

where t_{var} is the estimated variability time scale in the considered time interval, E_{cut} the energy of the detected cutoff, E_* is the typical energy of the photons interacting with those at the cutoff energy, s is the photon index of the seed spectrum close to E_*, and $F(E_*)$ is the photon fluence at E_* integrated over t_{var}. As mentioned in § 5.2.5, I chose the final values of E_{cut} from the *pyXSPEC* fit of BandExpCut on GBM+LLE data (see Table 5.9). These values are reported in Table 5.15, along with all other quantities that are needed to compute the opacity. In the following, I use a systematic error of $+19/-2$ MeV on E_{cut} (see the end of § 5.2.5), added quadratically to its statistical error.

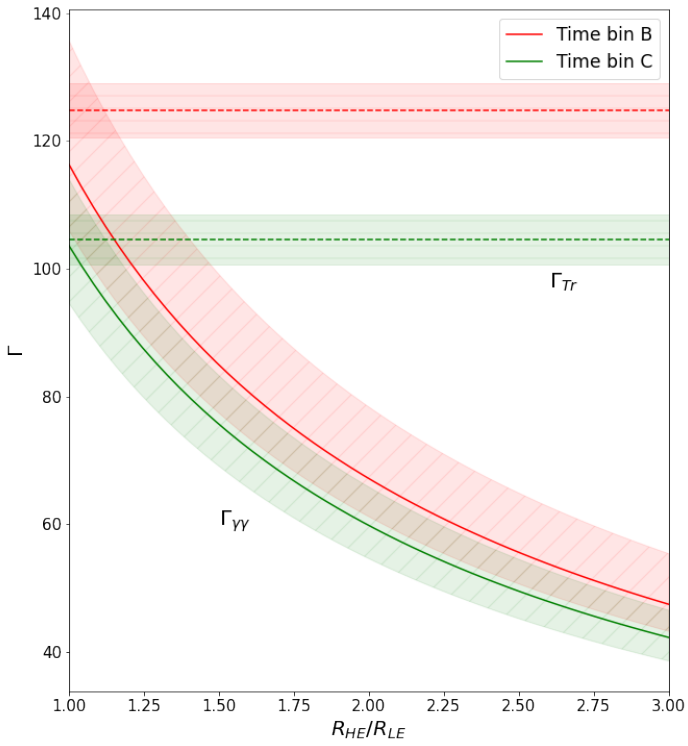

Figure 5.8: $\Gamma_{\gamma\gamma}$ as a function of R_{HE}/R_{LE}. At $R_{HE}/R_{LE} \sim 1$, $\Gamma_{\gamma\gamma}$ is similar or larger than Γ_{Tr} within errors.

The photosperic radius R_{ph} at which the jet becomes transparent to Thomson scattering, as well as the minimal bulk Lorentz factor Γ_{Tr} defining this transparency condition are computed as in Yassine et al. 2017.

$$R_{ph} \simeq \frac{\sigma_T \dot{E}}{8\pi c^3 m_p \bar{\Gamma}^3} \tag{5.6}$$

where $\sigma_T = 6.65 \times 10^{-29}\,\mathrm{m}^2$ is the Thomson cross-section, $\dot{E}$ is the total power injected in the flow, $m_p = 1.67 \times 10^{-27}\,\mathrm{kg}$ is the proton mass, and $\bar{\Gamma} = \frac{1+\kappa}{2}\Gamma_{\gamma\gamma}$ is the average Lorentz factor in the flow with κ the ratio between the highest and the lowest value of Γ_{bulk}. The transparency condition $R_{LE} \geq R_{ph}$ translates into:

$$\Gamma_{\gamma\gamma} > \Gamma_{Tr} \simeq \left[\frac{\sigma_T \dot{E}}{8\pi c^4 m_p t_{var}}\right]^{1/5} \tag{5.7}$$

where Γ_{Tr} is the bulk Lorentz factor corresponding to the transparency condition. The values of the mentioned quantities are reported in Table 5.16 along with the other results. Note that the value of $R_{ph} \sim 10^{14}$ cm is higher than the typical value of 10^{10-11} cm because of the high luminosity (see Table 5.15). Figure 5.8 presents $\Gamma_{\gamma\gamma}$ and Γ_{Tr} as a function of the ratio between the radii at which the high-energy emission and the low-energy emission have been produced. All contours in this figure have been obtained by accounting for the statistical errors quoted in Table 5.15, also including the systematic errors on E_{cut} discussed in § 5.2.5. This figure shows that at $R_{HE}/R_{LE} \sim 1$, $\Gamma_{\gamma\gamma}$ lies between 100 and 120 and is similar to or larger than Γ_{Tr}. The transparency condition is thus fulfilled, and the corresponding emission radius is similar or larger than the photospheric radius, at $\sim 10^{14}$ cm from the central engine (Table 5.16). **In summary, I find a moderate Lorentz factor of ~ 110, and that all of the observed high-energy emission of GRB 220101A took place just above its jet photosphere, in a region that is typical of internal shocks**.

Burst	z	$E_{cut,obs}$ [MeV]	$E_{cut,ref}$ [MeV]	Γ_{bulk}	Bibliography
GRB 090926A	2.1062[a]	370 -50/+60	1150 -155/+186	230-100	Yassine et al. 2017
GRB 100724B	unknown	20-60	-	100-400 depending on z	Vianello et al. 2018
GRB 160509A	1.17[b]	80-150	170-330	100-400	Vianello et al. 2018
GRB 170405A	3.510[c]	50	225	170-420	Arimoto et al. 2020
GRB 220101A	4.618[d]	40	230	105	This analysis

[a] Malesani et al. 2009.
[b] Tanvir et al. 2016.
[c] de Ugarte Postigo et al. 2017.
[d] Fu et al. 2022.

Table 5.17: List of LAT detected bursts which present a significant cutoff at high energies. For the ones with a redshift measurement the cutoff energy is also reported in the source reference frame.

5.5 Comparison with other similar LAT detected bursts

Table 5.17 lists the LAT detected bursts which present an high-energy cutoff and for which the Γ_{bulk} was estimated. For four of them a spectroscopic measurement of the redshift is available, thus I computed the high-energy cutoff in their reference frame. As a common feature the Γ_{bulk} of all the listed burst is order of ~ 100. For GRBs 090926A and 220101A the bulk Lorentz factor has been computed following the procedure described in the previous section. For GRBs 100724B and 160509A Vianello et al. 2018 also estimated directly the bulk Lorentz factor: two different models (the internal shocks motivated one of Granot et al. 2008, and the photospheric one by Gill et al. 2014) which also assume that the cutoff arises from intrinsic opacity to pair creation yield a Γ_{bulk} in the range $100 - 400$. For GRB 170405A Arimoto et al. 2020 also interpreted the depletion at high energies as arising from opacity to pair creation, and they provided a lower and upper limit of the bulk Lorentz factor by adopting the approach of Granot et al. 2008 to estimate the lower limit (170) and the approach of Gill et al. 2018 to estimate the upper limit (420).

The listed bursts are precious and rare cases in which a spectral cutoff at high energies has been detected. The approach presented in this chapter, following Hascoët et al. 2012 and Yassine et al. 2017, couples the value of the detected spectral cutoff with the observed emission variability, and yields a direct estimation of Γ_{bulk} regardless of the emission mechanism of the bulk spectral component. **Moreover, it allows to determine the radius at which the observed emission was produced, which is found to be similar to the typical radius of internal shocks (10^{14} cm). These results are consistent with the conclusions of the study of selected GBM bursts presented in § 3, and reinforces the internal-shock synchrotron origin of the non-thermal component of GRB spectra.**

Conclusions and perspectives

The physical mechanisms that are responsible for the keV-MeV prompt emission of GRBs are an active subject of debate. Two scenarios can be distinguished depending on the initial allocation of the energy budget. In the standard fireball model, the initial energy reservoir is the central engine gravitational energy, which is deposited as thermal energy in a plasma that is confined in a small volume. The subsequent thermal acceleration increases the jet kinetic energy which is dissipated by shocks into internal energy. Internal shocks accelerate particles with in turn emit synchrotron radiation. A thermal spectrum is also expected when the photospheric radius is reached, and observed in the first instants of the GRB prompt phase. In another scenario, the rotational energy of the central engine is transported by the Poynting flux, which accelerates the jet and/or is directly dissipated by physical mechanisms such as the magnetic reconnection. As a result, the prompt GRB spectra are a mixture of a thermal and a non-thermal component. The prompt emission of the majority of *Fermi* bursts is adequately described by spectral functions such as the Band one, which is generally believed to account the non-thermal emission. However, these functions are ad-hoc mathematical formulae, which do not rely on theoretical grounds. In my work I investigated the prompt emission spectra of *Fermi* GRBs within the framework of the internal shock model proposed by the "Institut d'Astrophysique de Paris" (IAP, Daigne et al. 1998). This numerical model couples the radiative processes, among which synchrotron emission, with the dynamical evolution of the GRB jet, providing realistic simulated light curves and spectra. I employed the Internal Shock Synchrotron Model (ISSM), which is a spectral function built directly on this model [Yassine et al. 2020], to determine to which extent it is able to account for the prompt spectra of *Fermi* GRBs.

At first, I get acquainted with the analysis tools necessary to analyse *Fermi* GRBs. In particular I used the *GBMtoolkit*, which is a tool developed within the *Fermi* GRB science group to perform GRB analysis. Among its broad capabilities, it allows to retrieve the observed data and prepare the spectral data for the analysis. By default the user is prompted to an interface to chose the desired intervals where to fit the background to estimate its contribution to the observed emission. I adapted the software to accomodate for a pre-defined number of time intervals. In this way it is possible to prepare the spectral data for a wide sample of *Fermi* GRBs. Secondly, I developed spectral analysis scripts based on the *pyXSPEC* fitting software, which implements the forward folding technique to compare the response folded spectral model with the GRB counts spectrum. Finally, I wrote post-processing scripts to display the analysis results.

As member of the *Fermi*/LAT collaboration I performed 18 Burst Advocate shifts, each one lasting one week. This experience helped me to familiarise with the LAT spectral analysis tools and to collaborate with the members of the *Fermi* GRB science group in distributing the results of the LAT analysis of remarkable detected bursts, such as GRB 220101A, and of follow-up observations of gravitational wave sources.

In order to investigate the prompt emission spectra of *Fermi* GRBs I carried on three complementary studies:

- **Analysis of the GBM 10-year GRB catalog**: I selected a significant sample of the GBM most fluent bursts and excluded the few cases which present one or more additional components in the keV-MeV range. 460 GRBs satisfied my selection criteria: in addition to the high fluence I required also a minimum detector signal to noise ratio to reach the spectroscopic precision necessary to distinguish the spectral models. The whole sample is 6 times greater than the sample previously considered by Yassine et al. 2020. I performed a time-integrated and time-resolved spectral analyses comparing the fitting performance and the fitted parameters of ISSM with ad-hoc models such as Band and SBPL. I

performed more than 37000 spectral fits. ISSM is a parametric function that represents the internal-shock synchrotron spectra in which the emission comes from a pulse or fraction of a pulse, but it has been tested only in time-integrated analysis. In this work ISSM is tested in time-resolved analysis for the first time. I defined three samples to study the performance of the spectral models, to estimate the high-energy spectral parameters (peak of their spectral energy distribution and high-energy spectral index), and the low-energy spectral index. Remarkably, ISSM outperforms all the other models in describing the prompt emission spectra both in time-integrated and in time-resolved analyses. At very high signal to noise ratio more than 80% of the spectra are well described by ISSM in both analyses, while only 23% and 32% respectively are well described by Band. As a result, the ISSM model is appropriate to describe the high-energy prompt emission spectra of GRBs, and it should be always preferred to the Band model, especially in (long) time intervals with a strong spectral evolution. Moreover, I confirmed that the peak of the spectral energy distribution E_p of ISSM is systematically greater than Band, and that the low and high-energy spectral indices α and β of ISSM are respectively harder and softer than the corresponding indices of Band. This is due to the continuous curvature of ISSM, which allows a greater parameter space to E_p, and lets the local photon index to increase asymptotically to harder values of α at low energies and to softer values of β at high energies. The local photon index at 10 keV, $\alpha_{10,ISSM}$, is above the slow-cooling value of $-2/3$, the hardest value expected from synchrotron theory, only for a small fraction of bursts (7%, Table 3.4) and time-resolved spectra (17%, Table 3.9). The vast majority of bursts and time-resolved spectra have an $\alpha_{10,ISSM}$ above the pure fast-cooling value $-3/2$, so the values found for $\alpha_{10,ISSM}$ are compatible with the intermediate marginally fast-cooling regime. The fast-cooling regime is suggested by the high luminosities observed in short time scales, but the pure fast-cooling regime is excluded so more variants of the fast cooling synchrotron model such as the marginally fast cooling should be more investigated in the future.

A physically motivated synchrotron interpretation of the prompt non-thermal emission of *Fermi* GRBs is then preferred over the description provided by ad-hoc models. Most of the fluent *Fermi* bursts find a good explanation within the framework of the internal shock synchrotron model, and no bright thermal component is required to describe their prompt emission spectra.

- **Photospheric emission in GRB prompt spectra**: this photospheric emission is expected in the standard fireball model, where the plasma of the ejecta expands under its own pressure to reach ultra-relativistic speeds. Previous analyses of the prompt emission spectra with the ad-hoc Band function revealed an excess at low-energy in some cases, which was interpreted as the contribution of such a photospheric component. I revisited the analyses of GRBs 100724B, 120323A, and 131014A in the framework of the internal shock synchrotron model and assessed the significance of a possible additional thermal component. I performed time-integrated and time-resolved analyses on the prompt emission spectra adopting Band and ISSM as non-thermal component and adding a thermal component in the form of a black-body (BB). I found that an additional thermal component is marginally detected with a confidence of 3σ and 4.4σ in the time-integrated spectra of GRBs 100724B and 120323A, respectively. In both cases the time-integrated spectra are best fitted by ISSM rather than Band, and adding the BB on ISSM improves marginally the fit. The time-integrated spectrum of GRB 131014A is adequately fitted by ISSM alone. I found a firm detection of the thermal component in one time bin of the time-resolved analysis. This time bin belongs to GRB 120323A, and in this case the ISSM+BB model outperforms all the others, with a statistical significance of 6.1σ for the additional thermal component.

  This work shows that the detection of a possible additional thermal component is highly dependent on the model chosen to describe the non-thermal one. Overall ISSM is preferred over Band to describe the emission spectra. The employment of a realistic model such as ISSM leaves little room for an additional thermal component. These results seem to favour an alternative scenario where the jet initial energy reservoir is partially constituted by the Poynting flux and not only by the thermal energy of the fireball in adiabatic expansion.

- **Analysis of the exceptional GRB 220101A**: I was BA when this GRB was detected by the LAT. It is the most distant LAT detected burst to date with a redshift $z = 4.618$. It is also a rare case in which a spectral cutoff is detected at high energies associated to a variable observed emission, along

with other 4 LAT detected bursts with similar feautures. I employed two different spectral models, Band and ISSM, with and without an high-energy cutoff to describe the prompt emission spectrum. Moreover, I employed two independent analysis chains, one based on *pyXSPEC* and one on *3ML*, and I compared their results to estimate the systematic errors on the spectral cutoff energies. As a common result, I found a significant cutoff in the prompt emission spectrum of GRB 220101A. The variability observed at high energies suggests that the spectral cutoff is due to opacity to pair creation. I directly estimated the bulk Lorentz factor of the jet and, at the same time, I localized the emission region of the observed variable emission, regardless of its nature. I found a moderate $\Gamma_{bulk} \sim 110$ and an emission radius of a few 10^{14} cm. This sets the emission region just above the photosphere, at a distance from the central engine that is typical of internal shocks, where synchrotron emission occurs. In conclusion, the observed prompt emission of GRB 220101A can be explained within the framework of the internal shock model. I presented the results of this work at the 7th Heidelberg International Symposium on High-Energy Gamma-Ray Astronomy in July 2022.

This work supports the internal shock synchrotron model as a plausible explanation of the *Fermi* GRB prompt emission spectra. Some applications and improvements can be envisaged to extend it in the future. For example, one should investigate how the new estimates of the SED peak energy provided by the ISSM model affect the so-called Amati and Yonetoku relations. These correlations have been tentatively (and unsuccessfully) used to standardize GRBs, and to constrain cosmological parameters as it is commonly performed with type-Ia supernovae. A more accurate spectroscopic precision should be seeked too. In this study the time bins of the time-resolved analysis are the optimal temporal segmentations of the burst light curves obtained with the Bayesian block approach, and requiring a signal to noise ratio high enough in each bin. An improved method should be developed to group the bins together until reaching a more realistic single-pulse precision, which is more suitable for the fit of the ISSM model which has been built on single-pulse simulations. Moreover, the assessment of a possible photospheric component in *Fermi* GRB prompt spectra should be systematically extended to the whole sample of the selected 460 bursts in time-integrated and in time-resolved analyses. This would show the contribution of the photospheric component in shaping the GRB prompt emission spectra, which as for now are satisfactorily described within the framework of the internal shock synchrotron model.

In this work I explored the capabilities of ISSM to describe the prompt emission spectra of *Fermi* GRBs. The relation between the spectral model parameters and the micro-physical parameters of the numerical internal shock model is still not precisely known. Simulations of the numerical model for different micro-physical parameters should be envisaged and relations between such parameters and the ISSM spectral parameters could be investigated. As following step the numerical internal shock model should be directly fitted to the observed data. This would require the realisation of a new and complex spectral analysis chain, for example based on a model truth bank and the spectral analysis chain developed in this work to achieve a direct data / model comparison.

Appendix A

Formulae

I present here the compilation of fit statistics that I adopted in my work. In the large sample limit each fit statistic converges to χ^2, the first of the presented fit statistics. More detailed information on each fit statistic can be found at Appendix B: Statistics in XSPEC.

- **Gaussian data**:

$$\chi^2 = \sum_{i=1}^{N} \frac{(y_i - m_i)^2}{\sigma_i^2} \tag{A.1}$$

  where the sum runs over the energy channels, y_i are the observed counts in the channel i, σ_i and m_i are the one sigma errors and the model expected number of counts for the same channel. This statistic is used for data that follow a Gaussian distribution.

- **Poisson data**:

  the likelihood for Poisson distributed data is:

$$L = \prod_{i=1}^{N} (tm_i)^{S_i} e^{-tm_i} / S_i! \tag{A.2}$$

  where S_i are the observed counts, t the exposure time, and m_i the predicted count rates based on the current model and instrumental response. The maximum likelihood-based statistic for Poisson data is given in Cash 1979:

$$C = 2 \sum_{i=1}^{N} (tm_i) - S_i \ln(tm_i) + \ln(S_i!) \tag{A.3}$$

  The final term depends only on the data so can be replaced by Stirling's approximation to give:

$$C = 2 \sum_{i=1}^{N} (tm_i) - S_i + S_i(\ln(S_i) - \ln(tm_i)) \tag{A.4}$$

  This fit statistic is called **Castor C-stat**, and it is what is used for the **statistic cstat** option in *XSPEC*.

- **Poisson data with Poisson background**:

$$W = 2 \sum_{i=1}^{N} t_s m_i + (t_s + t_b) b_i - S_i \ln(t_s m_i + t_s b_i) - B_i \ln(t_b b_i) - S_i(1 - \ln S_i) - B_i(1 - \ln B_i) \tag{A.5}$$

where t_s and t_b are the exposure times for the source and background spectra, B_i are the background data and b_i the predicted rates from the model of the expected background. This fit statistic is used when both the total counts spectra and the background counts spectra are Poisson distributed.

If there is no appropriate model for the background, it is still possible to define the fit statistic. After supposing that each bin in the background spectrum is given its parameters so that the background $b_i = f_i$, it is possible to express analytically f_i by maximizing the likelihood over which the fit statistic is based, i.e.:

$$L = \prod_{i=1}^{N} \frac{(t_s(m_i + b_i))^{S_i} \exp^{-t_s(m_i+b_i)}}{S_i!} \times \frac{(t_b b_i)^{B_i} \exp^{-t_b b_i}}{B_i!} \tag{A.6}$$

The resulting fit statistic is equal to W with $b_i = f_i$, where f_i is given by:

$$f_i = \frac{S_i + B_i - (t_s + t_b)m_i + d_i}{2(t_s + t_b)} \tag{A.7}$$

- **Poisson data with Gaussian background**:

$$PG = 2\sum_{i=1}^{N} t_s(m_i + b_i) - S_i \ln(t_s m_i + t_s b_i) + \frac{1}{2\sigma_i^2}(B_i - t_b b_i)^2 - S_i(1 - \ln S_i) \tag{A.8}$$

where σ_i are the source and background errors added in quadrature. This fit statistic is used when the total counts spectra are Poisson distributed, with a known background counts spectra which are Gaussian distributed. More specifically the background counts spectra is for example the result of polynomial fits. This is the case when preparing the spectral data with the *GBMtoolkit* and *gtburst*. In these cases the PG fit statistic is the more appropriate.

Appendix B

Comparison with the GBM Burst Catalog

This section presents the comparison of my time-integrated analysis versus the GBM catalog for the spectral models COMP, SBPL, and BAND. I considered the cases where the spectral fits were of good quality, namely their *PG-stat* reduced was smaller than 3. This selection had a low impact on the global sample. In fact, it selected 78% of the cases for COMP, 67% for SBPL, and 74% for BAND, as shown in Figure 3.5.

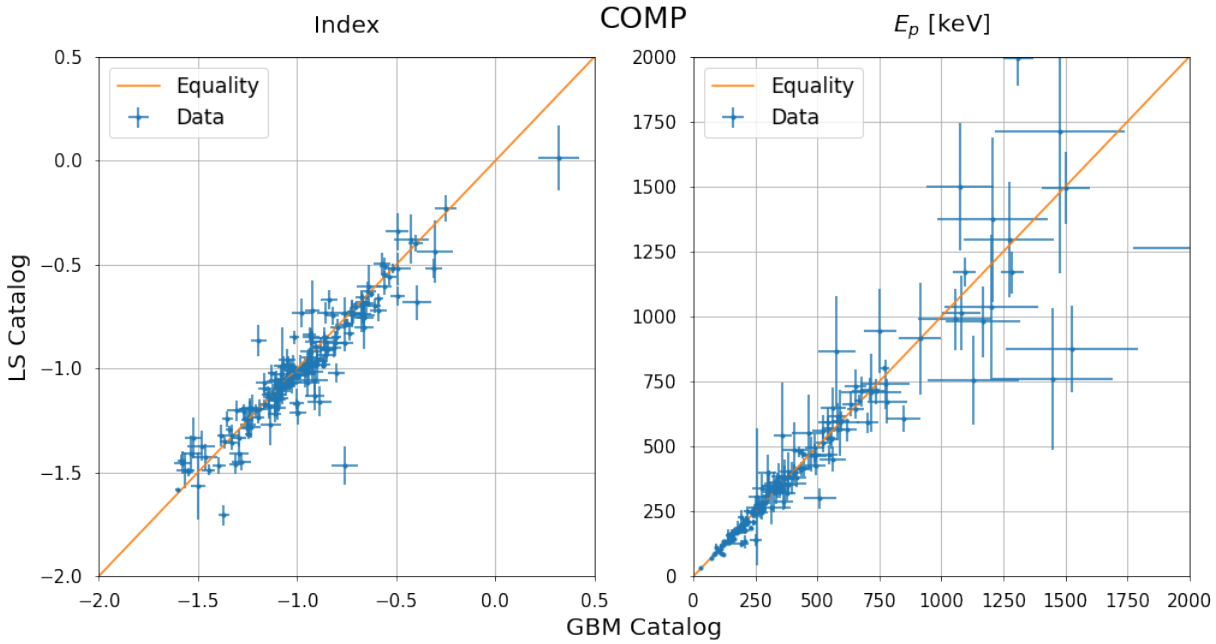

Figure B.1: Scatter plots of COMP parameters to compare my results to the GBM catalog results.

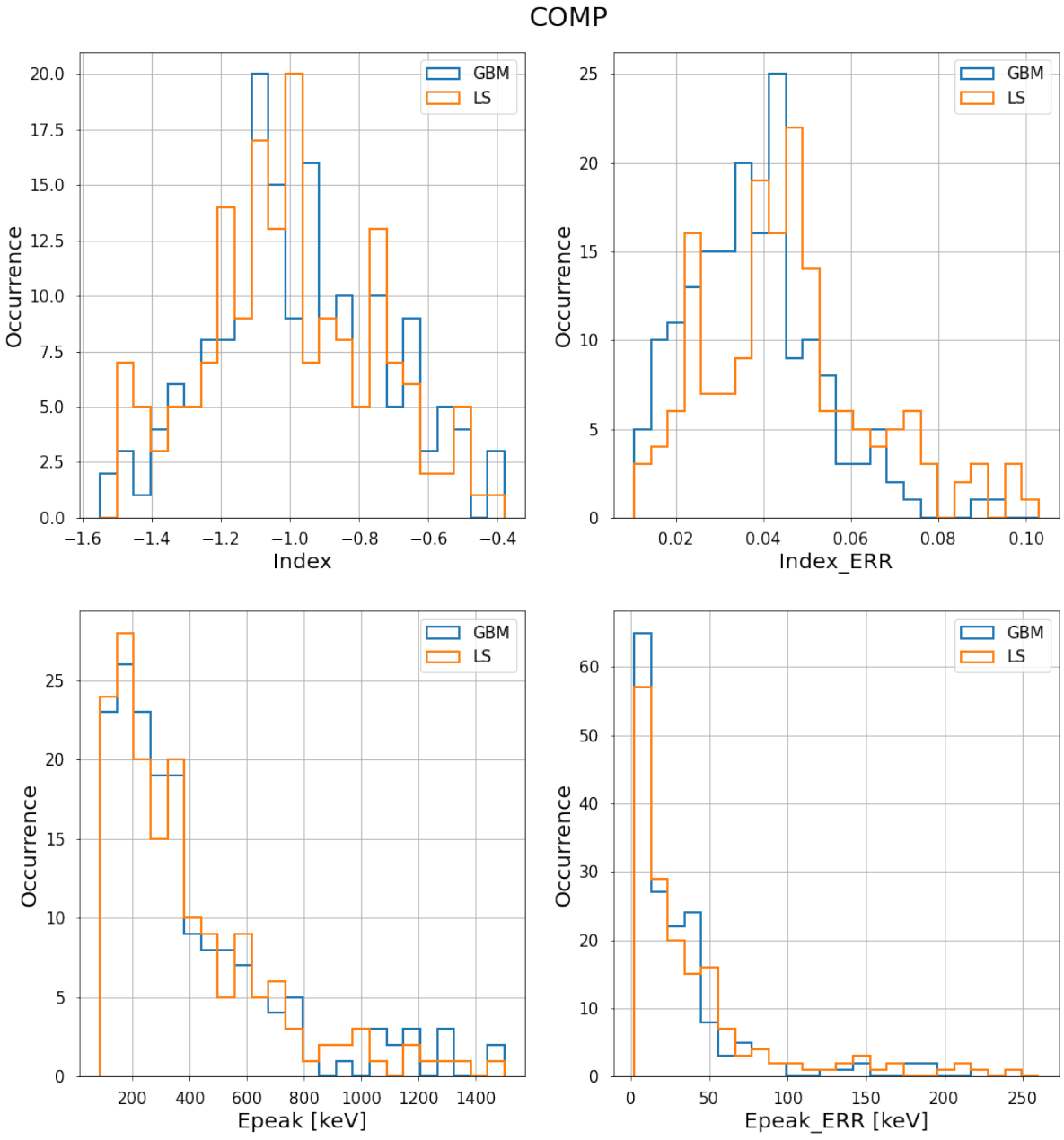

Figure B.2: Histograms of COMP parameters and their errors to compare my results to the GBM catalog results.

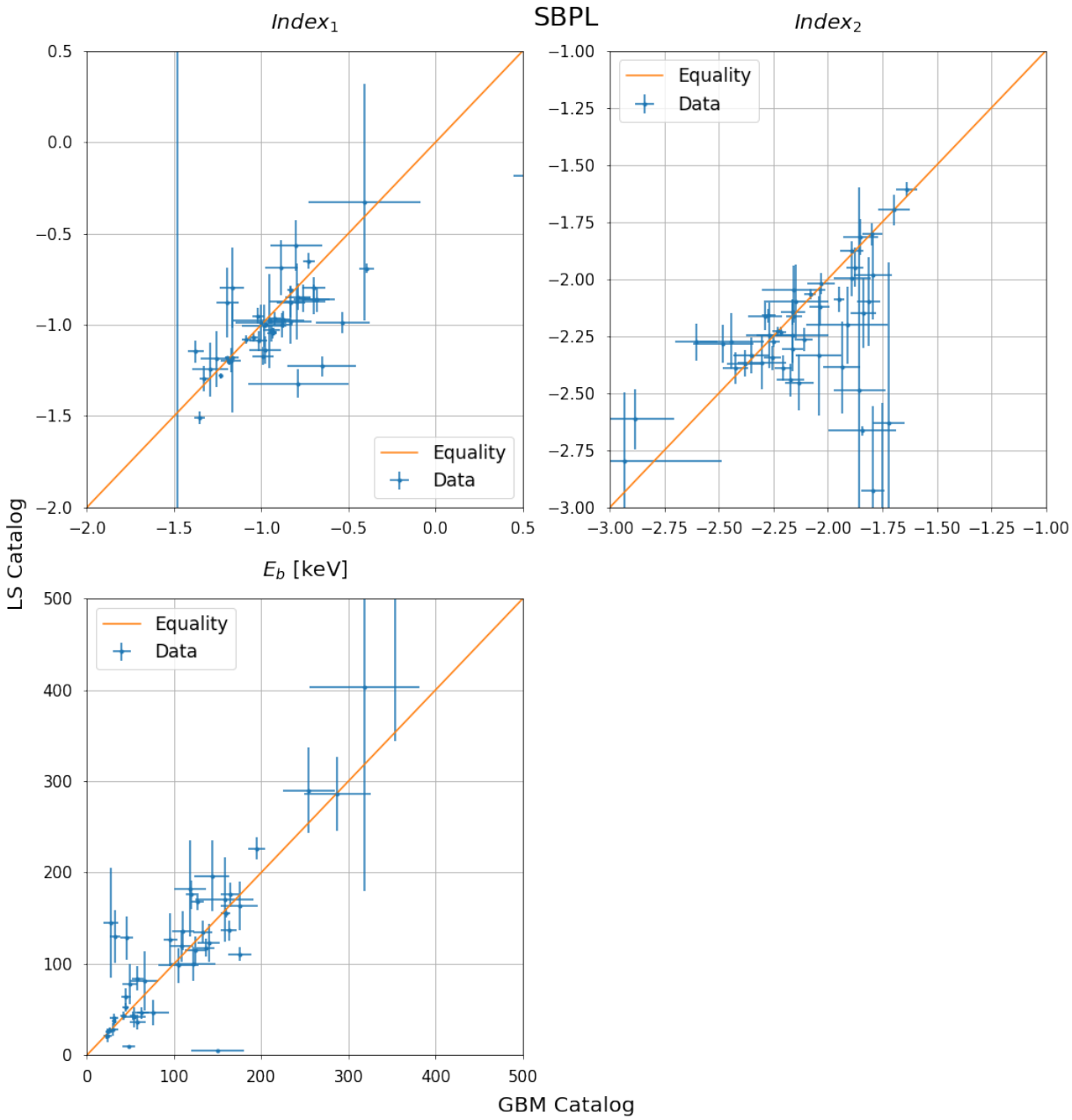

Figure B.3: Scatter plots of SBPL parameters to compare my results to the GBM catalog results.

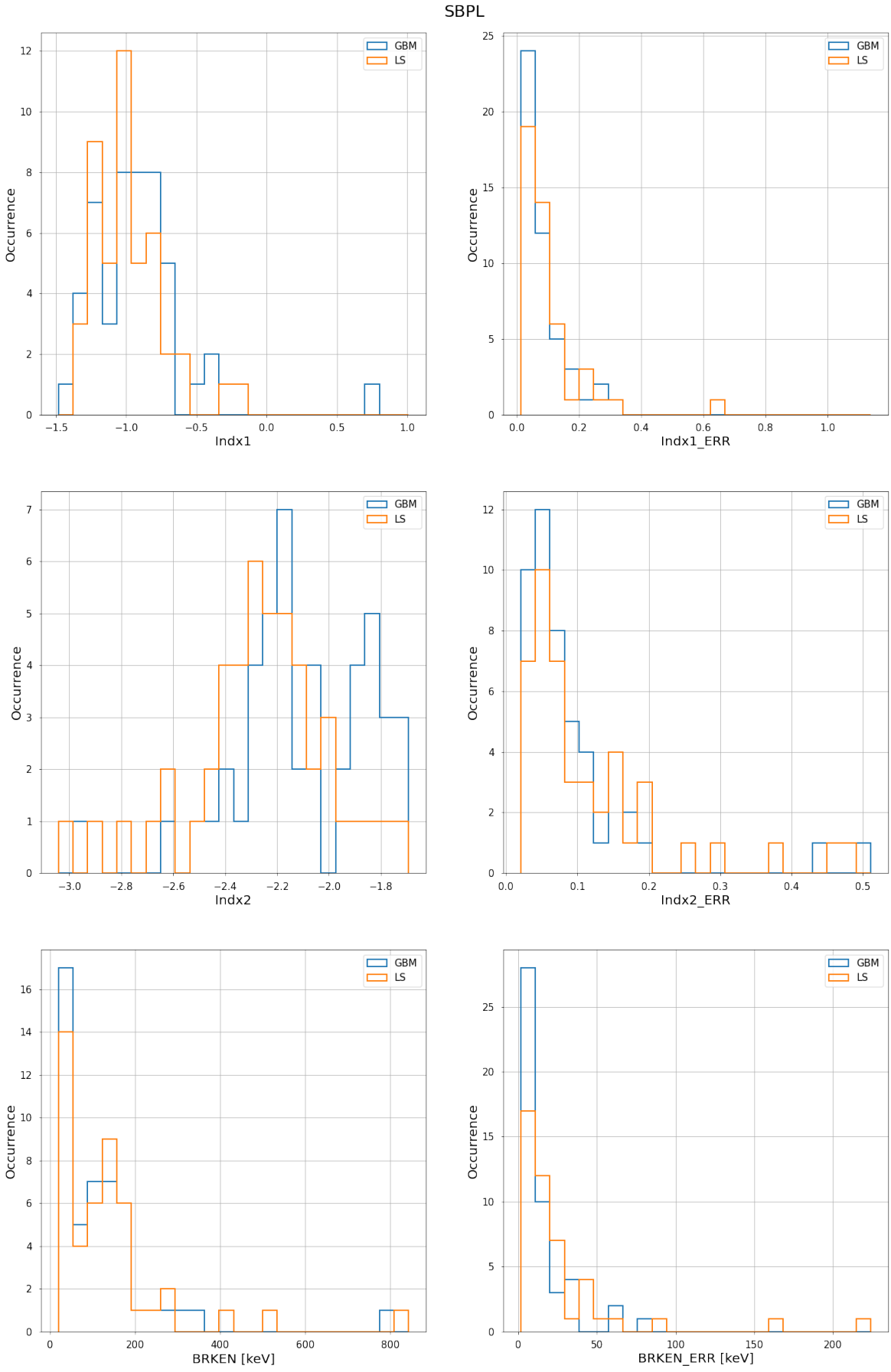

Figure B.4: Histograms of SBPL parameters and their errors to compare my results to the GBM catalog results.

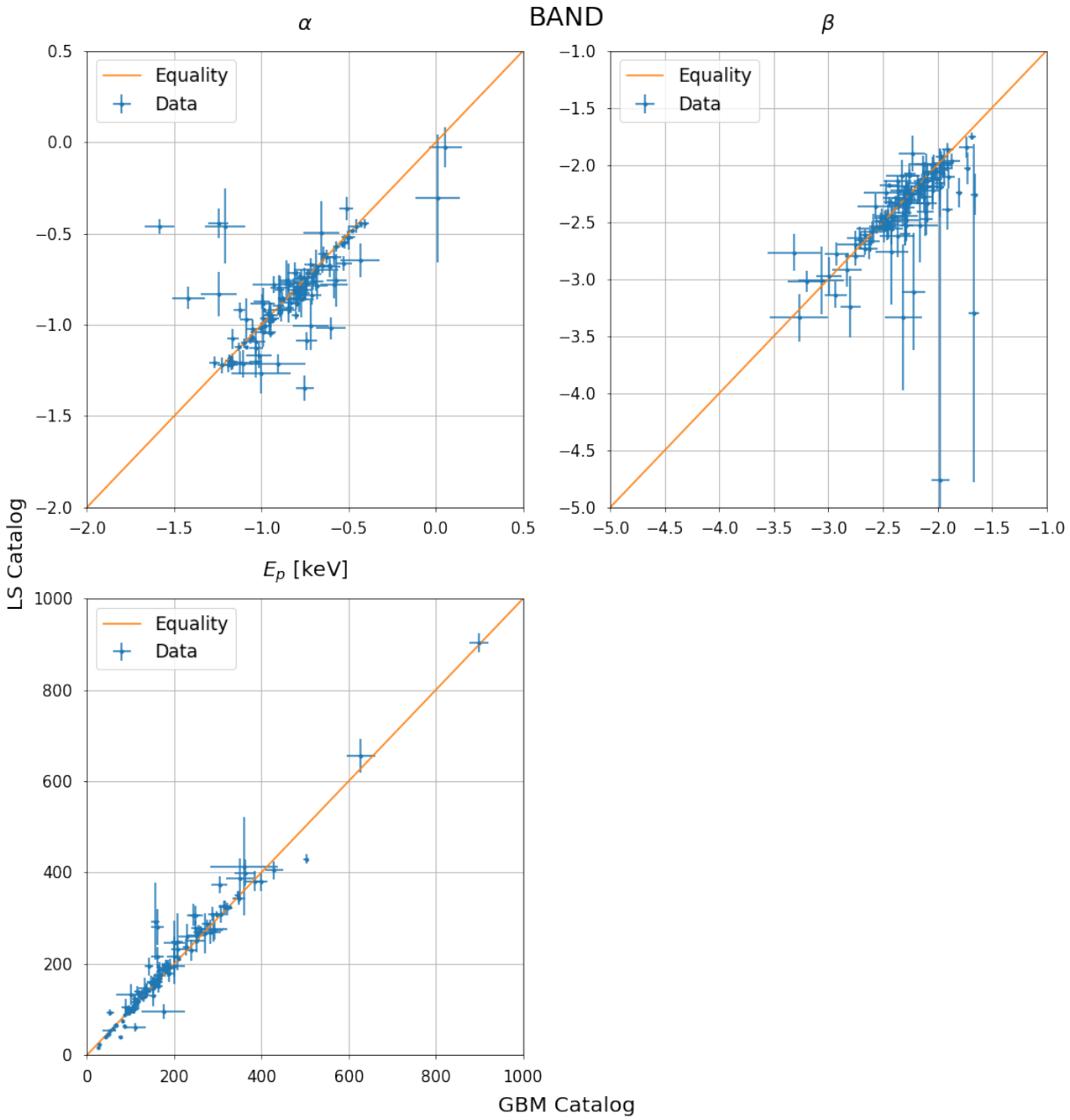

Figure B.5: Scatter plots of BAND parameters to compare my results to the GBM spectral catalog results.

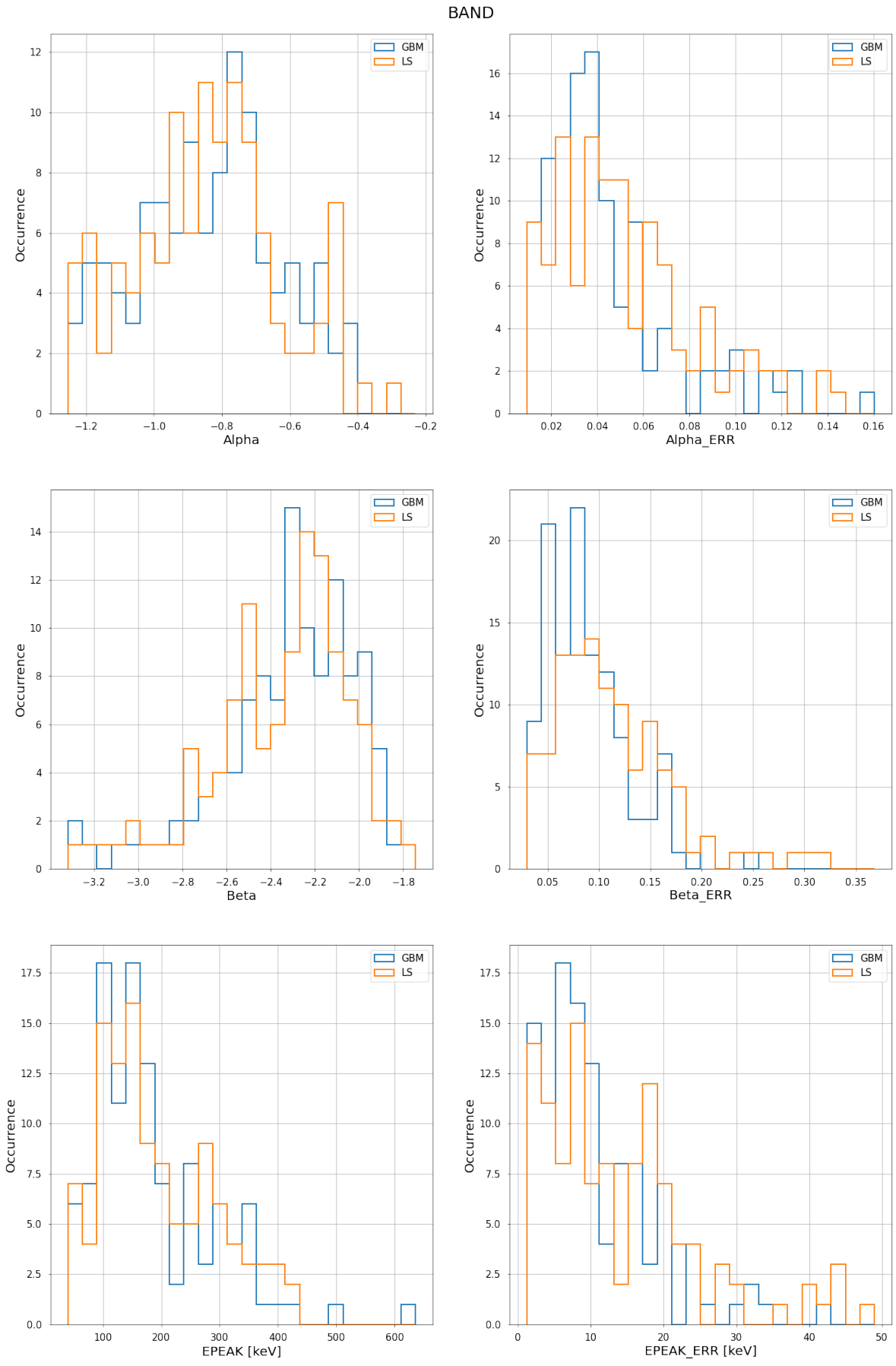

Figure B.6: Histograms of BAND parameters and their errors to compare my results to the GBM spectral catalog results.

Appendix C

Résumé du travail de thèse de Lorenzo Scotton

Titre: Analyse et interprétation des sursauts gamma de *Fermi* dans le cadre d'un modèle d'émission synchrotron aux chocs internes, et contribution à l'astronomie multi-messagers

C.1 Les sursauts gamma à haute énergie

Les sursauts gamma (Gamma-Ray Bursts en anglais, ou GRBs) sont des sources astrophysiques transitoires très énergétiques qui apparaissent de manière isotrope dans le ciel et à des distances cosmologiques. Leur luminosité extrêmement élevée suggère qu'ils sont produits par des événements cataclysmiques tels que l'effondrement d'une étoile massive ou la fusion d'un système binaire d'objets compacts. Dans les deux scénarios, il est généralement admis que le moteur central d'un GRB est un trou noir de masse stellaire qui alimente un éjecta collimaté (jet) ultra-relativiste qui accélère les particules chargées, lesquelles émettent un rayonnement électromagnétique.

Les GRBs sont observés suivant deux phases consécutives : une émission précoce, rapide et très variable de rayons X durs et gamma est observée durant une fraction de seconde jusqu'à plusieurs minutes. Cette émission dite prompte est suivie d'une émission rémanente de longue durée et à décroissance régulière et rapide, durant quelques heures jusqu'à plusieurs jours voire mois suivant les cas. Dans le scénario communément admis de la boule de feu, le jet devient transparent à son propre rayonnement à une distance de quelques 10^{11-12} cm du moteur central (rayon photosphérique). A un rayon de l'ordre de 10^{14-15} cm, l'énergie cinétique du jet est dissipée via des chocs internes ou par reconnexion magnétique. L'énergie interne est distribuée entre le champ magnétique turbulent et une certaine fraction des particules chargées qui sont accélérées et émettent un rayonnement gamma non thermique (processus synchrotron et Compton inverse). Ce rayonnement émis dans la phase prompte est caractérisé par une grande variabilité temporelle et il est principalement détecté dans la gamme d'energie keV-MeV. A plus grande distance du moteur central (10^{16-17} cm), le jet heurte le milieu environnant et produit un choc ulta-relativisite extrêmement violent qui accélère les particules chargées. Leur rayonnement non thermique décroît rapidement avec le temps tout en se décalant vers les plus grandes longueurs d'onde (jusqu'au domaine radio).

Lorsque la distance de luminosité d'un GRB est connue (par la mesure de son décalage cosmologique vers le rouge), la vitesse du jet (i.e. son facteur de Lorentz d'ensemble Γ_{bulk}) peut être contrainte à partir des observations des émissions prompte et rémanente. Lorsque l'émission gamma en phase prompte présente une variabilité rapide, une limite inférieure peut être estimée à partir de l'énergie du photon le plus énergétique détecté. Dans les rares cas où une cassure spectrale est détectée en fin de spectre, Γ_{bulk} peut être estimé directement et la région d'émission peut être localisée dans le jet.

La partie keV-MeV du spectre différentiel en photons d'un GRB fluent est typiquement bien décrite par la fonction phénoménologique de Band, qui consiste en deux lois de puissance reliées de manière lisse par une coupure exponentielle. Les valeurs typiques de l'indice spectral à basse et haute énergie sont -1.1 et -2.20, respectivement (catalogue spectral de l'instrument GBM de l'observatoire *Fermi*, Poolakkil et al.

2021). A plus haute énergie (> 100 MeV), l'émission observée est globalement retardée et une composante spectrale supplémentaire est nécessaire sous la forme d'une loi de puissance pour la majorité des GRBs les plus brillants. Cette émission dure aussi typiquement plus longtemps que l'émission prompte keV-MeV et son flux décroît avec le temps sous la forme d'une loi de puissance d'indice ~ -1 (2nd catalogue GRB du LAT, Ajello et al. 2019). En raison de ces caractéristiques, l'émission au GeV est souvent attribuée à la phase de rémanence. Cependant, certains GRBs tels que 090926A et 131008A présentent une variabilité temporelle remarquable qui suggère qu'elle peut également trouver son origine au sein du jet.

L'origine de l'émission prompte des GRBs fait encore l'objet de débats. Deux principaux scénarios physiques ont été proposés : (i) les modèles synchrotron invoquent le rayonnement synchrotron émis par des particules accélérées dans les chocs internes ou par reconnexion magnétique. Dans ces modèles, la principale source d'énergie est le flux de Poynting émis par le moteur central et le réservoir thermique du jet ; (ii) les modèles photosphériques invoquent le rayonnement thermique émis par la boule de feu en expansion adiabatique. Dans cette deuxième classe de modèles, le réservoir d'énergie est principalement thermique. Les deux scénarios ont leurs propres limites : les modèles synchrotron purs impliquent un indice spectral à basse énergie aussi petit que -1.5, tandis que les modèles photosphériques prédisent des valeurs plus élevées, mais difficilement conciliables avec la valeur observée typique de ~ -1.1. Certaines solutions du côté théorique ont été proposées, comme des variantes des modèles synchrotron qui prédisent des valeurs plus dures de l'indice spectral à basse énergie, qui sont plus cohérentes avec les valeurs observées. Alternativement, invoquer des processus de dissipation au niveau de la photosphère pourrait conduire à des spectres non thermiques plus réalistes.

Dans mon travail de thèse, j'ai étudié le modèle de chocs internes développé par l'équipe de l'Institut d'Astrophysique de Paris. Ce modèle numérique simule les chocs internes sous la forme de collisions entre des couches se déplaçant à des vitesses différentes à l'intérieur du jet. Le code numérique couple les processus radiatifs avec l'évolution dynamique des conditions physiques à l'intérieur du jet. Les résultats du code sont des spectres et des courbes de lumière de GRB dans le référentiel de l'observateur. Comme il n'a pas encore été possible d'ajuster directement ce modèle numérique aux données en raison de sa mise en œuvre complexe, une fonction spectrale qui agit comme un proxy de ce modèle a été développée par Yassine et al. 2020. Baptisée *Internal Shock Synchrotron Model* (ISSM), elle a été construite à partir des spectres keV-MeV d'un sursaut gamma synthétique simulé par le code numérique et dont la courbe de lumière est constituée d'un pulse unique.

C.2 Le télescope spatial à rayons gamma *Fermi*

Fermi est un observatoire spatial consacré à l'observation du ciel à haute énergie. La charge utile de son satellite comprend deux instruments: le Large Area Telescope (LAT) et le Gamma-ray Burst Monitor (GBM). Ensemble, ces deux instruments fournissent une couverture spectrale qui s'étend sur plus de 7 décades en énergie (10 keV à plus de 300 GeV), et observent une large portion du ciel.

Fermi a été lancé le 11 juin 2008 en orbite basse ($\sim$ 565 km) avec une inclinaison de 25.3°. Ses instruments sont composés de matériaux qui ne se dégradent pas avec le temps, et après plus de 14 ans, ils continuent de fonctionner à pleine efficacité.

C.2.1 Le Gamma-ray Burst Monitor

Le Gamma-ray Burst Monitor (GBM) se compose de 12 scintillateurs en iodure de sodium (NaI) placés autour du satellite de manière à couvrir la portion du ciel non occultée par la Terre la plus vaste et la plus uniforme possible. Ensemble, ils offrent un champ de vue de 9 stéradians, soit 70% du ciel. Ces scintillateurs sont sensibles dans la gamme d'énergie $8 - 1000$ keV, et couvrent la majeure partie des spectres prompts des GRBs. Ils sont utilisés pour localiser les GRBs et d'autres sources transitoires de rayons gamma. Deux détecteurs au germanate de bismuth (BGO) accompagnent les NaIs : ils sont sensibles dans la gamme d'énergie de 150 keV à 30 MeV, fournissant un recouvrement spectral avec les NaIs et le LAT. Les 2 BGOs sont placés de part et d'autre du satellite pour garantir que chaque GRB soit observable par au moins l'un d'entre eux.

Le GBM produit normalement deux types de données, CSPEC et CTIME, qui sont des histogrammes de spectres de comptage avec une résolution spectrale et temporelle différente. Lorsqu'un sursaut gamma se produit, des données *Time Tagged Events* (TTE) sont générées: elles contiennent la date d'arrivée et le canal d'énergie mesuré correspondant pour chaque événement.

C.2.2 Le Large Area Telescope

Le Large Area Telescope (LAT) est le principal instrument à bord de *Fermi*. Son objectif scientifique est l'étude et la cartographie du ciel de haute énergie. Il vise ainsi à détecter et identifier les sources de photons gamma, à discerner l'origine des émissions gamma diffuses galactique et extra-galactique, et à comprendre les mécanismes physiques à l'œuvre dans les phénomènes de haute énergie tels que les noyaux actifs de galaxie, les pulsars, les restes de supernova, et les sources transitoires tels que les GRBs.

Le LAT est un télescope imageur à conversion de paires à haute énergie. Il possède un large champ de vue de 2.4 stéradians, couvrant ainsi environ 20% du ciel à chaque instant. Cet instrument est sensible de 20 MeV à plus de 300 GeV, et il est constitué de plusieurs sous-systèmes : (i) un convertisseur-trajectographe composé de feuilles de tungstène pour la conversion des photons gamma en paires, et de détecteurs de précision au silicium pour la mesure de leur direction d'origine, (ii) un calorimètre au CsI(Tl) pour la mesure de leur énergie, (iii) un détecteur anti-coïncidence segmenté qui couvre le trajectographe pour le rejet d'une grande partie du fond de rayonnement cosmique chargé, (iv) un système de déclenchement et d'acquisition de données programmable. Le principe de détection d'un photon gamma incident est sa conversion en une paire électron-positron lorsqu'il interagit avec un atome de tungstène. Cette paire est suivie par le trajectographe et son énergie est collectée par le calorimètre.

Les événements détectés par le LAT sont sélectionnés et classés en fonction de leur probabilité d'être des photons plutôt que des rayons cosmiques chargés, et de la qualité de leur reconstruction. En particulier, ils sont regroupés en différentes classes d'événements correspondant à différents jeux de fonctions de réponse instrumentale (surface effective de détection, fonction de redistribution en énergie, fonction d'étalement du point). La classe pertinente pour l'analyse des GRBs est la classe *transient*. Elle conserve une grande partie des événements, qui sur de courtes échelles de temps de quelques dizaines de secondes sont principalement issus du sursaut, avec une contribution négligeable du fond.

Chaque événement dans les données standard du LAT est caractérisé par son énergie mesurée, sa direction reconstruite, sa date d'arrivée et sa classe. Les données du LAT comprennent également les événements dits "de basse énergie" (*LAT Low Energy*, ou LLE), détectés par le LAT au-dessus de 30 MeV et issus d'une sélection moins stricte que celle des données standard afin d'augmenter autant que possible la surface effective de détection et la statistique en photons disponible. Les données LLE étendent la couverture spectrale du LAT jusqu'à la gamme d'énergie des BGOs du GBM et la recouvrent. Ceci améliore nettement la mesure spectrale de l'émission prompte keV-MeV des GRBs. Enfin, les données du LAT contiennent l'évolution en fonction du temps de la position et de l'orientation du satellite sur son orbite.

C.2.3 Analyse spectrale

Analyse spectrale avec le GBM

La réponse des détecteurs du GBM étant hautement non linéraire et difficile à inverser, le spectre vrai d'une source détectée par cet instrument ne peut être reconstruit simplement par déconvolution. Une convolution vers l'avant (*forward folding*) est préférée, dans laquelle la matrice de réponse de chaque détecteur du GBM (i.e. la matrice de redistribution de l'énergie, multipliée par la surface effective de détection) est convoluée avec le modèle de spectre différentiel en photons de la source, dont les paramètres sont ajustés de sorte que le taux différentiel d'événements prédit soit statistiquement en accord avec le spectre en coups réellement observé (après prise en compte du spectre en coups du fond, estimé généralement en utilisant les données recueillies quelques dizaines ou centaines de secondes avant et après le sursaut). L'analyse spectrale des observations d'un GRB avec le GBM repose ainsi sur la méthode fréquentiste d'estimation de paramètres par maximisation d'une fonction de vraisemblance L, qui représente la probabilité d'obtenir les coups observés (coups spectraux totaux et coups du fond) étant donné le modèle spectral supposé et ses paramètres. La vraisemblance est maximisée par rapport aux paramètres libres du modèle : le meilleur jeu de paramètres est

celui qui maximise la fonction de vraisemblance. En pratique, la fonction $-2\log L$ (statistique d'ajustement) est minimisée. En outre, j'ai choisi la statistique d'ajustement *PG-stat* disponible dans le logiciel *pyXSPEC*, car le spectre en coups observé suit une distribution de Poisson, tandis que le spectre en coups du fond est supposé gaussien car résultant d'un ajustement préalable des données pre- et post-sursaut.

Analyse spectrale avec le LAT

La méthode statistique utilisée pour détecter un GRB avec le LAT est le test du rapport de vraisemblance. Ce test compare deux hypothèses: l'une comprenant le fond (hyp 0) et l'autre comprenant le fond plus la source supplémentaire à une position donnée et avec des paramètres spectraux définis (hyp 1). Pour chaque hypothèse, la vraisemblance est maximisée et la statistique du test $TS = -2\log\left(L_{hyp\,0,max}/L_{hyp\,1,max}\right)$ est évaluée. Une fois que la localisation de la source est connue, et que son modèle est choisi comme une loi de puissance avec l'indice -2 comme pour de nombreux GRBs détectés par le LAT, la signification statistique gaussienne de la source supplémentaire peut être estimée comme $\sigma_{GRB} = \sqrt{TS}$. Une détection est déclarée lorsque $TS_{GRB} > 25$ ($\sigma_{GRB} > 5\sigma$). L'analyse spectrale subséquente repose aussi sur la technique de convolution vers l'avant, implémentée dans la suite logicielle publique des *Fermi tools*.

Travail effectué dans le cadre de la thèse

L'objectif principal de ma thèse est d'évaluer dans quelle mesure le modèle synchrotron aux chocs internes est capable de rendre compte des spectres prompts des GRBs observés par *Fermi*. Dans la première partie de mon travail, j'ai évalué la capacité du modèle ISSM et de la fonction de Band à décrire les spectres keV-MeV des sursauts les plus fluents du GBM. J'ai comparé les valeurs ajustées des indices de basse et haute énergie aux prédictions du modèle aux chocs internes. Par ailleurs, une composante thermique peut contribuer aux spectres prompts des GRBs comme expliqué au § C.1. Dans certains cas remarquables tels que les GRBs 100724B, 120323A, et 131014A, une composante thermique est significativement détectée en plus de la composante non thermique de Band. Dans la deuxième partie de mon travail, j'ai réexaminé ces conclusions et évalué la signification statistique de cette composante thermique additionnelle lorsque la composante non thermique principale est ajustée par le modèle ISSM. Enfin, mon travail de thèse était également consacré au suivi avec le LAT des sursauts détectés par le GBM et des sources d'ondes gravitationnelles. Le sursaut très distant et énergétique GRB 220101A a été détecté par le LAT durant l'une de mes astreintes en tant que *Burst Advocate* (BA). Comme quelques autres sursauts détectés par le LAT, GRB 220101A est très intéressant de part l'atténuation spectrale qu'il présente aux plus hautes énergies lors d'un épisode d'émission hautement variable en phase prompte. Ces caractéristiques rares indiquent qu'une opacité importante à la création de paires empêche le rayonnement gamma le plus énergétique de s'échapper du jet, et peuvent être utilisées pour inférer les propriétés macroscopiques de ce dernier. Dans le cadre du modèle d'opacité de Hascoët et al. 2012 déjà utilisé par Yassine et al. 2017, j'ai ainsi analysé GRB 220101A dans la troisième partie de mon travail, j'ai estimé la vitesse de son jet et localisé la région des émissions de haute énergie.

C.3 LAT Burst Advocate

Les données du LAT sont automatiquement analysées par deux pipelines lorsqu'une alerte GRB est reçue, par exemple en provenance du GBM ou de l'observatoire Swift. Les résultats de l'analyse sont le niveau de détection de la source (signification statistique), sa localisation et l'estimation de son spectre (indice spectral, flux au-delà de 100 MeV). Le rôle du BA est de vérifier les résultats des pipelines, de les affiner au besoin par des analyses complémentaires, et d'envoyer dès que possible la meilleure localisation du LAT de la source aux autres observatoires via une circulaire GCN (*Gamma-ray Coordinates Network*). Un canal *Slack* dédié est disponible pour discuter avec les autres membres du groupe scientifique *Fermi* GRB afin d'évaluer si la source détectée est bien un GRB ou non. Au cours de ma thèse j'ai effectué 18 astreintes BA, et j'ai contribué à 5 circulaires GCN de GRBs et à 7 circulaires GCN de suivi de sources d'ondes gravitationnelles.

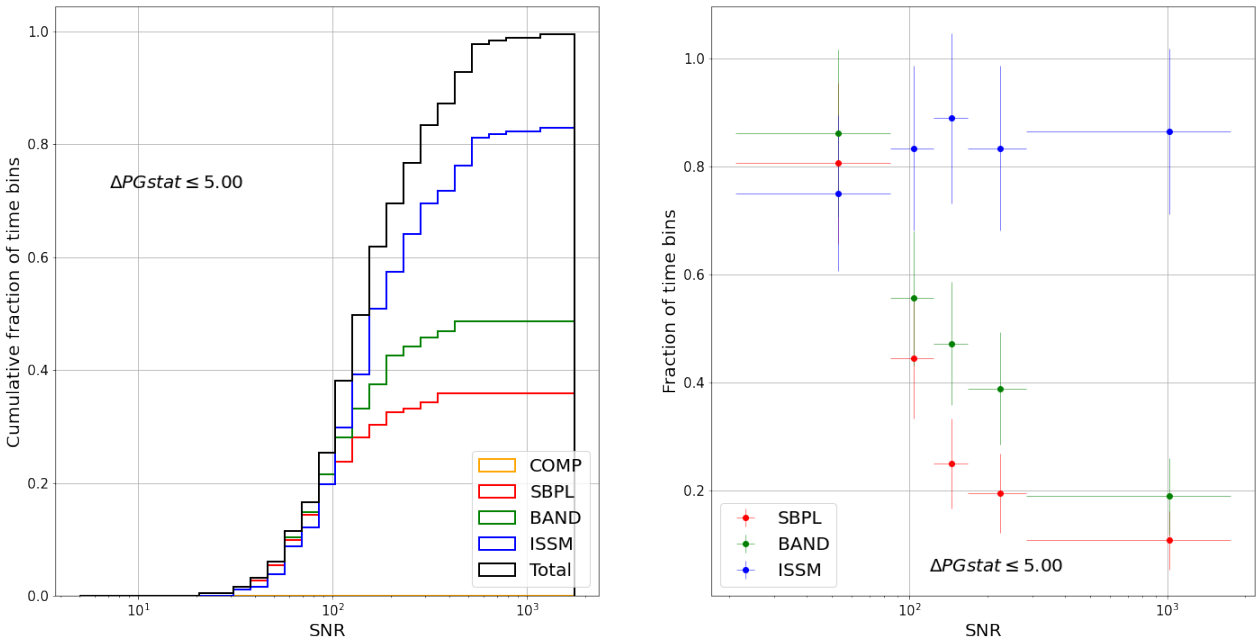

Figure C.1: À gauche: distribution cumulative de *SNR* pour chaque modèle lorsque le $\Delta PGstat$ correspondant par rapport au modèle de référence est inférieur à 5 (analyse spectrale intégrée en temps). La ligne noire indique la distribution cumulative de *SNR* sur la totalité des sursauts. À droite: fraction de sursauts avec la même coupe sur $\Delta PGstat$ en fonction du *SNR*.

C.4 L'émission prompte non thermique des GRBs de *Fermi*

Lors de la reconstruction du spectre prompt des GRBs de *Fermi*, leur composante non thermique est souvent ajustée de manière purement phénoménologique par des modèles ad-hoc tels que Band et SBPL (*Smoothly Broken Power Law*), qui sont des fonctions mathématiques sans réel fondement physique. Dans cette partie de mon travail, j'ai étudié l'émission prompte à l'aide de la fonction paramétrique ISSM qui fournit une représentation spectrale du modèle numérique d'émission synchrotron aux chocs internes. Cette fonction a été construite à partir des spectres keV-MeV d'un sursaut gamma synthétique dont la courbe de lumière est constituée d'un pulse unique. Yassine et al. 2020 a montré qu'elle est appropriée pour ajuster les spectres intégrés en temps des sursauts gamma observés par *Fermi*.

J'ai consolidé cette étude et l'ai étendue avec l'ajout d'une analyse spectrale résolue en temps. J'ai sélectionné 460 GRBs détecté par le GBM en utilisant des critères de sélection basés sur la fluence du GRB, sur la position du GRB dans le champ de vue des détecteurs, sur la qualité de l'ajustement du fond, et enfin sur le rapport signal/bruit du GRB dans les détecteurs (*SNR*). Cet échantillon est six fois plus important que l'échantillon précédemment considéré par Yassine et al. 2020. J'ai développé une chaîne d'analyse complète comprenant la préparation des données à l'aide de la suite logicielle *GBMtoolkit* (développée au sein du groupe scientifique *Fermi* GRB), l'analyse spectrale basée sur *pyXSPEC*, et le post-traitement des résultats à l'aide de nombreux scripts python. Pour chaque GRB de l'échantillon, j'ai effectué des analyses intégrées et résolues en temps afin de tester les performances d'ajustement de ISSM et de Band et de comparer leurs paramètres spectraux avec les prédictions théoriques.

Le panneau gauche de Figure C.1 montre la distribution cumulative du *SNR* pour chaque modèle lorsque le modèle donne un $\Delta PGstat$ inférieur à 5 par rapport au modèle le mieux ajusté (modèle de référence) dans l'analyse intégrée en temps. Le panneau de droite montre la fraction de sursauts avec la même coupure sur $\Delta PGstat$ en fonction du *SNR* pour la même analyse. On constate que ISSM surpasse toutes les autres fonctions spectrales pour décrire les spectres d'émission prompte dans les analyses intégrées et résolues en temps. Lorsque le *SNR* est élevé, plus de 80% des spectres sont bien décrits par ISSM, alors que seulement 23% et 32% sont bien décrits par la fonction de Band dans les deux types d'analyse, respectivement.

Les valeurs de l'énergie du pic de la distribution spectrale d'énergie (*Spectral Energy Distribution*, ou SED) des ajustements rélisés avec la fonction ISSM sont systématiquement supérieures à celles de la fonction

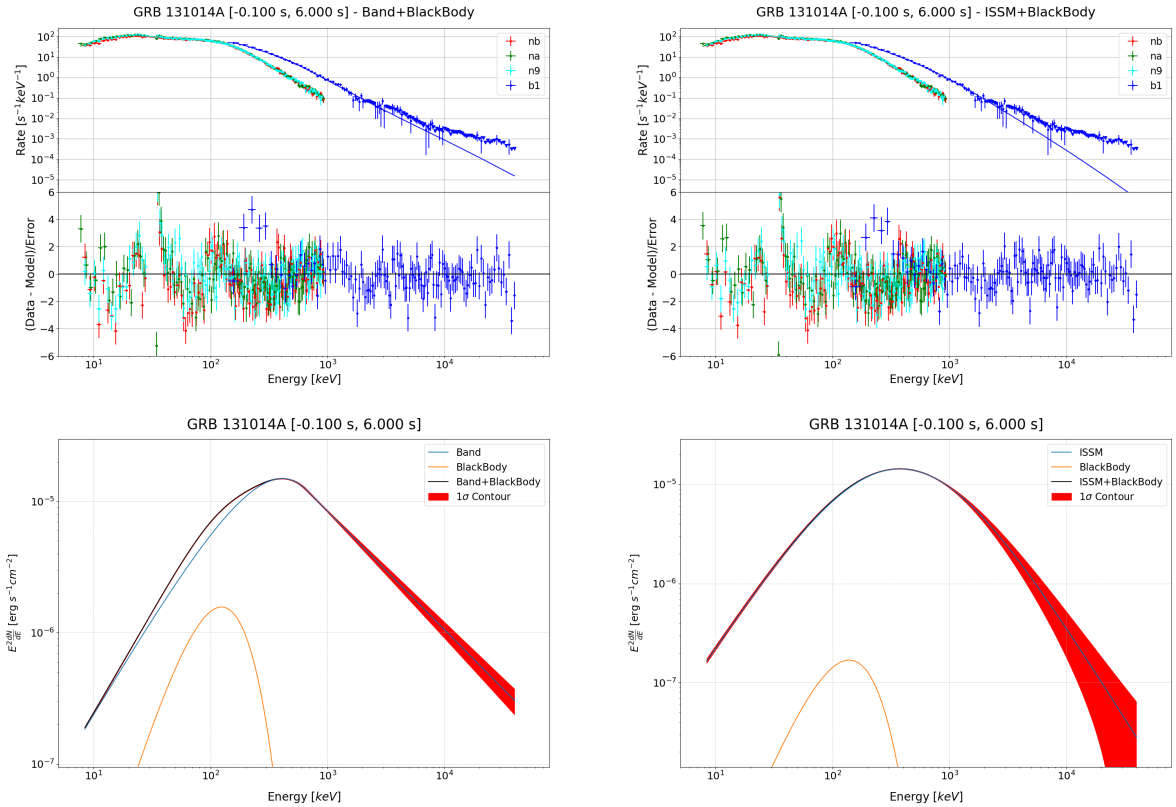

Figure C.2: Résidus et SED lors de l'ajustement de Band+BB (gauche) et ISSM+BB (droite) au spectre intégré en temps de GRB 131014A.

de Band, et l'indice de basse énergie et l'indice de haute énergie sont plus durs et plus doux que les indices spectraux correspondants de Band, comme l'avait déjà constaté Yassine et al. 2020, mais cette fois sur un échantillon plus grand et en analyse résolue en temps.

Il est intéressant de noter que l'indice de basse énergie de ISSM est supérieur à la valeur de $-2/3$ maximale possible dans la théorie du rayonnement synchrotron (dans le cas d'un refroidissement synchrotron lent des électrons) uniquement pour une petite fraction des sursauts (7%) et des spectres résolus en temps (17%). Dans la grande majorité des cas, l'indice de basse énergie est supérieur à la valeur de refroidissement rapide pur de $-3/2$ (avec un intervalle de confiance de 95%). La plupart des sursauts et des spectres résolus en temps sont ainsi compatibles avec le régime intermédiaire de refroidissement rapide marginal. La valeur moyenne des indices de haute énergie est quant à elle conforme aux prédictions théoriques du rayonnement synchrotron.

C.5 L'émission photosphérique des GRBs de *Fermi*

Le modèle dit de la boule de feu prédit la présence d'une composante photosphérique aux premiers instants de l'émission prompte des GRBs. Une preuve en a été donnée par GRB 090902B, où la composante photosphérique est dominante, et par GRB 100724B, 120323A, et 131014A où une émission thermique sous-dominante accompagne la composante principale, non thermique, décrite par la fonction de Band. Dans cette partie de mon travail, j'ai réexaminé ces trois sursauts et évalué la pertinence d'une composante thermique additionnelle lorsque la composante non thermique principale est ajustée par la fonction ISSM, plus physique. Avec ISSM, la composante thermique s'avère moins nécessaire statistiquement pour les GRB 100724B et 120323A. Par ailleurs, Figure C.2 montre les spectres en coups ajustés, les résidus et les SED issus de l'ajustement du spectre intégré en temps de GRB 131014A par une une composante thermique en plus de la fonction de Band ou de la fonction ISSM. Pour ce sursaut, la contribution de la composante thermique devient négligeable quand ISSM est utilisé comme modèle non thermique en place de Band. La courbure continue de la fonction ISSM permet en effet d'ajuster la courbure spectrale naturelle des GRBs contraire-

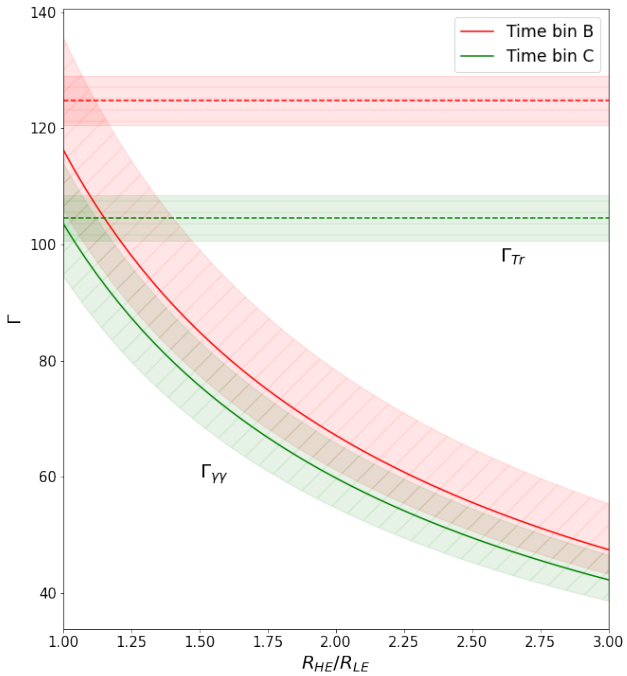

Figure C.3: $\Gamma_{\gamma\gamma}$ en fonction de R_{HE}/R_{LE}. R_{HE} et R_{LE} sont les rayons auxquels les émissions à haute énergie et à basse énergie se produisent.

ment à la fonction de Band, plus rigide. Au final, mon étude montre que la détection d'une éventuelle composante thermique supplémentaire est très sensible au modèle adopté pour décrire la composante non thermique principale des spectres keV-MeV prompts des GRBs. Elle tend à favoriser un scénario dans lequel le réservoir initial d'énergie est constitué en partie d'un flux de Poynting et non pas uniquement de l'énergie thermique de la boule de feu en expansion adiabatique.

C.6 GRB 220101A : le sursaut gamma du LAT le plus lointain

GRB 220101A est le sursaut le plus distant détecté par le LAT à ce jour ($z = 4.618$). Cet événement s'est produit pendant l'une de mes astreintes BA. Son épisode principal d'émission en phase prompte est marqué par l'absence significative de photons aux plus hautes énergies et par une cassure spectrale dans le domaine de fonctionnement du LAT. La haute luminosité et la variabilité de l'émission observée suggèrent que cette cassure spectrale est due à l'opacité à la création de paires qui empêche le rayonnement gamma le plus énergétique de s'échapper du jet. J'ai réalisé une analyse spectrale conjointe des données des instruments GBM (détecteurs NaI et BGO) et LAT (données standard et données LLE) à l'aide de deux chaînes de traitement indépendantes, l'une basée sur *pyXSPEC* et l'autre sur *3ML*, pour évaluer l'énergie et la signification statistique de la cassure spectrale. J'ai démontré que cette cassure est hautement significative quel que soit le modèle utilisé pour ajuster la composante non thermique (Band ou ISSM). Avec l'estimation de l'échelle temporelle de variabilité de l'émission à haute énergie, et à l'aide d'un calcul réaliste d'opacité gamma-gamma, cette atténuation spectrale m'a permis de mesurer la vitesse du jet ultra-relativiste (facteur de Lorentz $\Gamma_{bulk} = \Gamma_{\gamma\gamma} \sim 110$) et d'y localiser les régions d'émission gamma, à une distance au trou noir central (quelques 10^{14} cm) similaire à celle où les chocs internes se produisent typiquement. Figure C.3 montre le facteur de Lorentz $\Gamma_{\gamma\gamma}$ issu du calcul d'opacité gamma-gamma en fonction du rapport entre les rayons où l'émission à haute énergie et l'émission à basse énergie ont eu lieu, ainsi que le facteur de Lorentz Γ_{Tr} correspondant à la transparence à la diffusion de Thompson. Comme on peut le voir sur cette figure, $\Gamma_{\gamma\gamma}$ est supérieur à Γ_{Tr} lorsque les émissions à basse et à haute énergie sont co-spatiales. J'ai présenté ces résultats au *7th Heidelberg International Symposium on High-Energy Gamma-Ray Astronomy* en juillet 2022.

Acknowledgements

I would like to thank my supervisor Frédéric Piron for his professional and human guidance. His patience, perseverance and competence have been a solid reference for my activity, and have greatly helped me to work in a pleasant and stimulant environment. Many thanks to Frédéric, Dahbia Talbi, and Denis Puy for their support during the challenging period that has followed the "confinement", and for their trust in my competences. Thanks to Sheila McBreen and Jean-Luc Atteia for accepting to report on my thesis manuscript, and to Ana Palacios and Elisabetta Bissaldi for accepting to be examiners at my thesis defense. A special thank to the non-permanent staff of the laboratory: the professional and friendly connections have been useful to build a nice working environment. I thank doctor Brigitte Rimlinger Abbar for her compentence and reference during this period. Many thanks to my friends Nadia and Pierre: we met in a particular time of our lives, and our friendship has been valuable during the thesis period. Many thanks to Geny Crastre: her meditation course and her friendly attitude have been particularly important for me to find an good equilibrium in my life. Thanks to Bernard: bringing me to my apartment from the meditation course each time was very kind of him. A great thanks to my italian friends Ambra, Laura, Leonardo, Marco, and Valentina: it is always agreable to keep a connection with them. Thanks to my family, which always welcomes me at home.

Bibliography

Abbott, B. P. et al. (Oct. 2017). "Multi-messenger Observations of a Binary Neutron Star Merger". In: *ApJL* 848.2, L12, p. L12. DOI: 10.3847/2041-8213/aa91c9. arXiv: 1710.05833 [astro-ph.HE].

Abdo, A. A. et al. (Nov. 2009a). "Fermi Observations of GRB 090902B: A Distinct Spectral Component in the Prompt and Delayed Emission". In: *ApJL* 706.1, pp. L138–L144. DOI: 10.1088/0004-637X/706/1/L138. arXiv: 0909.2470 [astro-ph.HE].

Abdo, A. A. et al. (Mar. 2009b). "Fermi Observations of High-Energy Gamma-Ray Emission from GRB 080916C". In: *Science* 323.5922, p. 1688. DOI: 10.1126/science.1169101.

Abdo, A. A. et al. (Oct. 2009c). "The on-orbit calibration of the Fermi Large Area Telescope". In: *Astroparticle Physics* 32.3-4, pp. 193–219. DOI: 10.1016/j.astropartphys.2009.08.002. arXiv: 0904.2226 [astro-ph.IM].

Abdo, A. A. et al. (Apr. 2010). "The First Fermi Large Area Telescope Catalog of Gamma-ray Pulsars". In: *ApJS* 187.2, pp. 460–494. DOI: 10.1088/0067-0049/187/2/460. arXiv: 0910.1608 [astro-ph.HE].

Abdollahi, S. et al. (Mar. 2020). "Fermi Large Area Telescope Fourth Source Catalog". In: *ApJS* 247.1, 33, p. 33. DOI: 10.3847/1538-4365/ab6bcb. arXiv: 1902.10045 [astro-ph.HE].

Ackermann, M. et al. (Mar. 2011). "Detection of a Spectral Break in the Extra Hard Component of GRB 090926A". In: *ApJ* 729.2, 114, p. 114. DOI: 10.1088/0004-637X/729/2/114. arXiv: 1101.2082 [astro-ph.HE].

Ackermann, M. et al. (Nov. 2013). "The First Fermi-LAT Gamma-Ray Burst Catalog". In: *ApJS* 209.1, 11, p. 11. DOI: 10.1088/0067-0049/209/1/11. arXiv: 1303.2908 [astro-ph.HE].

Ackermann, M. et al. (Jan. 2014). "Fermi-LAT Observations of the Gamma-Ray Burst GRB 130427A". In: *Science* 343.6166, pp. 42–47. DOI: 10.1126/science.1242353. arXiv: 1311.5623 [astro-ph.HE].

Ajello, M. et al. (June 2019). "A Decade of Gamma-Ray Bursts Observed by Fermi-LAT: The Second GRB Catalog". In: *ApJ* 878.1, 52, p. 52. DOI: 10.3847/1538-4357/ab1d4e. arXiv: 1906.11403 [astro-ph.HE].

Ajello, M. et al. (Feb. 2020a). "Fermi and Swift Observations of GRB 190114C: Tracing the Evolution of High-energy Emission from Prompt to Afterglow". In: *ApJ* 890.1, 9, p. 9. DOI: 10.3847/1538-4357/ab5b05. arXiv: 1909.10605 [astro-ph.HE].

Ajello, M. et al. (Apr. 2020b). "The Fourth Catalog of Active Galactic Nuclei Detected by the Fermi Large Area Telescope". In: *ApJ* 892.2, 105, p. 105. DOI: 10.3847/1538-4357/ab791e. arXiv: 1905.10771 [astro-ph.HE].

Ajello, M. et al. (Sept. 2021). "Fermi Large Area Telescope Performance after 10 Years of Operation". In: *ApJS* 256.1, 12, p. 12. DOI: 10.3847/1538-4365/ac0ceb. arXiv: 2106.12203 [astro-ph.IM].

Amati, L. et al. (July 2002). "Intrinsic spectra and energetics of BeppoSAX Gamma-Ray Bursts with known redshifts". In: *AAP* 390, pp. 81–89. DOI: 10.1051/0004-6361:20020722. arXiv: astro-ph/0205230 [astro-ph].

Angelakis, E. et al. (Dec. 2016). "RoboPol: the optical polarization of gamma-ray-loud and gamma-ray-quiet blazars". In: *MNRAS* 463.3, pp. 3365–3380. DOI: 10.1093/mnras/stw2217. arXiv: 1609.00640 [astro-ph.HE].

Arimoto, M. et al. (Mar. 2020). "Physical Origin of GeV Emission in the Early Phase of GRB 170405A: Clues from Emission Onsets with Multiwavelength Observations". In: *ApJ* 891.2, 106, p. 106. DOI: 10.3847/1538-4357/ab72f7. arXiv: 2002.00305 [astro-ph.HE].

Arimoto, M. et al. (Jan. 2022). "GRB 220101A: Fermi-LAT detection". In: *GRB Coordinates Network* 31350, p. 1.

Atwood, W. et al. (June 2009). "The Large Area Telescope on the Fermi Gamma-Ray Space Telescope Mission". In: *ApJ* 697.2, pp. 1071–1102. DOI: 10.1088/0004-637X/697/2/1071. arXiv: 0902.1089 [astro-ph.IM].

Atwood, W. et al. (Mar. 2013). "Pass 8: Toward the Full Realization of the Fermi-LAT Scientific Potential". In: *arXiv e-prints*, arXiv:1303.3514, arXiv:1303.3514. arXiv: 1303.3514 [astro-ph.IM].

Axelsson, M. et al. (Oct. 2012). "GRB110721A: An Extreme Peak Energy and Signatures of the Photosphere". In: *ApJL* 757.2, L31, p. L31. DOI: 10.1088/2041-8205/757/2/L31. arXiv: 1207.6109 [astro-ph.HE].

Band, D. et al. (Aug. 1993). "BATSE Observations of Gamma-Ray Burst Spectra. I. Spectral Diversity". In: *ApJ* 413, p. 281. DOI: 10.1086/172995.

Beloborodov, Andrei M. (Feb. 2013). "Regulation of the Spectral Peak in Gamma-Ray Bursts". In: *ApJ* 764.2, 157, p. 157. DOI: 10.1088/0004-637X/764/2/157. arXiv: 1207.2707 [astro-ph.HE].

— (Apr. 2017). "Sub-photospheric Shocks in Relativistic Explosions". In: *ApJ* 838.2, 125, p. 125. DOI: 10.3847/1538-4357/aa5c8c. arXiv: 1604.02794 [astro-ph.HE].

Beniamini, Paz and Tsvi Piran (May 2013). "Constraints on the Synchrotron Emission Mechanism in Gamma-Ray Bursts". In: *ApJ* 769.1, 69, p. 69. DOI: 10.1088/0004-637X/769/1/69. arXiv: 1301.5575 [astro-ph.HE].

Bhat, P. N. (Jan. 2010). "GRB 100724B: Fermi GBM detection." In: *GRB Coordinates Network* 10977, p. 1.

Bloom, J. S., S. R. Kulkarni, and S. G. Djorgovski (Mar. 2002). "The Observed Offset Distribution of Gamma-Ray Bursts from Their Host Galaxies: A Robust Clue to the Nature of the Progenitors". In: *The Astronomical Journal* 123.3, pp. 1111–1148. DOI: 10.1086/33889310.48550/arXiv.astro-ph/0010176. arXiv: astro-ph/0010176 [astro-ph].

Bošnjak, Z. and F. Daigne (Aug. 2014). "Spectral evolution in gamma-ray bursts: Predictions of the internal shock model and comparison to observations". In: *AAP* 568, A45, A45. DOI: 10.1051/0004-6361/201322341. arXiv: 1404.4577 [astro-ph.HE].

— (2022). "GRB prompt emission from the synchrotron radiation of relativistic electrons in a decaying magnetic field". In: *7th Heidelberg International Symposium on High-Energy Gamma-Ray Astronomy*. URL: https://indico.icc.ub.edu/event/46/contributions/1256/.

Bošnjak, Z., F. Daigne, and G. Dubus (May 2009). "Prompt high-energy emission from gamma-ray bursts in the internal shock model". In: *AAP* 498.3, pp. 677–703. DOI: 10.1051/0004-6361/200811375. arXiv: 0811.2956 [astro-ph].

Cash, W. (Mar. 1979). "Parameter estimation in astronomy through application of the likelihood ratio." In: *ApJ* 228, pp. 939–947. DOI: 10.1086/156922.

Connaughton, V. et al. (Feb. 2015). "Localization of Gamma-Ray Bursts Using the Fermi Gamma-Ray Burst Monitor". In: *ApJS* 216.2, 32, p. 32. DOI: 10.1088/0067-0049/216/2/32. arXiv: 1411.2685 [astro-ph.IM].

Daigne, F., Ž. Bošnjak, and G. Dubus (Feb. 2011). "Reconciling observed gamma-ray burst prompt spectra with synchrotron radiation?" In: *AAP* 526, A110, A110. DOI: 10.1051/0004-6361/201015457. arXiv: 1009.2636 [astro-ph.HE].

Daigne, F. and R. Mochkovitch (May 1998). "Gamma-ray bursts from internal shocks in a relativistic wind: temporal and spectral properties". In: *MNRAS* 296.2, pp. 275–286. DOI: 10.1046/j.1365-8711.1998.01305.x. arXiv: astro-ph/9801245 [astro-ph].

de Ugarte Postigo, A. et al. (Jan. 2017). "GRB 170405A: Redshift from OSIRIS/GTC." In: *GRB Coordinates Network* 20990, p. 1.

Derishev, E. V. (June 2007). "Synchrotron emission in the fast cooling regime: which spectra can be explained?" In: *ApSS* 309.1-4, pp. 157–161. DOI: 10.1007/s10509-007-9421-z. arXiv: astro-ph/0611260 [astro-ph].

Derishev, E. V., V. V. Kocharovsky, and Vl. V. Kocharovsky (June 2001). "Physical parameters and emission mechanism in gamma-ray bursts". In: *AAP* 372, pp. 1071–1077. DOI: 10.1051/0004-6361:20010586. arXiv: astro-ph/0006239 [astro-ph].

Desiante, R. et al. (Jan. 2013). "GRB 131014A: Fermi-LAT detection." In: *GRB Coordinates Network* 15333, p. 1.

Dzhappuev, D. D. et al. (Oct. 2022). "Swift J1913.1+1946/GRB 221009A: detection of a 250-TeV photon-like air shower by Carpet-2". In: *The Astronomer's Telegram* 15669, p. 1.

Eichler, David et al. (July 1989). "Nucleosynthesis, neutrino bursts and γ-rays from coalescing neutron stars". In: *Nature* 340.6229, pp. 126–128. DOI: 10.1038/340126a0.

Evans, P. A. and J. P. Osborne (Jan. 2013). "GRB 131014A: XRT position information." In: *GRB Coordinates Network* 15351, p. 1.

Fana Dirirsa, F. et al. (Dec. 2019). "Spectral Analysis of Fermi-LAT Gamma-Ray Bursts with Known Redshift and their Potential Use as Cosmological Standard Candles". In: *ApJ* 887.1, 13, p. 13. DOI: 10.3847/1538-4357/ab4e11. arXiv: 1910.07009 [astro-ph.HE].

Fermi-LAT Collaboration et al. (Apr. 2021). "High-energy emission from a magnetar giant flare in the Sculptor galaxy". In: *Nature Astronomy* 5, pp. 385–391. DOI: 10.1038/s41550-020-01287-8.

Fitzpatrick, G. and S. Xiong (Jan. 2013). "GRB 131014A: Fermi GBM detection." In: *GRB Coordinates Network* 15332, p. 1.

Fu, S. Y. et al. (Jan. 2022). "GRB 220101A: Xinglong-2.16m photometry and spectroscopy". In: *GRB Coordinates Network* 31353, p. 1.

Fynbo, J. P. U. et al. (Jan. 2022). "GRB 220101A: NOT redshift confirmation". In: *GRB Coordinates Network* 31359, p. 1.

Galama, T. J. et al. (Oct. 1998). "An unusual supernova in the error box of the γ-ray burst of 25 April 1998". In: *Nature* 395.6703, pp. 670–672. DOI: 10.1038/2715010.48550/arXiv.astro-ph/9806175. arXiv: astro-ph/9806175 [astro-ph].

Gehrels, N., E. Chipman, and D. Kniffen (June 1994). "The Compton Gamma Ray Observatory". In: *ApJS* 92, p. 351. DOI: 10.1086/191978.

Ghisellini, G. et al. (July 2017). "The Fermi blazar sequence". In: *MNRAS* 469.1, pp. 255–266. DOI: 10.1093/mnras/stx806. arXiv: 1702.02571 [astro-ph.HE].

Gill, Ramandeep and Jonathan Granot (Mar. 2018). "The effect of pair cascades on the high-energy spectral cut-off in gamma-ray bursts". In: *MNRAS* 475.1, pp. L1–L5. DOI: 10.1093/mnrasl/slx199. arXiv: 1710.11114 [astro-ph.HE].

Gill, Ramandeep and Christopher Thompson (Dec. 2014). "Non-thermal Gamma-Ray Emission from Delayed Pair Breakdown in a Magnetized and Photon-rich Outflow". In: *ApJ* 796.2, 81, p. 81. DOI: 10.1088/0004-637X/796/2/81. arXiv: 1406.4774 [astro-ph.HE].

Goldstein, Adam et al. (Oct. 2013). "The BATSE 5B Gamma-Ray Burst Spectral Catalog". In: *ApJS* 208.2, 21, p. 21. DOI: 10.1088/0067-0049/208/2/21. arXiv: 1311.7135 [astro-ph.HE].

Golenetskii, S. et al. (Jan. 2012). "IPN triangulation of GRB 120323A (short/very intense)." In: *GRB Coordinates Network* 13102, p. 1.

Granot, Jonathan (May 2009). "GRB Theory in the Fermi Era". In: *arXiv e-prints*, arXiv:0905.2206, arXiv:0905.2206. arXiv: 0905.2206 [astro-ph.HE].

Granot, Jonathan, Johann Cohen-Tanugi, and Eduardo do Couto e. Silva (Apr. 2008). "Opacity Buildup in Impulsive Relativistic Sources". In: *ApJ* 677.1, pp. 92–126. DOI: 10.1086/526414. arXiv: 0708.4228 [astro-ph].

Gruber, D. and V. Connaughton (Jan. 2012). "GRB 120323A: Fermi GBM detection." In: *GRB Coordinates Network* 13099, p. 1.

Gruber, D. et al. (Mar. 2014). "The Fermi GBM Gamma-Ray Burst Spectral Catalog: Four Years of Data". In: *ApJS* 211.1, 12, p. 12. DOI: 10.1088/0067-0049/211/1/12. arXiv: 1401.5069 [astro-ph.HE].

Guiriec, S. et al. (Feb. 2011). "Detection of a Thermal Spectral Component in the Prompt Emission of GRB 100724B". In: *ApJL* 727.2, L33, p. L33. DOI: 10.1088/2041-8205/727/2/L33. arXiv: 1010.4601 [astro-ph.HE].

Guiriec, S. et al. (June 2013). "Evidence for a Photospheric Component in the Prompt Emission of the Short GRB 120323A and Its Effects on the GRB Hardness-Luminosity Relation". In: *ApJ* 770.1, 32, p. 32. DOI: 10.1088/0004-637X/770/1/32. arXiv: 1210.7252 [astro-ph.HE].

Guiriec, S. et al. (Nov. 2015a). "GRB 131014A: A Laboratory for Studying the Thermal-like and Non-thermal Emissions in Gamma-Ray Bursts, and the New $L^{nTh}{}_i$-$E^{nTh,rest}{}_{peak,i}$ Relation". In: *ApJ* 814.1, 10, p. 10. DOI: 10.1088/0004-637X/814/1/10. arXiv: 1507.06976 [astro-ph.HE].

Guiriec, S. et al. (July 2015b). "Toward a Better Understanding of the GRB Phenomenon: a New Model for GRB Prompt Emission and its Effects on the New $L_i{}^{NT}$- $E_{peak,i}{}^{rest,NT}$ Relation". In: *ApJ* 807.2, 148, p. 148. DOI: 10.1088/0004-637X/807/2/148. arXiv: 1501.07028 [astro-ph.HE].

Harrison, F. A. et al. (Oct. 1999). "Optical and Radio Observations of the Afterglow from GRB 990510: Evidence for a Jet". In: *ApJL* 523.2, pp. L121–L124. DOI: 10.1086/31228210.48550/arXiv.astro-ph/9905306. arXiv: astro-ph/9905306 [astro-ph].

Hascoët, R. et al. (Mar. 2012). "Do Fermi Large Area Telescope observations imply very large Lorentz factors in gamma-ray burst outflows?" In: *MNRAS* 421.1, pp. 525–545. DOI: 10.1111/j.1365-2966.2011.20332.x. arXiv: 1107.5737 [astro-ph.HE].

Heussaff, V., J. -L. Atteia, and Y. Zolnierowski (Sept. 2013). "The E_{peak} - E_{iso} relation revisited with Fermi GRBs. Resolving a long-standing debate?" In: *AAP* 557, A100, A100. DOI: 10.1051/0004-6361/201321528. arXiv: 1306.1757 [astro-ph.HE].

Hjorth, Jens et al. (June 2003). "A very energetic supernova associated with the γ-ray burst of 29 March 2003". In: *Nature* 423.6942, pp. 847–850. DOI: 10.1038/nature0175010.48550/arXiv.astro-ph/0306347. arXiv: astro-ph/0306347 [astro-ph].

Huang, Yong et al. (Oct. 2022). "LHAASO observed GRB 221009A with more than 5000 VHE photons up to around 18 TeV". In: *GRB Coordinates Network* 32677, p. 1.

Kagaya, Mika et al. (Nov. 2017). "Constraints on Physical Conditions for the Acceleration on Ultra-high-energy Cosmic Rays in Nearby Active Galactic Nuclei (AGNs) Observed with the Fermi Large Area Telescope". In: *ApJ* 850.1, 33, p. 33. DOI: 10.3847/1538-4357/aa9226. arXiv: 1710.02649 [astro-ph.HE].

Kaneko, Yuki et al. (Sept. 2006). "The Complete Spectral Catalog of Bright BATSE Gamma-Ray Bursts". In: *ApJS* 166.1, pp. 298–340. DOI: 10.1086/505911. arXiv: astro-ph/0601188 [astro-ph].

Kouveliotou, Chryssa et al. (Aug. 1993). "Identification of Two Classes of Gamma-Ray Bursts". In: *ApJL* 413, p. L101. DOI: 10.1086/186969.

Laskar, T. (Jan. 2022). "GRB 220101A: ALMA detection". In: *GRB Coordinates Network* 31372, p. 1.

Lesage, S., C. Meegan, and Fermi Gamma-ray Burst Monitor Team (Jan. 2022). "GRB 220101A: Fermi GBM Detection". In: *GRB Coordinates Network* 31360, p. 1.

Lien, Amy et al. (Sept. 2016). "The Third Swift Burst Alert Telescope Gamma-Ray Burst Catalog". In: *ApJ* 829.1, 7, p. 7. DOI: 10.3847/0004-637X/829/1/7. arXiv: 1606.01956 [astro-ph.HE].

MAGIC Collaboration, V. A. Acciari, and S. Ansoldi (Nov. 2019). "Observation of inverse Compton emission from a long gamma-ray burst". In: *Nature* 575.7783, pp. 459–463. DOI: 10.1038/s41586-019-1754-6. arXiv: 2006.07251 [astro-ph.HE].

Malesani, D. et al. (Jan. 2009). "GRB 090926A: VLT/X-shooter redshift." In: *GRB Coordinates Network* 9942, p. 1.

Meegan, Charles et al. (Sept. 2009). "The Fermi Gamma-ray Burst Monitor". In: *ApJ* 702.1, pp. 791–804. DOI: 10.1088/0004-637X/702/1/791. arXiv: 0908.0450 [astro-ph.IM].

Meszaros, P. and M. J. Rees (Mar. 1993). "Relativistic Fireballs and Their Impact on External Matter: Models for Cosmological Gamma-Ray Bursts". In: *ApJ* 405, p. 278. DOI: 10.1086/172360.

Narayan, Ramesh, Bohdan Paczynski, and Tsvi Piran (Aug. 1992). "Gamma-Ray Bursts as the Death Throes of Massive Binary Stars". In: *ApJL* 395, p. L83. DOI: 10.1086/18649310.48550/arXiv.astro-ph/9204001. arXiv: astro-ph/9204001 [astro-ph].

Neyman, J. and E. S. Pearson (July 1928). "On the Use and Interpretation of Certain Test Criteria for Purposes of Statistical Inference: Part I". In: *Oxford Journals*, pp. 175–240.

Noda, Koji and Robert Daniel Parsons (Jan. 2022). "Gamma-Ray Bursts at TeV Energies: Observational Status". In: *Galaxies* 10.1, p. 7. DOI: 10.3390/galaxies10010007.

Norris, J. P. et al. (July 2005). "Long-Lag, Wide-Pulse Gamma-Ray Bursts". In: *ApJ* 627.1, pp. 324–345. DOI: 10.1086/430294. arXiv: astro-ph/0503383 [astro-ph].

Oganesyan, G. et al. (Sept. 2017). "Detection of Low-energy Breaks in Gamma-Ray Burst Prompt Emission Spectra". In: *ApJ* 846.2, 137, p. 137. DOI: 10.3847/1538-4357/aa831e. arXiv: 1709.04689 [astro-ph.HE].

Oganesyan, G. et al. (Sept. 2018). "Characterization of gamma-ray burst prompt emission spectra down to soft X-rays". In: *AAP* 616, A138, A138. DOI: 10.1051/0004-6361/201732172. arXiv: 1710.09383 [astro-ph.HE].

Omodei, N. et al. (Apr. 2020). "GRB 200415A: Fermi-LAT detection". In: *GRB Coordinates Network* 27586, p. 1.

Paciesas, William S. et al. (Mar. 2012). "The Fermi GBM Gamma-Ray Burst Catalog: The First Two Years". In: *ApJS* 199.1, 18, p. 18. DOI: 10.1088/0067-0049/199/1/18. arXiv: 1201.3099 [astro-ph.HE].

Paczynski, Bohdan (Jan. 1991). "Cosmological gamma-ray bursts." In: *Acta Astronomica* 41, pp. 257–267.

Padovani, P. et al. (Apr. 2016). "Extreme blazars as counterparts of IceCube astrophysical neutrinos". In: *MNRAS* 457.4, pp. 3582–3592. DOI: 10.1093/mnras/stw228. arXiv: 1601.06550 [astro-ph.HE].

Palit, Sourav, Akash Anumarlapudi, and Varun Bhalerao (Oct. 2021). "Revisiting the Earth's atmospheric scattering of X-ray/γ-rays and its effect on space observation: Implication for GRB spectral analysis". In: *Journal of Astrophysics and Astronomy* 42.2, 69, p. 69. DOI: 10.1007/s12036-021-09759-7.

Pe'er, Asaf and Bing Zhang (Dec. 2006). "Synchrotron Emission in Small-Scale Magnetic Fields as a Possible Explanation for Prompt Emission Spectra of Gamma-Ray Bursts". In: *ApJ* 653.1, pp. 454–461. DOI: 10.1086/508681. arXiv: astro-ph/0605641 [astro-ph].

Pelassa, V. et al. (Feb. 2010). "The LAT Low-Energy technique for Fermi Gamma-Ray Bursts spectral analysis". In: *arXiv e-prints*, arXiv:1002.2617, arXiv:1002.2617. arXiv: 1002.2617 [astro-ph.HE].

Perley, D. A. (Jan. 2022). "GRB 220101A: Liverpool telescope imaging of a high-redshift afterglow". In: *GRB Coordinates Network* 31357, p. 1.

Pillera, R. et al. (Oct. 2022). "GRB 221009A: Fermi-LAT refined analysis". In: *GRB Coordinates Network* 32658, p. 1.

Piran, Tsvi (Oct. 2004). "The physics of gamma-ray bursts". In: *Reviews of Modern Physics* 76.4, pp. 1143–1210. DOI: 10.1103/RevModPhys.76.114310.48550/arXiv.astro-ph/0405503. arXiv: astro-ph/0405503 [astro-ph].

Poolakkil, S. et al. (May 2021). "The Fermi-GBM Gamma-Ray Burst Spectral Catalog: 10 yr of Data". In: *ApJ* 913.1, 60, p. 60. DOI: 10.3847/1538-4357/abf24d. arXiv: 2103.13528 [astro-ph.HE].

Preece, R. et al. (Oct. 1998). "The Synchrotron Shock Model Confronts a "Line of Death" in the BATSE Gamma-Ray Burst Data". In: *ApJL* 506.1, pp. L23–L26. DOI: 10.1086/311644. arXiv: astro-ph/9808184 [astro-ph].

Preece, R. et al. (Jan. 2014). "The First Pulse of the Extremely Bright GRB 130427A: A Test Lab for Synchrotron Shocks". In: *Science* 343.6166, pp. 51–54. DOI: 10.1126/science.1242302. arXiv: 1311.5581 [astro-ph.HE].

Racusin, J. L. et al. (June 2009). "Jet Breaks and Energetics of Swift Gamma-Ray Burst X-Ray Afterglows". In: *ApJ* 698.1, pp. 43–74. DOI: 10.1088/0004-637X/698/1/43. arXiv: 0812.4780 [astro-ph].

Ravasio, M. E. et al. (May 2018). "Consistency with synchrotron emission in the bright GRB 160625B observed by Fermi". In: *AAP* 613, A16, A16. DOI: 10.1051/0004-6361/201732245. arXiv: 1711.03106 [astro-ph.HE].

Ravasio, M. E. et al. (May 2019). "Evidence of two spectral breaks in the prompt emission of gamma-ray bursts". In: *AAP* 625, A60, A60. DOI: 10.1051/0004-6361/201834987. arXiv: 1903.02555 [astro-ph.HE].

Rhoads, James E. (Nov. 1999). "The Dynamics and Light Curves of Beamed Gamma-Ray Burst Afterglows". In: *ApJ* 525.2, pp. 737–749. DOI: 10.1086/30790710.48550/arXiv.astro-ph/9903399. arXiv: astro-ph/9903399 [astro-ph].

Romani, Roger W. and I. -A. Yadigaroglu (Jan. 1995). "Gamma-Ray Pulsars: Emission Zones and Viewing Geometries". In: *ApJ* 438, p. 314. DOI: 10.1086/175076. arXiv: astro-ph/9401045 [astro-ph].

Ryde, F. (Jan. 1999). "Smoothly Broken Power Law Spectra of Gamma-Ray Bursts". In: *Astrophysical Letters and Communications* 39, p. 281. arXiv: astro-ph/9811462 [astro-ph].

Ryde, F. and A. Pe'er (Sept. 2009). "Quasi-blackbody Component and Radiative Efficiency of the Prompt Emission of Gamma-ray Bursts". In: *ApJ* 702.2, pp. 1211–1229. DOI: 10.1088/0004-637X/702/2/1211. arXiv: 0811.4135 [astro-ph].

Ryde, F. and R. Svensson (Jan. 2000). "On the Time Evolution of Gamma-Ray Burst Pulses: A Self-Consistent Description". In: *ApJL* 529.1, pp. L13–L16. DOI: 10.1086/312443. arXiv: astro-ph/9912351 [astro-ph].

Ryde, F. et al. (Feb. 2010). "Identification and Properties of the Photospheric Emission in GRB090902B". In: *ApJL* 709.2, pp. L172–L177. DOI: 10.1088/2041-8205/709/2/L172. arXiv: 0911.2025 [astro-ph.HE].

Sari, Re'em, Tsvi Piran, and Ramesh Narayan (Apr. 1998). "Spectra and Light Curves of Gamma-Ray Burst Afterglows". In: *ApJL* 497.1, pp. L17–L20. DOI: 10.1086/311269. arXiv: astro-ph/9712005 [astro-ph].

Scargle, Jeffrey D. et al. (Feb. 2013). "Studies in Astronomical Time Series Analysis. VI. Bayesian Block Representations". In: *ApJ* 764.2, 167, p. 167. DOI: 10.1088/0004-637X/764/2/167. arXiv: 1207.5578 [astro-ph.IM].

Stanek, K. Z. et al. (Sept. 1999). "BVRI Observations of the Optical Afterglow of GRB 990510". In: *ApJL* 522.1, pp. L39–L42. DOI: 10.1086/31221910.48550/arXiv.astro-ph/9905304. arXiv: astro-ph/9905304 [astro-ph].

Tanaka, Y. et al. (Jan. 2010). "GRB 100724B: Fermi LAT and GBM analysis." In: *GRB Coordinates Network* 10978, p. 1.

Tanvir, N. R. et al. (Jan. 2016). "GRB 160509A Gemini North redshift." In: *GRB Coordinates Network* 19419, p. 1.

Tierney, D. et al. (Feb. 2013). "Anomalies in low-energy gamma-ray burst spectra with the Fermi Gamma-ray Burst Monitor". In: *AAP* 550, A102, A102. DOI: 10.1051/0004-6361/201220710. arXiv: 1301.4859 [astro-ph.HE].

Toffano, M. et al. (Aug. 2021). "The slope of the low-energy spectrum of prompt gamma-ray burst emission". In: *AAP* 652, A123, A123. DOI: 10.1051/0004-6361/202141032. arXiv: 2106.03868 [astro-ph.HE].

Tohuvavohu, A. et al. (Jan. 2022). "GRB 220101A: Swift detection of a burst with a bright optical counterpart". In: *GRB Coordinates Network* 31347, p. 1.

Vianello, G. et al. (May 2017). "Searching for High-energy Gamma-ray Counterparts to Gravitational-wave Sources with Fermi-LAT: A Needle in a Haystack". In: *ApJL* 841.1, L16, p. L16. DOI: 10.3847/2041-8213/aa7262. arXiv: 1607.01793 [astro-ph.HE].

Vianello, G. et al. (Sept. 2018). "The Bright and the Slow—GRBs 100724B and 160509A with High-energy Cutoffs at $\lesssim$100 MeV". In: *ApJ* 864.2, 163, p. 163. DOI: 10.3847/1538-4357/aad6ea. arXiv: 1706.01481 [astro-ph.HE].

von Kienlin, A. et al. (Apr. 2020). "The Fourth Fermi-GBM Gamma-Ray Burst Catalog: A Decade of Data". In: *ApJ* 893.1, 46, p. 46. DOI: 10.3847/1538-4357/ab7a18. arXiv: 2002.11460 [astro-ph.HE].

Wilks, S. S. (1938). "The Large-Sample Distribution of the Likelihood Ratio for Testing Composite Hypotheses". In: *The Annals of Mathematical Statistics*, pp. 60–62.

Woosley, S. E. (Mar. 1993). "Gamma-Ray Bursts from Stellar Mass Accretion Disks around Black Holes". In: *ApJ* 405, p. 273. DOI: 10.1086/172359.

Yassine, M. (Sept. 2017). "The prompt emission of Gamma-Ray Bursts : analysis and interpretation of Fermi observations". Theses. Université Montpellier. URL: https://tel.archives-ouvertes.fr/tel-01739257.

Yassine, M. et al. (Oct. 2017). "Time evolution of the spectral break in the high-energy extra component of GRB 090926A". In: *AAP* 606, A93, A93. DOI: 10.1051/0004-6361/201630353. arXiv: 1705.03384 [astro-ph.HE].

Yassine, M. et al. (Aug. 2020). "A new fitting function for GRB MeV spectra based on the internal shock synchrotron model". In: *AAP* 640, A91, A91. DOI: 10.1051/0004-6361/201937057. arXiv: 2004.03987 [astro-ph.HE].

Yonetoku, D. et al. (July 2004). "Gamma-Ray Burst Formation Rate Inferred from the Spectral Peak Energy-Peak Luminosity Relation". In: *ApJ* 609.2, pp. 935–951. DOI: 10.1086/421285. arXiv: astro-ph/0309217 [astro-ph].

Zhang, B. (2019). *The physics of gamma-ray bursts*.

— (Feb. 2020). "Synchrotron radiation in γ-ray bursts prompt emission". In: *Nature Astronomy* 4, pp. 210–211. DOI: 10.1038/s41550-020-1041-3. arXiv: 2002.09638 [astro-ph.HE].

Résumé

Cinquante cinq ans après la découverte des sursauts gamma (GRBs), les mécanismes physiques à l'origine de l'émission prompte ($\sim 0.1 - 100\,\mathrm{s}$) de leur jet ultra-relativiste font encore l'objet de débats. La thèse porte sur cette courte phase d'émission, très variable et très énergétique, en particulier à haute énergie (du keV au MeV). Schématiquement, on peut distinguer l'émission non thermique d'électrons accélérés par les ondes de choc dans le jet ou par reconnexion magnétique, de l'émission quasi-thermique proche de la photosphère. Mon travail est basé sur l'utilisation d'une version du modèle de chocs internes, et sur la paramétrisation des spectres synchrotron que le code numérique prédit aux keV-MeV. Ce modèle spectral ("Internal Shock Synchrotron Model", ISSM) présente une courbure continue résultant de la superposition des spectres synchrotron instantanés qui évoluent rapidement aux chocs. Dans la première partie de la thèse, j'ai confronté ce modèle aux spectres d'émission prompte des GRBs détectés par l'instrument GBM de la mission spatiale *Fermi*, et j'ai comparé ses performances à celles de modèles phénoménologiques tels que la fonction ad-hoc de Band. Ces derniers modèles mathématiques sont couramment utilisés dans la communauté pour ajuster sommairement les spectres de GRBs aux keV-MeV. J'ai utilisé 460 GRBs détectés par le GBM, que j'ai sélectionnés pour leur grande fluence afin d'atteindre la précision spectrale requise pour distinguer les modèles entre eux. J'ai développé une chaîne complète d'analyse (préparation des données, sélection des détecteurs du GBM sur des critères quantitatifs précis, segmentation des courbes de lumière, ajustements spectraux, scripts de post-traitement). J'ai montré que le modèle physique ISSM surclasse tous les modèles phénoménologiques, qu'il reproduit mieux les spectres observés sur de courtes échelles de temps, et encore mieux lorsque ces spectres sont moyennés. Ces résultats renforcent avec un haut niveau de confiance l'hypothèse d'une origine synchrotron aux chocs internes de l'émission prompte non thermique des GRBs. Dans une deuxième partie, j'ai étudié les quelques rares GRBs présentant une composante spectrale quasi-thermique additionnelle à basse énergie. Cette émission photosphérique est attendue dans le scénario dit de la "boule de feu", dans lequel le plasma des éjecta entre en expansion sous l'effet de sa propre pression pour atteindre une vitesse ultra-relativiste. J'ai démontré que la détection de cette composante spectrale est fortement conditionnée à la modélisation de la composante non thermique synchrotron. En particulier, l'utilisation d'un modèle réaliste comme ISSM laisse peu de place à une composante additionnelle. Ces résultats semblent ainsi indiquer un réservoir initial d'énergie constitué en partie d'un flux de Poynting et non pas uniquement de l'énergie thermique de la boule de feu en expansion adiabatique. La dernière partie de la thèse concerne l'étude du sursaut gamma exceptionnel GRB 220101A avec les instruments GBM et LAT de *Fermi*. Ce sursaut très énergétique est le plus lointain jamais détecté par le LAT (z=4.618). Il s'ajoute aux quatre rares GRBs qui présentent une cassure spectrale à haute énergie associée à une émission variable. A l'aide d'un calcul réaliste d'opacité gamma-gamma, cette atténuation spectrale m'a permis de mesurer la vitesse du jet ultra-relativiste (facteur de Lorentz $\Gamma \sim 110$) et d'y localiser les régions d'émission gamma, à une distance au trou noir central (quelques $10^{14}\,\mathrm{cm}$) similaire à celle où les chocs internes se produisent typiquement.

Mots clés: sursauts gamma - émission prompte - opacité gamma à la création de paires - facteur de Lorentz du jet - émission synchrotron - satellite *Fermi*

Abstract

Fifty five years after the discovery of gamma-ray bursts (GRBs), the physical mechanisms responsible for the prompt emission ($\sim 0.1-100\,\mathrm{s}$) of their ultra-relativistic jet are still debated. This thesis deals with this short emission phase, very variable and very energetic, in particular at high energy (from keV to MeV). Schematically, one can distinguish the non-thermal emission of electrons accelerated by shocks in the jet or by magnetic reconnection, from the quasi-thermal emission near the photosphere. My work is based on a version of the internal-shock model, and on the parameterization of the synchrotron spectra that the numerical code predicts at keV-MeV energies. This spectral model (Internal Shock Synchrotron Model, ISSM) presents a continuous curvature resulting from the superposition of instantaneous synchrotron spectra which evolve rapidly in the shocked regions. In the first part of the thesis, I confronted this model to the prompt emission spectra of GRBs detected by the GBM instrument of the *Fermi* space mission, and I compared its performance to phenomenological models such as the ad-hoc Band function. The latter mathematical models are commonly used in the community to summarily fit GRB keV-MeV spectra. I used 460 GRBs detected by the GBM, which I selected for their high fluence in order to reach the spectral accuracy that is required to distinguish between models. I developed a complete analysis chain (data preparation, selection of GBM detectors on precise quantitative criteria, light curve segmentation, spectral fits, post-processing scripts). I showed that the ISSM physical model outperforms all phenomenological models, that it reproduces better the observed spectra on short timescales, and even better when these spectra are averaged. These results reinforce with a high level of confidence the hypothesis of an internal-shock synchrotron origin of the non-thermal prompt emission of GRBs. In a second part, I studied the few rare GRBs showing an additional quasi-thermal spectral component at low energy. This photospheric emission is expected in the so-called "fireball" scenario, in which the plasma of the ejecta expands under its own pressure and reach an ultra-relativistic speed. I showed that the detection of this spectral component depends strongly on the modeling of the non-thermal synchrotron component. In particular, the use of a realistic model like ISSM leaves little room for an additional component. These results thus seem to indicate an initial energy reservoir consisting partly of a Poynting flux and not only of the thermal energy of the adiabatically expanding fireball. The last part of the thesis concerns the study of the exceptional gamma-ray burst GRB 220101A with the GBM and LAT instruments of *Fermi*. This very energetic burst is the most distant ever detected by the LAT (z=4.618). It lies among the five rare GRBs which present a spectral break at high energy associated with a variable emission. Using a realistic gamma-gamma opacity calculation, this spectral attenuation allowed to measure the velocity of the ultra-relativistic jet (Lorentz factor $\Gamma \sim 110$) and to locate the gamma emission regions, at a distance from the central black hole (a few $10^{14}\,\mathrm{cm}$) where internal shocks typically take place.

Keywords: gamma-ray bursts - prompt emission - gamma-ray opacity to pair creation - jet Lorentz factor - synchrotron radiation - *Fermi* gamma-ray space telescope